UNIVERSITY OF SOUTHAMPTON

An Investigation of the Oceanic Skin Temperature Devation

by

C J Donlon

Submitted in partial fulfilment for the degree of Doctor of Philosophy

Department of Oceanography, Faculty of Science, University of Southampton

Submitted in October 1994

UNIVERSITY OF SOUTHAMPTON

ABSTRACT

FACULTY OF SCIENCE
DEPARTMENT OF OCEANOGRAPHY
Doctor of Philosophy

An Investigation of the Oceanic Skin Temperature Deviation

by Craig James Donlon

Satellite and *in-situ* radiometric measurements of sea surface temperature (SST) together with conventional SST and meteorological parameters are used to provide a description of the ocean surface skin temperature deviation (skin temperature - bulk temperature, ΔT) for a transect made across the Atlantic ocean from 50°N 00°W to 23°S 35°W during September and October 1992. Methods of *in-situ* SST measurement are discussed and the errors associated with each technique are given. The principles of infra red radiometry are explained. The differences between the calibration strategies used to determine SST using infra-red radiometers from both *in-situ* and satellite platforms are reviewed and the errors associated with each technique are given. Differences between published *in-situ* infra red SST data indicate that there may be a bias in these data as a consequence of the calibration strategy adopted. The need for an inter calibration of *in-situ* infra red radiometer systems used for the validaion of satellite SST is highlighted. Satellite SST algorithms are discussed and the principles of atmospheric correction are explained. The difference between the radiometric 'skin' temperature of the ocean and the conventional 'bulk' temperature at depth is defined. A review of current observations of ΔT is given. Several theoretical treatments of ΔT are reviewed. The definitions of the surface fluxes of heat and momentum are given. A description of the collection of data and an analysis of the calibration of the infra-red radiometer used to measure the skin temperature is presented.

Data have been processed to obtain ΔT and the surface fluxes of heat and momentum nave been evaluated according to the bulk aerodynamic formulae. The relationships between ΔT and the measurements made are presented for the entire data set and for day and night time observations separately. Four time series of observed data are presented and the local conditions during the time of measurement are used to discuss ΔT. ΔT has a mean value of 0.39°C ±0.3°C and is shown to be a persistent feature of the Atlantic ocean. Correlation analyses reveal the skin and bulk temperature fields to be correlated at length scales > 155 km. Night time correlations are consistently higher than the day time at all length scales. For this reason it is recommended that satellite validation data are only collected during the night. High sea states are shown to affect both *in-situ* and satellite observations of SST biasing these data warm. The regional nature of ΔT is presented which is related to the dominant atmosphere-ocean conditions for each region. ΔT is shown to be greatest at the higher latitudes and weak in the tropical regions.

Several parameterisations of ΔT are used to obtain estimates of ΔT using the data collected. These are found to be inadequate to predict ΔT at small temporal scales. A regional dependence of ΔT is found in these parameterisations. The coefficient λ of the Saunders (1969) parameterisation has been evaluated and is shown to have a regional dependence on the local atmosphere ocean conditions. The coefficient C_1 and C_2 of the Hasse (1971) parameterisation have been evaluated using the data collected. These are C_1=4.74 and C_2=1.22.

A comparison between the Along Track Scanning Radiometer Average SST is presented. Satellite - *in-situ* bulk ΔT has been obtained and shown to be comparable to that observed *in-situ*. This comparison highlights the need to make skin SST validation measurements rather than bulk SST measurements. The ATSR ASST data are shown to return a SST accurate to better than 0.3°C.

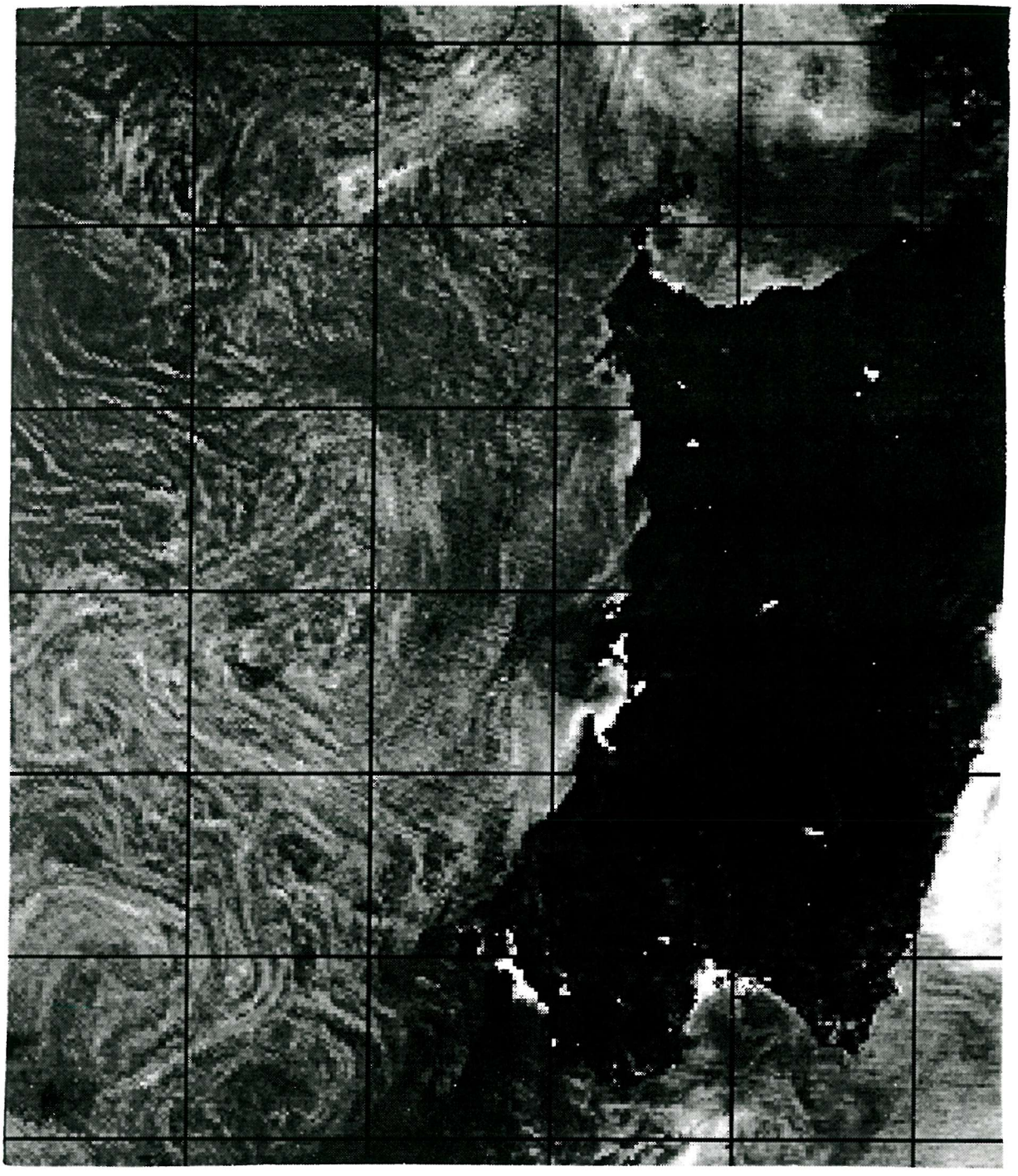

Cover plate: Swirling Eddies off the coast of Corsica. 11μm ATSR brightness temperature image. Temperature diffwerences of > 0.7°C exist within the streaky areas. Image size is 400 x 400 km

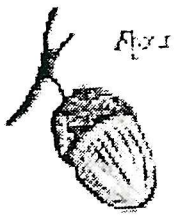

To Ruth and Aaron Joe

Table of Contents

Acknowledgements

I would like to thank the following for their help, patience and assistance during the course of this work:

British Antarctic Survey: J Thomas (especially), J Turner, B Althouse, J Turner, P Woodruff C Day, Harry the Doc and King Fid for their help.

RRS *'James Clark Ross':* The Captain, Officers and Crew with special thanks to Mick, Danny, Ali and 'Shady'.

Rutherford Appleton Laboratories: C Mutlow, A Zavody, P Bailey, M Panter, I Barton (CSRIO), R Knight, T Nightingale and P Kent.

Southampton University: I Robinson, N Ward, M Tenorio, D Woolf, *Dr* S L D Jones, J Taylor, G Fisher, N Jenkinson, B Stringer J Gibbs, J Dix and J Smith.

Special thanks go to John McArdle for his confidence in my work and for his dedicated help. Cheers mate !

Also thanks to PRANGLE, Nicci P, Marcel C, Grant L, Maitham, Cress, and all of the others at no 6 and 56 !

The greatest thanks of all go to Ruth.

List of figures.

List of Tables

Acronyms used in this study

ΔT	Skin-Bulk temperature deviation
AATSR	Advanced Along Track Scanning Radiometer.
AO-GGM	Atmosphere-Ocean General Circulation Model
APT	Automatic Picture Transfer
ATM	Airborne Thematic Mapper
ATSR	Along Track Scanning Radiometer
AVHRR	Advanced Very High Resolution Radiometer
BAS	British Antarctic Survey
CSIRO	Commonwealth Scientific and Industrial Research Organisation, Australia
EMIN	European Marine Interdisciplinary Network
ERS	European Remote Sensing satellite
ESA	European Space Agency
FFT	Fast Fourier Transform
FoV	Field of View
GCM	General Circulation Model
GPS	Global Positioning System
HRPT	High Resolution Picture Transfer
IDL	Interactive Data Language
IFoV	Instantaneous Field of View
IOS	Institute of Oceanographic Sciences, Uk
IPCC	Intergovernmental Panel on Climate Change
JCR	RRS *'James Clark Ross'*
JPL	Jet Propulsion Laboratory, USA
NASA	National Aeronautics and Space Administration, USA
NASDA	National Space Development Administration, Japan
NEΔT	Noise Equivalent Difference Temperature
NOAA	National Oceanic and Atmospheric Administration, USA

NRSC	National Remote Sensing Centre, UK
PC	Personal Computer
PRT	Platinum Resistance Thermometer
RAL	Rutherford Appleton Laboratory, UK
SADIST	Synthesis of ATSR Data Into Sea-surface Temperature
SAR	Synthetic Aperture Radar
SIL	Satellites International Limited, UK
SST	Sea Surface Temperature
TOGA	Tropical Ocean and Global Atmosphere (programme)
UKMO	United Kingdom Meteorological Office
UKMOSST	United Kingdom Meterological Office Sea Surface Temperature
UNESCO	United Nations Educational, Scientific and Cultural Organization
VISR	Visible and Infra-red Scanning Radiometer
VOS	Voulunteer Observing Ships
VTIR	Visible and Thermal Infra-red Radiometer
WCRP	World Climate Research Programme
WMO	World Meterological Organisation
WOCE	World Ocean Circulation Experiment

Chapter 1. Introduction.

Over the last twenty years there has been a dramatic increase in the number of observations made in the ocean as scientists search for fuller descriptions of the earth's fluid environment. Sea surface temperature (SST) is one of the most frequent of these measurements and the importance of this parameter for both oceanographers and meteorologists must not be underestimated (Data requirements for climate change, Hadley Centre, 1994).

The oceans and atmosphere form a coupled system separated by an interface through which heat, moisture and momentum are exchanged. This system is forced by solar radiation which warms the earth's surface unevenly. Excess heating at the equator relative to the polar regions maintains a latitudinal temperature gradient driving fluid motions, in both the atmosphere and the oceans. Such movements result in a redistribution of heat throughout the earth's thermal system as it attempts to achieve thermal equilibrium. The transfer of thermal energy is dependent on dynamic processes that have long term mean, seasonal, diurnal and transient components. Examples of such processes include oceanic basin scale currents, mesoscale eddies and atmospheric pressure systems with their associated frontal features.

SST is the parameter that critically controls the surface heat fluxes which in turn define the physical state of the ocean-atmosphere boundary conditions. The high thermal capacity of water causes the oceans to act as a huge climate moderator via the exchange of heat through the air-sea interface. SST is also important in the exchange of gasses between the atmosphere and ocean systems. For example SST limits the ability of the ocean to assimilate atmospheric $C0_2$ which has a significant role in defining present scenarios of global warming. In addition, SST anomalies are key indicators of environmental change, for instance the cyclic El ninô phenomena, which may be a response to long term climatic warming or cooling events.

SST is thus a vital parameter to consider when attempting to describe and quantify the state of the earth's climatic change. It is a key factor in the physical processes underpinning the earth's surface energy balance. It forces the radiative, sensible and latent heat transports across the air - sea interface and ultimately, the overall circulation of the oceans and atmosphere systems.

The techniques used to measure SST over the last century have continuously evolved and have varied in their precision and accuracy. Hand held mercury in glass thermometers were originally used by early observers employing a variety of sampling techniques of which the simple 'ship's bucket' was the most popular. The bucket was thrown into the water and when hauled back onto deck the water temperature was taken. Such data were limited in their geographic extent and were poorly calibrated. More recently many ships have been fitted with hull mounted thermistor sensors which can be read from an analogue bridge mounted display easing the burden of measurement. Today daily global SST measurements are made using infra-red radiometers mounted on earth orbiting satellite systems. These have the important advantage of synoptically measuring the two dimensional structure of the sea surface temperature field.

Each of the techniques used to determine SST delivers a biased SST data set dependant on the particular technique used. Bucket SST measures are not only affected by solar warming and evaporative cooling but also by errors when reading the thermometer. Warming of hull mounted thermistors can occur as a result of installing such sensors close to the ships bunker tank or within the engine cooling system. Infra red satellite radiometers measure only the top 10 - 20 μm of the ocean surface which is generally cooler than the bulk sea temperature (Hasse, 1971). Consequently, for any meaningful 'long term' estimate of SST change, a combination of detailed statistical analyses and mathematical modelling are required to remove any bias present between the different data series. The removal of such biases is one of the major tasks presented to the global climate prediction community (Folland *et al*, 1993; Allen *et al*, 1994)

Atmospheric global climate models (AGCM) and oceanic GCM are both 'forced' using observed SST measurements as a boundary condition for calculating heat exchange across the air - sea interface. When AGCM and OGCM are coupled SST is extremely important as a principal diagnostic variable. Such models have been developed to simulate both past and current climatic states and a measure of the reliability of present A-OGCM's is given by their ability to reproduce present climatic conditions. Determination of present day global SST fields are therefore required for the validation of A-OGCM simulations. In 1985 the WCRP (World Climate Research Programme) defined an accuracy of 0.3 K for global SST observations in order to detect global climate change. More recently, the Hadley Centre for Climate research has defined a SST accuracy requirement of $\leq$0.1 K for both short term observations and long term stability.

Several global data sets are in existence which are derived from a combination of SST observations made by the AVHRR (Advanced Very High Resolution Radiometer) and routine ship measurements. AVHRR data are calibrated against a series of drifting buoy data sets which enable a 'pseudo-bulk' SST to be generated using algorithms such as the Multi Channel SST (MCSST: McClain, 1985). Such an approach suffers from many imperfections due to *in-situ* calibration sensor warming (Saur, 1962; Bitterman and Hansen, 1993). Data are then blended from several sources (buoys, ships, coastal stations and satellite observations) to achieve an accuracy of ~0.5 K for monthly mean SST and 0.3 K for seasonal mean SST at a 5° latitude by longitude grid scale (Folland *et al*, 1993). This is considered only marginally adequate for A-OGCM validation purpose (Bates and Diaz, 1991).

As a response to the demands made by global climate SST data requirements, a consortium, led by the Rutherford Appleton Laboratories (RAL), Mullard Space Science Laboratories (MSSL) and Oxford University, set about the design of a new generation of IR radiometers for the accurate measurement of SST for global

climate studies. This project cumulated in 1991 with the successful launch of the European Space Agency satellite ERS-1 which carried the Along Track Scanning Radiometer (ATSR). This radiometer is extremely sensitive and capable of measuring SST to the WCRP requirements (Mutlow *et al*, 1992;*in- press*).

Satellite observations offer the only measure of SST in many areas of the earth's oceans and it is these data that will be used to validate present and future global climatic models. These data must be used with care as a small but persistent temperature gradient exists in the top 'skin' (10-20 μm) layer of the ocean, the oceanic skin temperature deviation. This thin surface layer is typically several tenths of a degree cooler than the 'bulk' water temperature at several centimetres depth (Schluessel *et al*, 1990). Because the sea surface has an extremely shallow optical depth in the infra-red region of the electromagnetic spectrum an infra-red SST measurement retrieves a 'skin' rather than a 'bulk' SST and a cool bias is introduced to the derived SST measurements. By using *in-situ* calibration data satellite SST algorithms have attempted to return a 'bulk' SST from a 'skin' SST measure eg the MCSST algorithms (McClain 1981). It is therefore no longer acceptable to assume that the more conventional 'bulk' SST measure is well represented by a 'pseudo-bulk skin' SST retrieved from a 'bulk' calibrated satellite infra red measure.

The purpose of the research presented here is to explore the relationship between the oceanic 'skin' temperature and the 'bulk' temperature by investigating the parameter ΔT, the skin SST minus the bulk SST. Parametisations of ΔT are the first steps towards the accurate prediction of the skin temperature deviation variability and magnitude and offer a potential solution to remove the cold bias present in satellite derived SST. Several current parametisations of ΔT are investigated in this context.

In this work the following questions are pursued:

❋ At what scale is the spatial and temporal variability of the oceanic skin temperature field representative of the bulk SST and what are the consequences for the interpretation of satellite SST data ?

❋ How do oceanographic and atmospheric processes characterise the ΔT temperature deviation and can these processes significantly bias (degrade) satellite SST data ?

An experiment was mounted during a passage from the UK to the South Atlantic in 1992 as part of the international Along Track Scanning Radiometer (ATSR) calibration and validation exercise. The use of a ship mounted IR radiometer and simultaneous supporting observations has produced a data set from which a quantification and characterisation of the oceanic skin temperature deviation can be undertaken. Using coincident satellite and ship measurements relationships between skin temperature, wind speed, air-sea temperature differences, humidity, and bulk SST are investigated in the context of satellite derived SST measurements.

Figure 2.1 (Overleaf) Photograph of several types of ships meterological buckets (UKMO photogrpaph courtesy of Rutherford Appleton Laboratories).

Chapter 2. The measurement of sea surface temperature.

There are a variety of techniques which can be used to determine the surface temperature of the ocean. These techniques vary according to the type of sensor package installed, measurement platform used and the vertical depth in the ocean water column at which the measurement is taken. In the context of satellite SST observations there are two measurements that need to be considered:

1. 'Bulk' SST which is the temperature measured by 'conventional' oceanographic methods. This is considered representative of the top 1 - 10 m of the ocean.

2. 'Skin' SST which is the temperature of the top 10 -20 μm of the ocean surface and is the SST measured by infra-red radiometry.

The following sections critically discuss the methods used to measure bulk and skin SST.

2.1 Bulk SST observations.

This section describes some of the more popular methods used to measure the bulk SST with reference to satellite SST.

2.1.2 Bucket SST measurements

Traditionally, a bulk SST sample is collected using a 'meteorological bucket' from ships and coastal stations. The bucket is simply attached to a line, thrown into the sea to collect a sea water sample and the temperature measured by a mercury in glass thermometer. Figure 2.1 shows a selection of older meteorological buckets indicating that one of the major problems with this method is the non standard design of the buckets used. The early designs of SST bucket were not able to retrieve a consistently accurate SST (Emery *et al*, 1994) and the modern UK bucket shown in figure 2.2, has significant design features in order to reduce the errors associated with this technique (Kent *et al*, 1992). These include the following:

1. The bulk sample is insulated from the warming influence of solar radiation by a sea water jacket retained by a double skin.

2. A synthetic material is used in the construction of the bucket which has small heat transfer properties (Kent *et al.*, 1992). This moderates temperature fluctuations caused by sensible heat transfer.

3. The mouth of the bucket is designed to protect the sample from the wind and reduce the effect of evaporative cooling.

The combination of these features are an attempt to reduce warming or cooling of the sample water as the bucket is brought onto deck where the measurement is made. Further such features are thought to reduce the cool bias often found in data collected prior to the development of the UK meteorological SST bucket (Emery *et al* ,1994).

In addition to the problems discussed above the depth at which a bulk sample is taken is also worth considering. If the SST measure is made from a moving ship then the depth from which the SST sample is taken will vary with the ship's speed. Often the height from which the bucket is deployed makes it difficult to judge how deep the bucket is in the water column. The SST measure is normally considered to represent a depth no greater than 2 - 4 m below the water surface and it is assumed that the temperature returned is representative of the oceanic 'mixed layer'. However this latter term is a relative one and should be treated with care as the definition of 'mixed layer depth' varies. In this work the term will refer to the depth at which the bulk SST measure is representative of the top 6 m meters of the ocean (assuming an isothermal condition which is not always the case especially in light winds). Other definitions consider the bucket sample to represent the temperature of surface water above the seasonal thermocline. However, despite these difficulties experienced operators can expect an acceptable accuracy of 0.1 - 0.2 K when using this technique.

Figure 2.2 Modern ships bucket shown with thermometer and halliard (photograph from JCR cruise).

2.1.2 Ship injection SST

As an alternative to the bucket SST measurement, many ships use a temperature sensor attached to a sea water intake pipe. Most ships use sea water as a coolant for their engines and this intake offers a convenient point for the installation of instrumentation. The devices used vary in type and quality ranging from 'hot well' mercury in glass thermometers (Saur, 1962) to modern day thermosalinograph units (TSG) which use precise platinum resistance thermometer sensors (PRT's). The installation of these devices varies considerably from vessel to vessel and different size pipes, flow rates, depths of intake, location of overboard discharge outlets and in some cases, auxiliary sea water lines for other equipment often modify the temperature of the sea water before it reaches the sensor. Commonly, installations are unfortunately required to be close by the ship's engine room where the water temperature may be highly variable in an often non-linear fashion. This is due to the warmth of the engine and other ships equipment warming the sea water. In order to reduce these effects, the installation of temperature sensors is critical and should be as close to the hull

apeture of the sea water intake pipe as possible. In practice sites vary from a few metres from the ships hull (as in the case of the British Antarctic Survey (BAS) vessel *RRS James Clark Ross*) to several tens of meters inboard.

All of these factors result in a highly variable global SST data set. Saur (1962) discusses these problems extensively and Kent *et al* (1992) highlights the problem with reference to the world meteorological organisation (WMO) volunteer observation ships (VOS).

2.1.3 Ship hull mounted devices

A third type of ship mounted SST measurement system is the hull mounted device which is currently considered to be more reliable than the injection method (Kent *et al*, 1992). Sensors are typically platinum resistance thermometers or ultra stable thermistors mounted either externally or internally directly on to the ships hull at some depth below the sea surface, normally between 1 - 8 m depending on the ship in question. These devices can be accurate to 0.05 K with careful and frequent calibrations. However damping of the sensor response time due to the effect of the ship's (normally steel plate) hull can be a problem. As for the injection method, if the site of the instrument is close to a local source of heat such as the ship's bunker, engine room or exhaust outlet, a warm bias can be present in the measurement. In many cases the bias is a simple offset which can easily be removed from the observations but in others the bias may be non linear and extremey difficult to account for.

However when installed correctly these systems are capable of making continuous minimum bias SST measures. A recent set of data collected from the M/V *'Håkon Mosby'* at 10°W of the Iberian peninsula is shown in figure 2.3. Here a hull mounted PRT sensor at 4.0 m depth located on inside of the ship's hull is plotted together with an in line Neil Brown Conductivity Temperature and Depth (CTD) instrument temperature having an amidships sea water intake at a depth of 4.0 m.

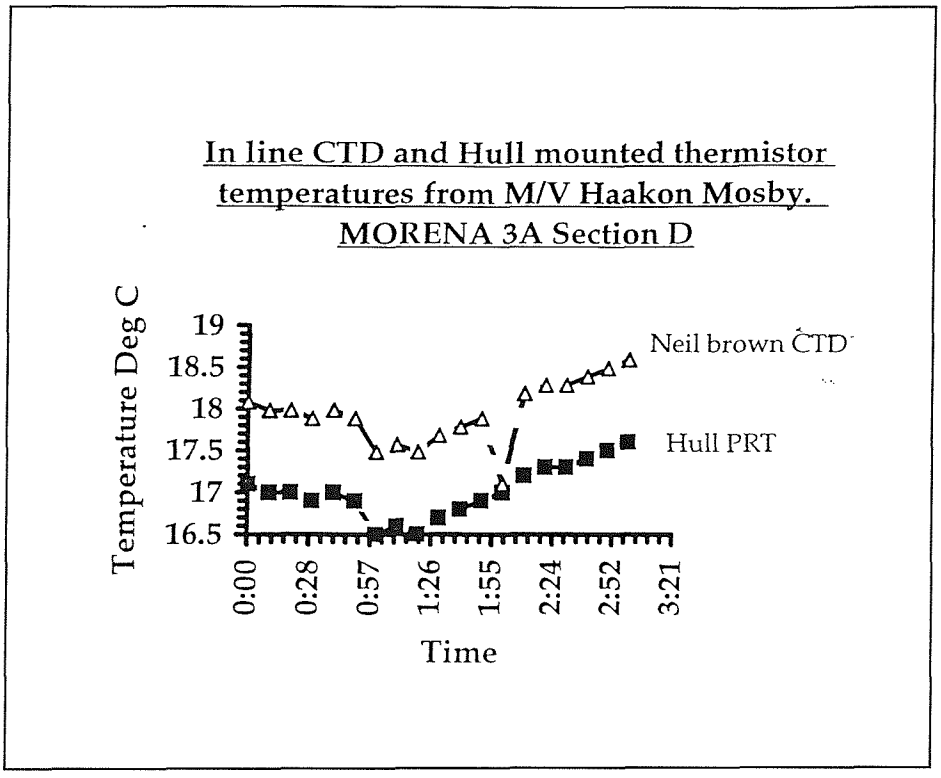

Figure 2.3 Comparison between MORENA 3 in line CTD and M/V *'Håkon Mosby'* hull mounted thermistor temperatures.

The warming effect discussed above on the injection SST is clearly visible. For this particular ship a steady positive bias was found on the injection temperature which can be compensated for by application of a constant term. During the collection of SST data from the RRS *'James Clark Ross'* an in line *'Sea Bird'* thermosalinograph unit was used having an intake at 5.5 m. A hull mounted PRT at 2.5 m and bucket sample SST was also collected during this cruise in order to define the surface temperature field.

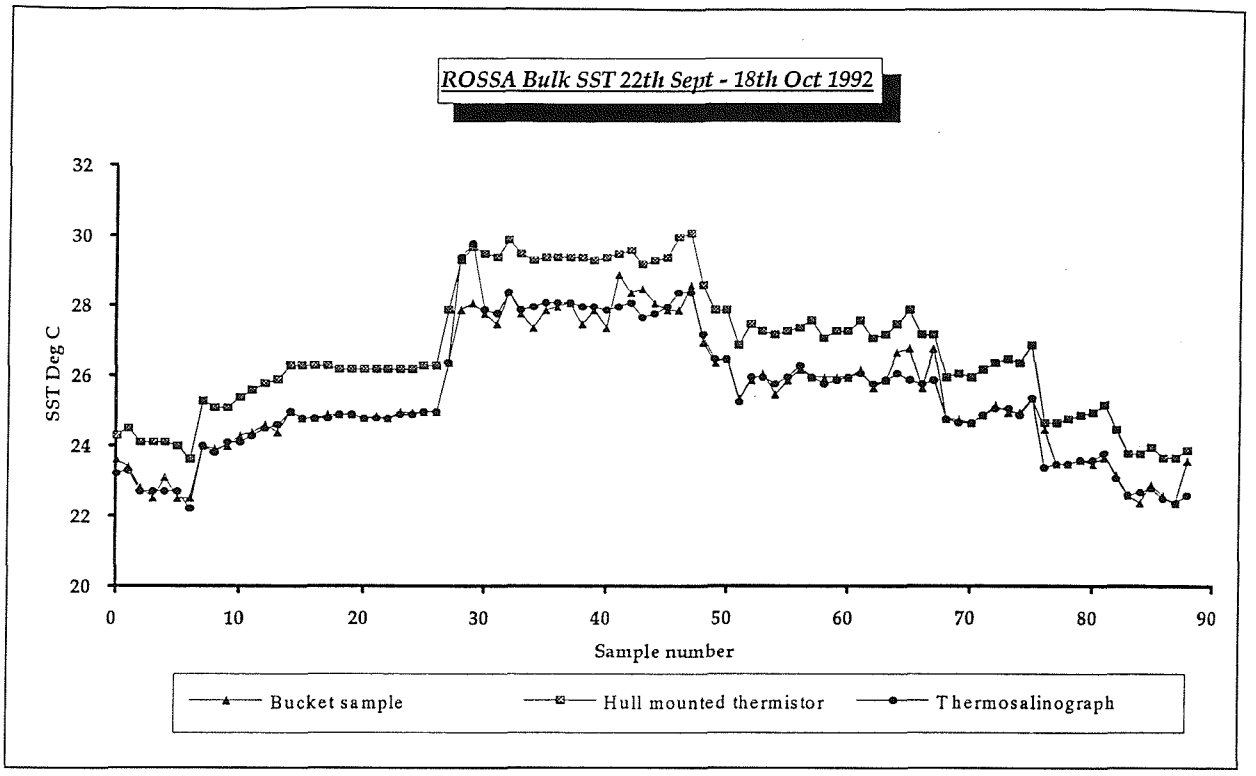

Figure 2.4 RRS *James Clark Ross* bulk SST relationships made over the equatorial leg of the 1992 JCR experiment.

Figure 2.4 shows a summary of these data plotted for the equatorial section of the *James Clark Ross* experiment. A warm bias is clearly evident in the hull mounted PRT measurements and the cause of this was eventually traced to the site of the PRT sensor which was located adjacent to one of the ship's heated bunkers.

As an further example, figure 2.5 shows SST data measured by ships in the North Atlantic. In this figure temperature anomalies are computed from the long term mean SST and are shown for ships' reports that are within 6 hours and 100 km of each other. There is a wide spread of data (standard deviation of 1.5°C) confirming the problems which occur when many ships using different measurement techniques are used to measure the same variable as discussed above.

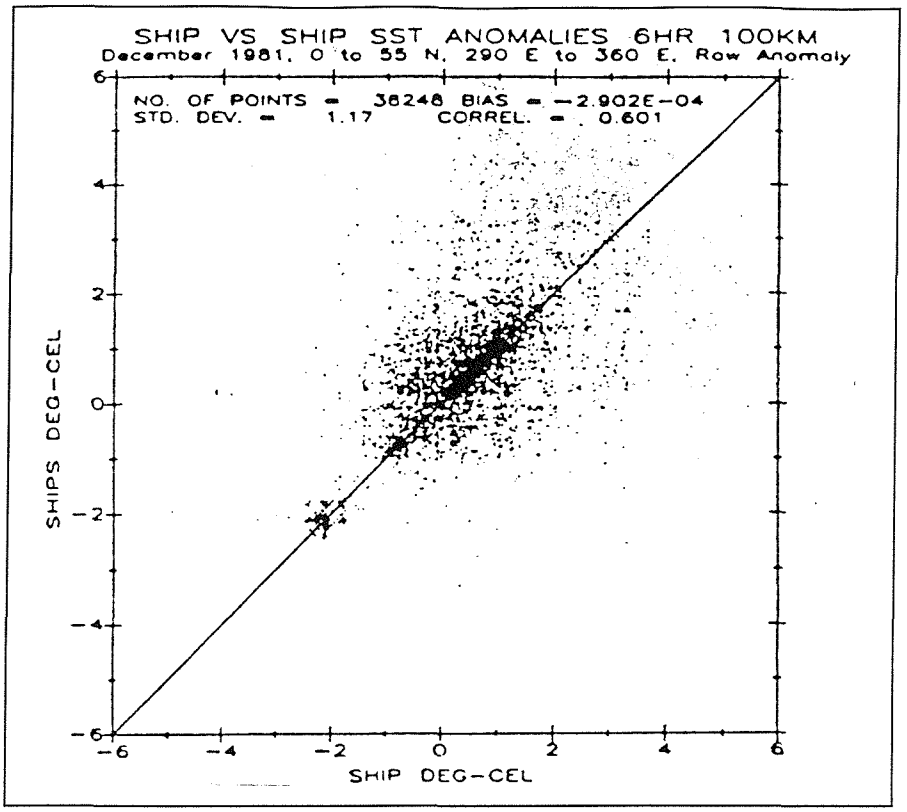

Figure 2.5 Ship SST observations taken in the North Atlantic within 6 hours and 100 km of each other during December 1981. Temperatures are expressed as anomalies with reference to the long term averages at each location. (From Minnet and Grassl, 1986).

2.1.4 Research SST measurements.

During large regional scale oceanographic research cruises many types of non-standard SST measurements have been made. These include the use of PRT sensors attached to small floats returning a temperature from the top 1 - 10 cm (Grassl, 1976). Other techniques include the use of moored thermistor arrays which measure the temperature at intervals of between 10 cm an 10 m depth (T Sherwin, personal communication) at a fixed position. In the context of satellite validation, the latter type of data are extremely useful in clearly defining the sub-skin temperature structure in the upper layers of the ocean.

One particular instrument of interest is the Chelsea instruments SeaSoar system which was used during a recent field study of the NE Atlantic. This system uses a CTD unit housed in a fibreglass 'fish' which is towed from the stern of a ship. The fish is able to undulate in the water column to depths of up to 500 m by using adjustable wings. Typically, in the 500 m depth configuration, the SeaSoar instrument will reach the surface layers of the ocean on a spatial scale of ~ 4 km.

SST data collected using this instrument can cover huge areas in a relatively short time. Careful operation and calibration is required when using this instrument to return a rerisentative temperature for the top 5 m of the ocean. Problems include the effects of the ships propellor mixing up the surface layers, the SeaSoar entering the atmosphere, and plankton contaminating the T/S probe. However the instrumrnt is able to return an accurate temperature for the top 2 - 4 m whn operated correctly. Figure 2.6 shows a typical SeaSoar profile made in the NE Atlantic during the MORENA 3A cruise of July 1994 (Data courtesy of O Johanessen, NERSC, Norway). In this figure the profile of the SeaSoar instrument is shown as a regular undulating solid line and nominal temperature contour at 1°C intervals are interpolated from the 'spot data' adjacent to theSeaSoar profile. Clearly such data are extremely useful in assessing the degree to which a satellite SST observation is representative of the subsurface temperature structure.

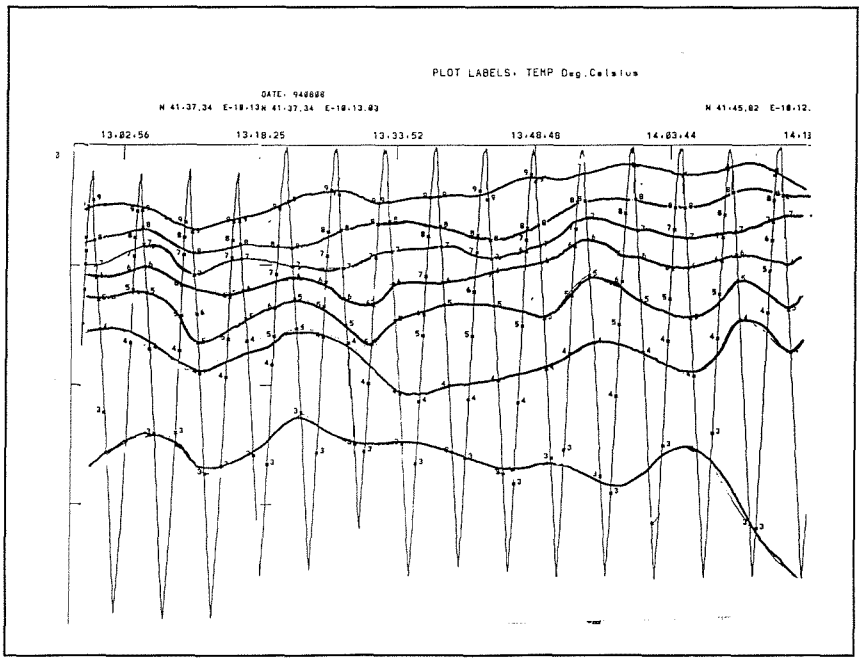

Figure 2.6. SeaSoar transect from 41° 37.34 N, 10° 13W to 41° 45.82 N 10° 12 W. contours show 1° interpreted temperature to a profile depth of 150 dbar. (Data courtesy of O Johannesen, NERSC, Norway)

An interesting technique used by Mammen and Von Bosse (1992) is that of an upward profiling fast response thermistor called STEP (the Skin TEmperature Profiler). This instrument is attached to a buoyant float and connected to a ship

winch via a sea floor pulley arrangement figure 2.7 (a). By repeatedly winching the cable in and out, this system can be constantly profiled while the ship is on station. Clearly this technique is not able to suppy the large spatial scale data such as that of the SeaSoar however, this technique should be viewed as a complimentary measure which is able to investigate the fine temperature structure of the upper ocean layers. Very fine resolution skin temperature data can be obtained using STEP which has a second sensor to determine when the profiler pierces the ocean surface. Figure 2.7 (b) shows an example of a typical near surface SST profile observed using this system. It is clear from these data that there is a strong contrast between the SST seen at a depth of several cm to that recorded immediately beneath the sea surface. As satellites return a skin temperature these data show how significant differences between the skin and bulk temperature fields can be.

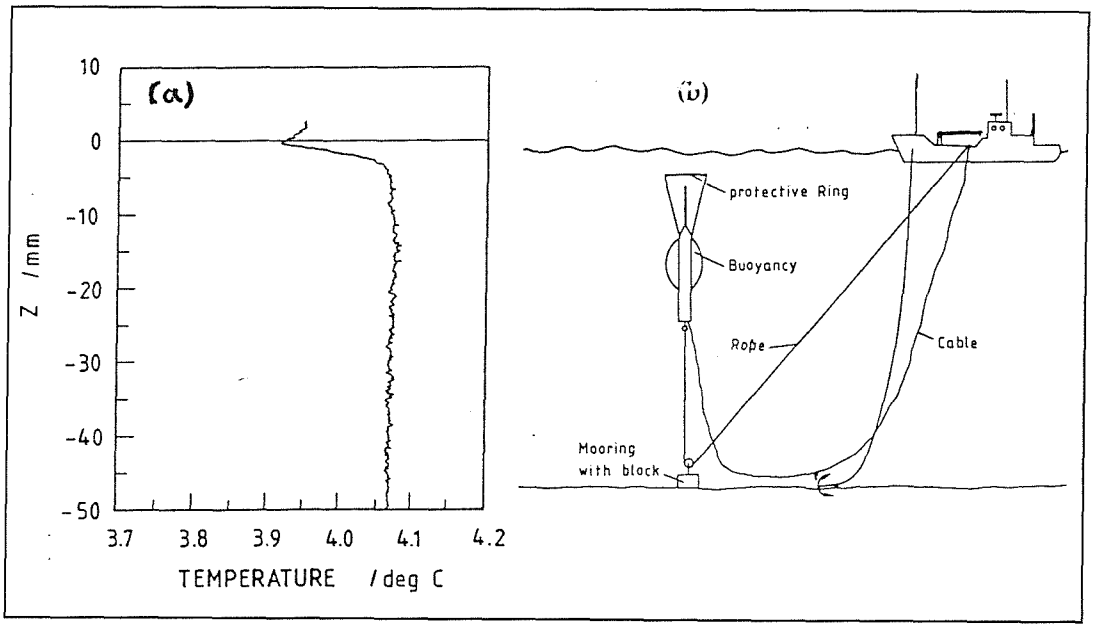

Figure 2.7. (a) The arrangement used y the STEP profiler to measure the fine temperature structure of the ocean and (b) SST observations made by the STEP profiler. (From Mammen and von Bosse, 1989).

2.1.5 Tethered and drifting buoys

Ships are expensive to run, limited in their availability and in their accuracy for measuring bulk SST. As a consequence, drifting and moored buoys have become a major source of *in-situ* SST observations. There are many designs of buoy systems which use a variety of hull designs and different sensor packages which

are installed in many ways to the buoy hull. Some systems measure the temperature of a small metal buoy hull floating on the surface or even that of a large deep sea spar buoy. Many have thermistors protruding from the buoy hull while others have the temperature sensor embedded into a glass fibre or plastic buoy hull. Depending on the thermistor type and installation, systematic errors of >0.1°C may be present in such data (Emery *et al*, 1994).

Most buoy designs place the temperature sensor on the underside of the buoy but as Emery *et al* (1994) point out, it is never clear how a buoy will float and that in the turbulent upper layer of the ocean the and the buoy hull depth may vary up to 4 m depending on the sea state. A further complication in the case of drifting buoys is noted by Minnet (1990) who suggests that these may become trapped in stable current fields. During a recent field experiment, the presence of internal waves was detected using a moored thermistor chain attached to a large Dan buoy. As the waves passed by, a slick was seen on the water surface indicative of vertical movements and the buoy was pulled down into the water column by local downwelling as a consequence of the passing wave. In this case the SST recorded by the buoy may be in error for two reasons;

1. The effect of surface slicks with reference to SST measures is unclear although local surface warming may be present if the slick inhibits the transfer of heat and momentum.

2. The buoy may be pulled down into strong thermal gradients which will be associated with frontal features recording a different temperature to the sea surface. In the case above deviations of up to 1°C were associated with the passing of an internal wave.

Synthetic Aperture Radar (SAR) images of the continental shelf area off the Iberian coast indicate that there are many internal waves in this area suggesting that in

such regions the deployment of drifting buoys for the measurement of SST may be unwise.

Figure 2.8 shows examples of the Tropical Ocean Global Atmosphere (TOGA) drifting buoy designs which are comprehensively reviewed by Bitterman and Hansen (1993). They compared monthly mean SST data returned from three different buoy designs; the Low Cost Drifter (LCD), the Low Cost Tropical Drifter (LCTD) and Ministar drifter against eXpendable BathyThermograph (XBT) and CTD data. The LCD design was shown to have a significant warm bias and suffers from diurnal warming effects which are attributed to the location of the temperature sensor on the buoy hull. This results in poor thermal contact with the surrounding water conclusively demonstrating the influence of different buoy design. It must be remembered that although CTD measurements are of a high quallity this may not be the case for XBT data wich often require the top 5 - 10 m of water to stabilise the T/S probes used in these devices.

The accuracy of the resultant SST returned from a buoy is also dependent on the accurate calibration of the sensor itself. Errors of the order of 0.1°C can be introduced due to improper calibration of the sensors themselves or long term drifts in their calibration. These are difficult to correct without periodic re-calibrations which defeats the purpose of using such autonomous packages. One major advantage of using both moored and drifting buoys is that data can be telemetered to a ground station on a regular basis via satellite link. This means that large volumes of data can be generated from a much wider area of the ocean than if ship SST were used alone. A severe limitation to the use of buoy observations is the poor spatial coverage that these systems offer requiring many deployments to effectively sample an area of the ocean. This is more than compensated for by their large temporal coverage as recently demonstrated by Mutlow *et al*, (1994).

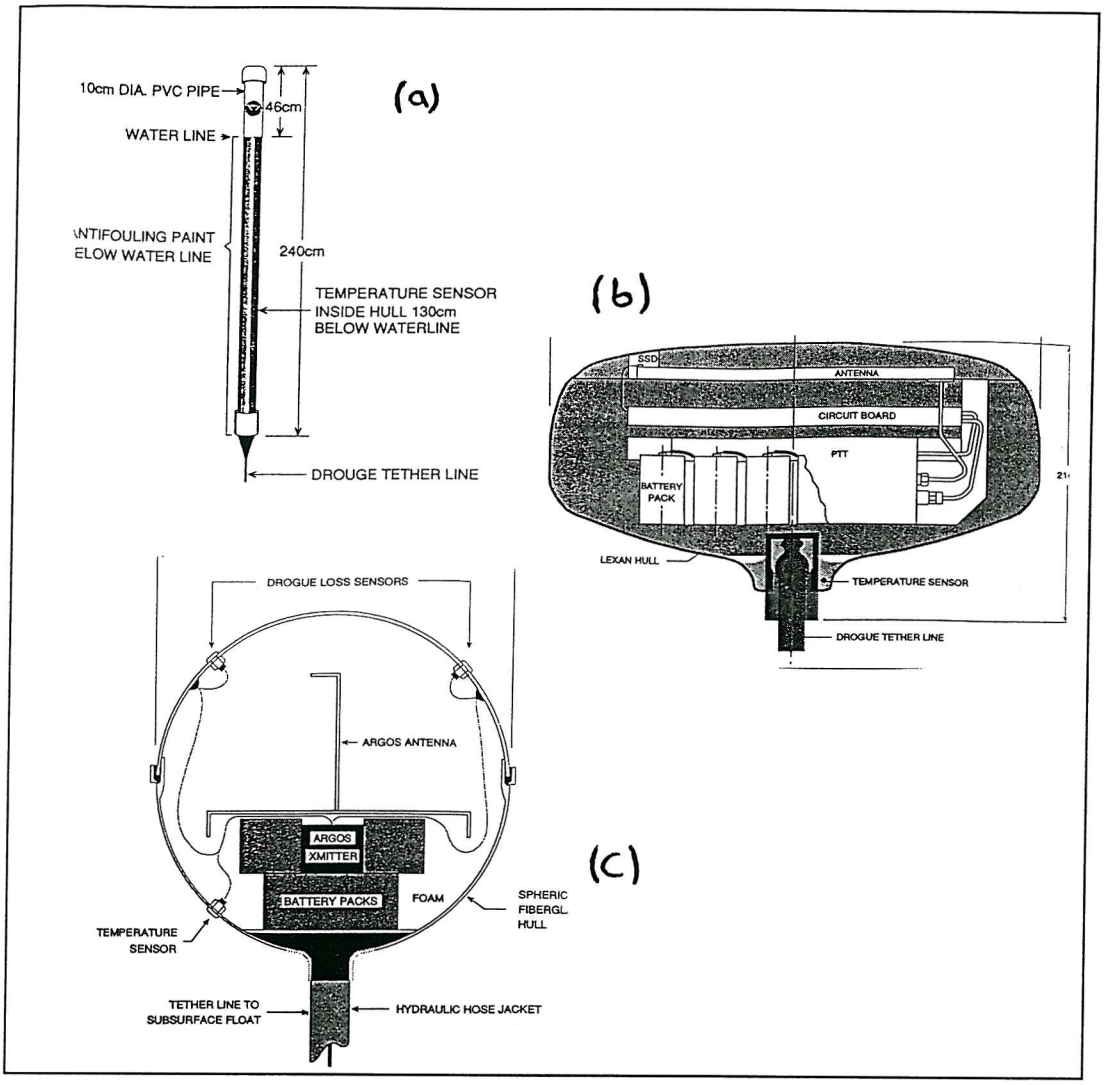

Figure 2.8 (a) The Low Cost Tropical Drifter (LCTD), (b) Ministar drifter and (c) the Low Cost Drifter (LCD) drifting buoy designs. (From Bitterman and Hansen 1993).

2.1.6 Summary of bulk SST measurements

The above examples have shown that bulk SST measurements are made using a number of techniques which use a variety of sensor packages. Many of these techniques sample at different temporal intervals and depths and there is no comprehensive definition of exactly how a bulk SST observation should be made. For these reasons significant errors will be present in combined global bulk SST estimates.

2.2 Infra red SST observations.

Over 25 years ago the development of earth observing satellite platforms enabled SST to be observed from space using infra-red signals emitted from the ocean surface. A generation of passive infra red radiometers known as the Very High

resolution Radiometer (VHRR) and Advanced VHRR (AVHRR) were developed and continue to deliver global coverage of the earth's ocean temperatures on a quasi-synoptic basis. More recently new radiometer systems such as the Along Track Scanning Radiometer (ATSR) are now in operation with a mission to generate a very accurate global SST time series. The most important attribute of these systems is the global coverage that they can offer at a spatial resolution of between 1.1 - 4.0 km at a temporal scale of between 2-3 days to 1 month.

Figure 2.9 shows the distribution of global in-situ SST measurements from ship reports for December 1981. SST data is confined to the major shipping routes of the oceans and many areas are poorly sampled. In particular the southern ocean has very poor coverage limited to the few research and supply vessels that operate in these waters. For this reason alone it is fair to argue that the only way to obtain a long term global SST data set is using satellite infra red radiometry.

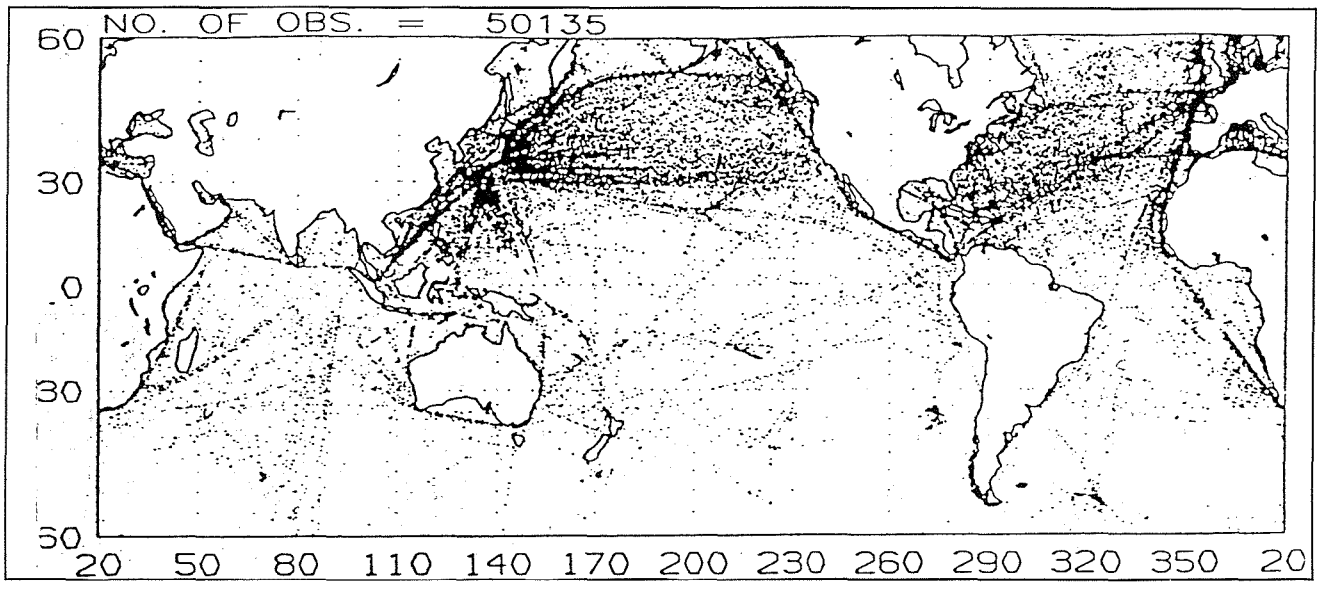

Figure 2.9 The distribution of *in-situ* SST measurements from ships' reports in December 1981. (From Minnet and Grassl, 1986, Courtesy of JPL Pasedena Ca).

2.2.1 Radiometric theory for SST retrieval in the infra red region of the electromagnetic spectrum.

An understanding of the processes which emit and scatter electromagnetic radiation at the sea surface and in the atmosphere is required to retrieve SST from radiance measurements made by an infra red radiometer which are well reviewed

by Minnet (1990). However it is necessary to summarise the principles involved for further discussion.

Planck's radiation law describes the spectral characteristics of thermal emission from the sea surface at temperature T and is given as:

$$B(T,\lambda)d\lambda = \frac{2\pi h c^2 d\lambda}{\lambda^5[e^{ch/\lambda\kappa T} - 1]} \qquad (2.1)$$

B is the spectral emmittance at wavelength λ μm in units of $Wm^{-2}sr^{-1}\mu m^{-1}$ which is the energy per unit wavelength radiated per unit area of the source into a unit solid angle; h is Planck's constant, κ is Boltzmann's constant and c is the speed of light in a vacuum. This is the amount of energy that will be measured for an instantaneous field of view (IFOV) by the detectors of an infra-red radiometer and is thus representative of the surface temperature of the ocean at temperature T and waveband λ. Figure 2.10 shows exitance curves computed using 2.1 for several black-body temperatures which show a clear peak of emission in the 8 - 14 μm waveband. Infra-red remote sensing capitalises on the fact that the maximum exitance from a black body at 300 K (a fair approximation for the mean surface temperature of the ocean) is in this region. The waveband of peak emission is defined by Wien's law:

$$\lambda_{max}T = 2897\mu mK^{-1} \qquad (2.2)$$

As the sea surface is not a perfect black body the curves presented in figure 2.10 are not strictly appropriate . A small amount of absorption at the sea surface reduces the amount of energy emitted and the sea is termed a grey body. The ratio of emissions for a grey body are described by the spectral emissivity, $\varepsilon(\lambda)$ which is given by:

$$\varepsilon(\lambda) = \frac{B(T_{sea}, \lambda)\, d\lambda}{B(T_{blackbody}, \lambda)\, d\lambda} \qquad (2.3)$$

which is weakly temperature dependent and approximately constant. Changes in radiative exitance can therefore be directly related to surface temperature. ε does however vary with wavelength, sea state (wind speed), surface slick material and zenith angle. For the sea surface typical values for ε are given as 0.98 - 0.94 (Masuda *et al*, 1988). Figure 2.11 plots ε as a function of zenith (look) angle and wind speed (sea state).

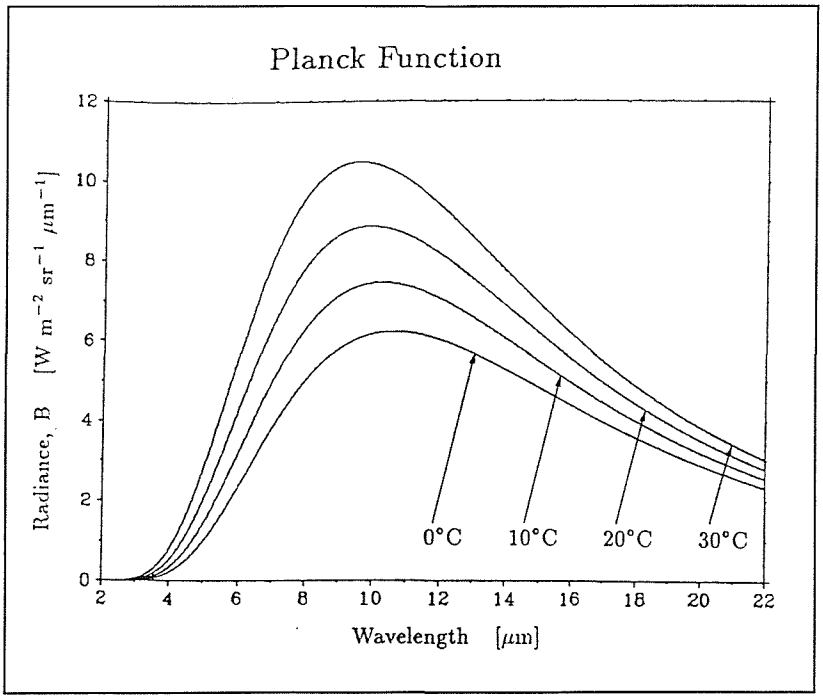

Figure 2.10 The spectral infra-red radiance of a black body at a variety of temperatures evaluated using equation 2.2 (from Minnet, 1992).

Given that the ε of sea water is nearly unity at infra-red wavelengths, radiometric determined SST is a measure which is representative of a thin layer (10 - 20 μm) below the sea surface as the depth of optical penetration at these wavelengths is small. Radiometric SST is thus a measure of the oceanic skin temperature rather than the bulk temperature as discussed in section 2.1

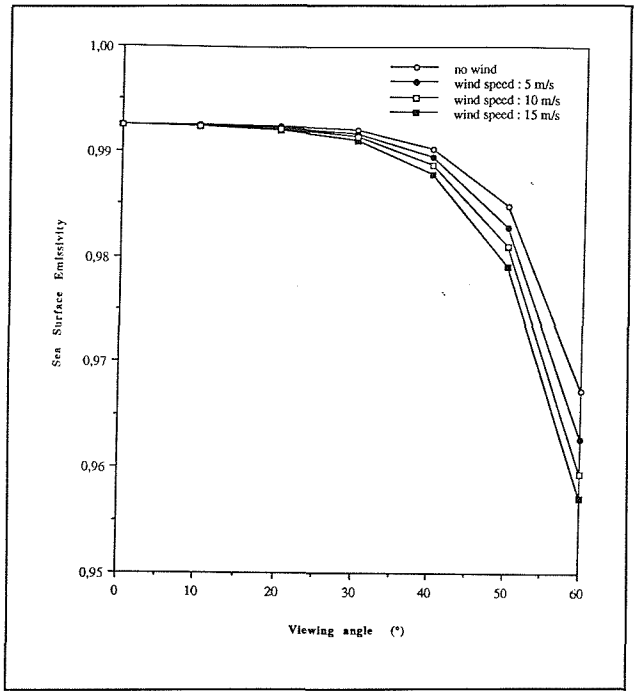

Figure 2.11 Variations in ε due to zenith angle and sea state. (After Masuda *et al*, 1988).

2.2.2 Radiative transfer in the atmosphere.

As the atmosphere is not opaque in the infra-red region its effect on the radiation leaving the sea surface needs to be accounted for. Figure 2.12 shows a schematic diagram of the physical processes involved in the radiative transfer of energy through the atmosphere for a limited waveband of the thermal infra-red at 10 - 13 μm. There are three significant components to consider shown on figure 2.12:

1. Surface emission from the sea surface modified by the intervening atmosphere.

2. Radiation emitted by the atmosphere into the radiometer field of view.

3. Radiation emitted by the atmosphere and reflected at the sea surface into the radiometer field of view.

Atmospheric transmittance is a function of a variety of absorbing and emitting aerosol and gaseous constituents of which water vapour (H_2O), carbon di-oxide (CO_2), ozone (O_3), nitrous oxide (N_2O) and methane (NH_4) are the most important. These gasses are well mixed and are therefore considered to have minimal

seasonal and regional variability. Water vapour is different in that it is highly variable both spatially and temporally. It has strong absorption and re-emission characteristics due to water vapour dimers and long polymer chains making it quasi continuous throughout the infra red spectrum. For this reason it is commonly referred to as the water vapour continuum. This is poorly understood and therefore difficult to account for using models of atmospheric transmittance (Zavody *et al*, 1994).

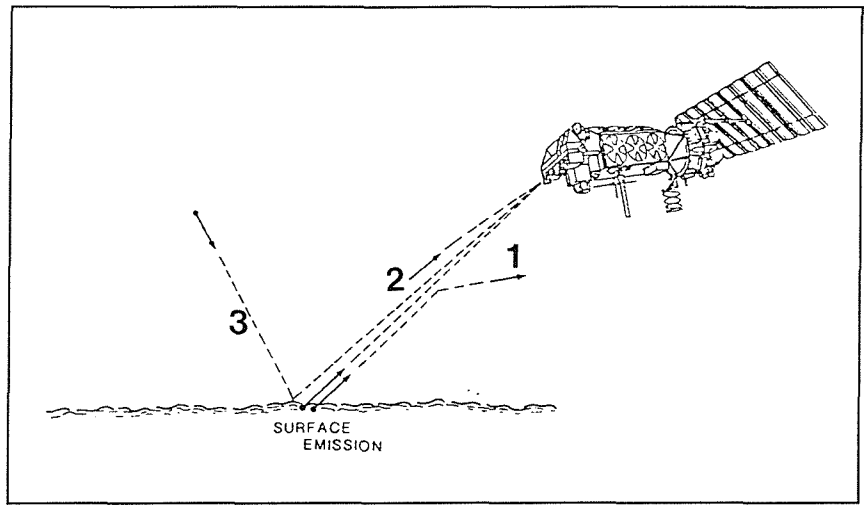

Figure 2.12 Schematic diagram of physical processes involved in radiative transfer through the amosphere. (from Minnet, 1990).

The presence of atmospheric aerosols such as those generated by the eruption of the Él Chichón volcano in 1992, have a significant impact on SST retrievals tending to lower the SST. This is due to the fact that some aerosol particles are effective at scattering infra-red radiation because they are of a similar size to the wavelength in this region of the electromagnetic spectrum (Bernstein and Chelton, 1988; Minnet, 1990). Thomas *et al*, (1994) attribute a 0.7 K cool bias in ATSR SST when compered to *in-situ* radiometric SST to the presence of stratospheric aerosol from the Mount Pinotubo volcanic eruption in June 1991.

Figure 2.13 shows the computed infrared transmittance for 3 different model atmospheres generated by the LOWTRAN-4 atmospheric transmittance and radiance model of Selby *et al* (1978). Several regions of the electromagnetic spectrum have high atmospheric transmittance (>0.8) where absorption and re-

emission due to the above molecules is at a minimum. Conversely, the effects of atmospheric water vapour in the tropical regions can clearly be seen in the 8 -12 μ m region. In this case less than half of the radiance seen by a satellite radiometer is from the sea surface with the remainder originating from the atmospheric water vapour load.

As the atmosphere is generally cooler than the land or sea, any radiation absorbed by the absorption constituents will be re-emitted at a lower temperature and longer wavelength. In terms of the atmospheric contribution made to a radiometer measure of SST, the atmospheric effect will reduce the amount of radiation reaching the radiometer and consequently lower the apparent SST. In order to accurately estimate the SST using satellite or airborne infra-red techniques an atmospheric correction needs to be applied to remove the cool bias imposed on the measurement by the atmospheric absorbers.

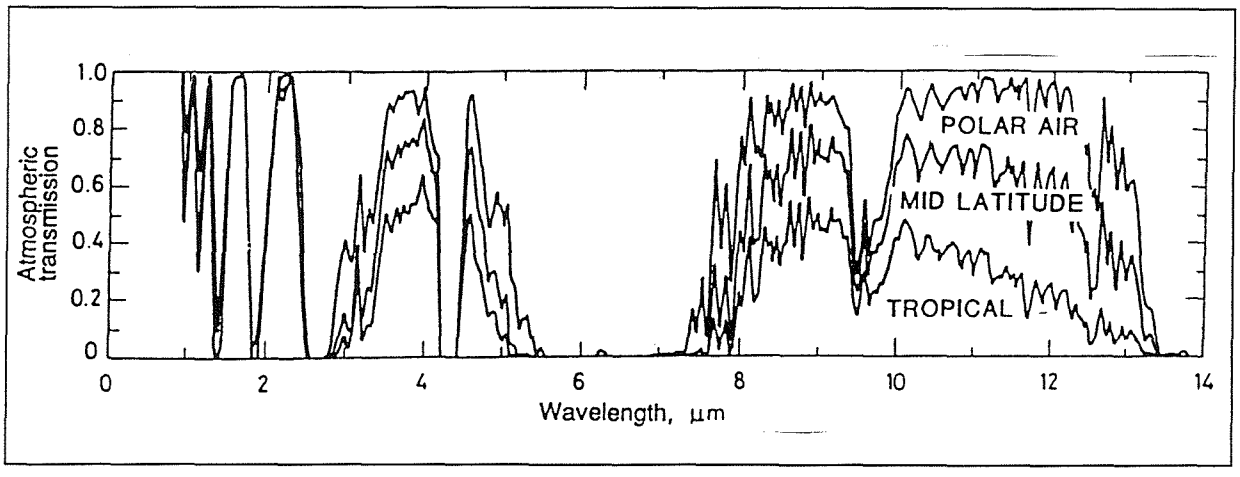

Figure 2.13 Atmospheric transmittance curves for three model atmospheres computed using the LOWTRAN model of Selby *et al* (1978)

2.2.3 Theoretical treatment of atmospheric absorption in the infra-red.

Following Minnet (1990), Bouguet's law describes the change in spectral radiance $L(\lambda)$, of a non-divergent, monochromatic beam at wavelength λ, when it traverses a thin layer of the atmosphere dz, at height z for which all properties are constant. This can be written as:

$$dL(\lambda) = -\kappa(z,\lambda)L(\lambda)dz \qquad (2.4)$$

where $\kappa(z,\lambda)$ is the absorption coefficient for the layer dz.
Now the atmosphere in this layer is emitting radiation into the beam which by Kirchoff's law is equal to the absorption, assuming thermodynamic equilibrium. This can be written as:

$$dL_e(\lambda) = \kappa(z,\lambda)B(z,\lambda,T_A)dz \qquad (2.5)$$

in which $B(z,\lambda,T_A)$ is given by (2.1) for local atmospheric temperature T_A at height z. Combining (2.4) and (2.5) using conditions at the sea surface, $z=0$ and at the height of the radiometer, $z=H$ the spectral radiance measured by a radiometer, $L_H(\lambda)$, is given by:

$$L_H(\lambda) = L_0(\lambda)\exp[-\tau(0,H)] + \int_0^H B(z,\lambda,T_A)\kappa(z,\lambda)\exp[-\tau(z,H)]dz \qquad (2.6)$$

where $L_o(\lambda)$ is the upwelling radiance at the bottom of the atmosphere and τ is the optical thickness of an atmospheric layer $z_2 - z_1$ written as:

$$\tau(z_1,z_2) = \int_{z_1}^{z_2} \kappa(z')dz' \qquad (2.7)$$

τ is the optical depth of the atmosphere. The sum of emissions from the sea surface at temperature T and the reflected downwelling atmospheric radiation, $r(\lambda)L_\downarrow(\lambda)$, where $r(\lambda)$ is the spectral reflectance of the sea surface, $L_o(\lambda)$ is:

$$L_o(\lambda) = \varepsilon(\lambda)B(T_s,\lambda) + r(\lambda)L_\Downarrow(\lambda) \qquad (2.8)$$

where $\varepsilon(\lambda)$ is the spectral emissivity of the sea surface given by (2.2) and is related to the spectral reflectance by Kirchoff's Law:

$$r(\lambda) = 1 - \varepsilon(\lambda) \qquad (2.9)$$

giving:

$$r(\lambda)L\Downarrow(\lambda) = (1-\varepsilon(\lambda))\int_{H}^{0} B(z,\lambda,T_A)\kappa(z,\lambda)\exp[-\tau(z,0)]dz \qquad (2.10)$$

Infra-red radiometers are normally band limited by the use of a high quality filter set and it is necessary to integrate the spectral radiance given by (2.6) across the filter bandwidth, to give the radiance L_i:

$$L_i = \frac{\int_0^{\infty} LH(\lambda)\phi i(\lambda)d\lambda}{\int_0^{\infty} \phi i(\lambda)d+\lambda} \qquad (2.11)$$

where Φ_i is the spectral response for the radiometer filter profile.
As the atmosphere is assumed to be horizontally stratified and stable in this model, where the beam does not propagate normal to the atmosphere at some zenith angle θ, the thickness of the thin layer dz should be replaced with $\sec\theta\, dz$ which is valid for zenith angles up to $\theta < 60$.

2.3 Atmospheric correction techniques for satellite SST retrievals

In practice it is seldom possible to solve the radiometric radiative transfer equations (2.7, 2.8, 2.10 and 2.11) to retrieve SST as a detailed knowledge of the state of the intervening atmosphere is required. The AVHRR radiometer has two channels in the infra-red region centred at 11 and 12 μm. As the atmospheric attenuation of infra red radiance is unequal in these two wavebands it is possible to derive an atmospheric correction scheme based on the radiance difference between the 11 and 12 μm wavebands (Prabhakara *et al*, 1974; McMillin and

Crosby, 1984; McClain *et al*, 1985). This principle forms the basis of the operational Multichannel SST (MCSST) and Cross Product SST (CPSST) algorithms used by NOAA/NESDIS to determine SST from the AVHRR. Both of these algorithms take the form:

$$T_s = T_j + \gamma (T_i - T_j) \qquad (2.12)$$

where Ti and Tj are the brightness temperatures at two different wavelengths in the infra-red spectral window and Ts is the SST. γ is a constant in the MCSST algorithm but has a dependence on the brightness temperatures in the CPSST (Walton, 1988) given as:

$$\gamma = \frac{a_0 + a_1 T_j}{b_0 + b_1 T_i + b_2 T_j} \qquad (2.13)$$

where a_0, a_1, b_0, b_1, and b_2 are constants which are normally derived by regression analyses using synchronous *in-situ* SST data.

Equation 2.12 suggests that SST is simply proportional to the brightness temperature measured by a radiometer and including γ as a term for the correction of atmospheric absorption. In the case of the MCSST algorithm the difference in brightness temperature between the 11 and 12 μm wavebands is assumed to be in some way representative of this absorption and the difference is simply added to a single channel multiplied by a constant factor γ (Yu and Barton, 1994). In the CPSST, the γ parameter is varied depending on the SST and the atmospheric conditions. This is shown to be a much more accurate algorithm than the MCSST in atmospheric extremes (Walton, 1988).

Saunders (1968) noted that the temperature difference between an aircraft radiometer and an *in-situ* measure of SST was approximately doubled when the radiometer viewed the sea surface at an angle of 60° to the nadir. This view angle

effectively doubles the atmospheric pathlength and is therefore a true measure of the atmospheric effect. The ATSR radiometer (see Edwards *et al*, 1990) carried aboard the ERS-1 satellite uses this technique to derive an improved atmospheric correction by viewing the sea surface at an angle of 55° to nadir and at nadir. Spatial and temporal homogeneity of both the atmosphere and the SST field are assumed in the 2 minutes it takes for the dual view SST measure to be made (See Vass and Handol, 1991). This is a direct measurement of the local atmospheric conditions and by combining the forward and nadir views made by the ATSR using equation 2.12 (up to 6 channels during the night) the SST can be retrieved. (Zavody *et al*, 1994).

The performance of these algorithms is obviously dependent on the empirical coefficients used in each algorithm which are normally derived by regressing coincident *in-situ* bulk temperatures collected from drifting buoys against the satellite radiometric brightness temperatures. This process raises several significant points:

(a) The bulk *in-situ* SST data are not measuring the same physical quantity as the satellite radiometric data and are consequently incompatible. Radiometric SST is returned from the top 10 - 20 μm of the sea surface - the sea surface 'skin', (§ 2.2.1) which is typically several tenths of a degree cooler than the SST at a depth of 1m (See table 3.1)).

(b) If the SST algorithm is to be used in different regions and seasons there needs to be a large set of different coefficients derived for each condition. As there is a limited amount of *truly* synchronous *in-situ* SST data (see Minnet, 1990 for a review of the criteria required for coincident measures to be valid) this makes the MCSST biased to certain seasons and regions.

(c) Variability in the temperature field makes the comparison of skin and bulk SST data uncertain. A satellite radiometer makes a measurement in 25-85 μs - a near

instantaneous average, whereas the bulk *in-situ* data may be derived from a 5 minute average.

(d) Contamination of satellite data by small unresolved clouds which tend to bias the satellite SST cool. Unresolved sub-pixel scale clouds within the field of view of the radiometer is arguably the greatest source of error in the SST retrieval at these wavebands. Clouds (water vapour) are opaque to infra red radiation and more importantly, are much cooler than the sea surface. Consequently they will tend to bias the retrieved SST measure cold. Many of the techniques used to 'cloud clear' infra red satellite data rely on the spatial characteristics of the cloud top and ocean surface temperature field (McClain *et al*, 1985; Coakley and Bretherton, 1982; Kelly, 1985). However in regions of large temperature gradients the spatial characteristics of clouds and SST are similar when viewed by infra red satellite radiometers and it is extremely difficult to account for all cloud contaminated pixels without flagging much of the useful SST data cloudy. The dual look technique offered by the ATSR radiometer employs a new generation of cloud clearing techniques in which both the forward and nadir views are used. The parallax difference as a consequence of the different angular views made by the instrument, enables cloud height to be estimated aiding their identification and removal.

(e) The number of truly coincident *in-situ* and satellite data is small. Conditions for coincidence must be relaxed to include *in-situ* observations made several hours from the time of satellite observation. Temporal and advective changes in the SST field can take place in such time frames rendering the coincidence invalid. Minnet (1990) suggests that the valid criteria for coincidence should be ± 2 hours from the time of overpass and within 10 km based on a detailed analysis of several coincident data sets.

(f) Instrumental calibration errors from both the satellite radiometer and *in-situ* method are carried over into the SST retrieval expression.

Yokoyama and Tanba (1990) evaluate many of the split window algorithms for the Mutsu Bay in Japan using the AVHRR radiometer and *in-situ* thermistor chains attached to telemetering spar buoys. They found RMS differences of >0.8°C between the different algorithms tested. This is not unexpected as the regression coefficients for each algorithm were derived from regional *in-situ* data. They conclude that a set of regional SST retrieval coefficients should be derived for explicit regions and seasons.

Table 2.1 summarises the possible errors associated with the derivation of an SST from a spaceborne radiometer system (in this case the AVHRR).

Error	Magnitude
Relative SST algorithm accuracy	0.8 K *(Yokayama and Tanba, 1990)*
Internal instrument calibration (non linearity)	0.4 - 1.0 K *(Steyn-Ross et al, 1992)*
Atmospheric variability	0.2 - 0.6 K *(Minnet, 1990)*

Table 2.1 Summary of errors associated with the derivation of SST from the AVHRR radiometer system.

2.4 The effect of ΔT in the retrieval of SST from satellite infra-red radiometers

It is clear that the algorithms discussed above assume that the temperature structure measured by a satellite radiometer is representative of the temperature structure at several meters depth and that the top layer of the ocean is well mixed. Figure 2.14 shows observations of the bulk SST at 2.0 m depth using a hull mounted PRT and coincident ship borne radiometric observations of the radiative SST (skin) taken in the North Atlantic ocean.

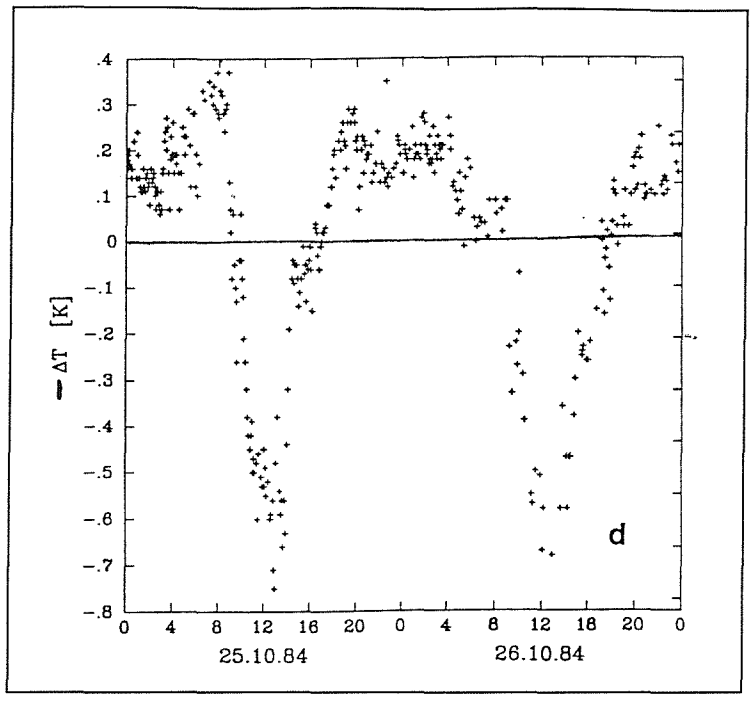

Figure 2.14 Five minute means of minus ΔT taken in the NE Atlantic. Data shown represent a two day period 25 -26th October 1984. (From Schluessel *et al*, 1989)

Bulk - skin (i.e. *minus* ΔT) temperatures range between -0.75 and 0.4 K the radiative temperature being positive during the day and negative during the night as a consequence of solar heating and longwave cooling of the sea surface respectively. These data represent a length scale comparable with that seen by a satellite radiometer and clearly demonstrate the variability of the ΔT relationship. Schluessel *et al* (1990) have observed extreme ΔT values of between ±1.0 K in the North East Atlantic ocean.

The ΔT effect can introduce a significant error into the retrieval of SST from space at two points in the retrieval process:

1. During the collection of *in-situ* calibration data. From figure 2.14 the only time a *true* calibration SST (ie when the bulk and skin temperatures are identical) is just before and after solar heating of the sea surface has stopped. A large number of coincident *in-situ* calibration data covering both day and night time situations is required to define a mean calibration encompassing both positive and negative ΔT values. Obviously if calibration data are collected predominantly during the day

or during the night then a bias will be introduced into the SST algorithms. Further complications arise when the diurnal warming of the top 10 - 100 cm of the sea surface is considered. Stramma *et al* (1986) found areas in excess of 30,000 km^2 could be affected by diurnal heating of >1.0 K based on climatology and SST image analyses. If the *in-situ* validation data are collected using bulk SST *beneath* the diurnal thermocline then extreme errors in the satellite data will be inferred. It is for these reasons that separate day and night time coefficients are derived for most of the current split window SST algorithms.

2. Variations in ΔT are greater during the day time than during the night so that night time calibration data will deliver a more robust SST from the satellite radiometer. However as the ΔT is dependent on the local conditions at the air sea interface, its spatial and temporal magnitude can significantly change with a consequent variation in the final retrieved SST. In this case a temporal mean skin temperature may be the best measure to use.

As the skin temperature is the fundamental geophysical quantity measured by a radiometer and that the new generation of satellite radiometers such as the ATSR are now able to measure SST to a degree of accuracy much smaller than the extremes of the cool skin (Mutlow *et al*, 1994) it is no longer acceptable to assume that the bulk and skin SST are the same.

Emery (1989) and Wick *et al* (1992) comprehensively discuss the problems associated with the use of the MCSST/CPSST SST algorithm pointing out that these algorithms do not specifically address the radiative skin of the ocean. They compute the Satellite Measured SST (SMSST) algorithm proposed by Schluessel *et al* (1987) which returns a true skin temperature based in the synergistic use of the AVHRR and the High resolution Infra Red Sounder (HIRS). For both local and global areas, an offset of 0.45°C is found between the MCSST and the SMSST and which is reduced to 0.1°C for the CPSST and the SMSST. RMS. differences of 0.7°C and 0.6°C are found between the MCSST-SMSST and CPSST-SMSST algorithms

respectively. The largest differences were found in the polar and tropical regions, an area for which the CPSST is expected to function well. These differences are seasonally independent as shown in figure 2.15 but vary strongly from region to region shown in figure 2.16.

Due to the lack of *in-situ* skin observations it is difficult to argue which of these algorithms produce the most accurate results although these differences are consistent with bulk-sea temperature differences observed *in-situ* by Schluessel *et al*, 1990.

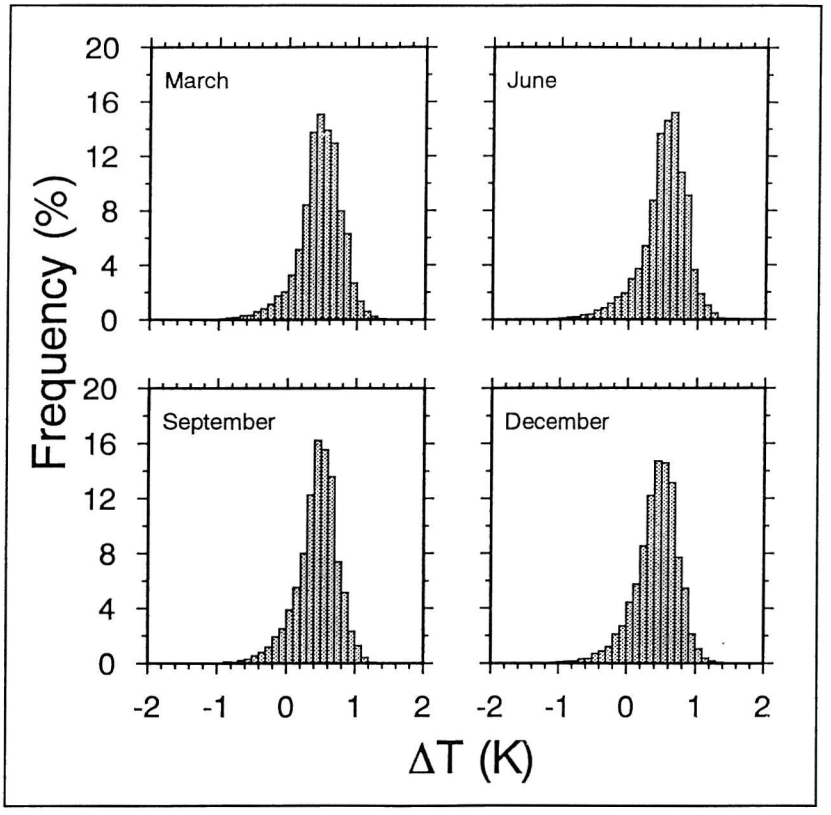

Figure 2.15 Distribution of MCSST versus MCSST-SMSST (ie minus ΔT) temperature differences in 1984. (from Schluessel *et al* 1992).

The development of new atmospheric correction schemes such as those proposed by Yu and Barton (1994) which build on the earlier work of Harris and Mason (1992) attempt to address some of the issues discussed above. In their scheme the ratio of the spread of brightness temperatures due to spatial variations in a small area (50 x 50 km) between two distinct wavebands (which is proportional to the ratio of atmospheric transmittance in one waveband to that in another), is used to derive appropriate local (i.e. within a scene) atmospheric correction coefficients.

This is potentially a powerful technique as the algorithm does not rely on any regression technique requiring the input of *in-situ* data. Also, a local set of atmospheric correction coefficients can be derived for each scene and a local atmospheric corrected skin SST can be retrieved. However this algorithm requires further validation.

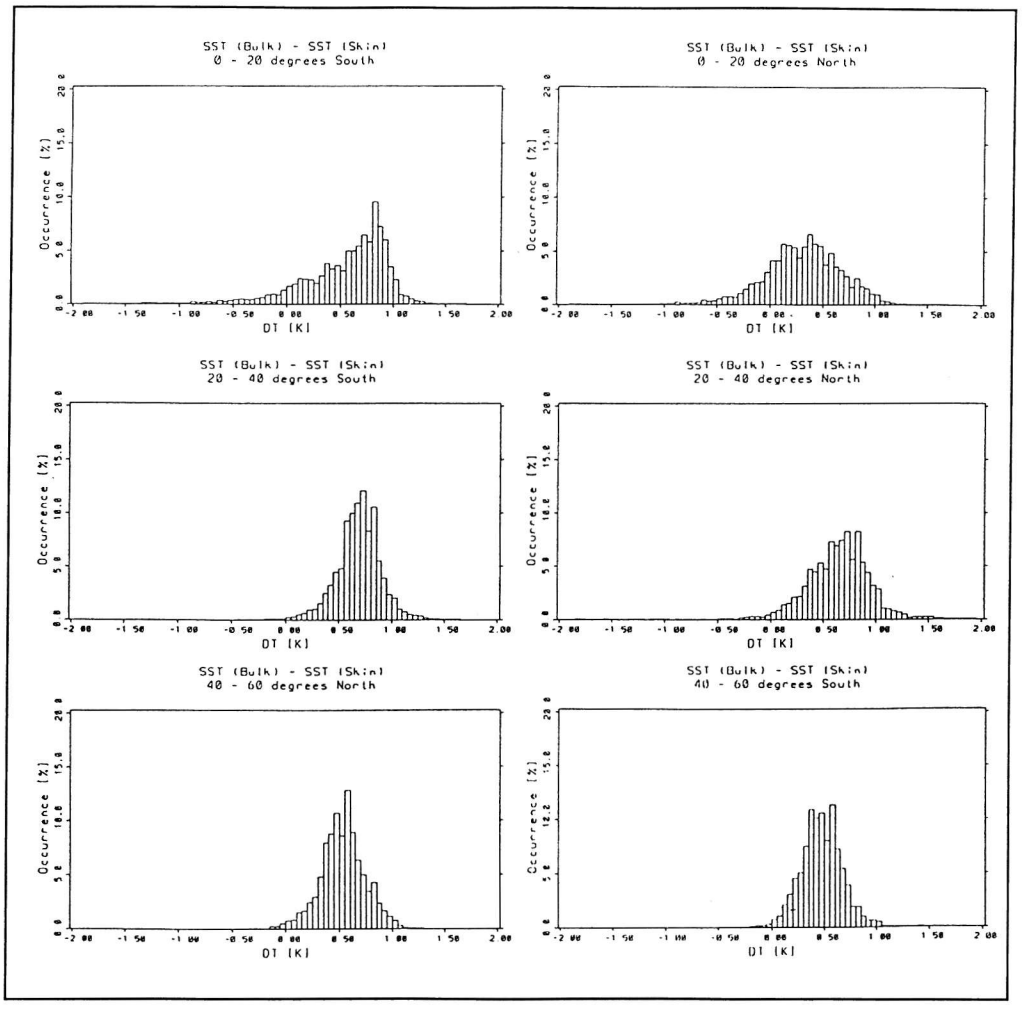

Figure 2.16 Histograms of MCSST versus MCSST-SMSST (ie minus ΔT) differences by 20° lattitude bands. (from Emery, 1989).

The character and variability of the skin effect has been observed both in the laboratory and in the ocean but the difficulties of using well calibrated infra red radiometers at sea has resulted in a limited set of coincident *in-situ* and satellite observations. Further, the processes occurring at the air sea interface are poorly understood at small scales due to the complexity of turbulent processes thought to govern fluid behaviour (Thorpe, 1985). This latter point is complicated by difficulties involved in the physical measurement of the quantities pertinent to

these processes in such a thin layer of the sea surface. Gemmerich and Hasse (1992) describe a series of field experiments in which they used fine cork powder spread over the sea surface in order to determine the small scale surface motions on the sea surface. Many patterns are observed which have dominant forms of lines, interconnected fingers and cellular structures with temporal scales of seconds and centimetre length scales demonstrating the complex nature of the air-sea interface. It is in this complex environment that the cool skin of the ocean is found.

2.5 Summary.

There are four major limitations to the accurate calibration and interpretation of satellite infra-red measurements of SST:

1. The lack of a comprehensive definition of SST.

2. The lack of detailed knowledge of the accuracy, reliability and performance of the *in-situ* measurement systems.

3. The need for further knowledge of the attenuation of the infra-red signal by the intervening atmosphere.

4. The lack of a comprehensive radiometric *in-situ* data set with which the relationships between the bulk and radiometric temperature of the sea surface can be described.

It does not seem possible to refine the accuracy of spaceborne infra-red SST retrieval to the degree required by the global climate research community (SST $\leq 0.1°C$) until these issues have been resolved. The lack of simultaneous well calibrated *in-situ* measurements of both the bulk and radiative SST (4 above) is a major constraint in the resolution of issues 1 and 2 above. Issue 3 is currently

being addressed by the development of new atmospheric correction techniques such as that described by Yu and Barton (1994).

As new and improved infra red radiometers come 'on-line' towards the end of the decade such as the ATSR/2, AATSR, AVHRR/3 and the VIRSR (Sherman, 1991), a clear definition is needed of which sea surface temperature field is required from each of these instruments, i.e. a skin or a bulk SST. The attraction of a bulk regression type of calibration should not be underestimated as a near zero biased data set will be generated, although with a limited accuracy, allowing the study of relative temperature differences. Further, blending techniques such as those used by Folland *et al* (1993) allow the assimilation of biased satellite SST fields into GCM. Fundamentally the user application will define the type of SST field to generate. For example, for the study of air-sea interactions a skin temperature may be the more useful parameter to develop heat exchange models for GCM's whereas for ocean dynamical modelling a bulk temperature representing the mixed layer (sea surface to seasonal thermocline) is the more useful measure. Of more importance is the continuity of new SST data with that already existing. As Allen *et al* (1992) points out, this may be the critical factor for the successful detection of global climate change in the next 50 years. In this case it is imperative that a cross calibration of new satellite and *in-situ* instruments is performed in order to achieve the required long term stability of global SST data.

It must be remembered that the pseudo-bulk satellite derived SST, will only be a fitting measure at long length scales where the skin temperature appears to be spatially coherent with the bulk. However, at small length scales (<12 Km) in conditions of large horizontal temperature gradients a skin measure may be the better parameter. Particular attention is required in understanding the physical processes dynamically connecting the skin and bulk temperature fields together. It is possible that important hitherto unseen, useful information at the smaller length scales is unused as these data are traditionally attributed to instrumental noise.

Chapter 3. The skin temperature deviation of the sea surface.

Chapter 2 explored the different methods used to measure SST and concluded that the skin- bulk temperature difference, ΔT, is an important parameter to consider in both the validation of satellite SST data and also in the derivation of the algorithms used to retrieve SST. Chapter 3 is dedicated to a discussion of the oceanic skin temperature deviation, ΔT.

3.1 The need to determine and study the magnitude and variability of the oceanic skin temperature deviation.

As infra red radiometers flown on orbiting spacecraft measure only the top ten microns of the ocean surface, the temperature is often biased cool with reference to a temperature at several centimetres depth as a consequence of the skin effect - this is ΔT. Historically it is the bulk SST measurement that is required by general circulation models. As satellite SST will be the main source of global monthly SST data in the future (Carson, 1991; Folland *et al*, 1993) it is imperative that the cool skin of the ocean be fully explored in the context of deriving global SST from space. A general correction scheme for the removal of the cool skin bias is required, preferably in the form of a 'skin to bulk' SST transfer algorithm or a ΔT climatology. In either case, the use of routine satellite observations such as wind speed and sea state from altimeter and scatterometer measurements, cloud cover from visible and IR measurements, skin temperatures from IR measurements and atmospheric humidity from IR soundings could be used in thier derivation. It may also be possible in the future to use microwave radiometry to return temperatures at several different depths within the skin layer (McAlistair and Mcleish, 1970) although the present theory and practice of such techniques is poor as there is little knowledge of microwave interactions with a water surface. Further complications arise as variations in the oceanic emissivity due to surface roughness at these wavelenghts are poorly understood (Robinson, 1985). However, critical to the characterisation and formulation of any 'skin to bulk' SST

algorithm is a thorough understanding of the physical processes that control the skin-bulk temperature relationship

3.2 The surface thermal sub-layer of the ocean - the cool skin phenomenon.

Typically within the top 10 - 20μm of the sea surface a strong temperature gradient exists which is quasi permanent in nature and is referred to as a 'cool oceanic skin'. Deviations from the bulk SST at a depth of <2.5 m are quoted as ±1°C (Saunders, 1969; Hepplewhite, 1989; Schluessel *et al*, 1987, 1990). Figure 3.1 shows a schematic diagram of one possible thermal structure at the sea surface and defines the bulk - skin temperature deviation, ΔT. In this diagram the depth of the oceanic skin is defined as δ_v and is contained within a conductive and viscous surface microlayer of the ocean which overlies a turbulent mixed layer. The thickness and temperature of the thermal skin are determined by the same heat exchange processes and are dependent on the local energy flux at the air - sea interface.

Short wave solar radiation penetrates the skin layer and in clear water 99% of all solar energy is absorbed within the top 100 m and the surface waters beneath the oceanic skin are directly warmed. Longwave radiation is emitted and absorbed from the skin of the ocean which depending on the direction of this flux, (negative out of the ocean, by convention) either warms or cools the skin layer. At the same time, the turbulent transfer of latent and sensible heat between the ocean and atmosphere driven by the wind causes additional cooling of the skin. However the wind is also responsible for turbulent mixing of the upper layers of the ocean tending to destroy the skin layer. Clearly the relationship between the fluxes of radiative, turbulent heat and momentum processes, the latter induced by the wind, is a complex one.

Both in the ocean and atmosphere turbulent eddy exchange processes driven by the vertical shear stress of the surface wind and local density differences are very effective at carrying heat away from the air - sea interface. However, surface tension restricts turbulent processes near the interface and therefore cannot be

responsible for thermal transport between the atmosphere and ocean (Hasse and Liss, 1980). With the exception of breaking waves, spray and bubble transports, this must be achieved via conductive molecular processes. Thus in typical conditions, when the sea surface temperature is greater than that of the atmosphere immediately above, heat flow is via molecular processes and a steep temperature gradient must exist in order to regulate the radiative and turbulent fluxes at the air sea interface. This produces the cool skin phenomenon (Saunders, 1967; Hasse, 1971; Schluessel *et al*, 1994).

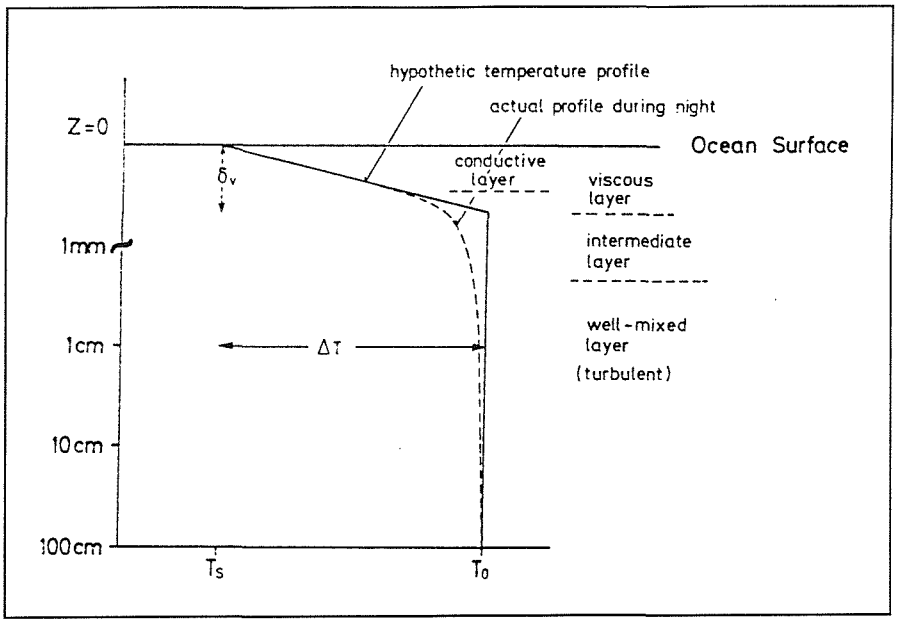

Figure 3.1 Schematic diagram of the skin-bulk (ΔT) parameter and a definition of the physical structure governing heat transfer through the air-sea interface (From Grassl, 1976).

In conditions when the sun is high, insolation may be much greater than the heat loss at the surface. However, as the layer of molecular transport is less than a millimeter thick, only 15 - 20% of the total insolation is absorped within it (Gemmrich and Hasse, 1992). Even in conditions of moderate or high insolation the absorption in the upper layer may not be sufficient to offset the heat loss from within. A condition may develop where heat is directed out of the ocean in the uppermost layers but at some depth the heat flux changes direction when the absorbed insolation exceeds the loss of heat from the ocean. Further, in this situation the cool skin of the ocean is a persistent phenomenon present both during night and day. The importance of this top layer should not be

underestimated as it is through this interface that energy is transported between the two components of the earth's atmosphere ocean system. Unfortunately the skin effect is expected to be at its greatest under clear skies at night which are the optimum conditions for IR observations of the SST from space.

Much interest in the cool skin phenomenon has been driven by a need to model and account for its effect on satellite infra red radiometry and in the exchange of gasses between the ocean and atmosphere (Saunders, 1969; Katsaros, 1980; Paulson and Simpson, 1981; Robinson *et al*, 1984 and Emery 1994; Schluessel 1987,1989,1994; Wick, 1993). The question that needs to be addressed is: "What are the characteristics of the cool skin measured by an infra red radiometer and how do these relate to the bulk SST field ?". Using this information a skin temperature correction in the final SST retrieval scheme can be applied to satellite data.

3.3 Observations of the cool skin phenomena

Because of the small depth of the skin layer the direct measurement of surface skin temperature is not a trivial task. Techniques include the use of mercury in glass thermometers, pop up sondes (Mammen and Von Bosse, 1990) and infra-red radiometetry

Woodcock (1941) and Woodcock and Stommel (1947) made some of the earliest measurements of temperature profiles at the air sea interface using a specially developed mercury in glass thermometer. They found a temperature difference of -0.5 to -1.0 K between a surface measurement and that at a depth of 20 cm in shallow salt water ponds at night . More recently, Schluessel *et al* (1990) measured the bulk-skin (-ΔT) temperature difference from the RV Meteor finding ΔT of $\pm$1°C in the north Atlantic ocean having typical mean day/night variations of 0.11 and 0.33°C respectively. Table 3.1 reports measured values of ΔT from various authors employing a variety of techniques.

Schluessel *et al* (1989) using spectral coherency analysis demonstrated that a high correlation exists between the skin and bulk temperature fields in regions of relatively weak horizontal temperature structure only at long length scales (>150 km). As a consequence, horizontal gradients in the bulk temperature field may be masked by the skin effect, an occurrence which has also been postulated by Gemmrich and Hasse (1992).

Figure 3.2 shows the squared coherency between the bulk SST at 2.5 m and that measured by a Barnes PRT-5 radiometer. The data presented represent a length of 3410 km taken in the North East Atlantic ocean. Two peaks are present in the spectra (at 115 and 65 km) which are attributed to the presence of mesoscale eddies. Taking a coherency of >0.7 (Schluessel *et al*, 1989) as defining the threshold of a "good correspondence" the skin SST is representative of the bulk SST at length scales of >150 km. In regions of strong horizontal variability it is expected that the skin-bulk coherence will be shifted to the lower wave-numbers. In this case stronger bulk temperature variability will be sufficient to overcome the small scale skin variability and a satellite SST will be representative of the bulk SST. This suggests that there is a characteristic spectrum of 'skin only' variability which will be a fundamental limit to the ability of a satellite to measure bulk SST.

Lancaster, (1994) used spectral analysis techniques on calibrated AVHRR data and found that SST energy spectra show two distinct regimes one at approximately 10-12 km and a second at >25 km. He suggests that a change in spectral slope is related to a dominance of instrumental noise from the AVHRR sensor at the smaller wavelengths and a true SST at the longer.

Author	Date	ΔT min K	ΔT max K	Method	Comments
Woodcock and Stommel	1947	-1.0	-0.5	Special mercury in glass thermometer	Nigh time observations over a calm pond
Ewing and McAlister	1960	-0.6	0.0	6 - 20 μm Radiometer and thermistor at depth	Sea surface measurement from pier. Used a subsurface pump to destroy the skin
Hasse	1963	-0.3	-0.1	Thermistor in sea ventilated dry and wet bulb temperatures	Used a drifting buoy developed by Brocks, 1959
Saunders	1967	-0.35	-0.2	Airborne radiometer; 8 - 13μm atmospherically corrected. *In situ* bucket temperatures	
Ogura *et a* al	1969	-0.6	0.8	Barnes PRT 14 radiometer and bucket temperatures	Measurements made around research vessel on station. Corruption due to engine room outlet water
Ogura*et al* b	1969	-0.6	0.2	Barnes PRT 14	Aircraft and ship mounted measurements in Kuroshio region west of Kyushu
Hill	1972	-2.0	-0.1	8.5 - 12.5μm radiometer	Laboratory measurements under wind speeds of 2 - 10m/sand roughness due to mechanical waves
Paulson and Parker	1972	-1.8	-1.4	Radiometer viewing specially constructed tank. Bulk by mercury in glass thermometer	Bulk at 10 cm
Grassl	1976	-0.21	-0.17	Barnes PRT-5 radiometer and resistance thermometer	Wind speeds 0f 1 - 10-m/s
Katsaros	1977	-0.4	-0.25	Barnes PRT-5 radiometer and 25μm thick resistance wire	Measurements both in the lab and field
Nicholls	1979	-0.8	-0.2	Barnes PRT-4 radiometer and bulk thermometer	Data atmospherically corrected

Simpson and Paulson	1980	-0.3	-0.15	Barnes PRT-5 radiometer measurements at sea. Bulk temperature inferred from maximum temperatures at wave peaks	Emissivity problems here
Paulson and Simpson	1981	-0.4	0.3	Barnes PRT-5 radiometer and bulk temperature at 1m	Observations from FLIP in the north Pacific ocean
Schluessel *et al*	1987	-0.3	0.6	Barnes PRT-5 8-14μm filter and bulk at 2, 4 and 7m depth	Observations in NE Atlantic from research vessel
Emery	1989	-2..0	2.0	Skin coefficients from Schluessel *et al* (1987) and MCSST. AVHRR data sets	Used AVHRR calibrated to bulk and skin measures
Hepplewhite	1989	-1.4	0.6	RAL type twin channel self calibrating radiometer and bucket samples	Data along transect N - S across the Atlantic. Day night and latitudinal variations reported
Coppin *et al*	1991	-1.5	1.0	RAL /SIL type radiometer	Data from the W Equatorial Pacific
Schluessel *et al*	1992	-1.0	1.0	PRT-5 stirred bucket calibration	Norwegian sea
Jessup	1992	-0.5	0.0	Agema 880 Thermovision camera Heimann KT-19 radiometer Barnes PRT-5	Observations from R/V FLIP in the eastern Pacific. Demonstrates thermal signature of breaking waves
Emery *et al*	1993-94	-1.0	1.0	OPHIR MISTRC radiometer using both on board black bodies and stirred tank	South Atlantic and equatorial Pacific

Table 3.1 Observations of ΔT reported by various authors.

Bearing in mind the above discussion it is also possible that the spectral change in slope is due to high frequency skin SST variability masking the lower frequency bulk SST variations.

The latter length scale of 10 - 12 km has serious implications for the collection of *in-situ* satellite validation data. As there is often a degree of uncertainty to the position of a ship many validation 'points' use a spatial average of satellite SST with which to derive a coincident satellite -ship pair (Thomas *et al*, 1992). Ideally, according to Forrester *et al* (1992), this should be in a region of low bulk SST variability which are the optimal conditions in which the bulk SST may be decoupled from the skin. However if the coincident validation data are collected in a region of high bulk SST variability, the errors associated with the position of the satellite data and the ship may result in an invalid coincident pair (Forrester *et al, ibid.*). Minnet (1990) suggests that 10 km is the maximum acceptable mis-match between satellite and *in-situ* data.

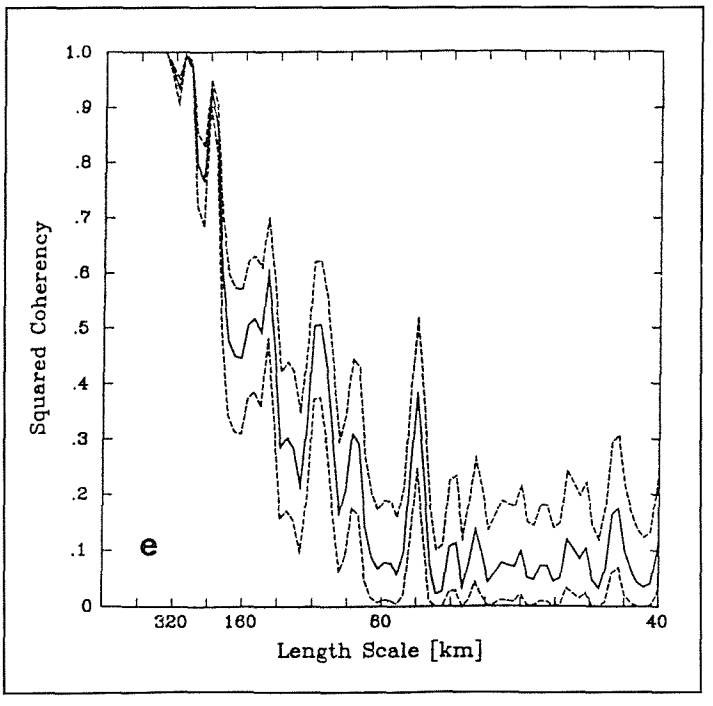

Figure 3.2 Spectra of squared coherency (solid lines) for a 3410 km transect taken on November 18th 1984 in the North East Atlantic. (From Schluessel *et al*, 1989).

A second situation in which the bulk (mixed layer) temperature field can be decoupled (masked) from the skin temperature is when a diurnal thermocline has formed. This feature of the ocean surface layers occurs in conditions of strong solar heating and light winds which may lead to a warm stable deck layer overlying the bulk water beneath. In the case of ΔT, this can lead to a situation where positive ΔT values are recorded.

It is expected that the skin effect will vary according to both regional and local atmospheric conditions. In tropical regions, a typical situation exists where very humid air, low wind speeds and an atmospheric temperature close to that of the sea surface exist. Under these conditions a small skin effect would be expected. At higher latitudes, where wind speed, air temperature and humidity variations are greater, a larger skin effect would be expected.

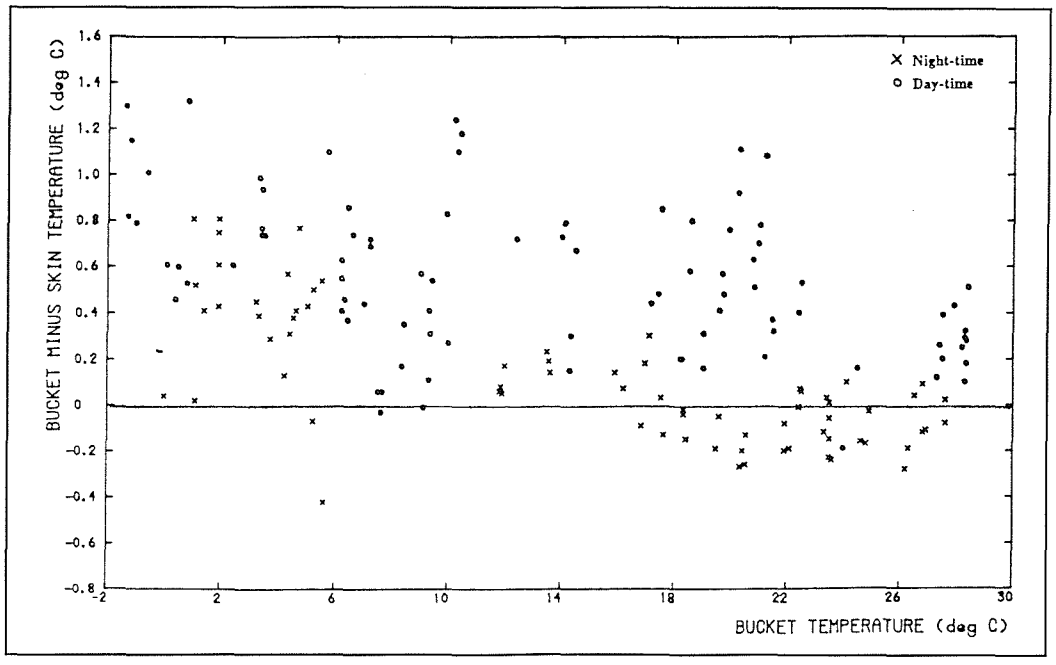

Figure 3.3 Observations of -ΔT (ie bulk *minus* skin) made on a transect from the UK to the Antarctic. The bucket temperature can be thought of as a latitudinal scale with the cooler temperatures representing the higher latitudes. (From Hepplewhite, 1989).

Figure 3.3 shows -ΔT (i.e. bulk *minus* skin) values collected on a transect from the UK to the Antarctic (Hepplewhite, 1989). These data also show that the skin effect is generally less in the warmer more humid tropical/mid latitude regions than in the dry cooler polar latitudes.

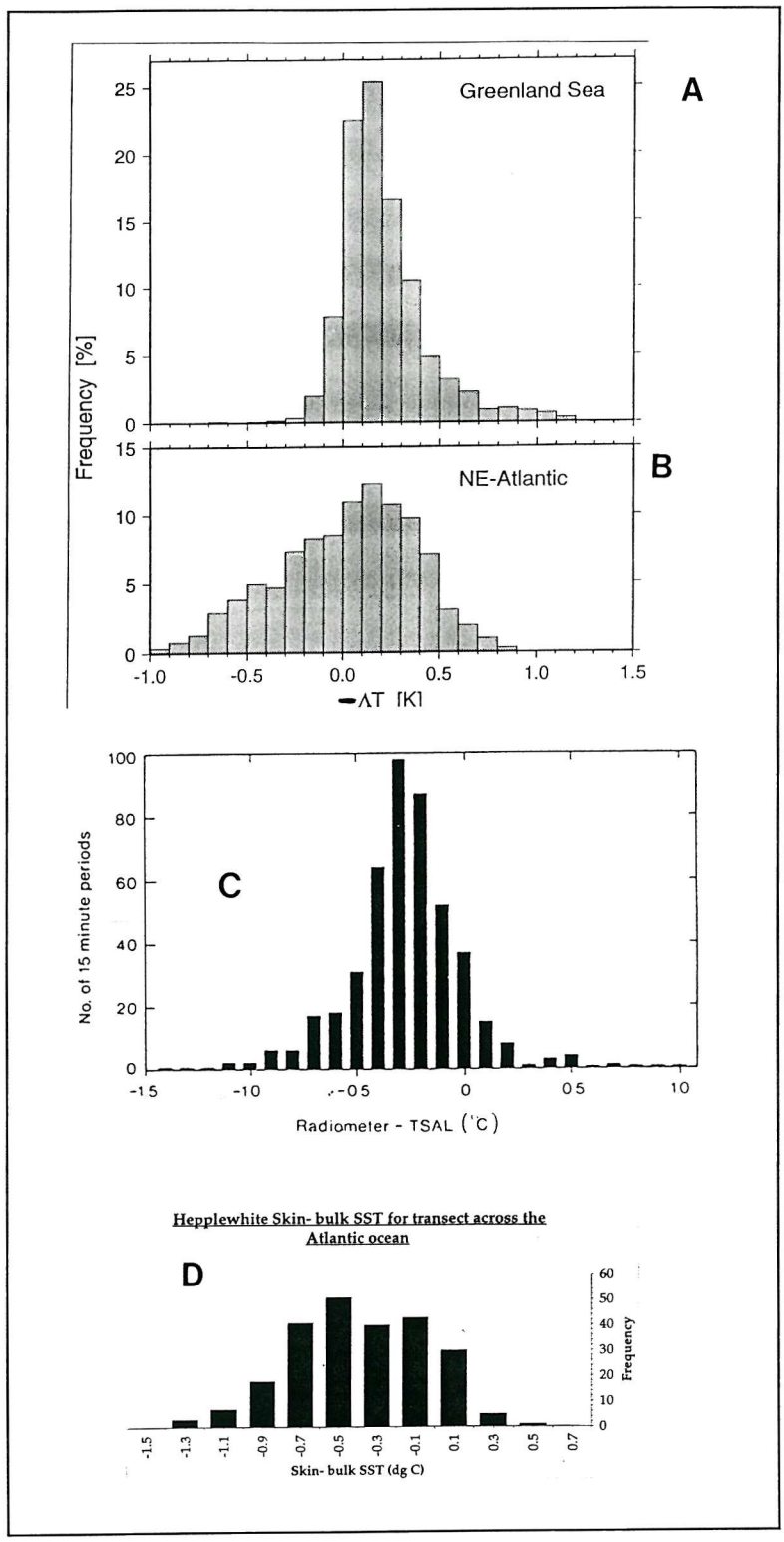

Figure 3.4 The distribution of -ΔT for the NE Atlantic (October and November 1984) and (b) the Greenland sea (February - March 1991 and 1993)(From Schluessel, In press). (c) ΔT in the West Equatorial Pacific (Coppin *et al*, 1991), (d) ΔT distribution from UK to Antarctic (Hepplewhite, 1989).

However, it must be remembered that locally these global situations are modified by the atmospheric variability of the dominant pressure systems having

characteristic humidity, wind speed and air temperature conditions. In this context and from figure 3.3, it is clear that ΔT has a regional dependence (§ 2.2.3).

Figure 3.4 (a) shows the distribution of $-\Delta T$ for the NE Atlantic and figure 3.4(b) the distribution of measured $-\Delta T$ in the Greenland sea (from Schluessel *et al, in press*). The characteristics of ΔT in these two regions differs greatly; the Greenland sea data having a greater negative skewness than for the NE Atlantic. The effect of stronger insolation in the lower latitudes is to generate a diurnal thermocline which is thought to be responsible for the more Gaussian distribution in the sub-tropical case while strong cooling is evident in the polar regions which have insufficient insolation to generate a diurnal effect.

Figure 3.3 also shows a significant difference between the day and night time observations. Daytime observations are nearly always higher in temperature and have a larger scatter than those at night. At night in the absence of insolation, the total heat flux is directed out of the ocean and heat loss at the sea surface is predominantly by long wave emission. Thus an increased skin effect compared to that observed during the day would be expected. However as already discussed above, even in conditions of high insolation an appreciable skin effect can still exist.

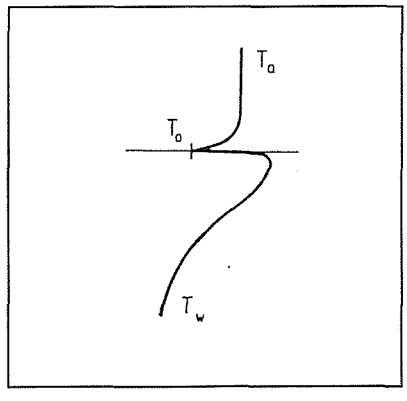

Figure 3.5 A schematic diagram of an idealised diurnal thermocline. Ta is the air temperature, Tw the bulk temperature at depth and To the interfacial temperature measured by a radiometer. (From Gemmrich and Hasse, 1992)

Figure 3.5 shows a schematic diagram of such a situation. This is an extremely important issue as it is the bulk temperature, uninfluenced by diurnal effects, that is required to be representative of the bulk ocean temperatures for climate models which often ruse mean monthly or weekly SST maps. If daytime ATSR imagery (having a return period of approximately 3 days in a 35 day repeat orbit configuration) is influenced by the diurnal effect, monthly or weekly derived SST maps may be in error as they will incorporate a warm bias from this transient phenomena unles explicit day and night time maps are derived. It must also be remembered that if it is the diurnal temperature that is required from such satellite imagery, the true temperature of this effect will be complicated by the cool skin which will still be present under such conditions.

ΔT has a dependency on the surface wind field which acts on the cool skin in two ways. Increased wind stress tends to produce mixing in the surface layers which will tend to destroy the cool skin exposing warmer water from beneath. At the same time the wind stress further increases the turbulent fluxes of latent and sensible heat which cooling the skin even more. This is clearly seen in figure 3.6 which shows ΔT plotted against wind speed. These data were obtained from an infra-red radiometer mounted on the German research ship *Meteor* during long night time hydrographic stations. ΔT is at a minimum when the wind speed is at 3 - 4 m/s and increases both in magnitude and scatter as the wind increases. The increase in scatter can be attributed in part to the presence of breaking waves and foam patches at the higher wind speeds contaminating the radiometric SST.

There are several other factors which may have an influence on the depth and magnitude of the oceanic skin. Katsaros (1980) describes how surface tension in areas possessing horizontal thermal gradients forces vertical circulation driven by convective instabilities, a process known as the Marangoni effect. ΔT may well be controlled by such a process and Katsaros, (1977) duly attempts to consider such motions in a parmeterisation. Surface slicks will affect ΔT by modifying the thermal characteristics of the skin layer as reported by Kropotkin *et al* (1978) and Katsaros (1980). Schluessel (*in press*) suggests that the major effect of surface slicks is to increase the amount of solar absorption and thus the skin temperature. Surface slicks can cover large areas of the ocean (observed in the NE Atlantic by the author) and maybe natural or anthropogenic in origin. Large raindrops will destroy the thermal sub-layer completely although the stabilising effect of a lower density freshwater layer at the sea surface, a type of surface 'slick', will tend to decrease the intensity of turbulence may lead to a deepening of the skin temperature (Katsaros, 1980).

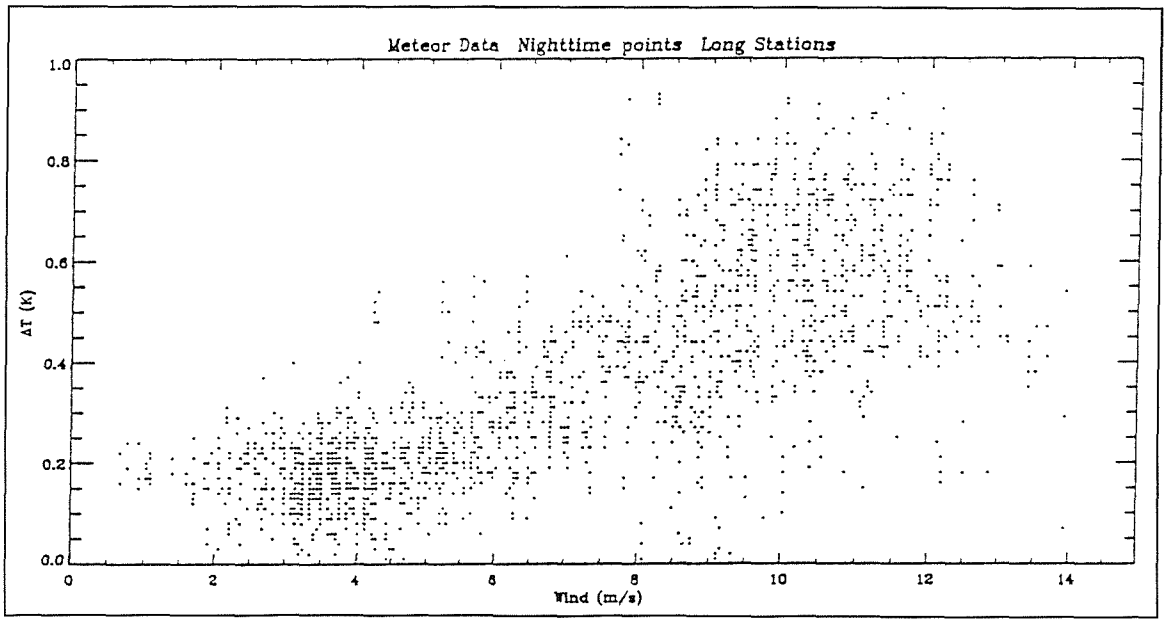

Figure 3.6 Night time observations of ΔT during long hydrographic stations from the research vessel Meteor. (From Emery, 1994).

3.4 Definitions of the fluxes occurring at the air sea interface.

In order to model the thermal skin effect, parameterisations of the processes acting at the air-sea interface need to be established. The magnitude of the turbulent fluxes defining the skin effect depends (amongst others) on the air-sea temperature difference, water vapour mixing ratio and surface wind stress. Such turbulent transports dominate the turbulent exchange of heat and momentum at the air-sea interface. It is extremely difficult to directly measure turbulent transfer processes although sonic anemometry has made significant advances in the last few years (Von Blank, 1985). Therfore parameterisations derive from a short set of observations made under a wide variety of atmospheric - oceanic conditions and seasons. The most reliable schemes are based on direct observations using eddy correlation methods and are well reviewed in Von Blank (1985). All parameterisations use a 10 minute mean of the observed values to account for the bursting nature of turbulence in the lower atmospheric boundary layer (Smith, 1988).

The surface wind stress, τ can be parameterised by the relation:

$$\tau = C_d \rho U^2 \qquad (3.1)$$

where C_d is a drag coefficient, ρ is the air density and U is the mean wind speed at the standard height. Smith, (1980;1988) discusses the drag coefficient for wind speed in the ocean and applies a stability correction for the effects of vertical eddies in the atmospheric boundary layer.
The sensible heat flux Q_H takes the form:

$$Q_H = C_h \rho c_p U (\theta - T_s) \qquad (3.2)$$

where C_h is a heat flux coefficient, c_p the specific heat capacity of air at potential temperature θ immediately above the sea surface , and T_s is the SST.

The following relationship defines the latent heat flux Q_L:

$$Q_L = C_l \rho L U (q_a - q_s) \qquad (3.3)$$

in which C_l is the latent heat coefficient, L the latent heat of evaporation of sea water, q_s the water vapour mixing ratio of the sea surface and q_a the water vapour mixing ratio of the atmosphere. The coefficients derived by Smith (1988) which depend on both atmospheric stability and wind speed are used throughout in this work. Parameterisations of the wind stress, sensible and latent heat flux are determined with accuracy's of approximately 0.2 N/m^2, ±25 W/m^2 and ±40 W/m^2 respectively (Von Blank, 1985).

The longwave radiative flux Q_T is the sum of the upward and downward radiation and is given by:

$$Q_T = L_d + L_u \qquad (3.4)$$

in which L_d and L_u are the downward and upward components.
Finally the Solar flux can be written as:

$$Q_S = (1 - a) S_d \qquad (3.5)$$

in which a is equal to the oceanic albedo (see Payne, 1972) and S is the direct solar flux measured at the sea surface.

Thus the total heat flux acting through the air - sea interface Q, is given by:

$$Q = Q_S + Q_L + Q_H + Q_T \qquad (3.6)$$

Ignoring the effect of slar radiation the heat flux can be described by Q_N:

$$Q_N = Q_L + Q_H + Q_T \qquad (3.7)$$

3.5 Theoretical treatments of the skin effect

Several authors have parameterised the skin effect in terms of the local heat fluxes and wind speed at the air sea interface. Mammen and Von Bosse, (1990) classify theoretical descriptions of the skin effect into three broad groups categorised by assumptions made about the turbulent state of the skin layer. These can be summarised as follows:

1. Stagnant-film models assume a laminar ocean skin layer at the air sea interface where all thermal transport is assumed to be via conductive molecular processes. Turbulent transport below gives way to a laminar sub-layer which in turn reduces to a diffusive molecular layer at the air-sea interface. The turbulent layer is characterised by an effectively infinite transport coefficient as proposed by Wu (1985). An example of this type of model was proposed by Saunders (1967) who using dimensional arguments suggested that the mean ΔT for night time condition could be approximated by:

$$\Delta T = -\frac{\lambda(\nu / \kappa)Q_N}{u_* c_p \rho} \qquad (3.8)$$

where ν and κ are the coefficients of molecular viscosity and thermal diffusion, u_* is the upper oceanic friction velocity , c_p is the specific heat capacity of sea water at a constant pressure, ρ is the sea water density and λ a constant of proportionality. λ varies with the wind speed and typical values of 1.1 @ u=1 m/s to 8.5 @ u=11 m/s are given (Schluessel *et al*, 1989). Although it is agreed that λ is wind speed dependent, the absolute value varies from author to author (Grassl, 1976, Paulson and Simpson, 1981; Wu, 1985; Schluessel *et al*, 1989). Under conditions of light wind where free convection has a major role, equation (3.7)

breaks down as surface tension begins to control the onset of convective instabilities.

For light wind conditions where free convection is prevalent Katsaros *et al* (1977) proposed the following relationship based on laboratory measurements which is applicable for wind speeds <2 m/s:

$$\Delta T = A^{1/3}\left(\frac{\alpha g \kappa^2}{\nu}\right)^{-1/4}\left(\frac{-Q_N}{c_p \rho}\right)^{3/4} \qquad (3.9)$$

where α is the coefficient of thermal expansion of water, g the acceleration due to gravity and A, a non dimensional coefficient. Katsaros *et al* (1977), derive A=0.156 from laboratory measurements made in a large tank of water.

2. Diffusion models are based on the flow patterns seen at rigid wall boundaries. Hasse, (1971) assumes that the efficiency of turbulent diffusion decreases approaching the wall so that the coefficient of turbulent diffusion is a function of distance from the boundary wall. By using a function of the turbulent diffusion coefficient for heat and a known heat flux, the temperature distribution can be calculated. Hasse shows that the ΔT is proportional to Q_N/U and proposed the following relationship which takes into account the influence of Q_S short wave radiation and the effect of the latent Q_L, sensible Q_H, longwave Q_T fluxes and U the wind speed, based on a linear regression fit to observed values of Q_N/U and ΔT;

$$\Delta T = C_1 \frac{Q_N}{U} + C_2 \frac{Q_S}{U} \qquad (3.10)$$

The coefficients C_1 and C_2 are derived from laboratory measurements and are shown to vary with depth as the absorption of solar radiation for various depths assumes a logarithmic absorption profile (Schmit, 1908). The transient effect of

clouds on Q_S is noted and Hasse argues that although this will affect the diffusive steady state assumptions of the model, these will be the best on average.

3. Surface renewal models describe the action of single turbulence elements in which it is assumed that each element will remain at the surface for a finite time after which it will be replaced by new elements from the bulk water beneath. The time each parcel remains at the surface is related to the intensity of the turbulence. Thus a cyclic growth and destruction of the molecular sub-layer is assumed. Kim *et al* (1971) observed that within a boundary wall turbulent momentum and transport takes place in intermittent bursting motions at small time and space scales. Lui and Businger (1975) developed a method for calculating temperature profiles in molecular sub-layers by assuming that these undergo cyclic growth and destruction. More recently Soloviev and Schluessel (1994) describe a model of this type drawing on the work of Lui and Businger (1975), which is able to parameterise both the cool skin of the ocean and the coefficient of direct air-sea gas transfer which result in the following three relationships for low convective regimes with wind speeds between 0 - 5 m/s, forced convective regimes having moderate wind speeds of 5 - 10 m/s and high wind speeds of >10 m/s;

$$\Delta T = \Lambda_0 \, \mathrm{Pr}^{1/2} \left(\frac{-\alpha g q_0 \nu}{R f_{cr}} \right)^{1/4} \qquad 2 < \mathrm{U} < 5 \ \mathrm{m/s} \qquad (3.11)$$

$$\Delta T = \Lambda_0 \, \mathrm{Pr}^{1/2} \, q_0 u_*^{-1} \qquad 5 < \mathrm{U} < 10 \ \mathrm{m/s} \qquad (3.12)$$

$$\Delta T = \Lambda_0 \, \mathrm{Pr}^{1/2} (\nu g K e_{cr})^{1/2} q_o u_*^{1/2} \qquad \mathrm{U} > 10 \ \mathrm{m/s} \qquad (3.13)$$

where $q_o = -Q_N / c_p \rho$, Pr is the Prandl number ν/κ and Λ_o is a function of the probability density for the time between bursts based on the experiments of Rao *et al* (1971). Soloviev and Schluessel estimate that $\Lambda_o = 13.3$ and the critical surface Richardson number $Rf_{cr} = -1.5 \times 10^{-4}$ at low wind speeds using Grassl's (1976) cool

skin data. Ke_{cr} is the critical Keugelan number ~0.18 based on the Keugelan number definition of $K=u^{*3}/gv$ and from the critical wind speed $U_{10\,m}$ =~ 10m/s. This is the wind speed at which according to the Beaufort scale longwave breaking sets in and white-capping gains control over the cool skin effect. This is the first attempt to parameterise the skin temperature at high wind speeds. The effects of bubbles and spray production increasing the heat transfer rate (Woolf and Thorpe, 1991) at high wind speeds is noted as raising uncertainties about such a parameterisation.

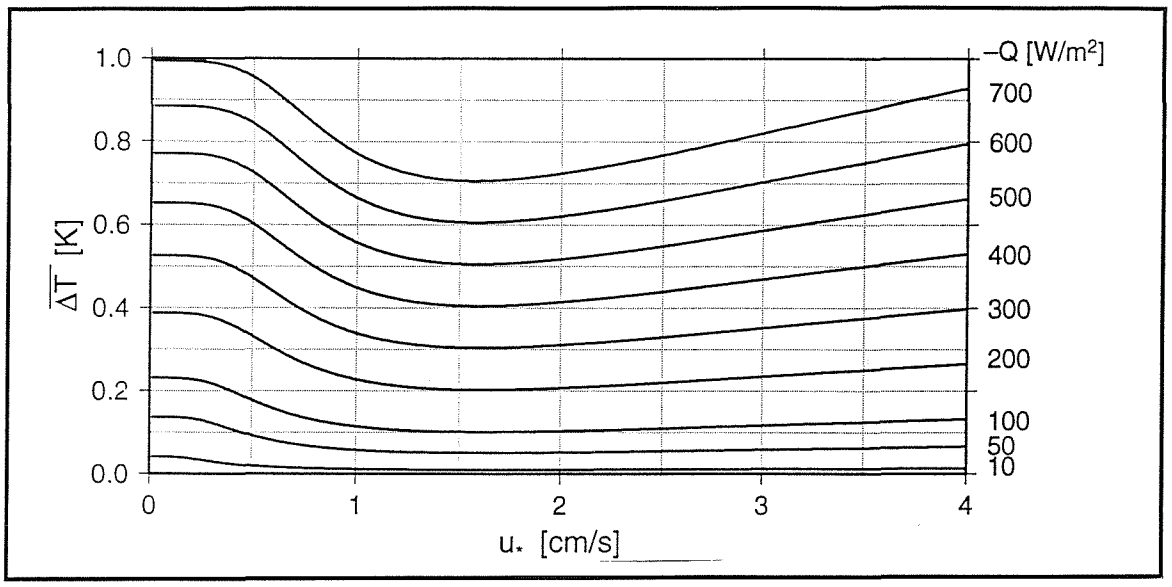

Figure 3.7 Output from the model proposed by Soloviev and Schluessel (1994) plotted against friction velocity, U*. (from Soloviev as Schluessel, *in press*).

Figure 3.7 plots the output of this model against the friction velocity, u_*. The model predicts that an initial increase in wind speed will tend to destroy the surface skin layer while a further increase forces the latent exchange of heat to become dominant and the skin begins to intensify.

Based on the laboratory observations made by Okuda *et al*, (1977), who show that there is an increase in surface friction and skin layer depth on the windward side of water waves shown in figure 3.8, Eifler (1992) assumes that small (< 3 cm) surface waves are the determinant factor in defining the surface renewal time scale of the skin layer via 'burst and sweep' processes (Kim *et al*, 1971). He describes a model which parameterises the cool skin as a function of the variability of surface

friction and heat fluxe across a wind wave. It is assumed that on the windward side of a water wave short young (< 3 cm) waves become superimposed on the longer waves and force the dominant process for mass transfer of momentum and heat. Surface renewal occurs in the form of 'burst' and associated 'sweep' events on the lee of wind waves as shown in figure 3.9.

The boundary layer growth-breakdown model of Nijling (1969) is modified to give similar form as that proposed by Saunders in equation (3.7) as follows:

$$\Delta T = [\frac{u_o^+}{\mathrm{Pr}^{1/3}} + \frac{1}{\kappa + \mathrm{Pr}} \ln \frac{h_{ref} u_*}{\nu y^+_o}] \frac{\nu Q_N}{k u_*} \tag{3.14}$$

where h_{ref} is the depth at which the bulk SST is measured, κ is Von Karmans constant = 0.472, u_o^+ is an estimate of the velocity at the maximum distance from the skin boundary y_o^+, given by:

$$u_o^+ = \frac{4}{3}\left[\frac{Lu^*}{\nu}\right]^{1/3} \tag{3.15}$$

and

$$y_o^+ = 3u_o^+ \tag{3.16}$$

where L is wavelength of the dominant wind wave. Eifler suggests a value for L of 0.03 m.

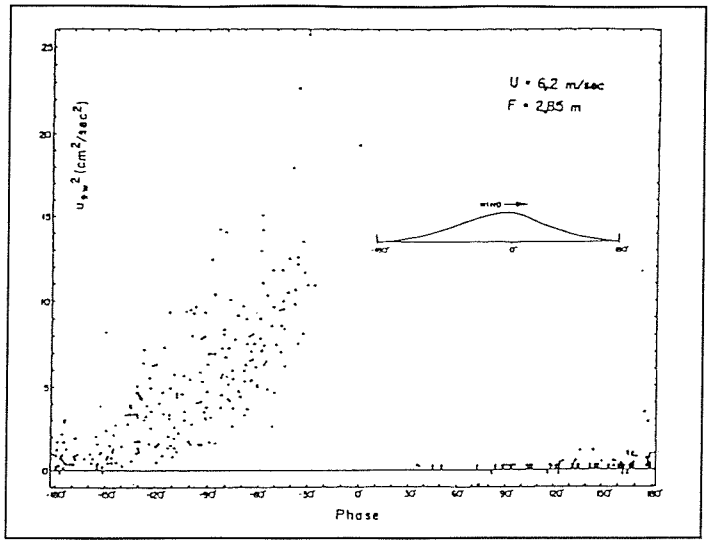

Figure 3.8 Shear stress distribution along the surface of a wind wave. (from Okuda et al, 1982).

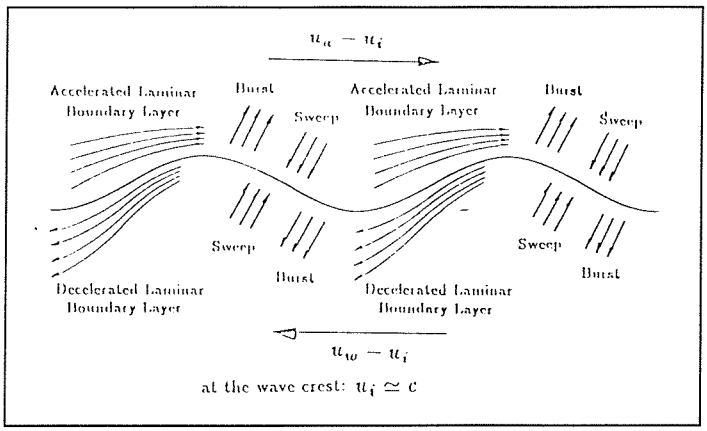

Figure 3.9 A schematic representation of the typical momentum, heat and mass transfer wave (from Eifler, 1992).

In this parameterisation the only free parameter is the average wavelength of the small wind waves ***L***, which are assumed to govern heat, momentum and mass transfer. Implicit in this relationship is that this transfer is independent of the wavelength ***L***, that is used.

Liu *et al* (1979) suggested that the time scale of surface renewal is related to the Kolmogorov micro-scale and by relating this to the thickness of the skin layer showed that ΔT could be estimated using:

$$\Delta T = G \frac{Q_N}{\rho c_p u^*} Rr^{1/4} \Pr^{1/2} \qquad (3.18)$$

where ***Rr*** is the roughness Reynolds number and ***G*** a proportionality constant. Liu *et al* suggest a value of ***G***=9.3.
Brutsaert (1975) suggests a similar model which does not include a dependence on ***Rr*** in the smooth flow regime i.e. when ***Rr*** <0.13.

4. Simple empirical parametersations based on *in-situ* observations such as that proposed by Schluessel *et al* (1989). Here ΔT is parametised by developing the Hasse, (1971) formulae given in equation (3.9). *In-situ* observations of ΔT and meteorological data are used in a multiple stepwise regression giving the following relationships are derived based on observations in the NE Atlantic:

$$\Delta T = a_o + a_1 u(T_s - T_a) + a_2 u(q_s - q_a) + a_3 Q_L \qquad (3.19)$$

which is representative for night time conditions and during the day:

$$\Delta T = \frac{a_o + a_1 Q_S}{u + a_2(q_s - q_a) + a_3 Q_L} \qquad (3.20)$$

where the coefficients a_1, a_2 and a_3 are constants determined from the regression analyses. If the Q_L term is ignored in these equations, which will then only use standard meteorological variables, results in a negligible decrease in the correlation of the regression analyses. The attraction of the latter approach is that the parametersation relies on routine meteorological measures made by ships and thus does not require any 'non standard' information to make an estimate of ΔT.

3.6 Conclusions

In the preceding two chapters the differences between the SST measured by a satellite radiometer and the SST measured in-situ have been comprehensively

discussed. The lack of detailed in-situ radiometric SST and environmental observations with which to explore the relationship between the skin and bulk temperature that are coincedent with satellite SST observations has resulted in inconsistent observations of ΔT (Coppin et al 1991; Schluessel et al, 1990) It is an immediate requirement that further in-situ observations of ΔT are collected for different regions in order to fully characterise the thermal skin effect with reference to infra-red SST retrievals from space. Ideally these data should be made routinely from many areas of the earth's oceans but the prohibitive cost of research ships and the difficulties involved in operating delicate instrumentation in the marine environment make this an unlikely proposition for the near future.

Chapter 4. An experiment to characterise the skin-bulk temperature deviation.

In order to explore the relationships between the skin and bulk temperature of the ocean discussed in the previous Chapters, a field program was undertaken to collect a suite of surface meteorological and oceanographic data. This chapter discusses the measurements made and the instruments used. Finally the errors associated with the data collected are presented.

4.1.1 Direct measurements of ΔT and satellite SST.

Perhaps the most difficult problem to address in an assessment of the mechanics and character of the bulk-skin relationship is the accurate determination of the skin temperature *in-situ*. One method has already been discussed in Chapter 2 using the STEP profiler of Mammen and Von Bosse (1990). However the preferred method is to use a ship mounted radiometer as discussed in Chapter 2.
There are insufficient *in-situ* infra-red radiometric measurements concurrent with satellite and bulk SST is due to a number of factors:

1. The difficulty of accurately calibrating an *in-situ* ship mounted radiometer.

2. The presence of cloudy conditions during a satellite overpass.

3. Bad weather periods prohibiting data collection.

4. Successfully navigating a ship into the field of view of a satellite.

5. The cost and availability of both suitable ships and instrumentation.

Some of the above problems are related to the environment in which the measurements are made wheras others are a consequence of the instrumentation used. It is the latter that is of interest in this chapter.

4.2 *In-situ* infra-red radiometer systems.

Over the years many authors have used a variety of infra-red radiometer systems deployed from many platforms, both stationary and while underway at sea. Many of these are described in table 3.1. A popular choice of instrument has been the Barnes PRT-4 or improved, PRT-5 radiometer. These instruments use a broad 8 - 14 μm filter and a single black body reference cavity for calibration. More recent developments have resulted in a new generation of infra-red *in-situ* radiometer design employing a variety of calibration techniques and innovative features to minimise the errors associated with such delicate instrumentation.

Unlike the space environment, which typically imposes large temperature variations, ultra low pressures requiring the careful selection of materials, and power limitations, the marine environment has its own impositions. High humidity and marine aerosol (composed almost exclusively of water and salt) demand that all electronic circuitry be enclosed in a waterproof housing. The ubiquitous deposition of salt while at sea further requires that instrument black body units and fore optics are effectively insulated from the environment. This can only be achieved with any degree of certainty by totally sealing the instrument using an infra-red 'window' material such as Germanium (Ge), Zinc Selinide (ZnSe) or Barium fluoride (BaFl). This has the further advantage that during periods of inclement weather, the instrument is fully protected and a minimal amount of attention by an operator is required. The latter consideration should not be underestimated as weather changes extremely quickly at sea and typical radiometer installations are in relatively dangerous locations (such as fore masts or booms) and may be difficult to attend to. In certain areas of the earth's oceans there may be extremes of environmental temperature in which the instrument is required to operate. Tropical regions will have a high amount of insolation during clear sky conditions which can appreciably heat the instrument and in some cases result in a null calibration. The electromagnetic noise levels found on typical ship installations are high. Sources include the high power radio transmitters, radar equipment and mechanical noise generated by the various attachments often

present on ships such as cranes, derricks, pumps, etc. Finally, problems in effectively grounding a ship to earth and the non-stationary nature of ships' power supplies add to the list of problems associated with the use of delicate instruments (such as a radiometer) on a ship.

Contrary to the requirement for protecting a radiometer fore optics from the elements in relation to accurate measurements it is preferable not to seal *in-situ* infra-red radiometers as any contamination due to water or salt on a window will nullify the instrument calibration. Further many of the infra-red window materials are easily corroded by salt water. I Barton (personal communication) has used a Ge window (Kodak Irtran) covered with a protective seal on an airborne IR radiometer which had a transmission of ~ 99% and was relatively robust. It must be stressed here that if an infra-red radiometer is windowed, careful thought must be given to the method chosen to clean the window to avoid calibration uncertainty. It is due principally to the latter reason that infra-red radiometer design has been reluctant to seal such instruments.

Unfortunately this means that a biased set of *in-situ* skin measurements may result as deployment of such costly and delicate instrumentation during heavy weather is hazardous to both instrument and operator; the bias tending towards the lower wind speed and sea state conditions. To minimise instrument degradation, many designs either bury the beam aperture deep within a protective cavity or require deployments in good weather only. In order to assess the degradation of the instrument black body cavities and instrument fore optics it is recommended that a pre- and post calibration of the instrument against a known black body source is performed before and after use at sea.

Typical installations at sea use custom regulated power supplies having surge protection devices. However such devices cannot compensate for a low current/voltage situation, which in many cases will have an unpredictable effect. To minimise this and the effects of electromagnetic interference, heavy duty

shielded cables are used especially over the long cable runs encountered on ship installations. These can cause problems if not earthed correctly or are so long that power loss occurs. Finally, the human element when working from a ship cannot be underestimated. A ship is a warren of cables and switches that can be 'tested' or 'checked' by any number of ships personnel which may affect some instruments ie they can be turned off.

4.3 Calibration of *in-situ* infra-red radiometers.

The method for calibration of sea going *in-situ* infra-red radiometers varies according to the instrument used and the author in question (McAlistair and McLeish, 1970; Katsaros, 1976; Hepplewhite, 1989; Schluessel *et al*, 1990). The optimum approach remains an on-going area of research. An infra-red radiometer detector will respond not only to radiation emitted from a target source but also stray radiation reflected into the radiometer field of view and changes of the detector temperature itself. Stray radiation will originate both from within the instrument itself and by reflection at the sea surface and if the temperature of the detector is not regulated, as is the case on many *in-situ* instruments, its response function will vary as the instrument temperature varies. This results in a gradual drift of the instrument gain. In order to correct for instrument drift, calibrations against a known black body source need to be made frequently. In general, the calibration of sea going *in-situ* radiometers falls into two distinct categories:

1. Those using internal reference black body cavities which are periodically viewed and are thus self calibrating.

2. Externally calibrated radiometers in which an external black body source is periodically viewed.

4.3.1 Internal calibration

Hepplewhite (1989) developed a self calibrating radiometer relying on the use of two internal black (grey) body units held at different temperatures for absolute

calibration of the instrument signal. This design has been modified by Barton and Knight, (1988) and further developed by Satellites International Limited (SIL, 1990). Absolute calibration during normal operations is quoted to ±0.1 K (SIL, 1991) although a detailed analysis undertaken by Thomas *et al* (in press) suggests that an accuracy of ±0.15 K is a reliable estimate.

The problems associated with this calibration philosophy include the following:

1. Black body temperature drift and thermal gradients within the cavities themselves lead to erroneous radiance to temperature calculations. To avoid this requires stringent black body design and construction (see Mason *et al*, 1989) with extensive calibration of the cavities once in place.

2. The accurate determination of black body cavity temperatures. This will become more difficult as the instrument logs more hours, because of drift in the calibration of the devices used to measure the physical temperature of the black body cavity (typically embedded platinum resistance thermometers). Periodic replacement/refurbishment of the black body cavities may be necessary.

3. Electronics non linearity. This can be avoided by the careful design of electronics packages. The SIL instrument used in this study required the exact voltage and current specifications to be met for reliable operation. Further problems with this particular instrument under this heading include a voltage drop associated with the activation of a solenoid (required to select between filters).

4. Black body and optical system degradation due to salt contamination. This requires that accurate pre- and post calibration of the entire system is undertaken before and after use at sea.

Although not part of the internal calibration itself but relevant to the total end-to-end calibration of the system are the following:

5. Deviation of the sea surface emissivity from unity and variations in the emissivity associated with ship roll and pitch motion. Methods of minimising this effect include mounting the instrument on a gimball mount or the direct measurement of ships roll and pitch. On many modern research vessels Acoustic Doppler Current Profiler (ADCP) systems often record the roll/pitch of the ship for use in their calibration routines and this offers a convenient data source for correcting emissivity due to radiometer zenith angle changes.

6. Contribution of downwelling radiation by reflection at the sea surface. To account for this effect requires an independent measure to be made of the downwelling radiance component temporally coincident with the SST measure. Saunders (1968) discusses the effect of low clouds moving into the direction of specular reflection of an infra-red radiometer viewing a calm sea. He notes that the downwelling radiance from the base of clouds is higher than for clear sky conditions and the effect of such a situation is to increase the *apparent* temperature of the sea surface when measured using an infra-red radiometer as shown in figure 4.1. However, Bradley, (1982) demonstrates that the ocean skin temperature, having a response time of ~ 10 seconds, should follow changes in the downward longwave flux due to the passage of low cumulus type clouds. Consequently this type of calibration method requires that an independent measure of downwelling 'sky' radiation is made temporally coincident with the SST measure and it is important to ensure that this measurement is made from an area of the sky from which radiation would be reflected into the incidence angle of the surface measurement.

With careful handling and vigilant monitoring of the prevalent weather conditions while at sea, this type of calibration can be most successful (Hepplewhite, 1989; Coppin *et al*, 1991; Thomas *et al*, in press).

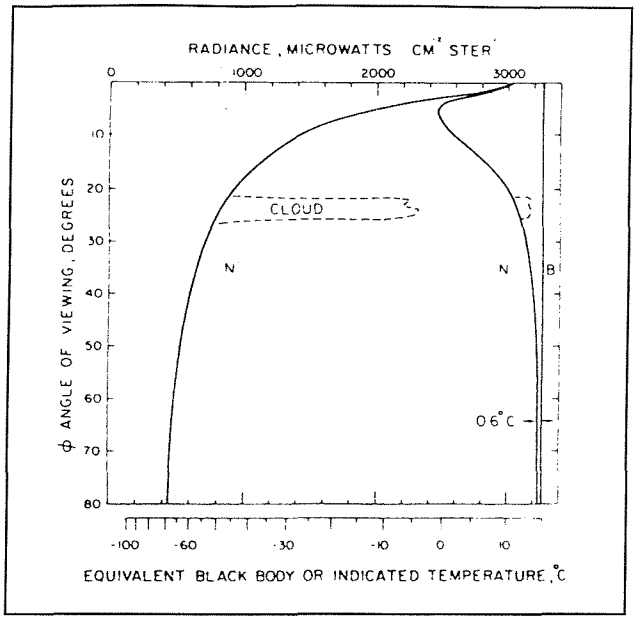

Figure 4.1 Typical distributions of the radiance of a calm sea N, and that of a cloudless sky, N' in the region 800 - 1200 cm^{-1}. B is the radiance of a black body having the same temperature as that of the ocean. The effect of a passing cloud increasing the total radiance measured by an infra-red radiometer is shown as a chain line. Φ is the radiometer zenith angle. (From Saunders, 1968).

4.3.2 External calibration, the 'Stirred tank' method.

Grassl and Hinzpeter (1975), developed an external calibration system for use with sea going infra-red radiometers which apparently compensates for most of the problems outlined above. In this calibration method, known as the 'stirred tank method', a well stirred tank of sea water is viewed alternately with a sea surface measurement. The temperature of the water in the tank is accurately determined and assuming a total breakdown of the thermal skin due to turbulent motion driven by stirring, the radiometer should be absolutely calibrated. In effect the stirred tank acts as an external black body source. An accuracy of ±0.05 K can is claimed when using this method (Scluessel *et al*, 1990) and a typical measurement cycle takes ~1 - 2 minutes (Schluessel *et al*, 1987,1989; W Emery personal communication).

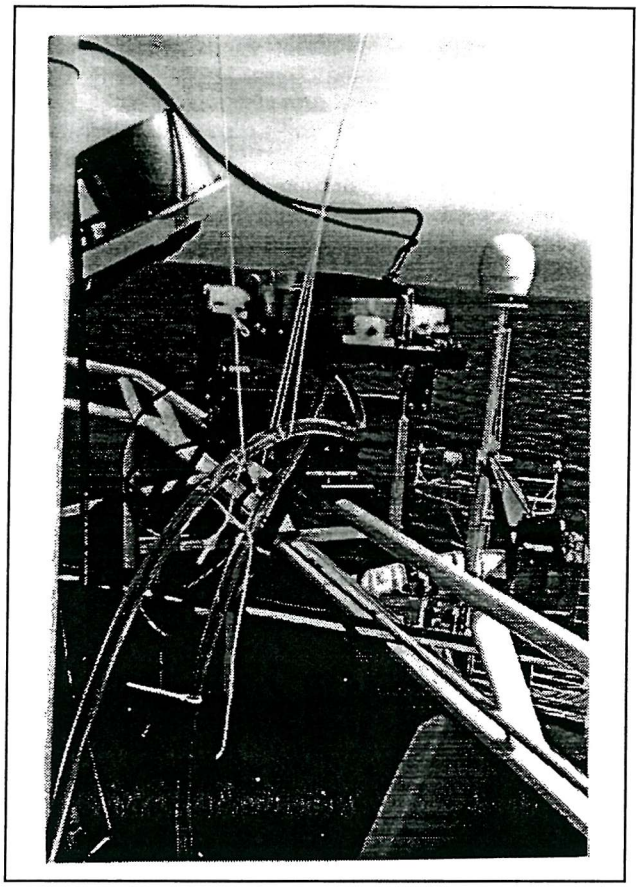

Figure 4.2 Installation ofthe stirred tank calibration system used by the OPHIR radiometer aboard the research vessel *Meteor*. (Courtesy of W Emery).

A major drawback is the implementation of this system as the radiometer or stirred tank needs to be physically moved on a regular basis. Most authors choose an automated system in which the stirred tank, rather than the radiometer, is moved into the field of view of the radiometer. Figure 4.2 shows the calibration system used by the OPHIR Multi-Band Infra-red Sea-truth Radiometric Calibrator (MISTRC) system. In this system two nested buckets are used in which sea water is pumped up to the base of the inner bucket through small holes producing strong vertical jets of water which, it is assumed, destroy the skin layer. Water then spills over the side of the inner bucket and is carried away via the outer bucket. The temperature in the inner bucket is continuously monitored with a PRT and a precision thermistor and the whole unit is mounted on a dual axis gimball frame to maintain a constant zenith angle view by the MISTRC. The bucket assembly is carried into the MISTRC field of view using a rail track assembly.

The assumption that the skin of a water bath is completely destroyed by vigorous stirring is the crux of this method. Laboratory work was undertaken to investigate the effect of stirring a busket of sea water to acertain wheather or not the skin was destroyed. For these experiments a self calibrating radiometer (RAL/SIL type) was suspended over a large (1.2 m diameter by 0.5m depth) bucket of sea water which was vigerously stirred by two vane stirrers. Stirring motions were directed near vertically to ensure that water was constantly upwelled to the surface of the bucket water. A desk top fan was used to determine the effect of wind (at a velocity of ~ 2 m/s) during stirring. The temperature of the water bath was accurately determined using a quartz thermometer.

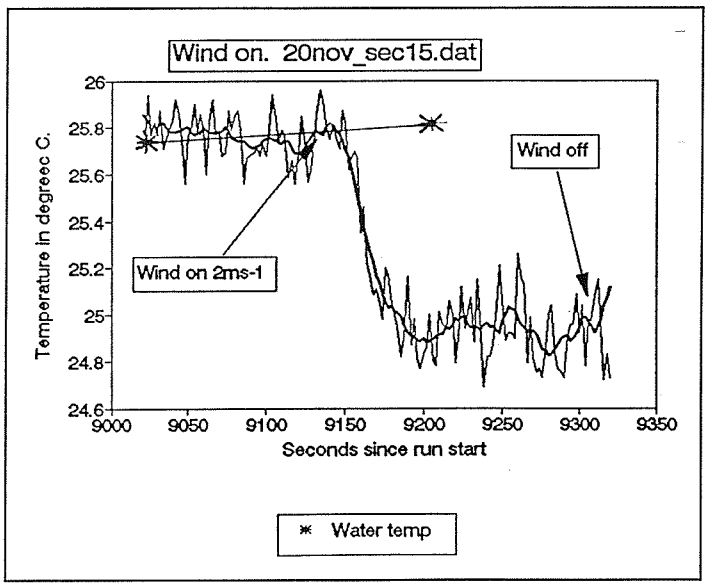

Figure 4.3 The effect of a 'wind' acting on a vigorously stirred tank of water. The heavy line represents the radiometric temperature smoothed using a 15 point weighted mean.

Figure 4.3 shows the radiometric temperature recorded by the radiometer when the water bath was stirred and a wind blown over the water surface. Clearly the cooling effect of a wind is able to dominate the effect of the stirring action and a cool skin remains at the water surface having a temperature difference of ~ 0.8 K. Although the conditions in the laboratory will enhance the latent and sensible heat fluxes (due to a dry atmosphere and large water air temperature differenceof ~

6°C), the wind effect will still be present on a ship. It is the authors' opinion that even with vigorous stirring, the effect of a wind acting on the water surface may cause horizontal thermal gradients to be present across the water bath.

Recently Grassl (personal communication), used a fast response thermistor to measure the temperature in the top millimetre of a stirred tank and found no such gradients. However, the skin of a water surface as seen by an infra-red radiometer is only micrometers deep and concern as to the validity of such a technique must be expressed; given the difficulty of following an uneven water surface with a thermistor and the thermal modifications made by the very presence of such a device within the skin layer, this determination remains questionable.

Jessup (1992) made detailed observations of a stirred tank using an Agema Thermovision 880 infra-red camera. This particular instrument is able to resolve relative temperature differences of 0.1 K. Images of the stirred tank revealed differences of >0.1 K across the water surface suggesting that the skin surface was not fully destroyed.

Simple laboratory experiments were conducted with an Agema 880 infra-red camera to further investigate the structure and behaviour of water in a bucket. Figure 4.4 shows an image taken with the Agema Thermovision infra-red camera of an unstirred warm bath of water (50 cm x 20 cm) in the laboratory. The plot beneath this image is a transect marked '1' in the image. Large temperature gradients of 0.4 K are present across the image demonstrating the large variability of the thermal skin under free convection conditions (ie no stirring and no wind forcing with a water temperature > than the air temperature). There is large spatial variability in this image demonstrating the need to stir the bucket and destroy the skin. Unfortunately it wa not possible to obtain imaary for the stirred bucket case during these experiments.

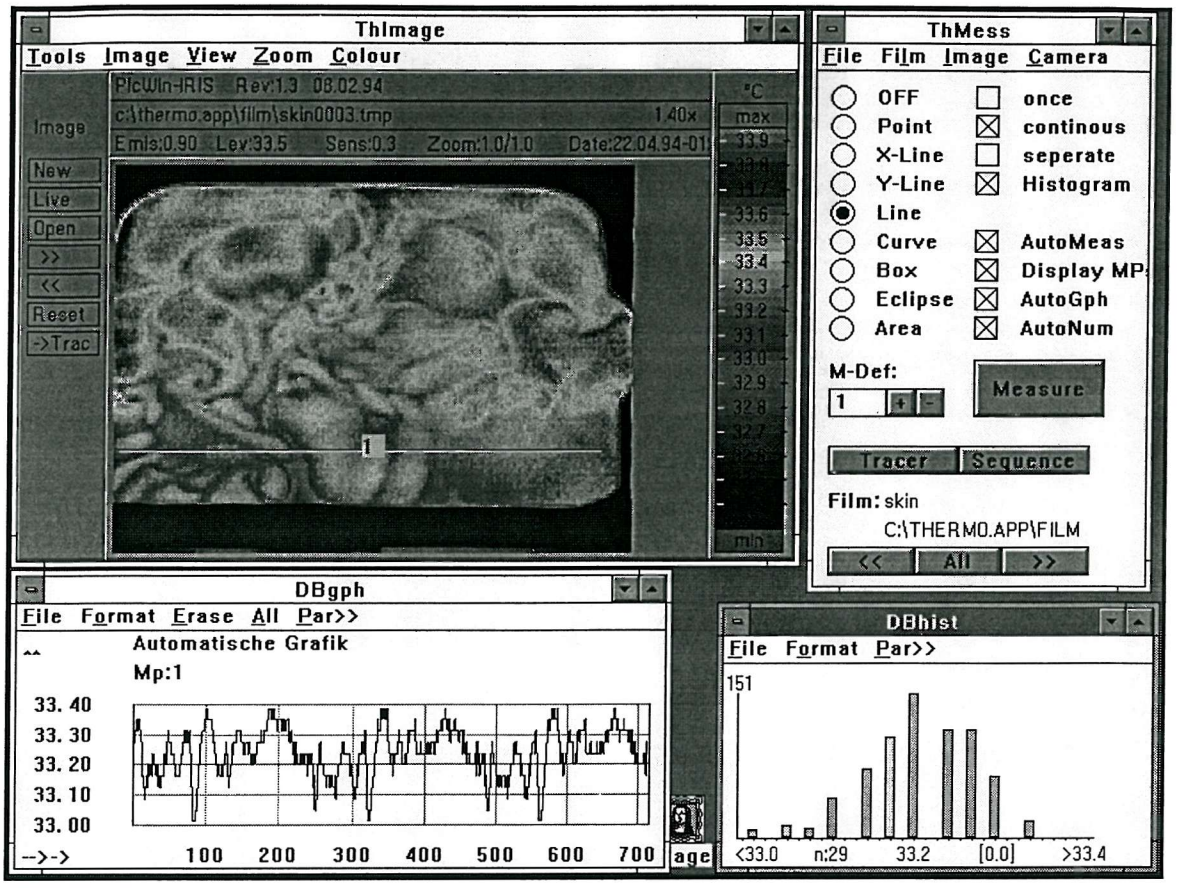

Figure 4.4 Thermal image of a tank of water under free convection conditions. The DBgph plot beneath the image is taken along the transect marked '1' on the above image.

Figure 4.5 shows a series of images taken at 1 second intervals of the same bucket which give a graphic example of the effect of a wind acting on the water surface. In this series the tank is left undisturbed (ie unstirred with no wind) for images 0 - 8 but for image 9 a 'wind' was forced over the water surface. The response time of the skin was extremely rapid with a general cooling in the centre of the bath. Note the effect of the water bath sides is to shield the effect of the 'wind' leaving a horizontal gradient present across the water surface.

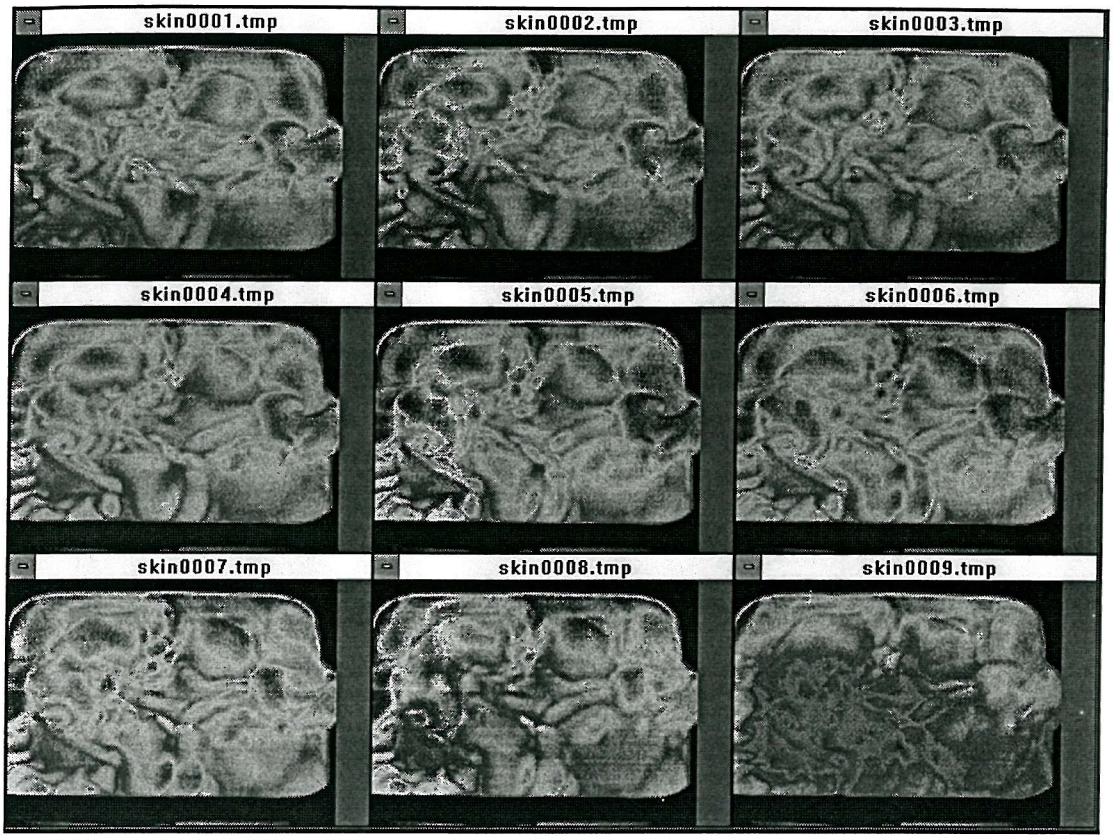

Figure 4.5 Images taken with the Agema Thermovision camera of a tank of water at 1 second intervals. The effect of 'wind' is clearly demonstrated in image 9. Temperature scale is the same as for figure 4.3.

Although these data are qualitative in nature (ie there is no *in-situ* temperature measure and no stirring action), they demonstrate the possibility that the skin temperature in a water bath may be extremely dynamic de to the effect of wind and may not poses the properties of a true black body as assumed in the stirred tank calibration method. Further investigation of these features of a stirred bath of water are required to validate the stirred tank calibration method.

A second criticism of this calibration method is the assumption that the downwelling radiation reflected into the incedence angle of the radiometer is fully accounted for. Figure 4.6 shows derived 'sky temperature' in °C (using Stefans law, equation 4.1) recorded in the north west Atlantic from the research vessel M/V *Håkon Mosby*.

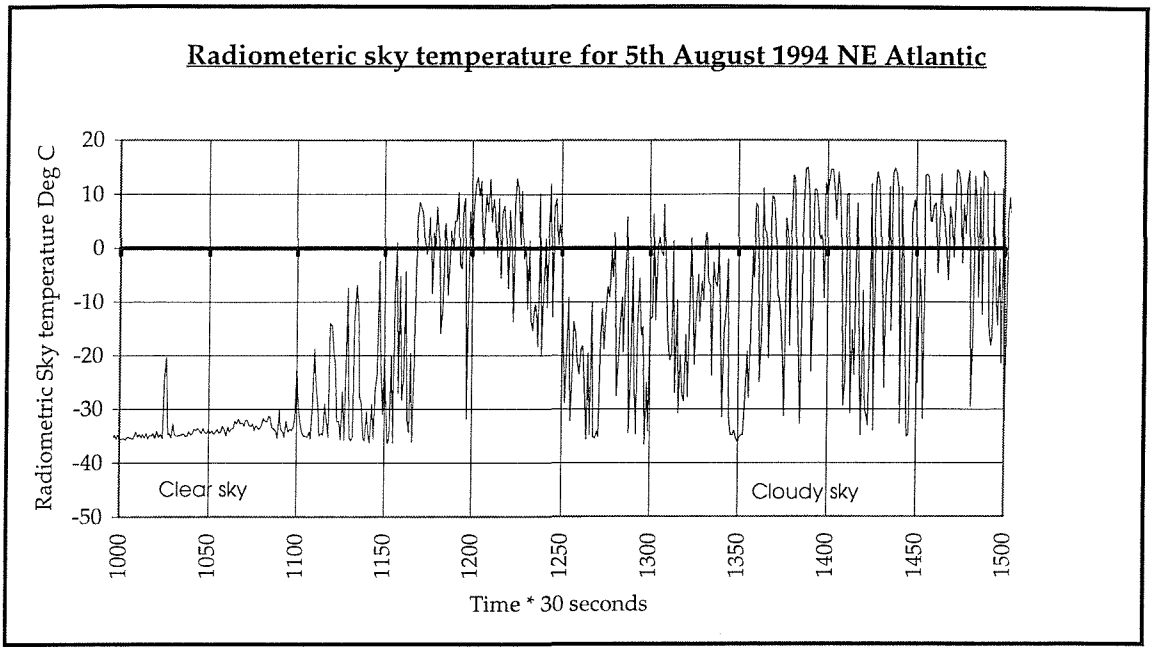

Figure 4.6 Sky temperature variability for the 5th August 1994 for a 4 hour period taken in the NE Atlantic from the M/V *Håkon Mosby*.

Clear sky conditions prevail at the beginning of the data record as shown by the low temperatures of -35°C. As the record progresses large variations in the downwelling radiance are seen at temporal scales of 1 - 2 minutes which are due to the increased downwelling radiance from the base of cumulous type clouds. In the case of clear skies or overcast skies (the latter not shown in figure 4.6), the downwelling radiance is nearly uniform at a negative temperature (positive temperature in the case of overcast skies). Under conditions of broken cloud cover the temperature swings voilently from positive to negative temperatures and it is clear that the stirred tank calibration method will be unable to account for the transient effect of passing cloud as the downwelling radiance can change significantly in the time it takes to complete a 'stirred tank' measurement cycle. Either the calibration measurement or the SST measurement when referenced to each other could be in error under such cloud conditions.

A final criticism of this method is the fact that the radiometer only has a single point calibration. Considering the discussion of the temperature stability of ships'sea water supplies in § 2.1, the effect of a warm bucket temperature relative to the sea surface may introduce significant errors as the slope of the calibration

gain relationship remains undetermined. In this case it is assumed that the gain is a constant term relative to the calibration measure which will introduce errors if the SST is not at a similar temperature to the water bath temperature used in the calibration.

4.3.3 New ship mounted infra red SST radiometer systems

Modern technology and more importantly, experience of operating sea going infra-red radiometers by several authors has led to the design of a new generation of *in-situ* SST radiometers. Two instruments are worthy of discussion the MISTRC and SISTeR radiometers.

4.3.3.1 The Multi-band Infra-red Sea-Truth Radiometric Calibrator (MISTRC)

Building on the experiences of German research groups in Kiel, Hamburg and the University of Colorado, OPHIR Corp. of Denver Colorado have designed the MISTRC radiometer system discussed above. This uses a combination of both internal calibration black bodies and the stirred tank method described above (see figure 4.2). The intrment is a 6 channel radiometer having both polarised and unpolarised near-infra red channels, polarisation is used here in an effort to reduce the amount of reflected radiation seen in the shorter wavelength channels. There are several design features worthy of note;

1. The instrument is shrouded in a sea water jacket and the detector unit (a Mercury Cadmium telluride element) is thermoelectrically cooled. This gives the instrument very stable thermal conditions (see section 4.2) which reduces the internal temperature drift of the instrument.

2. The instrument is fully sealed and relies on the use of a stirred bucket to monitor any degradation of the optical system.

The use of a window is questionable. The users guide clearly states the problems of window contamination and it is recommended that this is cleaned at least twice per day.

4.3.3.2 The Scanning Infra-red Sea surface Temperature Radiometer (SISTeR)

This instrument has been developed by the Rutherford Appleton Laboratory UK and is an internally calibrated system. During the design process of this instrument the Rutherford team, led by Dr T Nightingale, consulted many of the UK scientists who have experience of *in-situ* SST calibration radiometers. This has led to a design whichis both robust at sea and well calibrated. Design elements include;

1. Two fixed position precision reference black bodies used as an absolute calibration source.

2. The instrument will use a scanning fore optics mirror which will enable a sequential measure of calibration target, sky temperature and SST to be made each scan removing the need for a separate sky temperature measure. There is potential to make a sequence of 5 independent SST measures at spatial distances of ~5m apart at various zenith angles. This feature may be particularily useful in exploring the zenith angle dependene of the sea surface emissivity.

3. Will be capable of remote automatic shutdown using baffles eliminating the need to manually attend to the instrument during bad weather.

4) Will have an on board PC computer for real time data processing and allowing operator/data communications to be made via optical link. This will reduce noise due to external electromagnetic sources.

5. Provision is made to fix infra-red transmission windows to the instrument which will require the use of an external calibration source as for the MISTRC

instrument above although the fore optics are well protected from the elements by a careful housing design without such a feature.

6. Roll and pitch sensors are internal to the instrument facilitating emissivity corrections.

One important point needs to be raised here. As there are now several radiometer systems in operation within the international oceanographic community there is an urgent need for an inter calibration experiment in order to ensure that the skin measurements made are consistent from each system. This is especially important as the small number of instruments used rely on different calibration techniques which are deliverinfg short, regional sea surface skin calibration/validation data sets. Further, as the current knowledge of the skin-bulk temperature difference is poor it would seem wise to remove yet another potential source of error in its determination.

4.4 Skin - bulk experiment aboard the RRS *James Clark Ross*

During September and October 1992 the RRS *James Clark Ross* (JCR) was deployed as part of the BAS ongoing calibration and validation exercise for the ATSR instrument. The objective of this experiment was to collect *in-situ* radiometric SST and other environmental measurements coincident with ATSR SST imagery. Using these data the ATSR instrument could be validated and a detailed characterisation of the oceanic skin effect could be made. Unfortunately a combination of the ERS-1 orbit geometry, the restrictions of ship movement, cloudy skies and a change in the ATSR SST processing algorithms have prevented the completion of the high resolution ATSR and ship comparison. Appendix B describes the ATSR data that have been ordered in order to complete this work.

4.4.1 Description of the JCR 1992 SST experiment

Figure 4.7 shows the passage taken by the JCR during the SST experiment. The JCR departed from Grimsby (UK) on the 15th September 1992 bound for

Montevideo (Uruguay), Husvik (South Georgia) and finally Port Stanley (Falkland Islands). The JCR was equipped with the instrumentation described in table 4.1 and the measurements made by each of these instruments is discussed in the following sections.

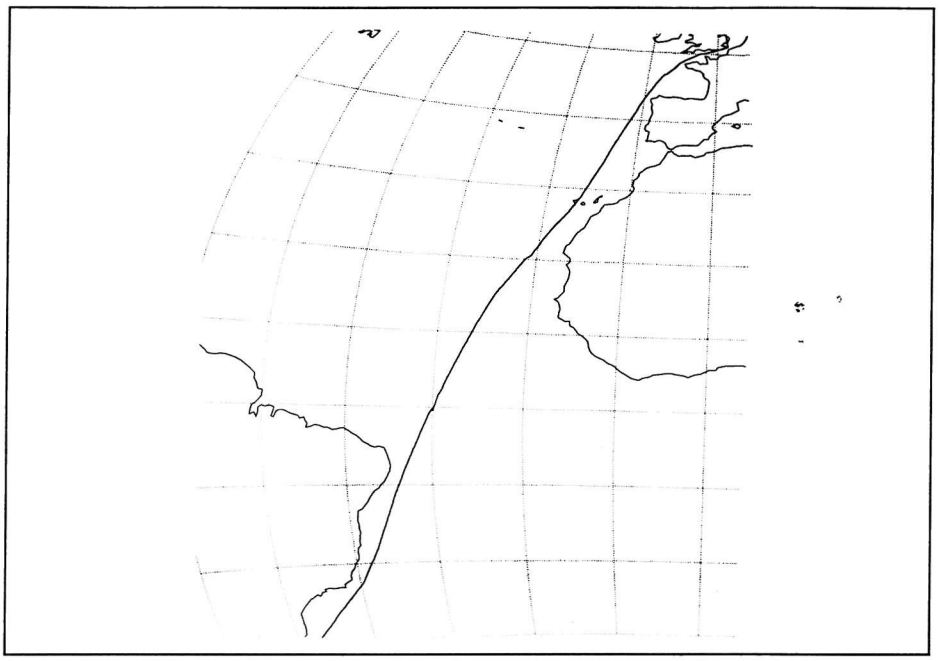

Figure 4.7 The passage of the RRS *James Clark Ross* during September and October 1992.

Parameter	Instrument	Height/depth above sea surface	Accuracy	Precision	Sample frequency
IR Skin SST	SIL STR-100 IR radiometer	+16.5	0.12K	±0.05K	7 seconds
Surface SST	Meteorological Bucket	-1.0 - 2.0 m	0.2K	±0.1K	Point sample
Bulk SST	In line Sea bird thermosalinograph	-5.5m	0.1K	±0.05K	5 seconds
Bulk SST	UK Met Office hull mounted thermistor	-2.5m	0.1 K	±0.05 K	5 seconds
Air temperature	Platinum resistance thermometer	+16 m	0.1K	±0.05 k	5 seconds
Wind speed	Vector instruments cup anemometer	+18 m	1 m/s	±. 1%	5 seconds
Wind dir.	Vector instruments wind vane	+18 m	1°	± 1%	5 seconds
Humidity	Vaisala HMP 35A	+16 m	1 %	± 0.5%	5 seconds
TIR	Kipp and Zonen CM-5 Pyranometer	+16 m	1 W m^2	± 0.5 %	5 seconds
Pressure	Digital solid state	+2 m	0.1 mbar	± 0.05 mbar	5 seconds
Sky radiance	TASCO THI-500 infra-red radiometer	+21 m	1 K	± 0.1 K	30 seconds

Table 4.1 Parameters measured and instruments deployed during the *James Clark Ross* cruise September - October 1992.

4.4.2 Bulk SST measurements

Bulk SST was primarily measured using a 'Sea Bird' thermosalinograph unit mounted on a dedicated high capacity sea water supply pipe. This instrument was located immediately above the intake pipe which was thermally insulated within the JCR minimising the effects of ship warming (§ 2.1). Sea water was pumped from a retractable probe having its intake 300 mm clear of the vessel hull giving a total depth of 5.5 m. Heating due to pumping and transit within the *James Clark Ross* is quoted to less than 0.05 K (P Woodruff personal communication). Data was logged at 5 second intervals to a resolution of 0.1K (pre set by the BAS data logging software) which, assuming a mean ship speed of 10 nm/h converts to a spatial sample of ~33 m. Figure 4.8 shows a photograph of the instrument.

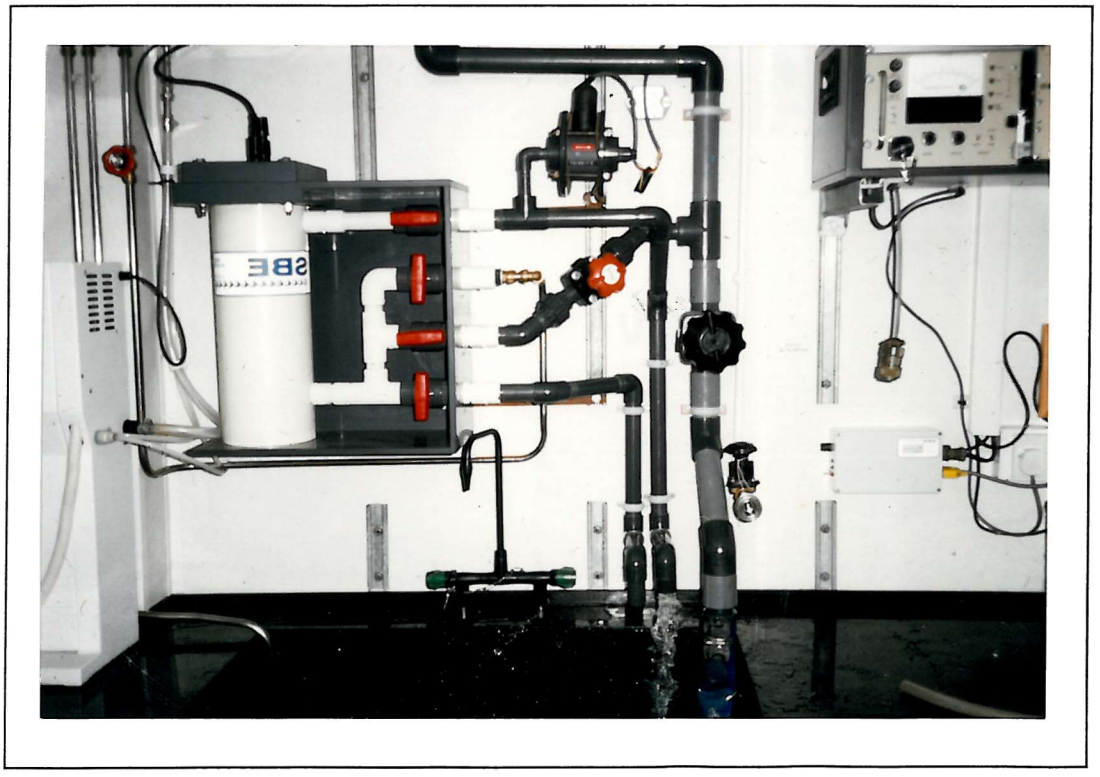

Figure 4.8 Photograph of the 'Sea Bird' thermosalinograph unit used on the RRS *James Clark Ross*.

SST was also measured by the standard Meteorological bucket method (§ 2.1) using mercury in glass thermometers. These data were taken where possible by routine throughout each day of the cruse. Such measurements are subject to

inaccuracies as the thermometer was only scaled at 0.2 K intervals. However, the scale is coarse enough to allow interpolation to a resolution of ±0.1K.

A hull mounted thermistor (installed by the UK Meteorological Office) logged bulk temperature at a depth of 2m. Unfortunately this instrument was found to be adversely affected by one of the heated ship's bunkers. Temperatures 1.5°C above those of the standard meteorological bucket samples were recorded throughout the cruise showing no systematic variation in offset between day or night time situations. A diurnal thermocline was therfore ruled out as the probable cause of this offset. Figure 2.4 (Chapter 2) shows the temperature relationships between the SST measurements for part of the cruise. The warming effect described above can be clearly seen in the hull mounted thermistor data. As a consequence, these data have been rejected on the grounds that the temperatures are unreliable having been warmed by the ships bunker.

4.4.3 Skin SST measurements

Skin SST was measured with an SIL twin channel radiometer mounted on the forward mast of the ship at a height of 18m. The instrument viewed the sea surface at an angle of 37° from the vertical giving a stationary atmospheric path length of 21m. This was found to be the smallest angle at which the beam would clear the ships' structure. The field of view of this instrument when mounted in the above fashion was approximately 1.5 m in diameter and a sample interval of 7 seconds equates to a spatial sample every 34 m (assuming mean ship speed of 10 nm/h). Figure 4.9 shows a photograph of the SIL radiometer installation.

Figure 4.9 Installation of the SIL STR-100 infra-red self calibrating radiometer installed o the forward mast of the RRS *James Clark Ross*.

Although equipped to measure SST at both 10.5 - 11.5 μm and 11.5 - 12.5 μm, the 12.5 μm channel was not used as this required a solenoid to be activated within the instrument in order to use the appropriate filter. Laboratory work with an earlier model of this design showed that the effect of using this solenoid was to destabilise the +5v supply rail within the instrument electronics package resulting in a spurious periodicity being introduced into the calibration data stream. Thomas et al (in press) have demonstrated that this is also the case for the BAS SIL radiometer. All skin SST data were therefore taken using the 10.5 -11.5 μm channel. SIL radiometer data were logged using a custom PC programme provided by J Thomas of BAS. The instrument failed due to spurious PRT temperatures from the hot black body PRT on the 4th October 1992 and was not used for the remainder of the passage. This fault was subsequently attributed to a combination of a low voltage supply caused by the long cable lengths used in the installation and the use of high power radar equipment. This combination corrupted the instrument's internal memory causing an erroneous PRT value to be reported from the hot black body unit.

4.4.4 Meteorological measurements

Meteorological measurements were made from the forward mast in clean air supported by visual observations taken at 15 minute intervals from the ship's bridge. Wind velocity and direction were measured using a Vector Instruments cup anemometer and wind vane which were calibrated before departure. Data were corrected for ships speed and normalised to a logarithmic profile at a 10 m height according to Smith (1980). Figure 4.10 shows a photograph of the anemometer and wind vane installation on board the RRS *James Clark Ross*

Figure 4.10 Installation of the Vector instruments cup anemometer and wind vane on the forward mast aboard the RRS *James Clark Ross*.

Total solar flux was measured by a Kipp and Zonen C-5 Pyranometer (0.3 - 3.0 μm) mounted on the forward mast in such a way as to minimise shadowing effects from the mast itself. This installation is shown in figure 4.11 below.

Figure 4.11 Installation of the Kipp and Zonen CM 5 pyranometer on the forward mast access platform aboard the RRS *James Clark Ross*.

A Vaisala HMP 35A humidity probe was used to measure relative humidity from the forward mast and air temperature was measured using a precise platinum resistance thermometer. Wet and dry bulb measurements were made as routine observations by the ship's meteorological officer throughout the cruise. Atmospheric pressure was determined using a digital barometer interfaced directly to a PC.

The downwelling flux of terrestrial radiation was measured using a TASCO THI-500 solid state infra-red radiometer. This instrument was windowed between 8 and 12 μm and the data were converted to a downwelling flux ($L\downarrow$) using Stefans law;

$$L\downarrow = \sigma T^4 \qquad \textbf{(4.1)}$$

Where σ is Boltzmann's constant. The beam width of the THI-500 instrument was 4.3° which will give a field of view of 150 m over a path length of 1 km.
This radiometer has a broader bandwidth than the SIL instrument and at the lower band (~8 μm) absorption by Ozone in the atmosphere occurs. However Saunders (1968) used a similar broad band instrument to measure sky radiance and concluded that the effects of absorption due to ozone were minimal in this context. The instrument was positioned to measure an area of the sky from which downwelling radiance would be expected to reflect into the incedence angle of the SIL instrument. This instrument logged to a solid state Campbell scientific data logger using software written by the author. This instrument was installed on the 'monkey island' (highest open deck) of the JCR as it required data to be manually down-loaded twice daily. The installation is shown in figure 4.12 below (Note that the probe unit is pointing vertically for this photograph).

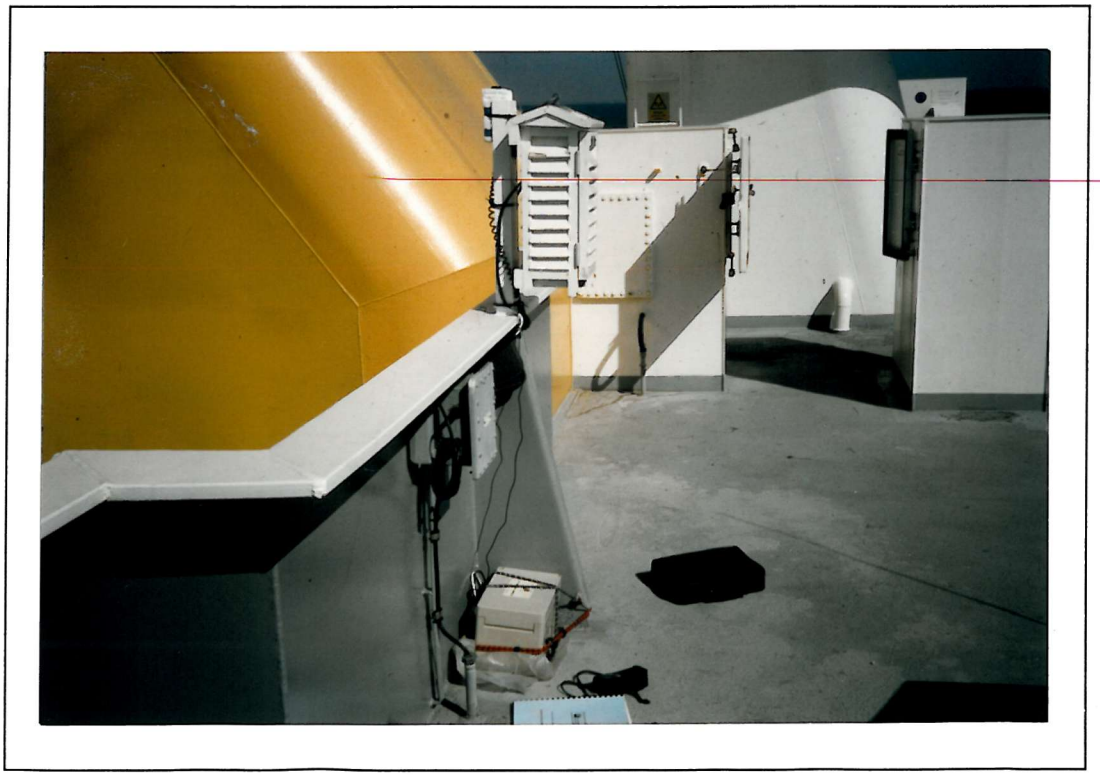

Figure 4.12 Installation of the TASCO THI-500 IR radiometer on the 'Monkey island' aboard the RRS *James Clark Ross*.

Each instrument was checked daily for signs of degradation and cleaned where necessary. Data were logged and calibrated at 5 second intervals using BAS

software. Additional meteorological data were taken from two bridge logs; the standard mariner's hourly log and the bridge experimental log taken by officers of the watch at (where possible) 15 minute intervals. These data enable a quantification of climatological conditions (especially cloud cover and type) to be made for the duration of the cruise.

4.4.5 Position data

Position was determined from an on board SPERRY marine navigation system using a custom Kalman filter taking information from the LORAN C and GPS systems. Position was accurate to GPS limits of ± 0.1 km. Data were logged at 5 minute intervals and in some cases 2 minute intervals.

4.4.6 Radiosonde launches

Radiosonde ascents were made on a daily basis where possible. These data were processed using BAS software. Data was supplied to the ATSR science team for algorithm development and in real time where possible to the UK Meteorological Office. Initial difficulties concerning the post processing of these data were overcome by writing a C language programme to re format all Radiosonde data prior to the execution of the BAS programmes. These delivered a standard WMO ships meteorological report message which was transmitted in near real time to the UK meteorological office, Bracknell.

4.4.7 Satellite position prediction

Satellite positions were predicted using the SATSCAN program taking weekly ephemeris data from BAS head quarters, Cambridge, UK. This programme was undocumented and was therefore difficult to use successfully.

Based on the output from the SATSCAN satellite prediction programme high resolution (1.1 x 1.1 km at nadir) ATSR SADIST (Synthesis of ATSR Data into SST, see Bailey, 1994) v400 SST and brightness temperature data coincident with the

JCR cruise path were supplied by the Rutherford Appleton Laboratory. Appendix B describes these data. Problems with the geolocation routines used in the ATSR algorithms required that the data were re-processed using the new generation SADIST 500 software. Comparisons between ATSR and *in situ* SST data are therefore limited to the ASST product produced from these data.

4.4.8 Data post processing and reduction

Interactive Data Language (IDL) and 'C' programs were developed by the author to calibrate all instrumentation and to reduce data to a variety of scales. All data sets were 'forced' onto a radiometer time stamp of 7 second intervals by taking the nearest data point in time. Data were then block averaged to 30 second intervals. Further reductions were made to 4 minute means which assuming a mean ship speed of 10 kt. equates to a spatial sample of 1.2 km comparable to the pixel size of the nadir ATSR pixel. This will eventually enable a direct comparison of the JCR data to the high resolution (1.1 x 1.1 km) ATSR SST satellite data.

A full cruise report is presented in appendix A describing the intallation, operation and problems encountered during this cruise.

4.5 Calibration of the SIL IR radiometer

The following section describes the SIL radiometer and the details of its calibration. For a full review of the procedure used see Thomas et al, (in press).

4.5.1 SIL/RAL type SST radiometer

The radiometer used on the *James Clark Ross* cruise was an STR-100 instrument manufactured by Satellites International Ltd. This instrument is based on a radiometer design similar to that of Hepplewhite (1989) and was built specifically for the calibration and validation of the ATSR instrument. The STR-100 is a twin

channel device having IR filters identical to that of the ATSR and is designed for ship deployments.

4.5.2 Principle of SIL radiometer operation

Figure 4.13 shows a schematic diagram of the SIL radiometer.

The STR-100 radiometer focuses radiation from a target source and a precision reference black body cavity using an off axis parabolic mirror and a beam chopper rotating at 30 Hz inclined at 45° on to a Phillips RPY98S pyroelectric detector. The radiation is band limited by a user selectable bandpass filter (central wavelengths of 11μm or 12μm). The detector output is amplified, rectified, filtered and finally digitised before transmission via a serial communications link to a control and logging PC computer.

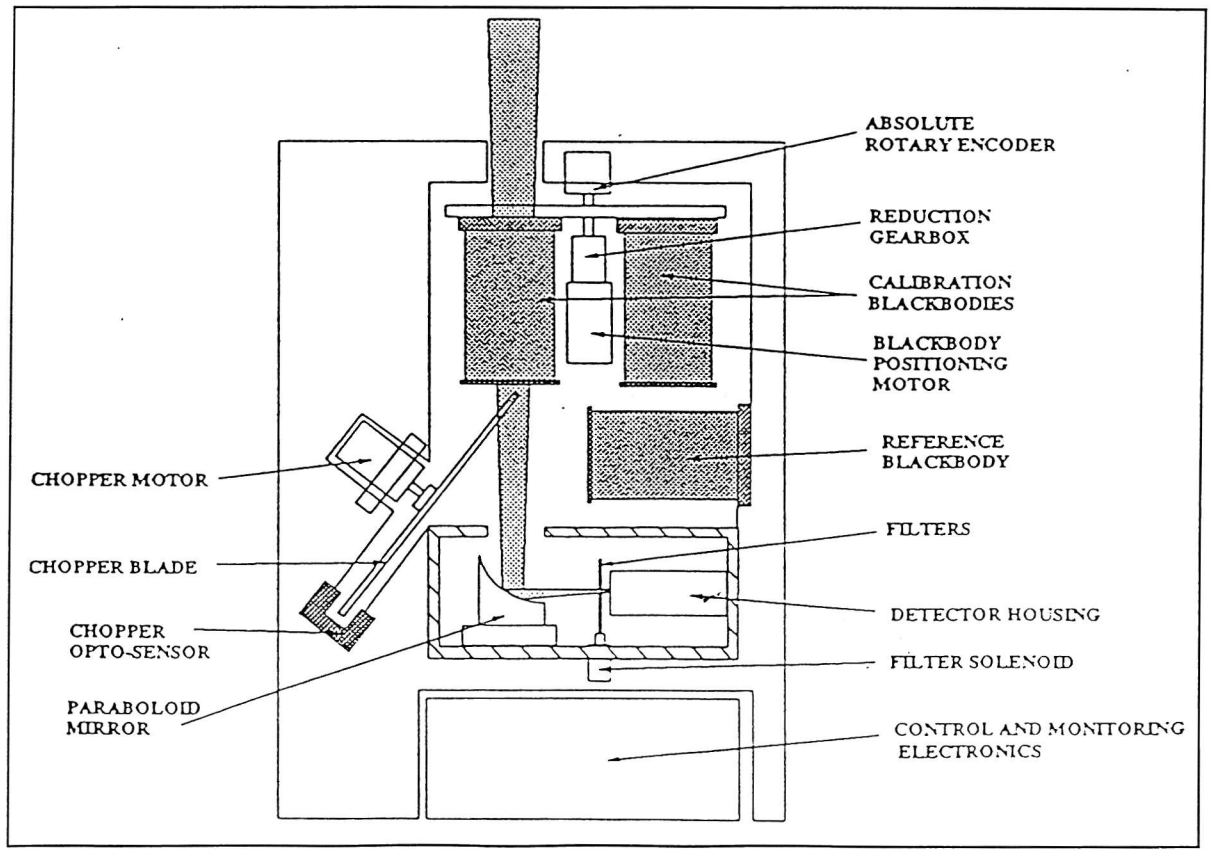

Figure 4.13 A schematic of the basic design of the RAL/SIL type infra-red radiometer (from Knight 1988)

The radiometer detector responds to radiation emitted from the target source, reflected stray radiation and changes of the detector temperature itself. As the temperature of the detector is not regulated its response function will vary as the instrument temperature varies. Stray radiation originates both from within the instrument itself and by reflection at the sea surface. The combined effect of detector temperature change and stray radiation from within the instrument is related to the internal temperature of the instrument housing and results in a gradual drift of the instrument internal calibration. In order to correct for the instrumental drift, calibrations against a known black body source need to be made. Two black body units are used for an absolute calibration of the system. One of these units is at the instruments internal ambient temperature and the second is held at a nominal 8 K above this by a heater unit. These units are referred to as the 'cold' and 'hot' blackbodies. Each has a high emissivity (ε=0.995, SIL; 1991) and a platinum resistance thermometer (PRT) embedded within. The emitted radiance for each unit can be calculated using the Plank radiation law (eq 1.1). By periodically swinging each black body unit into the detector field of view the radiance signal can be calibrated and any instrumental drift can be compensated for.

4.5.3 Theoretical radiometric calibration of the SIL radiometer

The radiance measured by the SIL radiometer at wavelength λ from a source at temperature T can be theoretically calculated using the Plank function given by equation 1.1 and will be referred to as $B(\lambda,T)$. The SIL radiometer has a limited bandwidth defined by the combined spectral response of the filter used and the spectral characteristics of the detector window. The integrated radiance for the SIL bandwidth will be referred to as $B'(T)$. The detector signal is a linear response to the radiance difference measured between the reference blackbody and the target in question (the sea surface, hot or cold black bodies) and can be expressed as follows;

$$S_w = G[\varepsilon_w B'(T_w) + (1-\varepsilon_w)B'(T_r)] + O \qquad \textbf{(4.2)}$$

The hot black body signal is given by;

$$S_h = G[B'(T_h) - B'(T_r)] + O \tag{4.3}$$

and the cold signal by;

$$S_c = G[B'(T_c) - B'(T_r)] + O \tag{4.4}$$

where ε_w is the emissivity of water, T_S is the brightness temperature of the sky and T_r, T_c and T_h are the temperatures of the reference, cold and hot black body cavities respectively.

As T_r remains constant during the hot and cold black body views as long as the time interval is small, equations 4.3 and 4.4 can be used to determine the system gain G and measurement offset O, written as

$$G = \frac{S_h - S_c}{B'(T_h) - B'(T_c)} \tag{4.5}$$

$$O = S_c - G[B'(T_c) - B'(T_r)] \tag{4.6}$$

These equations assume that the calibration and reference black body cavities are all perfect black bodies having an emissivity of 1.0 and therefore all internal reflections from the cavities are ignored. As the cold and reference black body cavities are at a similar temperature to the instrument this is a valid assumption as any reflections would be at a similar temperature to the cavities themselves. The hot black body will be affected by stray reflections from within the instrument which will be 8 - 10 K cooler than itself. This effect is however minimal and equates to a SST error of ~0.08 K (Knight, 1989).

In order to determine a water temperature from equation 4.2 the relationship between radiance and temperature B(T) must be known. This can be approximated by a quadratic function when the Plank function is evaluated over a limited range of wavelengths and temperatures typically encountered at sea using the SIL instrument 250 - 320 K and 10 - 20μm as shown in figure 4.14.

Using this assumption equation 4.2 can be reduced to

$$aT_w^2 + bT_w^2 + C = 0 \qquad (4.7)$$

where C is given by

$$C = c + \varepsilon_w^{-1}\{(1-\varepsilon_w)(aT_s^2 + bT_s) - (sT_r^2 - bT_r) + [\frac{O - S_w}{G}]\} \qquad (4.8)$$

and a, b and c are the coefficients for the quadratic fit to the relationship B'(T) for the SIL instrument (see § 4.5.4 below) given as

a = 2.0269265x10^{-3} b = -0.64038485 and c = 54.98475 based on the work of R Knight (personal communication).

The PRT calibration coefficients used by the radiometer were thought to be incorrect due to the calibration procedure adopted by SIL Ltd (J Thomas, personal communication). Incorrect PRT calibrations would result errounous radiance measurements from the black body cavities and therefore incorrect values of calibration gain and offset used to derive a water temperature.

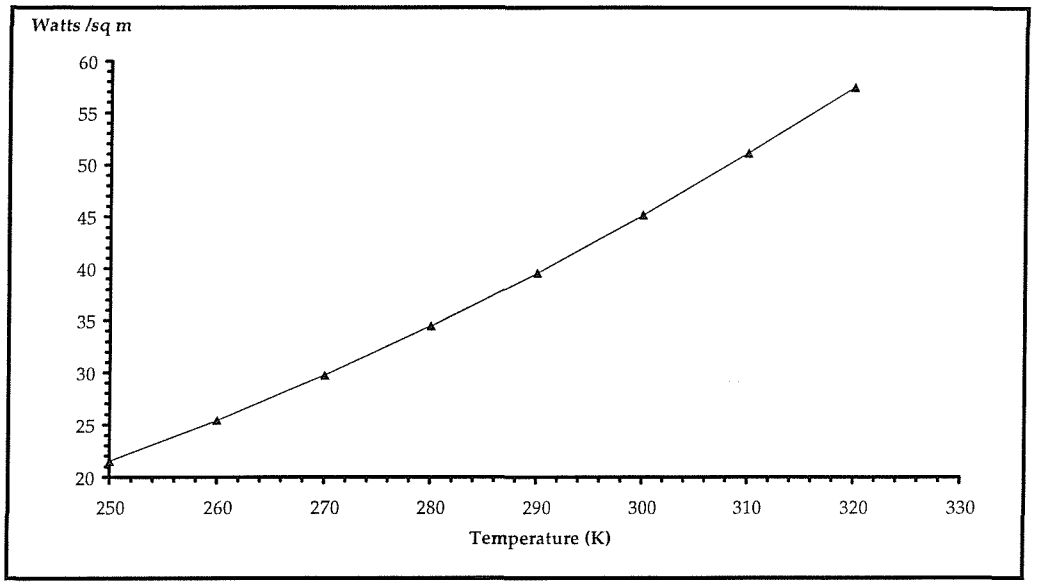

Figure 4.14 Radiance versus Temperature integrated over the 11μm waveband of the SIL radiometer (After R Knight personal communication)

Using validation/calibration measurements mae with an *in-situ* stirred tank a correction coefficient was derived by minimising the difference between the radiometric temperature solutions and the thermometric water bath measurements (Thomas *et al,* in press). The effects of a small radiance difference for the hot cold and reference black body will be small. However the most significant error is in equation 4.2 which will become;

$$S_w = G\{\varepsilon_w B'(T_w) + (1-\varepsilon_w)B'(T_s) - [B'(T_r) - \Delta B'(T_r)]\} + O \qquad \textbf{(4.9)}$$

where an additional term $\Delta B'(T_r)$ is due to a temperature error ΔT, in the temperature derived from the reference black body PRT measurement. As the PRT voltage to temperature relationship is non linear it is assumed that the there was a temperature dependence and ΔT can be written as

$$\Delta T = \alpha T_r \qquad \textbf{(4.10)}$$

where $\alpha < 1.0$.

Using 4.10 the following relationship is obtained:

$$\Delta B'(T_r) = a\alpha(\alpha + 2)T_r^2 + b\alpha T_r \qquad (4.11)$$

where ***a*** and ***b*** are the quadratic terms from the quadratic approximation of the Plank function (equation 3.1). By adopting this calibration strategy the SIL radiometer is shown to be accurate to ±0.12 K (Thomas *et al*, in press).

Another source of error may be due to atmospheric absorption integrated over the path length between the SIL radiometer and the sea surface. The SIL instrument is a dual filter instrument which in theory allows an atmospheric correction to be made using the same assumptions as the MCSST algorithm described in chapter 2. Unfortunately as the 12 μm channel was unusable this was not possible. However, appendix C presents a discussion of the atmospheric effect in relation to the SIL instrument and describes an atmospheric correction method with can be applied to the SIL radiometer.

4.5.4 Variations in emissivity due to ship movements

As discussed in section appendix B, the SIL filter profiles have a small 'leak' centred at 20 μm. This is due to the fact that the initial specification was for filter profiles to be exactly the same as the ATSR instrument. The ATSR detector windows however block this leak which is not the case for the SIL radiometer. As ε is a function of wavelength at these longer wavebands allowance must be made for this. The SIL filter profiles were convolved with spectral-directional emissivity values which were taken from Masuda *et al*, (1988) for the region 750 - 1100 cm^{-1} and from Ray (1972) for the longer wavelength region by R Knight of RAL. In the latter case pure water values were used as no data for sea water were available (R Knight, personal communication). Table 4.2 describes the derived emissivity values for the SIL radiometer 11 μm filter profile.

Masuda et al (1988) show that the emissivity of the sea surface is dependent on a number of parameters including the surface wind field, sea surface temperature

and the zenith angle used to make the radiometric measurement. Emissivities corrected for the effects of wind speed and bulk SST have been used in the SIL radiometer calibration scheme.

	Wind Speed in m/s				
Zenith angle °	0	3	5	10	15
0	0.9786	0.9786	0.9786	0.9786	0.9875
40	0.9747	0.9742	0.9739	0.9730	0.9722
50	0..9663	0.9640	0.9643	0.9623	0.9605
60	0.9421	0.9349	0.9348	0.9345	0.9323

Table 4.2 The variation in emissivity of sea water as a function of wind speed and incedence angle for the 11μm channel of the SIL radiometer (R Knight, personal communication). A temperature correction of $1.3x10^{-4}$ is required for each 1 K fall or rise in temperature from a base of 290 K.

Emissivity ε, will also vary with salinity, which will in this case be a small effect, but ε may vary significantly due to the contamination of the sea surface by surface slick material. Such slicks are common in the ocean surface and are poorly understood at present. There are two types; the most common is a result of decaying organic matter and can be extensive in size, and the second anthropogenic which tend to be localised and are of particular concern in coastal areas. However in wind speeds of > ~6.0 m/s most surface slicks are effectively dispersed. As no independent measure of such phenomena could be made such effects have been neglected.

Unfortunately even though the RRS *James Clark Ross* is fitted with a state of the art stabilising system, as for any ship, the vessel did roll and pitch. These movements will have the effect of changing the radiometer zenith angle and consequently at zenith angles greater than 40°, (see figure 1.9) ε values can change significantly. As there was no independent measure of the roll and pitch of the JCR during the experiment a typical roll/pitch value was used to asses this effect. During the maximum sea state conditions encountered the ships chief engineer suggested a typical roll/pitch variation of ± 5° and this was further confirmed using a plumb line. The temperature variation as a consequence of these changes

in radiometer zenith angle were computed using the figures supplied by Masuda et al (1988) and are summarised in table 4.3.

Zenith angle	ε variation from zenith = 37°	SST error
32° (-5°)	+0.000582	+0.03 K
43° (+5°)	-0.002150	-0.1075 K

Table 4.3 Summary of SST due to varying radiometer zenith angles.

Assuming that the ship roll/pitch averages out over an integration period of 30 seconds (as used in this work) this table indicates that the effect of ship roll/pitch effect tends to bias the SST measurement cool by ~ 0.5 K. In more typical conditions of light wind and swell errors due to ε variations will be less than the 'worst case' scenario outlined above.

Emissivity is also dependent on wind speed as the surface roughness characteristics of the sea surface change with increasing wind speed. At wind speeds of > 10 m/s, according to the Beaufort scale, long wave breaking begins producing foam and white caps which significantly modify the mean ε value; the exact result of such effects are unquantified. Although Masuda et al (1988) address the issue of a rough sea surface modifying the reflection characteristics of the sea surface they do not include the effects of long wave breaking outlined above. This latter point is important as the IR SST measure may be in error due to sea state. Given that under such heavy seas areas of longwave breaking and associated foam patches are a ubiquitous feature of the sea surface such effects may be present in satellite IR SST measures.

4.5.5 Correction for reflection into the incidence angle of the radiometer

As the sea surface is not a perfect black body, reflection of the downwelling radiance at the sea surface into the radiometer field of view will make a contribution to the measured signal. There are two potential sources of reflection

(ignoring the direct reflection from the instrument itself as the zenith angle was > 15° (Jessup, 1992)):

1. Reflection of the ship itself.

2. Reflection of the downwelling longwave flux emanating from the sky.

If the instrument is mounted less than 5 m from the sea surface a contribution from the reflection of the instrument itself is possible. Jessup (1992) making infra-red camera observations shows that a boom deployed from the spar buoy 'FLIP' (FLoating Instrument Platform) is clearly visible in infra-red camera images and in general any visible reflection seen at the water surface will have a similar appearance in the infra-red image. This is in contradiction to Simpson and Paulson (1980) who argue that such reflection is minimal aboard 'FLIP'. As the SIL instrument was installed at +16.5 m from the sea surface and viewed an area forward and to port of the JCR bow there will be no reflection of the ship contaminating the SIL field of view.

Radiation emanating from the sky ('sky temperature') will generally be from a source at a lower temperature than the sea surface and reflection will into the radiometer field of view will result in a lower SST (see chapter 2). The magnitude of downwelling radiance will vary depending upon the latitude, humidity and cloud cover with typical source temperatures of 120 K in the polar regions to 290 K in the tropics (Knight, 1989). Clearly as the sky temperature approaches that of the SST the cooling/warming effect is reduced. Table 4.4 summarises the SST error associated with an incorrect estimate of sky temperature for an ε value of 0.97 (close to that used by the SIL radiometer).

Sky temperature	247 K	252 K	257 K	262 K	267 K
SST error	-0.322 K	-0.128	0	0.169	0.344

Table 4.4 Summary of errors associated with the incorrect estimate of sky temperature. (after Knight, 1989)

An error of 15 K in the sky temperature estimate will result in an SST error of 0.32 K. Sky temperature was required to an accuracy of ±3 - 5 K in order to minimise the errors associated with reflection at the sea surface for the SIL radiometer. This was achieved using the THI-500 IR radiometer described in section 4.4.3

4.5.6 Practical calibration of the SIL radiometer

Calibration of the SIL instrument was undertaken at 3 minute intervals throughout the *James Clark Ross* passage. Data were logged at seven second intervals. The instrument calibration was found to be unstable between calibrations and the SST measure had an offset after each calibration cycle had completed. Figure 4.15 shows an example of 'raw calibration' SST derived using the equations 4.2 - 4.11 described above.

The most important assumption concerning the derivation of an accurate calibration using this method is that the black body temperatures, especially the reference black body, are stable during the measurement/calibration period. Errors of >0.7 K can result if variations of 0.5 K are present between these temperatures (Knight, 1989). Figure 4.16 shows the temperature of the reference black body T_{rbb}, subtracted from T_{rbb} + 1 calibration cycle (a temporal interval of ~2 minutes).

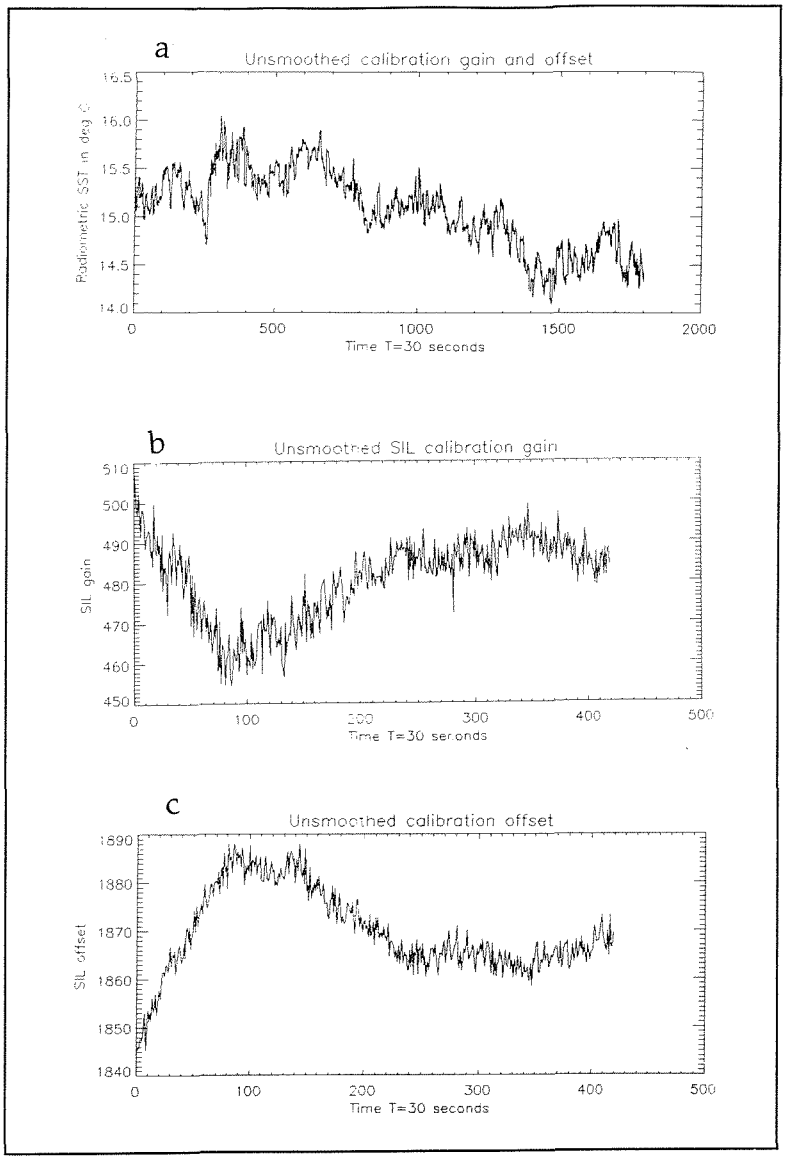

Figure 4.15 (a) Calibrated SST using an unsmoothed calibration gain (b) and offset (c).

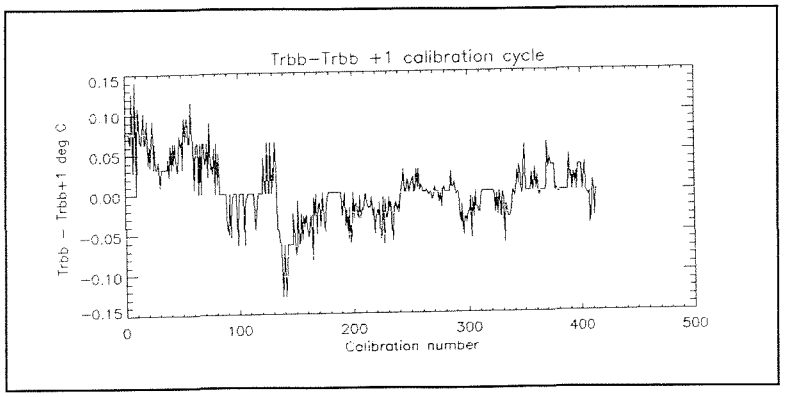

Figure 4.16 Reference black body PRT temperature (T_{rbb}) minus T_{rbb} + 1 calibration cycle for 16th September 1992.

Maximum deviations of ± 0.15 K between individual calibration cycles are found which can result in an error of ±0.15 K in the SST measurement if not corrected for. Deviations in T_{rbb} within a calibration sequence (i.e. the deviation between the cold and hot black body views) are negligible as shown in figure 4.17 having a maximum deviation of ±0.004 K which is an error attributable to the resolution of the on board analogue to digital (A/D) converter.

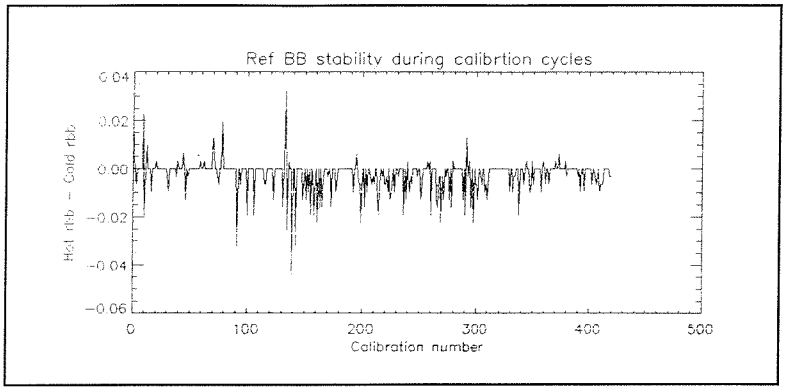

Figure 4.17 Reference black body PRT temperature (T_{rbb}) deviations within a calibration sequence typically 15-20 seconds.

The stability of this unit indicates that this is not the source of noise seen in figure 4.16. Figure 4.18 shows the detector signal output recorded during the hot and cold black body views taken during the 16th September 1992. Also shown are the black body PRT outputs.

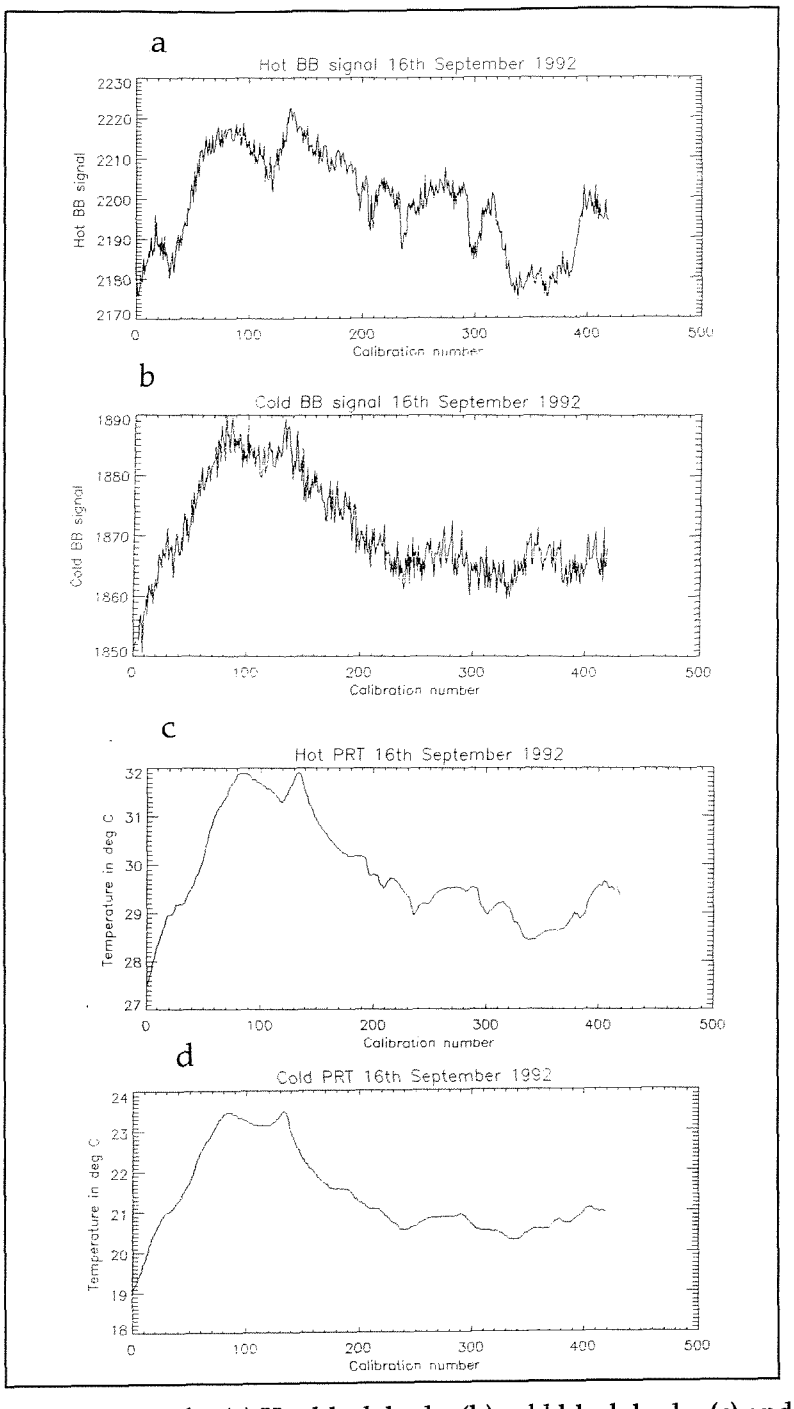

Figure 4.18 Detector output for (a) Hot black body, (b) cold black body. (c) and (d) show the black body PRT outputs for the same period.

The detector signal, when compared to the black body PRT data, have an element of noise superimposed on to the general trend. The mean deviations of the hot and cold black body signal are similar having values of ± 4 counts. This equates to a temperature error of ~±0.05 K assuming a mean relationship of 10 counts per 0.1 K. This relationship will change as the instrument warms and cools as the A/D output will vary with temperature. One method of noise reduction is to take a

larger number of samples during the black body views. In these data a sample of 30 was used, which in hindsight was probably too small a sample. C Clayson (private communication) suggests that a minimum sample should be of the order 60 - 80 samples both for the sea look and the calibration look although at the lower communication baud rate of the instrument this takes ~ 30 seconds per view.

Clearly figure 4.18 shows that the general trend of the detector signal is similar to that of the PRT measurement. Small scale temperature changes of 0.3 K are present in the PRT data at scales of 10 calibrations representing a temporal scale of 20 minutes. In order to stabilise the radiometer calibration gain and offset values, a weighted moving average filter was applied to the hot and cold black body detector signal following the comments of Knight (1989). A window of 15 samples was found to be sufficient to smooth the data without smearing the true small scale temperature fluctuations described above. Figure 4.19 shows the effect of this procedure on the final SST data for the 16th September 1992 and the effect of smoothing the signal gain and offset is shown for completeness. The remaining noise seen in the SST signal is a combination of system noise, natural variability of the sea surface and changes in emissivity due to the ships movement. This is a very complex signal and has therefore had no signal processing applied apart from the block avenge from a 7 second sample to a 30 second mean value. Data collected by the SIL radiometer were calibrated using the scheme outlined above.

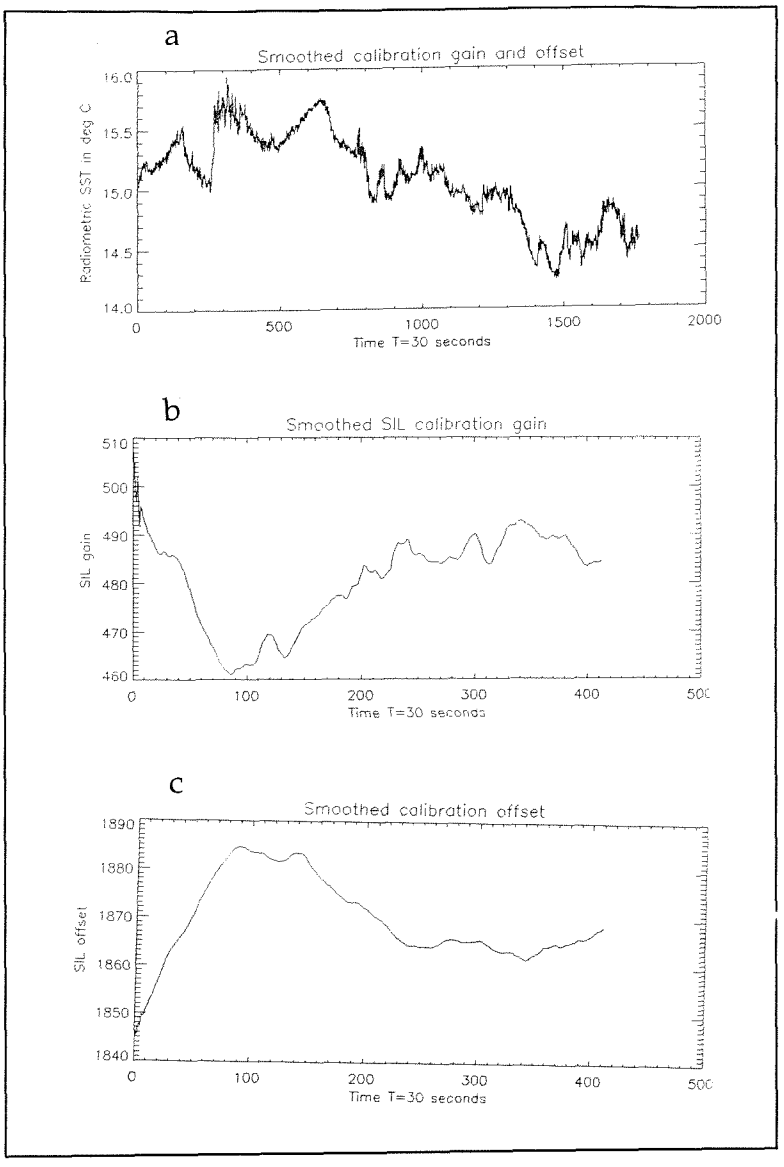

Figure 4.19. (a) Derived SST using a smoothed calibration gain (b) and (c) offset value.

Chapter 5. Results from the *James Clark Ross* skin-bulk SST experiment.

During the skin-bulk SST experiment described in Chapter 4, a near continuous record of observations were made from 50° N 01°W to 22°S 39°W. In this chapter data from this experiment are used to investigate the skin-bulk SST relationship ΔT, for different latitudes and environmental conditions.

5.1 Sampling strategy for observing the skin-bulk SST relationship.

One of the major limitations when working from a moving platform, such as a ship, is that both oceanic and atmospheric variables are dynamic both in space and time. This is especially important considering that the temporal scale of the radiometric temperature of the sea surface is of the order of 3 - 10 seconds (Jessup, 1992). Such a situation leads to uncertainty about the relationship between ΔT and atmosphere - ocean observations. This situation is further complicated as the sampling strategy when using a moving platform is neither eulerian or lagrangian in nature but rather somewhere in between. When using an eulerian strategy time series observations are made at a fixed spatial point. Consequently the number of degrees of freedom for a particular set of observations is reduced by one as the spatial dynamics of the measured process are unobserved. Conversely the lagrangian method in which the observations are made while moving with a particular process in space (e.g. a surface drifter), allows measured processes to be followed both spatially and temporally. For the study of the skin-bulk relationship there is a need for both lagrangian and eulerian observations. Figure 5.1 shows the relationship between the bulk minus skin SST (minus ΔT with reference to this work) and wind speed made from the research vessel 'Meteor' while underway. Comparing 5.1 to figure 3.6 which plots $-\Delta T$ vs. wind speed while the ship is stationary, the relationship between $-\Delta T$ and wind speed is very different. This difference could be due to an imperfect correction applied to relative wind speed in order to account for the movement of the ship itself. However it must be remembered that as the ship is moving it will be observing a

dynamic system in which the parameters defining this relationship are spatially changing.

The main advantage in the use of a moving platform is that a large area can be measured and thus a range of climatic regions can be sampled. In the context of satellite SST measurements this is especially important. If a correction is to be applied to global satellite SST observations then the skin-bulk relationship must be quantified not only for different climatic states, but also for different climatic regions. Using the data presented here the need for a regional or global ΔT correction scheme can be assessed.

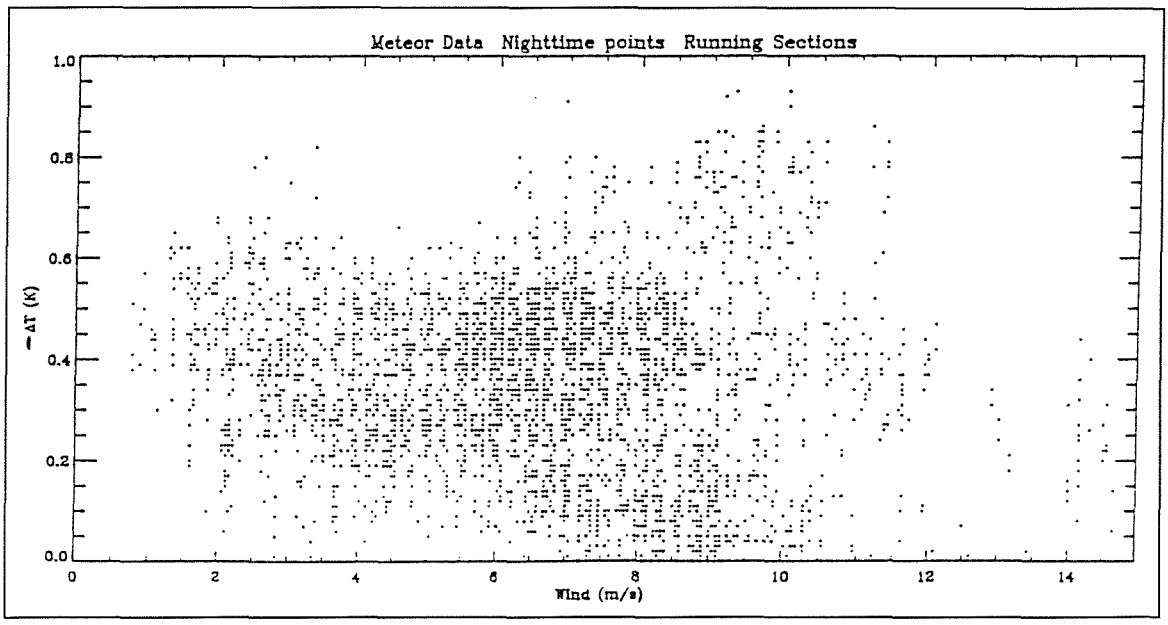

Figure 5.1 Bulk minus skin (ie -ΔT) plotted as a function of wind speed for night time conditions only and when the *Meteor* was underway. (From Emery *et al*, 1994).

5.1.1 Criteria for inclusion of data collected.

The observations made during the *James Clark Ross* SST experiment (JCR SST) were all collected while the ship was moving. As the amount of data collected during this experiment was large not all of the data collected have been processed to date. It was therefore necessary to select a sub-set of the total data series as representative of the conditions encountered during the experiment. In order that

ΔT can be assessed for a variety of regions the following criteria were used to select the final data presented here:

1. A range of latitudes are included in order to assess the nature of the skin-bulk relationship in different atmospheric and oceanic regions.

2. For each climatic region when possible, observations are presented during local day and night time conditions. The effects of solar heating on the ΔT relationship can then be investigated.

3. Both coastal water and open ocean situations are included. As the atmospheric and oceanic conditions in the coastal zone are different from those of the deep sea (e.g. less humid air masses and steeper oceanic and atmospheric temperature gradients) it would be expected that the ΔT relationship will be different.

5.1.2 Definition of selected data series.

The data sets used in this work are defined in table 5.1 below. For convenience individual time series are assigned to a letter A to N. The position of each series is shown in figure 5.2 and table 5.1 describes the start and end points, time of data collection (GMT) and the length of each transect in km. The data lie within the period 16th September - 2nd October 1992 and describe a transect made from 55° 40′ 00 N 00° 43′ 17 E to 22° 18′ 00 S 39° 28′ 16 W. Figure 5.2 shows that both coastal areas and open ocean regions are included satisfying the third criteria of § 5.1.

Data for all measurements were block averaged to a sample interval of 30 seconds. This is half of the minimum temporal sampling interval used by other authors who use 1 minute, 5 minute and hourly means (Schluessel *et al*, 1987, 1990; Emery *et al* 1994). The shorter sampling interval used here has been chosen in order to minimise the smoothing out of local changes in the magnitude of the radiometric SST. In the case of meteorological measurements, the standard 10 minute mean

value has been used. This temporal resolution is required for the computation of momentum fluxes using the bulk aerodynamic formulae. As discussed in Chapter 3, § 3.4, these parametersations are derived from 10 minute mean observations in order to smooth out turbulent gusts in the lower atmosphere which may alias the results obtained from such formulae.

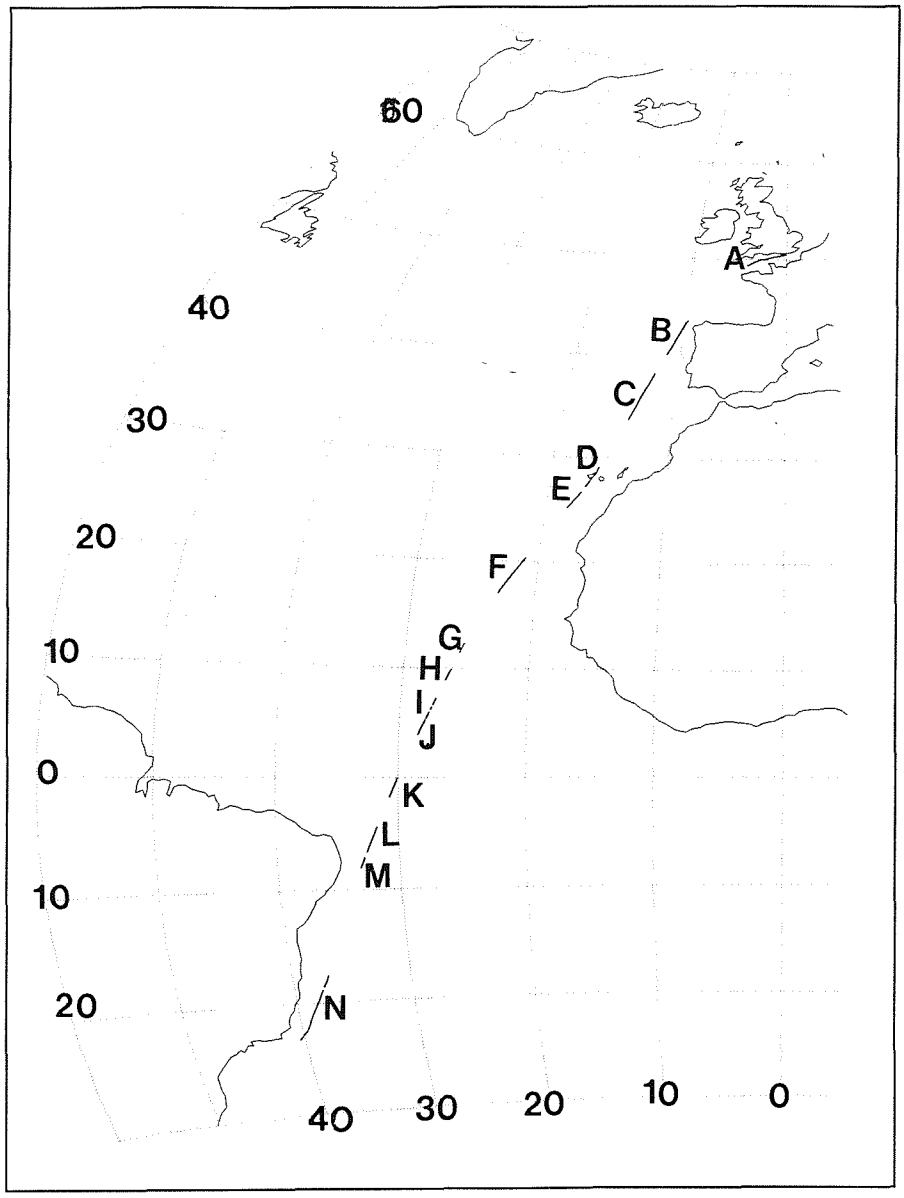

Figure 5.2 Positions of the data sets A - N described in table 5.1 for the JCR SST experiment.

Symbol on fig 5.2	Filename	Start date	Time	Latitude	Longitude	Stop date	Time	Latitude	Longitude	Length (km)
A	16091337.jcr	16th Sep 1992	13:37	50 42.94 N	00 43.17 E	17th Sep 1992	04:54	49 22.84 N	04 07.09 W	366
B	18091356.jcr	18th Sep 1992	13:56	43 46.13N	09 37.73W	19th Sep 1992	06:10	40 15.59N	11 14.64W	389
C	19091454.jcr	19th Sep 1992	14:54	38 25.10N	12 02.28W	20th Sep 1992	13:46	33 47.30N	13 53.25W	548
D	21091303.jcr	21st Sep 1992	13:03	29 07.19N	15 52.50W	21st Sep 1992	22:50	27 13.47N	16 52.20W	232
E	22090056.jcr	22nd Sep 1992	00:56	26 47.40N	17 06.77W	22nd Sep 1992	09:13	25 13.63N	18 08.95W	197
F	23091024.jcr	23rd Sep 1992	10:24	20 23.53N	21 01.10W	24th Sep 1992	04:45	17 02.24N	22 56.46W	438
G	25091747.jcr	25th Sep 1992	17:47	09 57.12N	26 07.27W	25th Sep 1992	23:11	08 54.63N	26 31.63W	127
H	26090735.jcr	26th Sep 1992	07:35	07 20.29N	27 08.26W	26th Sep 1992	11:00	06 42.44N	27 22.98W	81
I	26091414.jcr	26th Sep 1992	14:14	06 03.50N	27 37.93W	26th Sep 1992	17:06	05 27.43N	27 51.90W	67
J	26091748.jcr	26th Sep 1992	17:48	05 19.09N	27 55.10W	27th Sep 1992	00:21	03 58.35N	28 26.29W	155
K	27092017.jcr	27th Sep 1992	20:17	00 00.07N	30 02.75W	28th Sep 1992	04:36	01 41.06S	30 39.04W	197
L	28091720.jcr	28th Sep 1992	17:20	04 21.99S	31 41.21W	29th Sep 1992	04:14	06 40.31S	32 34.87W	260
M	29090616.jcr	29th Sep 1992	06:16	07 05.61S	32 44.54W	29th Sep 1992	10:55	08 04.71S	33 07.45W	107
N	01101856.jcr	1st Oct 1992	18:56	18 50.28S	37 28.84W	2nd Oct 1992	11:45	22 18.39S	39 28.16W	401

Table 5.1 Characteristics of the data used in this work. All times are GMT.

Several data sets were rejected from these analyses for a variety of reasons including power supply spikes, instrumental errors, computer errors, incomplete data logging, heavy most air contamination of the SIL radiometer signal and shielding of instrumentation by the ship's superstructure. The latter is a serious problem at sea, especially for the meteorological instruments and Kent *et al* (1991) extensively discuss the errors associated with this problem. In the case of the *James Clark Ross* installation, these errors were minimised by careful installation of instruments by experienced BAS personnel. Rejected data accounted for ~40% of the total data set analysed to date.

The collected data have been collated into a single data set which has then decomposed into day and night time situations. Using these results a selection of individual time series have been chosen to investigate and illustrate some of the more interesting aspects of the skin-bulk relationship.

5.2 The distribution of ΔT compared with measured variables for the entire *James Clark Ross* data set.

The following section presents the distribution of the observation made during the whole JCR experiment. ΔT and the environmental conditions encountered during the whole experiment were extremely varied and it is important to recognise that the figures discussed here include data from all latitudes and for both day and night time observations.

5.2.1 The distribution of ΔT

Figure 5.3 (a) describes the distribution of observed ΔT for the entire data set and indicates that ±1 σ of the data lie within the range -0.7 - 0.1°C with a mean value of ΔT= -0.4 °C ±0.31°C.

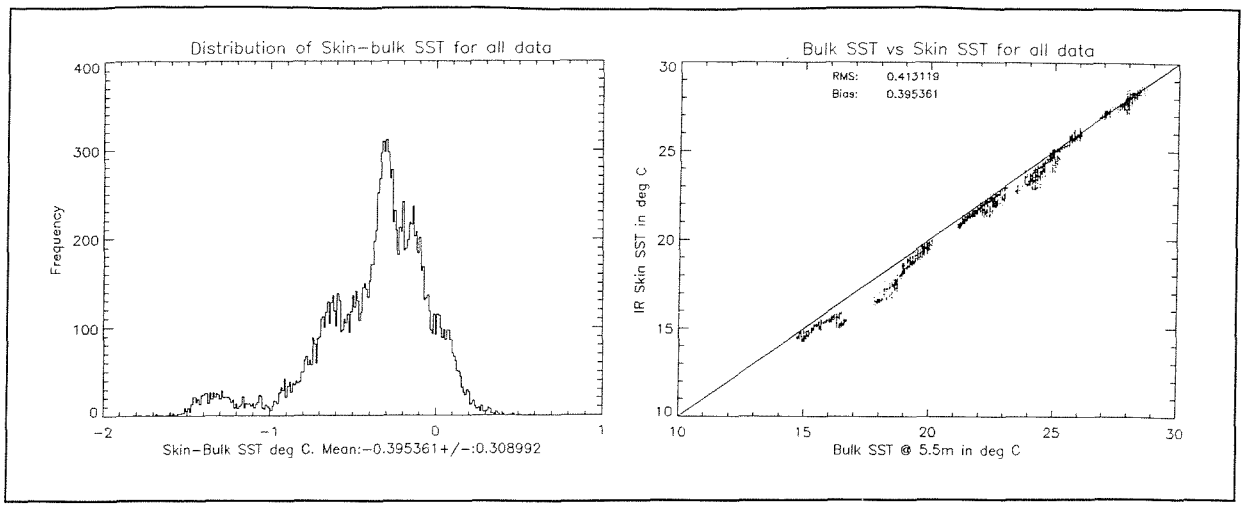

Figure 5.3 (a) Distribution of ΔT and (b) plot of radiometric SST against the bulk SST at 5.5m for entire *James Clark Ross* data set.

This distribution indicates that there is a consistent cool skin of the ocean for the majority of the JCR experiment. Maximum and minimum ΔT values of 0.5°C and -1.8 show the skin-bulk relationship to have a negative skewness and the mean value is in good agreement with other authors' results described in Chapter 3 table 3.1. Coppin *et al* (1991) report a similar ΔT distribution (mean of -0.3 ±0.14°C) having extreme ΔT values of 1.0 and -1.5°C for the western equatorial Pacific shown in figure 3.4(c). Hepplewhite, (1989) on a transect similar to that followed by the JCR (British Antarctic Survey vessel *'John Biscoe'*) also reports a similar distribution to that presented here (mean ΔT of -0.3°C ±0.3°C) and this is shown in figure 3.4 (d). Conversely, Schluessel *et al* (1990) find that in the NE Atlantic ocean, there is a positive skewness to the skin-bulk distribution shown in figure 3.4 (b) and 3.4 (e). They argue that at high latitudes the influence of direct insolation on ΔT is reduced compared to than in the mid latitude regions where the formation of a diurnal thermocline is more likely. In the case of the JCR experiment, the distribution is similar to the higher latitude distribution of the Greenland Sea area shown in figure 3.4(a) (shownhere as -ΔT) having a marked negative skewness.

Bearing the discussion of Chapter 4 § 4.3 in mind, it is interesting to note that the data of Schluessel *et al*, (1989; 1990) were collected using a Barnes PRT-5

radiometer calibrated using the stirred tank method. The Coppin *et al*, (1992) and Hepplewhite, (1989) data sets were collected with an SIL type radiometer having an internal calibration. The conflicting results discussed here indicate that variations in ΔT may be due to the different *in-situ* SST radiometer systems. This highlights the need to undertake a cross calibration of *in-situ* SST radiometer systems. ΔT is a quantity relating the skin temperature of the ocean to the bulk temperature and some of the differences between different author's results can be explained by the non standard depth at which the bulk SST measure was made. Hepplewhite uses meteorological bucket samples, Emery *et al* a hull mounted thermistor at 4.0 m depth and Schluessel *et al* a selection of bulk temperatures ranging from 10 cm to 7.5 m. If *in-situ* radiometric measurements are to be used for the validation of satellite SST in the context of deriving a global 'skin to bulk' transfer algorithm, then the depth to which the skin measurement is referenced needs to be standardised.

5.2.2 ΔT, bulk SST and air temperature.

Figure 5.3 (b) shows the radiometric skin temperature plotted against the bulk SST at 5.5 m. A perfect correspondence line is drawn into this figure to aid interpretation. The most obvious feature to note from this plot is that the larger skin-bulk differences are found at the lower bulk SST and that positive skin temperatures are seen at the higher bulk SST. If the bulk temperature is considered as representative of the latitudinal position from which the data were collected, then clearly there is a dominance of cool ΔT at the higher latitudes and sub tropical regions. In the warmer tropical waters ΔT appears to be less well defined and can be either positive or negative. This has serious implications for the application of a mean ΔT correction to satellite SST data. To simply apply a mean ΔT correction of -0.3°C (using these results) will, in this case produce a SST error of greater than 0.6°C.

The sign dependence of ΔT on the bulk SST can be explored further by considering the air-sea temperature difference. Figure 5.4 (a), (b) and (c) show the distribution of the bulk SST, radiometric SST and air temperature observations respectively.

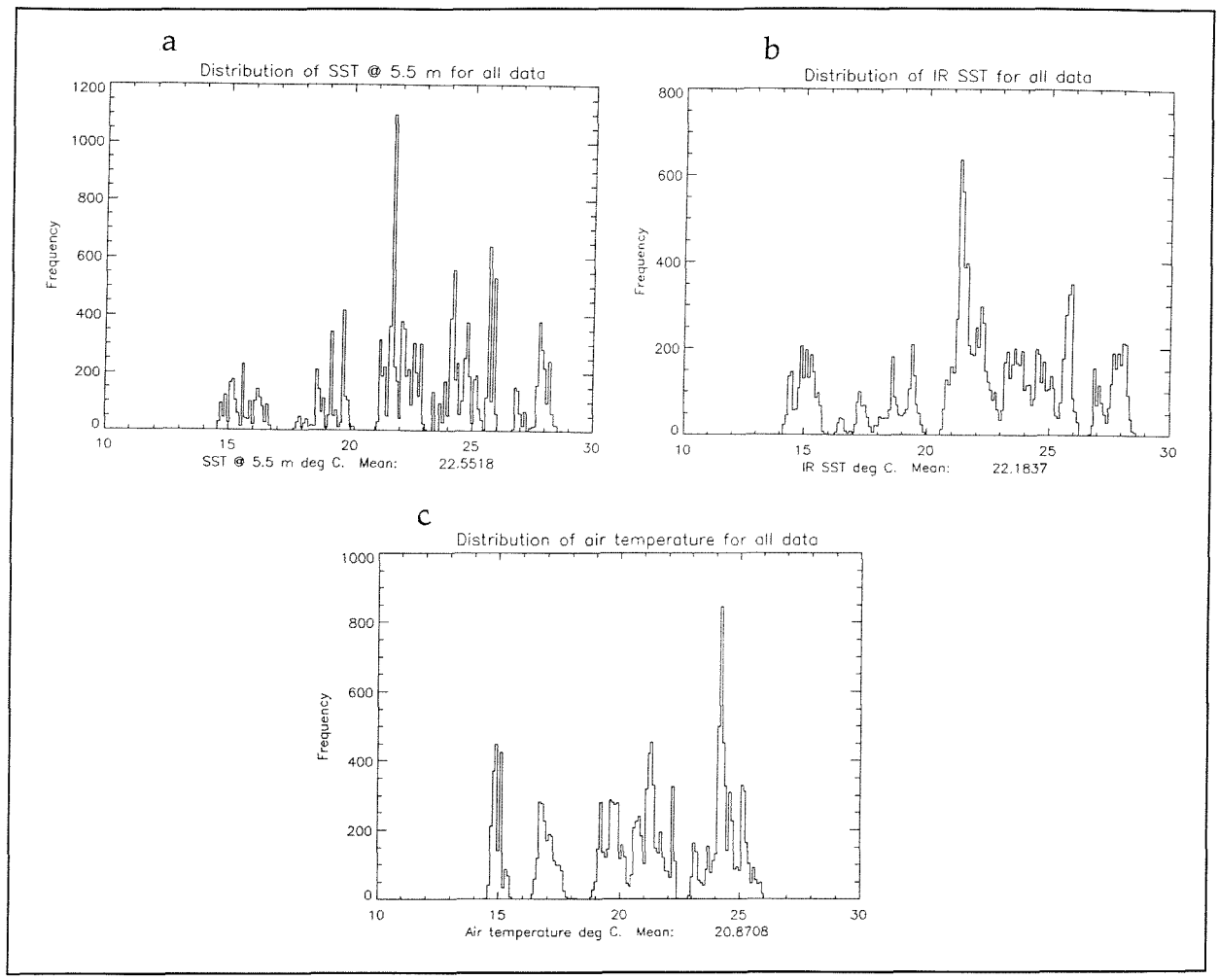

Figure 5.4 (a) Bulk SST at 5.5 m, (b) radiometric skin temperature and (c) air temperature distributions for the entire *James Clark Ross* data set.

The range of SST measured is from 14 - 28.5 °C and a range of air temperature of 14 - 26 °C was measured. The mean air-sea temperature difference was -1.68 °C. Using this value and assuming free convection conditions (i.e. very low wind speed and clear skies), the mean direction of conductive heat flow at the air sea interface will be out of the ocean (Shonting, 1963). However, these conditions are rare (Katsaros, 1977) and the air-sea temperature difference is more important as a direct input into the determination of the turbulent heat fluxes. These fluxes can have a strong influence on the magnitude of ΔT.

5.2.3 ΔT and the sensible heat flux Q_H

In this work negative values for all fluxes indicate flow out of the ocean to the atmosphere. Figure 5.5 plots ΔT against the calculated sensible heat flux Q_H using equation 3.2.

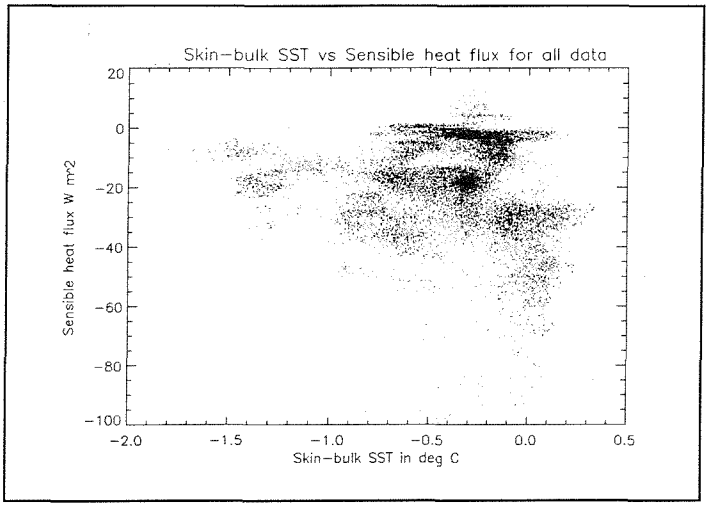

Figure 5.5 ΔT plotted against the sensible heat flux for the entire *James Clark Ross* data set. Sensible heat flux was calculated using the coefficients given by S Smith, personal communication.

This figure shows that the largest negative ΔT is associated with a small sensible heat flux of 0 to -20 W/m² and is indicative of low wind speed. There is a relationship between Q_H and ΔT until a Q_H value of ~ -40 W/m² is approached at which point the relationship breaks down and ΔT remains constant as Q_H out of the ocean increases. It is clear form this figure that ΔT appears to have only a weak dependence on the sensible heat flux Q_H. In this plot there is a region that shows Q_H to be positive. This is during high negative Q_H. These data are indicative of strong winds and when the air-sea temperature difference is positive indicating that the air temperature is warmer than the sea.

5.2.4 ΔT and humidity

During the experiment the relative humidity (RH) varied from 58 - 95% shown in figure 5.6 (a). The entire JCR data set has a mean RH of 77.7% and a pseudo gaussian distribution between 60 and 94% RH. These are expected values for the ocean and include the humidity values >90% of the tropical Atlantic. At values

greater than 95% RH there was a noticeable effect in the SIL radiometer data due to absorption and re-radiation of infra-red energy (Chapter 2 § 2.2.2 - 2.2.3). In such conditions a haze is ubiquitous and condensation can readily occur. Because of this all data above 95% RH have been rejected from this analysis.

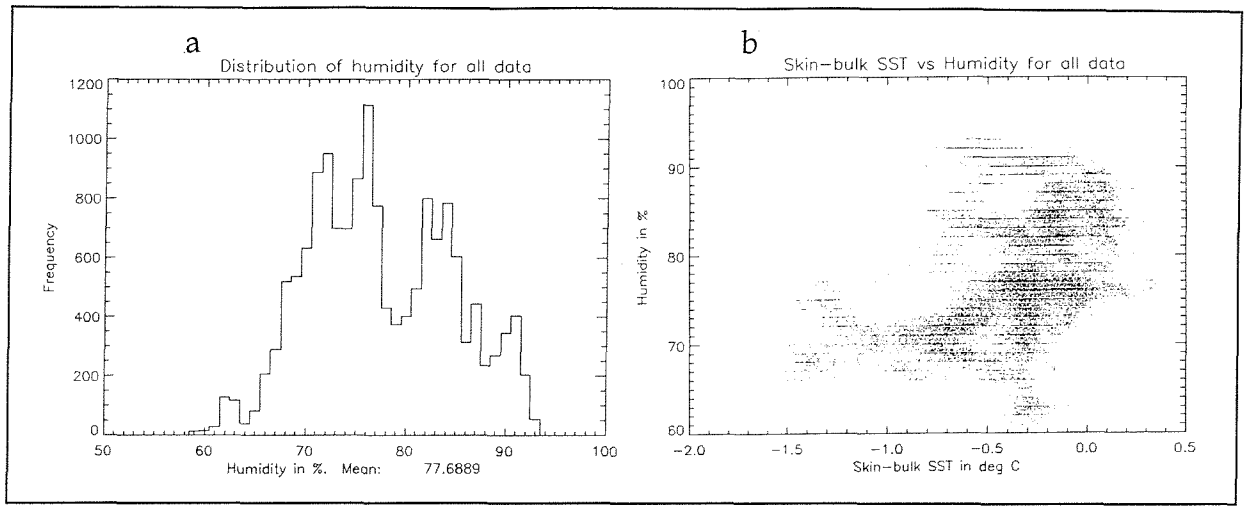

Figure 5.6 (a) Distribution of relative humidity and (b) ΔT plotted against humidity for the entire *James Clark Ross* data set.

The effect of humidity on the ΔT of the ocean will be twofold. Firstly, a humid atmosphere will reduce the magnitude of the latent heat flux, Q_L (equation 2.3) as evaporation from the surface water requires more energy per unit mass of water vapour. As air temperatures are typically close to those of the sea surface in high humidity conditions, the sensible heat flux (Q_H, equation 2.2) will also be reduced.

Secondly, the atmosphere will be radiating longwave energy at a temperature similar to that of the sea in the infra red region of the electromagnetic spectrum (Chapter 2, § 2.2). In this case the balance of longwave energy described by the terrestrial heat flux Q_T will result in less energy moving out of the ocean and in to the atmosphere and the magnitude of Q_T is reduced. The net effect of high humidity is therefore to reduce the radiative and turbulent fluxes out of the ocean.

Figure 5.6 (b) plots ΔT against relative humidity and the general trend in these data supports the hypotheses above. A maximum negative ΔT is found at RH <80% and steadily decreases as the humidity rises to a maximum of 95%. Positive

ΔT values are only seen in the high humidity regime indicative of warm air temperatures associated with the equatorial regions.

5.2.5 ΔT and the latent heat flux Q_L

The atmospheric humidity is a direct input into the latent heat flux (Q_L) bulk parametisation (equation 3.4) and figure 5.7 plots the relationship between ΔT and the latent heat flux Q_L.

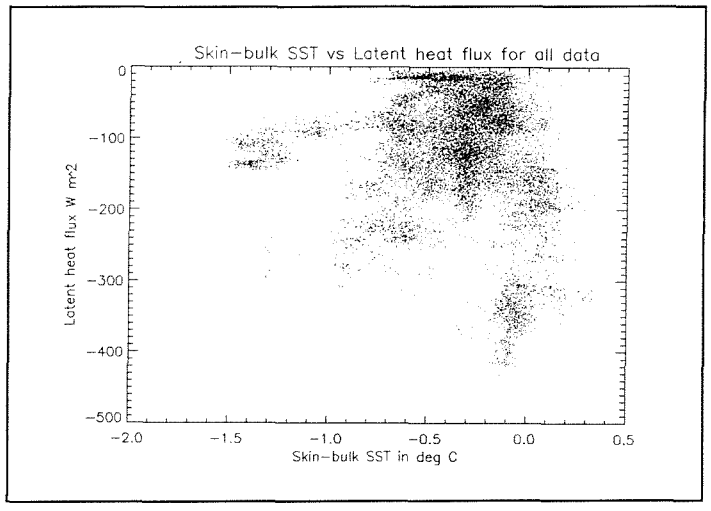

Figure 5.7 ΔT plotted against the latent heat flux for the whole *James Clark Ross* data set.

There are three regimes revealed in this plot;

1. The general relationship shows a mean decrease in ΔT with decreasing Q_L. This is to be expected as the latent heat of vaporisation of water is large 2.5×10^6 J kg^{-1} and is capable of removing a substantial amount of thermal energy from the sea surface. Under low humidity and moderate to strong winds the effect of the latent heat flux is to increase negative ΔT which is clearly shown in figure 5.7.

2. A low magnitude Q_L regime where $Q_L < 150$ W/m^2 in which the largest negative ΔT values are found. In this case Q_L will be weak either due to high surface humidity or low wind speeds. The low magnitude negative ΔT values are probably a consequence of longwave radiative cooling described by the terrestrial heat flux Q_T.

3. A regime in which Q_L decreases to its maximum negative value (a high wind speed/low humidity regime) for which ΔT is positive or at a mean value of ~ 0°C which contradicts previous observations of an increasing ΔT with wind speed. For the ΔT data which lie at or less then 0°C, this regime can be explained by a total destruction of the oceanic skin due to enhanced oceanic turbulence induced by a high wind stress. This in fact is the principle of the stirred bucket calibration discussed in Chapter 4. However for ΔT values to be greater than 0°C in such high wind conditions does not seem plausible. One possible explanation is that at high wind speeds (> 10m/s) the surface emissivity characteristics of sea water change. The Beaufort scale derived from visual observations of the sea surface suggests that at wind speeds > 10 m/s longwave breaking will begin. Associated with breaking waves are white caps and large foam regions lying in their wake. These surface features will accordingly modify the emissivity of sea water (Masuda *et al*, 1988) resulting in unpredictable radiometric SST retrievals.

5.2.6 Positive ΔT.

During the *James Clark Ross* SST experiment, wind speeds of > 20 m/s were encountered on the 27th of September and as the wind was from slightly abeam of the RRS *James Clark Ross*, radiometric measurements of the skin temperature could be continued. These data form transect 'K' shown in figure 5.2 and table 5.1. Figure 5.7 presents a description of the observations made during this period.

In 5.7 (a) the bulk and skin SST are plotted on the same axis. Although the skin temperatures (solid line) are reasonably correlated with the bulk SST (r=0.86), the skin SST is nearly always warmer. Towards the end of this time series there are significant fluctuations in the skin temperature observations. This is more clearly seen in the plot of ΔT, shown in 5.7 (b).

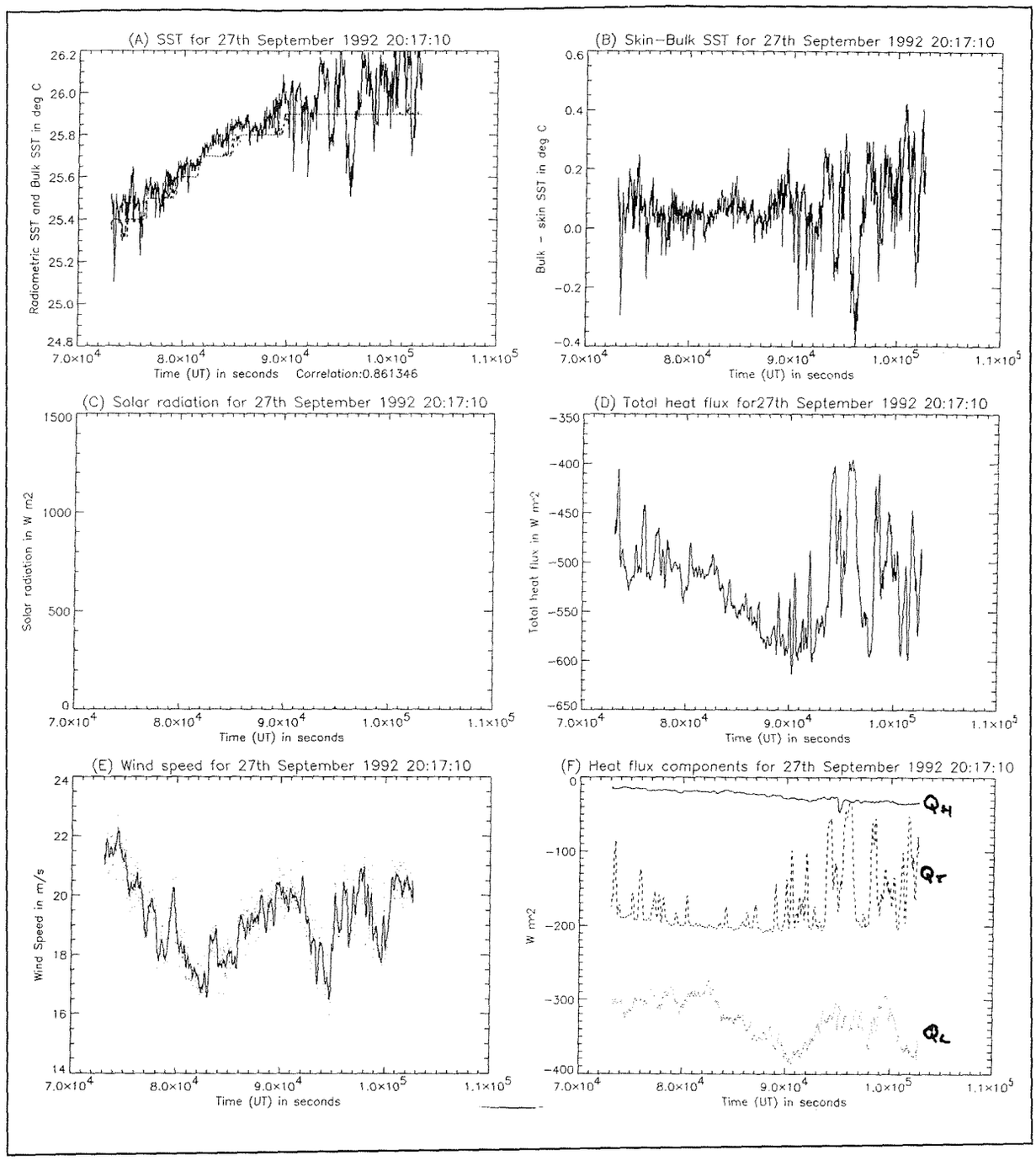

Figure 5.7 (a) Bulk (dashed line) and skin SST (solid line), (b) ΔT, (c) Solar flux, (d) net heat flux Q, (e) Wind speed (solid line is a 10 minute mean, (f) Latent heat flux (dotted line), sensible heat flux (solid line) and terrestrial heat flux (dashed line) and (g) the distribution of ΔT. All data from transect K given in table 5.1

These data were collected during the night beginning at 22:00 and continuing until just before dawn the following day so that solar heating during this time was zero. Wind speed is shown in figure 5.7 (e) and varied between 22 and 16.5 m/s, which as outlined above will significantly change the surface characteristics of the sea. The Beaufort scale suggests that at these wind speeds the tops of wave crests are

blown off as spindrift and large streaks of foam are present on the sea surface. Visual observations of the sea surface made from the ships bridge before sunset recorded chaotic sea conditions with large areas of foam and white caps all around the ship. During the early evening the wind speed steadily increased to the maximum values recorded here. Large negative Q_L, Q_H and Q_T heat fluxes are seen in figure 5.7 (f) and a strong negative net heat flux Q, prevailed for the whole time series as shown in figure 5.7 (d). There are a few broken clouds shown as warm spikes in the plot of the Q_T which increase towards the end of the time series. The data used for Q_T in this case may be unreliable as the radiometric temperature (used in the derivation of the terrestrial heat flux) are though to be corrupted.

High wind speed is associated with intense mixing of the sea surface layers of the ocean. During these conditions the skin of the ocean should be completely destroyed by turbulent mixing and a free exchange of heat from the ocean to the atmosphere should take place via long wave cooling (inferred from the negative Q_T plot of 5.7 (d)) and the turbulent flux $Q_L + Q_H$; the latter driven by strong winds and the former by clear skies. Mixing will penetrate beyond the 5.5 m thermosalinograph intake of the JCR and the radiometric temperature of the sea surface should be identical to the bulk at depth i.e. an expected $\Delta T=0$. However the data presented above indicate that this is not always the case and extreme positive ΔT values are found. The magnitude of positive ΔT is greater than the expected error associated with the combined bulk and skin instrumentation.

In the authors opinion it is a physical impossibility for the skin temperature of the ocean to be higher than that of the bulk temperature in such circumstances. Two explanations for these recorded data are:

1. That the radiometer itself has been contaminated with water. If this were the case then a higher radiometric temperature would have been recorded as the contaminant water will act as a black body at a similar temperature to that of the

instrument. This would change the system gain and offset values used in the calibration (Chapter 4). Although this cannot be dismissed conclusively, a close watch on the conditions was kept at all times because to operate the radiometer in such conditions was fraught with danger; a shift in the wind direction would have resulted in damage as the instrument would have been exposed to the effect of oncoming waves and spray. As the wind was from slightly aft of the ship's beam (~ 260° relative to the ship) contamination was thought not to be the case although an increased water aerosol load may be significant. Inspection of the SIL radiometer the following morning confirmed that there was no visible sign of contamination due to water ingress suggesting that contamination of the instrument fore optics is not the cause of positive ΔT.

2. That the conditions at the sea surface have significantly modified the emissivity characteristics assumed in the processing of the SIL radiometer data which, are no longer valid. Although Masuda *et al* (1988) consider the effect of sea state due to high wind speeds, their data treat wind speeds only from 0 to 15 m/s. Further they assume that the sea surface remains intact ignoring the presence of foam and white caps. As larger wave braking will begin at a wind speed of ~10 m/s, their data is only applicable at wind speeds < 10 m/s. Gardashov *et al* (1988) calculate ε values for wind speeds < 15 m/s but here again these data are for foam free conditions. To the authors knowledge there are no direct measurements of the surface emissivity of sea water during such conditions as those described above and consequently the SIL radiometric data cannot be relied on at wind speeds > 10 m/s.

The SIL radiometer takes a sample of 20 individual readings during a single SST measurement giving a total number of 100 samples every 30 seconds. It would be expected that the standard deviation of each SST measurement would increase as the sea state increased owing to the rapidly changing emissivity of sea water. Figure 5.8 plots the SIL SST standard deviation against wind speed for the entire night time JCR SST experiment data set.

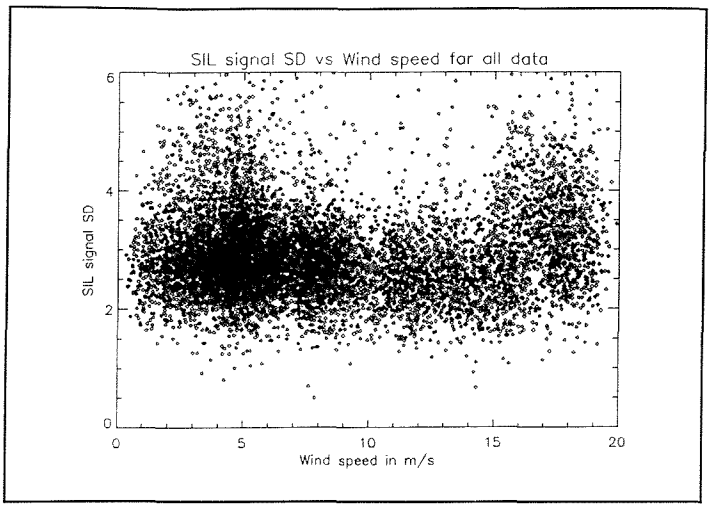

Figure 5.8 SIL radiometer signal standard deviation for night time water views.

In this plot there are two areas of high standard deviation;

1. Wind speeds of between 2 - 8 m/s. The signal variability at this range of wind speeds is the natural skin variability on short time scales as indicated by the measurements of Jessup, (1992). As the mean wind speed for the entire JCR data set was 7.7 m/s this is not unexpected (see next section).

2. A more definite peak in the standard deviation associated with wind speeds greater than 15 m/s. This is clearly a wind speed at which a very disturbed sea surface would be present. This is in agreement with Gardashov *et al*(1988) who suggest that large ε variations occur at wind speeds > 15 m/s.

Figure 5.8 gives credence to the hypotheses that the sea state changes the surface emissivity properties of the radiometric measurements discussed here. Chapter 4 explained how small errors in the emissivity of the sea surface will carry through the calibration of the radiometer and return incorrect SST. Schluessel *et al* (1990) present ΔT data collected in the NE Atlantic which show maximum ΔT values at high wind speeds. They conclude that ΔT increases with wind speed as a consequence of the enhanced turbulent fluxes at wind speeds > 10m/s. These data show that this is not the case and that positive ΔT is probably due to a change in the surface emissivity of the sea surface during high wind regimes. The ε values used by the SIL radiometer are significantly less than the typical assumed ε value

of 0.98 (Coppin *et al*, 1991). The argument here is that the change of sea state will increase the optical depth of sea water in condition of foam and white capping and as a consequence the boundary conditions used by current models used to calculate sea water emissivity are inappropriate. Unfortunately there are no measurements available with which to prove this hypotheses. On these grounds time series K has been excluded from any overall statistical analyses although will be included in the following discussions.

Considering the effect of the ocean surface characteristics in the high wind regime described above it is interesting to estimate the effect of such a positive temperature difference on a satellite SST measure. The radiometer data collected here indicate a mean warm bias of ~0.3°C. Assuming this to be a reasonable figure to use, then for 100% foam/white caps in an individual pixel (1 km^2) there would be a 0.3°C positive bias in the SST measure. It follows that 33% foam/white caps within a pixel equating to an area of 0.3 km^2 will produce an error of 0.1°C. The latter figure is significant as this is the SST accuracy required by the global climate research community to monitor global climate change (Hadley Centre Climate data requirements, 1994). The effect of such emissivity characteristics is as yet un-quantified and requires further research. The use of thermal imagers such as the AGEMA 880 themovision infra-red camera (discussed in chapter 4) will be extremely valuable in resolving the issue of changing sea surface emissvity at high wind speed - an area of research which has received little attention.

5.2.7 AT and wind speed

Figure 5.9 describes the distribution of wind speeds encompassed in the ΔT distribution shown in figure 5.3. These data are corrected to the standard meteorological height of 10 m following the work of Smith (1980; 1988). A broad range of wind speeds from 0 to 20 m/s were encountered (now excluding series K) and the distribution has a mean wind speed for the entire experiment of 7.6 m/s. For the mean case discussed here , a sensible heat flux (equation 3.2) of -1 W/m^2 and a mean latent heat flux (equation 3.3) of -7 W/m^2 are derived.

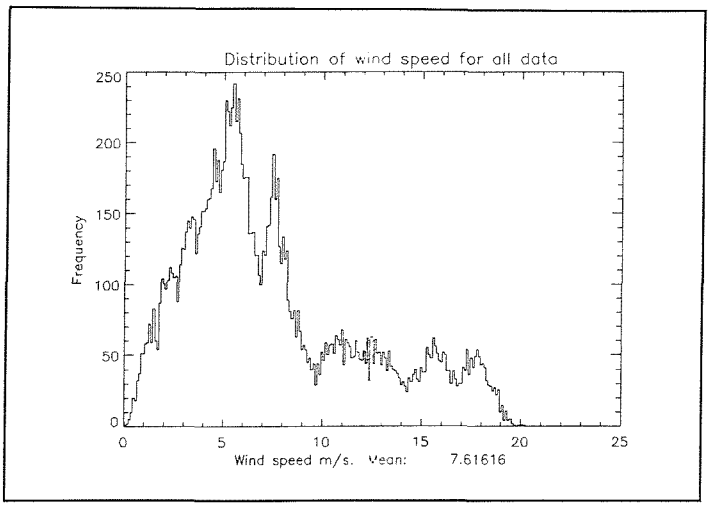

Figure 5.9 Wind speed at 10 m for the entire duration of the *James Clark Ross* data set.

As the turbulent fluxes of latent and sensible heat are wind speed dependent (eq.3.2 and 3.3), at the higher wind speeds these fluxes will dominate the net heat flux equation (eq 3.6) and the magnitude of negative ΔT is expected to increase. However at high wind speeds turbulent mixing is enhanced and there should be a total destruction of the cool skin. ΔT in this case should be zero. In reality both turbulent both processes are thought to occur simultaneously (Wick *et al*, 1994); increases in wind speed will increase turbulent mixing at the air-sea interface via an increased wind stress (τ) reducing negative ΔT while concurrent increases in the turbulent fluxes lead to an increase in negative ΔT. The magnitude of ΔT at any particular time should therefore be defined by the balance between these two processes.

Figure 5.10 (a) plots ΔT against the wind speed at 10 m, (b) against oceanic friction velocity u* (equation 2.6) and (c) surface wind stress τ (equation 2.1). In this figure, ΔT is related to the wind in three general modes;

1. Negative ΔT increases with increasing wind speed up to a wind speed of 8 - 10 m/s. Maximum negative ΔT is recorded at a wind speed of ~7 m/s

2. At wind speeds greater than 10 - 11 m/s ΔT gives positive values..

3. Positive values of ΔT are observed in the low wind speeds of < 5 m/s.

Wind speed at a height of 10 m is a coarse estimate of the wind effect found at the air-sea interface and wind speed decreases logarithmically as the sea surface is approached. The sea surface is not a solid boundary and a proportion of the wind energy will be imparted into the surface layer enhancing the turbulent transport of heat, momentum and velocity (Gill, 1982). U^* (figure 5.10 (b)) relates the frictional drag component of the wind stress (τ, figure 5.10 (c)) to the wind measurement at a height above the sea surface (10 m in the case of the JCR experiment). Although (a), (b) and (c) have similar relationships (they all use the measured wind speed), u^* and τ define the relationship of ΔT to the wind more clearly and a critical wind stress of 0.2 N m^2 and $U^*=0.015$ marks the transition region between strong negative ΔT and strong positive ΔT. The values of $U^*=0.005$ and $\tau=0.03$ N m^2 mark the upper limit of the light wind positive ΔT mode. Under light wind conditions a positive ΔT can be adequately explained as a consequence of the diurnal thermocline, where warming the upper layers leading to a positive ΔT with reference to the 5.5 m bulk temperature.

In the case of the strong negative ΔT case, it would seem that these data support the hypotheses of Wick *et al* (1994) discussed above. A combination of a moderate wind forcing the turbulent fluxes of heat and moisture occur during clear sky conditions when the radiative transfer of longwave energy is at its greatest resulting in a strong negative ΔT.

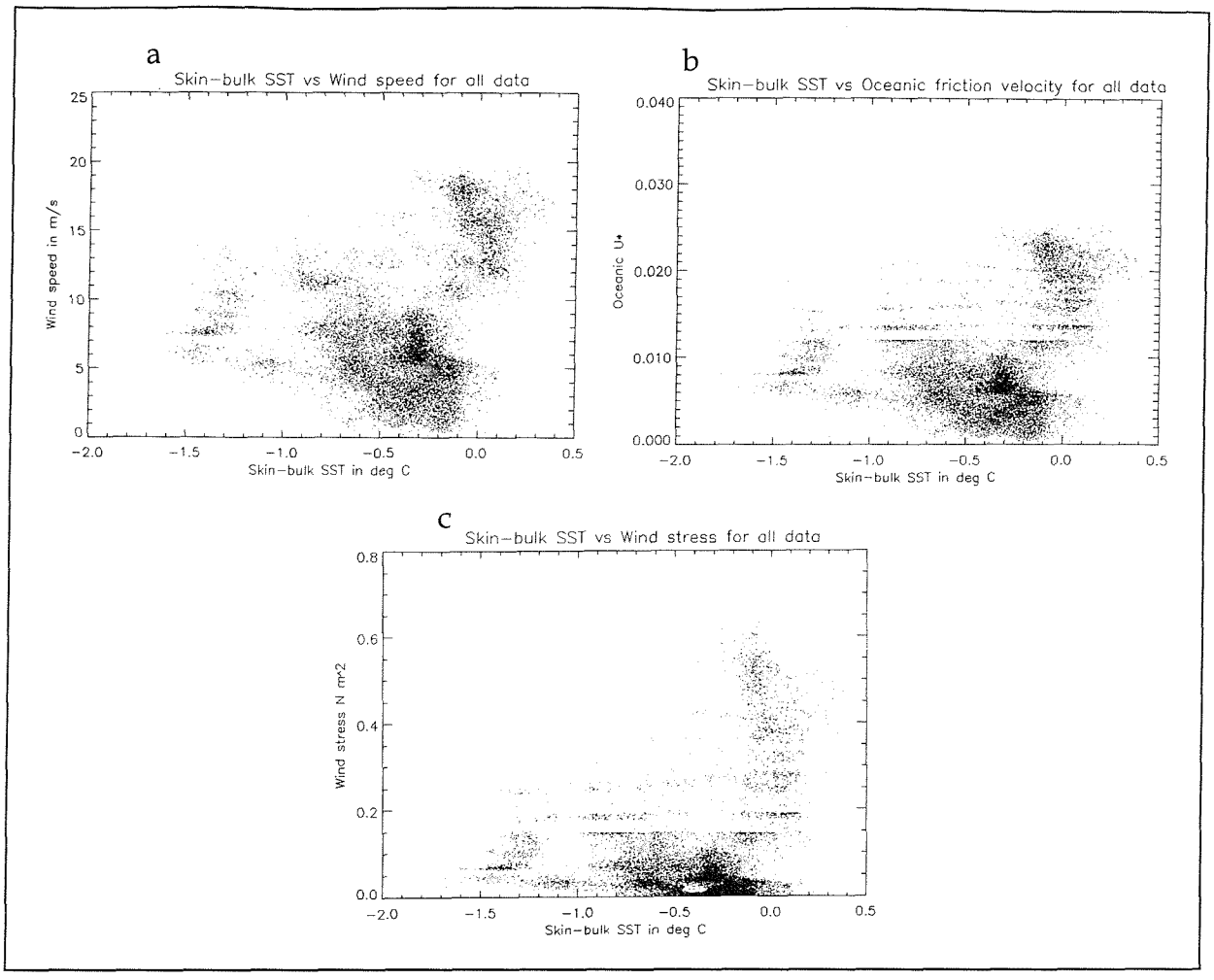

Figure 5.10 (a) Wind speed at 10 m Vs ΔT, (b) friction velocity (u^*) Vs ΔT and (c) wind stress (τ) Vs ΔT for the entire *James Clark Ross* data set.

5.2.8 ΔT and the longwave radiative flux Q_T

For confirmation of this explanation, ΔT was plotted against the downwelling longwave flux L_d, adopting the assumption that clear sky conditions will be represented by cooler sky temperatures (see below for further discussion), and against the terrestrial heat flux Q_T. These are shown in figure 5.11 (a) and (b) respectively. These figures show that is indeed the case and the maximum negative ΔT occur during cold (clear) sky conditions when Q_T shows a maximum radiative loss from the sea surface.

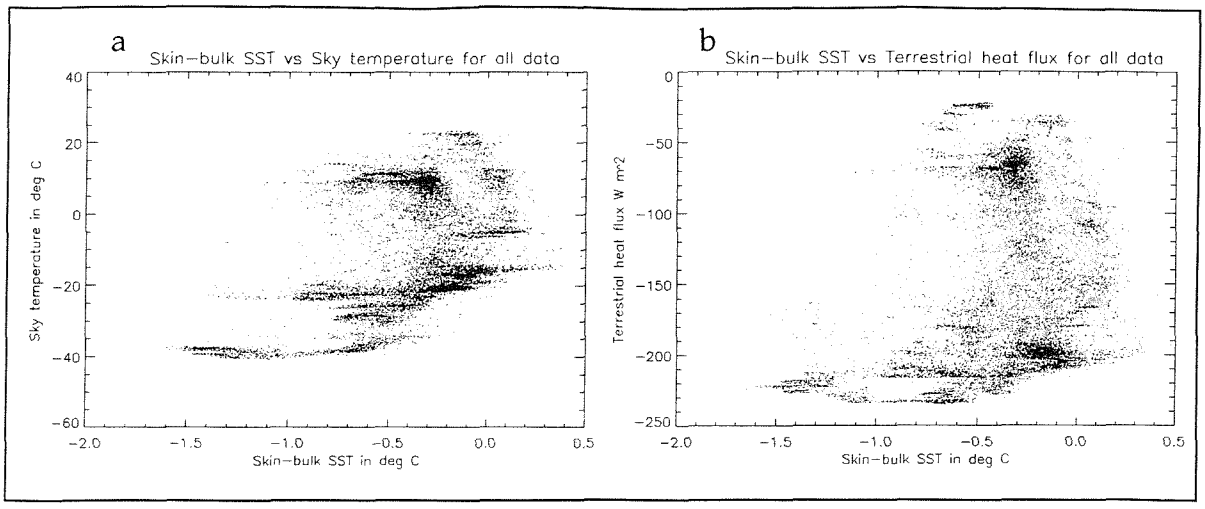

Figure 5.11 (a) ΔT plotted against sky temperature (downwelling longwave radiation L_d) and (b) Vs the net terrestrial heat flux Q_T for the entire *James Clark Ross* data set.

Returning to figure 5.3, it is worth noting here that the distribution of ΔT shown incorporates ΔT components from both clear and cloudy sky conditions. Sky temperature (downwelling longwave radiation L_d) can be used as a proxy estimator of the cloud cover as in general cloud free skies will have cooler temperatures. However, it must be pointed out that in tropical conditions, warmer cloud free sky temperatures will be recorded due to the increased water vapour load found at these latitudes (see Chapter 1). Figure 5.12 shows the distribution of sky temperature for the entire JCR data set. A mean sky temperature of -10°C equates to a downwelling radiative flux of 265 W m^2. These data are used in for direct determination of the terrestrial heat flux Q_T and to correct the SIL radiometer for reflections at the sea surface.

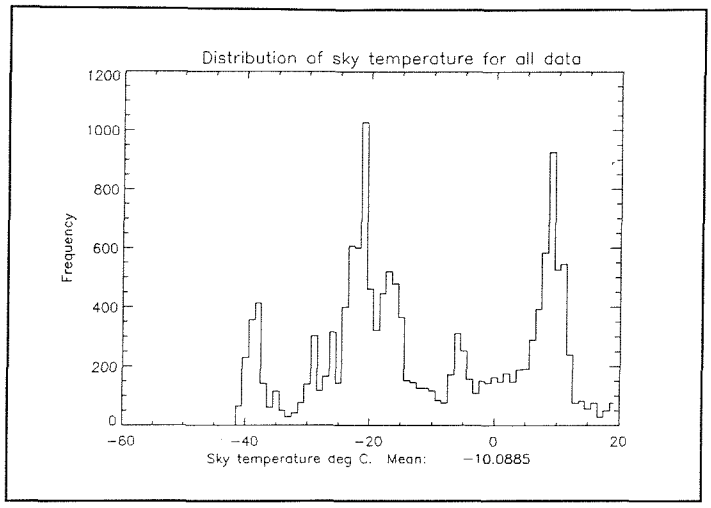

Figure 5.12 The distribution of sky temperature measured during the *James Clark Ross* SST experiment.

5.2.9 ΔT and the solar flux Q_S

Figure 5.13 (a) presents the distribution of the solar flux Q_S for the JCR SST experiment and (b) ΔT plotted as a function of Q_S. The general trend shown is that negative ΔT increases with increasing solar flux. Even in high solar flux conditions of >1000 Wm^2 a cool skin persists. This is in contradiction to the results presented by Schluessel *et al*, (1989) who concluded that positive ΔT are associated with an increased solar flux. In the case of the ocean, solar absorption penetrating the ocean surface follows an exponential profile having an extinction coefficient that is wavelength dependent (Schmidt, 1980). This is the only way in which direct heating of the surface waters can occur and is concentrated in the upper 1-2 m. Diurnal warming of the upper layer of the ocean is possible during light winds (a reduced turbulent mixing regime) and although a cool skin will still persist on the sea surface, there will be sufficient warming of the upper layers to derive a positive ΔT when referenced to a bulk SST at depth.

In the case of the JCR SST experiment ΔT observations have been observed under a wide range of solar flux values up to 1200 W/m^2 and the mean solar flux for the entire experiment was 357.5 W/m^2. However the relationship between the solar flux and ΔT is unexpected. This is an important point as satellite observations of SST are made both during the day and in the evening and clearly the effect of solar

input on the distribution of ΔT needs to be separated from other factors. Following the results of Schluessel *et al* (1990) a mean *warm* ΔT correction would be made to daytime satellite SST observations. The data presented here suggest that this would be in error and further investigation is required. This aspect of ΔT is discussed in the following sections.

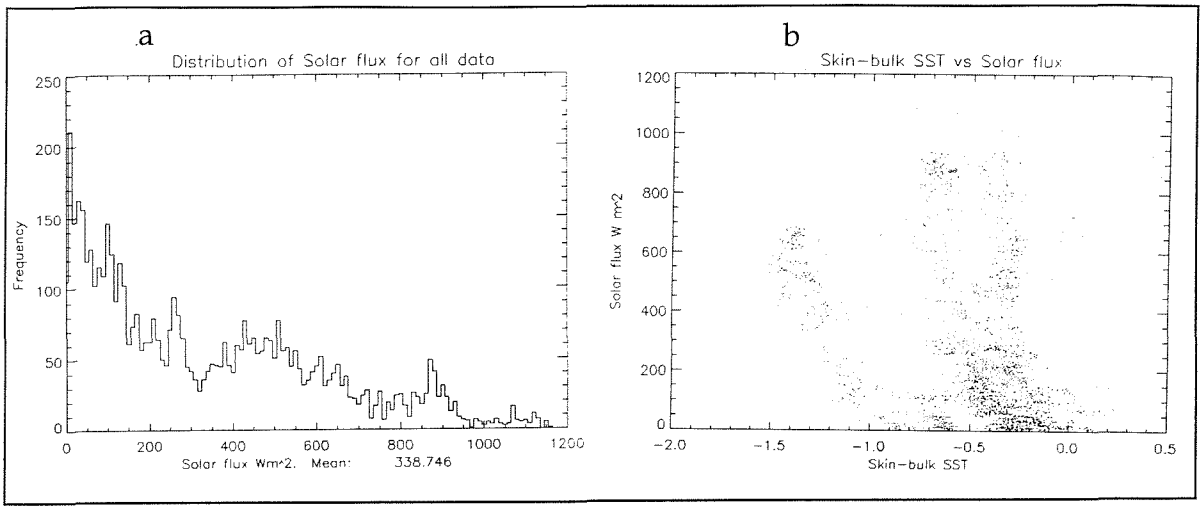

Figure 5.13 (a) The distribution of the solar flux Q_S and (b) ΔT plotted as a function of Q_S for the entire *James Clark Ross* data set.

5.2.9 ΔT and the net heat flux Q

The mean direction of heat flow at the air-sea interface for the entire data set is described by the net heat flux (Q) using equation 2.6. This was calculated as -201 W/m^2 with maximum and minimum values of 587 W/m^2 and -792 W/m^2. The distribution of ΔT in figure 5.3(a) is therefore representative of mean heat flow out of the ocean. Figure 5.14 shows ΔT plotted against the total heat flux Q, for the entire JCR data set.

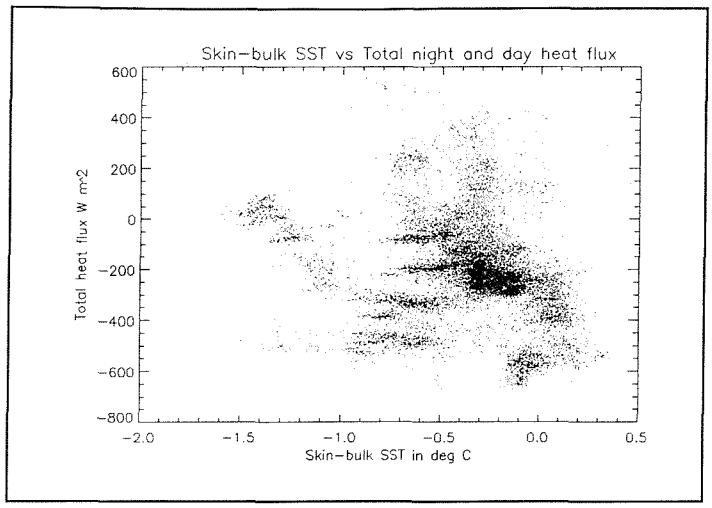

Figure 5.14 ΔT plotted as a function of the net heat flux Q, for the entire *James Clark Ross* data set.

The largest negative ΔT is found when the total heat flux approaches a value of zero. A net heat loss from the ocean surface during the night via radiative and turbulent exchange will lead to the maximum negative ΔT values occurring in the early morning hours. As the solar flux increases, this reverses the sign of Q but it is important to realise here that the processes of longwave cooling and turbulent transport of heat still continue and hence there will still be a cool skin at the surface of the ocean. Positive values of ΔT are found during periods of little solar input as a consequence of the unreliable radiometric temperatures at high wind speeds. A small number of data are found to be positive in the positive Q regime although it is difficult to attributed these to diurnal warming events as when a greater clustering of data would be expected.

5.2.10 ΔT and the interrelationship between wind speed, radiative and turbulent fluxes; conclusions

In order to consolidate the discussions above the heat flux components Q_L, Q_H, and Q_T were plotted against ΔT and wind speed. These data are presented in figure 5.12 as three dimensional 'wire mesh' drapes. In these figures the z axis plots ΔT while the x and y axes plot wind speed and fluxes respectively. Figure 5.15 (a) shows the latent heat flux case in which the deepening 'trough' running into the page shows the increasing Q_L out of the ocean associated with an

increasing negative ΔT. ΔT changes sign as the wind rises above ~ 10m/s (seen as a 'ridge'). This plot clearly shows that at a critical wind speed of > 10 -15m/s there is a distinct change of polarity in ΔT associated with a sea surface emissivity change. Unsurprisingly the same pattern is shown when the sensible heat flux is plotted in this way (figure 5.15 (b)). Negative ΔT increases in magnitude as the wind speed increases until turbulent mixing begins to dominate (~ - 100 Wm^2) at which point negative ΔT begins to decrease. The relationship between ΔT - wind speed and Q_T is slightly different (5.15 (c)); ΔT intensifies with an increasing Q_T out of the ocean but is wind speed independent and only becomes positive at wind speeds greater than 10 - 12 m/s. Clearly the effect of a strong wind has an overriding effect on ΔT when using infra red observations to measure SST.

5.2.11 Summary of general observations

The purpose of the above discussion is to draw attention to the fact that the ΔT distribution shown in figure 5.3 (a) is representative of a wide variety of local, regional, oceanic and atmospheric conditions. The exact inter-relationships between the local fluxes of energy and momentum at the air-sea interface define the magnitude and variability of negative ΔT at a particular point in time and space.

The data presented suggest that negative ΔT is at its greatest value during the day time. This is inconsistent with the observations made by other authors.

There is a marked change in the character of ΔT at wind speeds in excess of 10 m/s which is to be due to a change in emissivity of sea water at the infra red wavelengths by the presence of foam and white caps. This feature of the observation technique has been highlighted as an area requiring immediate research.

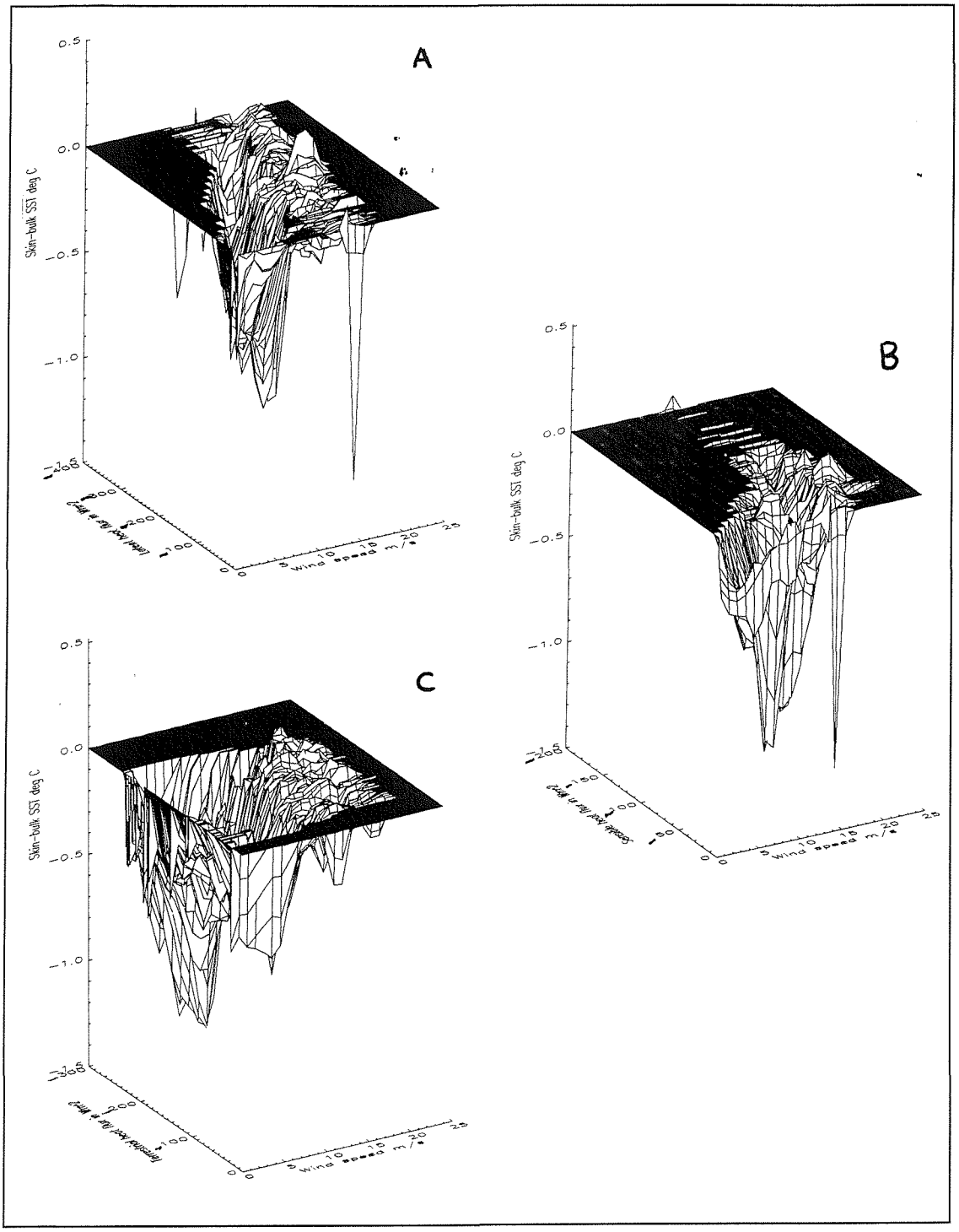

Figure 5.15 The relationship between the mean wind speed, mean ΔT and (a) the latent heat flux, (b) the sensible heat flux and (c) the terrestrial heat flux.

5.3 Differences between day and night time observations of ΔT

Part of the motivation driving the SST experiment aboard the JCR was to measure and characterise the oceanic skin temperature deviation for a variety of ocean - atmosphere conditions in several different regions. If a ΔT correction scheme is to be successfully applied to IR satellite SST data, the nature of ΔT needs to be quantified in the typical situations encountered during the satellite measurement. The optimal conditions for SST retrievals from space are during day and night clear sky situations (Chapter 1). This leads to a natural distinction between the clear sky and cloudy sky, day and night time ΔT values.

5.3.1 Day and night time distributions of ΔT

Figure 5.16 decomposes the total *James Clark Ross* data set in to night and day observations from the entire data set using the definition:

$$night\_data = solar\ flux < 5\ W/m^2$$

Figure 5.16 (a) and (b) show ΔT as a function of the bulk SST for night and day conditions and (c) and (d) give the respective distributions of ΔT. The most obvious feature of these plots is that a maximum negative ΔT is seen in the day time ΔT distributions as discussed in section 5.2.9.

Gemmrich and Hasse (1992) suggest that heating of the thin ocean skin layer accounts for only 15 - 20 % of the total oceanic warming due to solar radiation. Such heating may be insufficient to compensate for heat loss via the turbulent and radiative processes occuring at the oean surface A situation could arise where the net heat flux is directed out of the ocean close to the air-sea interface maintaining a cool skin (ie $Q_N < -Q_S$) while at some depth below this, direct solar warming exceeds the outgoing radiative and turbulent heat loss and the direction of the net heat flux reverses and is positive into the ocean. This process may occur even in high wind regimes.

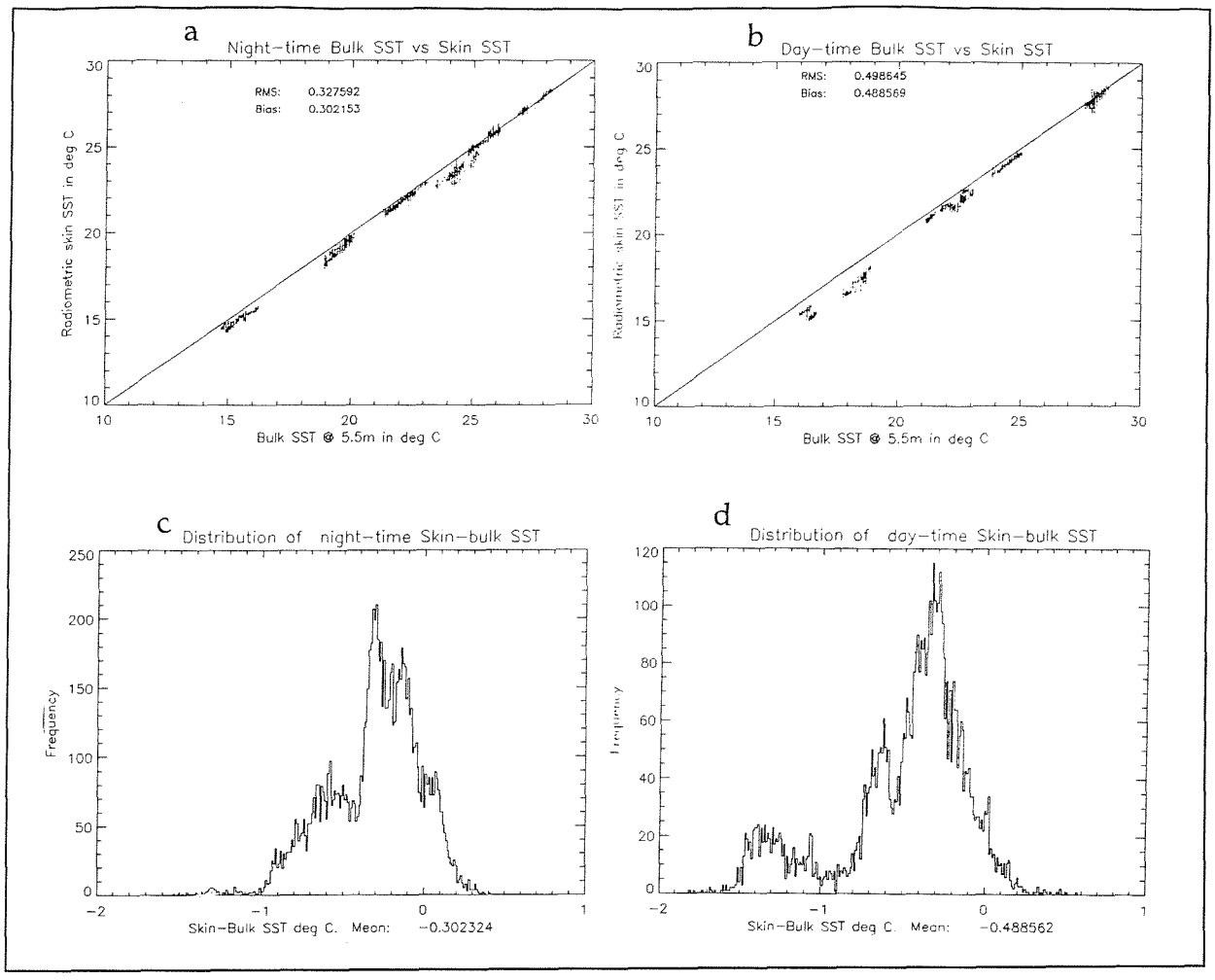

Figure 5.16 (a) Night time ΔT plotted against bulk SST at 5.5 m, (b) day time ΔT plotted against bulk SST at 5.5 m, (c) distribution of night time ΔT and (d) distribution of day time ΔT. Plots include all data from the *James Clark Ross* where *night=solar flux<5 Wm²*.

The mean ΔT for day and night time observations are -0.48°C ±0.38 and -0.3°C ±0.31 respectively for these observations (i.e. bulk measured at a depth of 5.5 m) giving a mean ΔT day time bias of -0.18°C with respect to the night time observations. Mutlow *et al* (in press) compare ATSR night and day time SST retrievals with the United Kingdom Meteorological Office SST (UKMOSST) fields which are derived from drifting buoy and ships reports of bulk SST for 24 hour periods at a spatial resolution of approximately 1.5° latitude by 1.9° longitude. They find that dual view ATSR SST data are biased by -0.33°C ±0.7 for the night time data and -0.89°C ±0.8 during the day time. There are limitations to the UKMOSST data as in cases of no ship or buoy reports a mean climatological value based on that of Bottomly *et al*, (1990) is used. To improve confidence in these results Mutlow *et al* (in press) compare ATSR ASST ½° SST data to drifting buoy

values finding biases of -0.03°C ±0.36° C for the night comparisons and -0.36°C ±0.42 during the daytime. These figures are reasonably consistent with those found for day and night ΔT values using the *James Clark Ross* data.

Conditions specific to the day time include those of strong insolation and low wind speeds and the possible generation of a diurnal thermocline leading to positive ΔT. As the diurnally warmed layer is buoyantly stable ΔT would be expected to be positive in sign when compared to a bulk temperature at 5.5 m. However the observations discussed above do not support this explanation. Table 5.2 shows that there is a systematic difference between the day and night time ΔT values. Day time ΔT is cooler than the night time data and has a larger standard deviation suggesting more variability in the ΔT relationship during the day time. Forrester *et al,* (1992) find that there is increased 'noise' in daytime ATSR ½° average SST data compared to the night time only data using *in-situ* thermosalinograph bulk SST validation data. They attribute this to the effect of ΔT.

Transect	Day mean	Day SD	Night mean	Night SD
A	-0.98	±0.32	-0.46	±0.13
B	-1.22	±0.21	-0.43	±0.18
C	-0.42	±0.16	-0.3	±0.05
D	-0.58	±0.12	-0.22	±0.08
E	-0.19	±0.08	-0.18	±0.08
F	-0.32	±0.08	-0.11	±0.08
G	-0.02	±0.09	-0.06	±0.05
H	-0.1	±0.12	-0.16	±0.24
I	-0.16	±0.09	-0.05	±0.09
J	-0.32	±0.07	-0.00	±0.14
K	-0.08	±0.12	-0.08	±0.06
L	-0.93	±0.15	-0.74	±0.19

Table 5.2 Mean and standard deviation of ΔT for the individual transects made during the JCR SST experiment. Both day and night time values are given. These data are plotted in figure 5.16 above.

Consider a situation during the day in light air and cloud free skies; the upper ocean layers are warmed by direct solar heating and the turbulent fluxes will be

minimal. Radiative cooling of the ocean is the major process maintaining a cool skin. If the wind speed now increases, turbulent mixing reduces the cool skin temperature difference but a further increase in wind speed will increase the turbulent fluxes and the cool skin is re-formed. The magnitude of the cool skin is thus defined by the dominant turbulent process independent of radiative cooling. A maximum negative ΔT can be expected when clear skies prevail (enhancing radiative cooling) and when the turbulent fluxes are able to dominate the increased mixing of the surface waters (acting to destroy the skin) due to the wind. Adopting the hypotheses of Gemmrich and Hasse, these processes should be independent of the solar flux. However, if the wind stress is sufficient to re-distribute the warmer water (warmed by solar heating) to the depth at which the bulk SST measurement is made (ie an isothermal layer is present in the upper layer of the sea), the situation arises where an extreme ΔT could be derived and a *maximum* ΔT can be expected during the day time.

This is a critical observation as it questions the measurement techniques used to determine ΔT; At what depth should the bulk SST measurement be made ? If the bulk sensor is not in the isothermal layer described above then *positive* ΔT can be expected. As for the majority of oceanographic fieldwork, the answer to this question is the dichotomy between what is desired, which is the temperature of the sea at a depth of several millimetres beneath the sea surface, and what is practical to measure. The latter is often the overriding limit on the depth at which a bulk SST measurement is made. Given the above observations, it is important that a standard depth for the measurement of bulk SST when used for the determination of ΔT is agreed. However these differencs may also be due to an increase in the variability of the surface wind fiels (itself an indirect function of solar heating) as the skin temperature is dominated by the latent heat flux, Q_L.

5.3.2 Day and night time ΔT relationships to the turbulent and radiative fluxes.

The discussions of section 5.2 focused on the interrelationships of the component parts of the net heat flux Q and the surface wind field. This described the general observed characteristics of ΔT. The differences apparent in table 5.2 should therefore be explained by differences in these parameters.

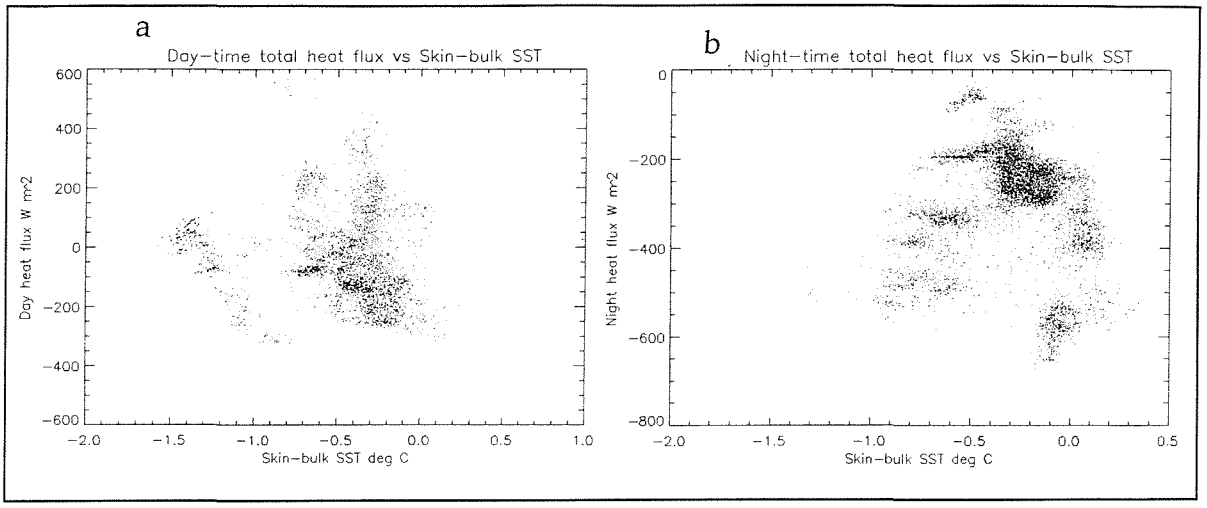

Figure 5.17 (a) Total heat flux plotted against ΔT for all day time data and (b) total heat flux plotted against ΔT for all night time data. All data from *James Clark Ross* are included.

5.3.2.1 ΔT and Q for day and night data

Figure 5.17 (a) and (b) show the net heat flux for the day and night time data respectively. 5.17 (a) shows that the maximum negative ΔT is recorded during the day time when Q is either negative or below 100 W/m^2. However using the definition of day and night given above this may correspond to the early morning situation where longwave cooling of the sea surface has led to a large negative ΔT. Consequently it would be expected to find a similar distribution in the night time data with ΔT having minimum values approaching zero. Figure 5.17 (b) shows that this is not the case and that the minimum ΔT is when Q is between -400 and -600 W/m^2. Further, a larger proportion of positive ΔT is found during the night rather than the day suggesting that the higher wind speeds are observed at night. 5.17 (a) shows two clusters of data; a large negative ΔT cluster in which ΔT becomes increasingly negative as Q decreases out of the ocean and a second cluster in which ΔT appear to be independent of Q having a range of values

between 0.25 and -0.6°C. Positive ΔT is found for a few outlying points at between 200 and 600 W/m². These latter data could be due to diurnal warming. Figure 5.17 (b) shows a regime in which ΔT becomes increasingly negative as Q decreases having maximum negative ΔT at ~ -500 W/m². This is to be expected as the strong heat flow out of the ocean leads to a large ΔT.

5.3.3 ΔT and wind speed for day and night data.

Figure 5.18 (a) and (b) show wind speed plotted against ΔT for the day and night time cases. There is clearly a dominance of higher wind speeds in the night time data (predominantly from time series K previously discussed). At the higher wind speeds (>10 m/s) ΔT is positive even though at such high winds there is not the possibility of a diurnal effect. In fact if any diurnal effect is present in these data at all it will be for the few positive ΔT data at low wind speeds shown in 5.18 (a).

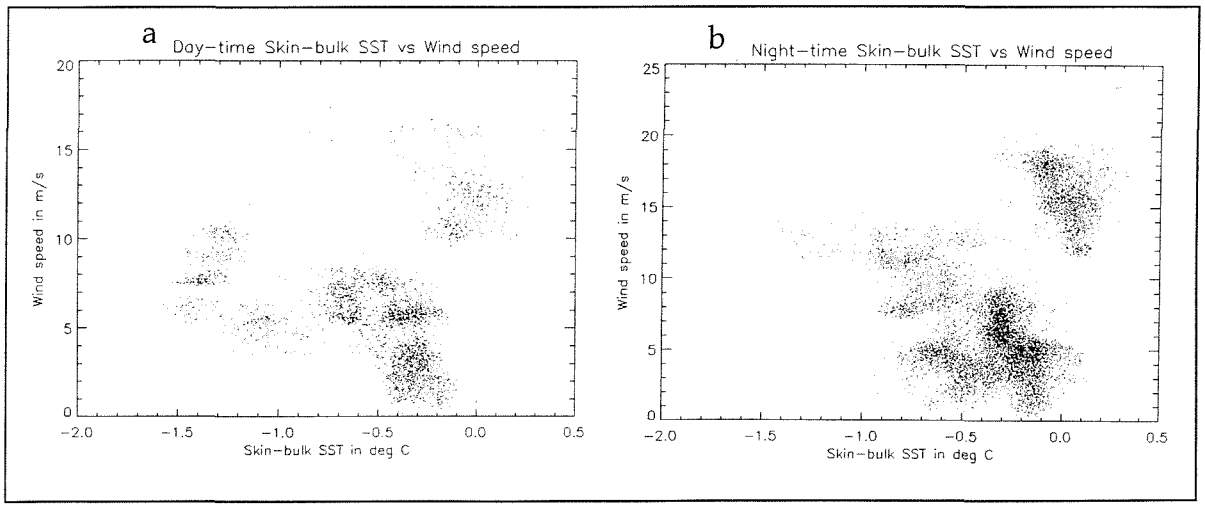

Figure 5.18 (a) Day time ΔT and (b) night time ΔT plotted as a function of wind speed.

5.3.4 ΔT and the component heat fluxes

The day and night time ΔT relationships to Q_L and Q_H are shown in figures 5.19 (a), (b), (c) and (d).

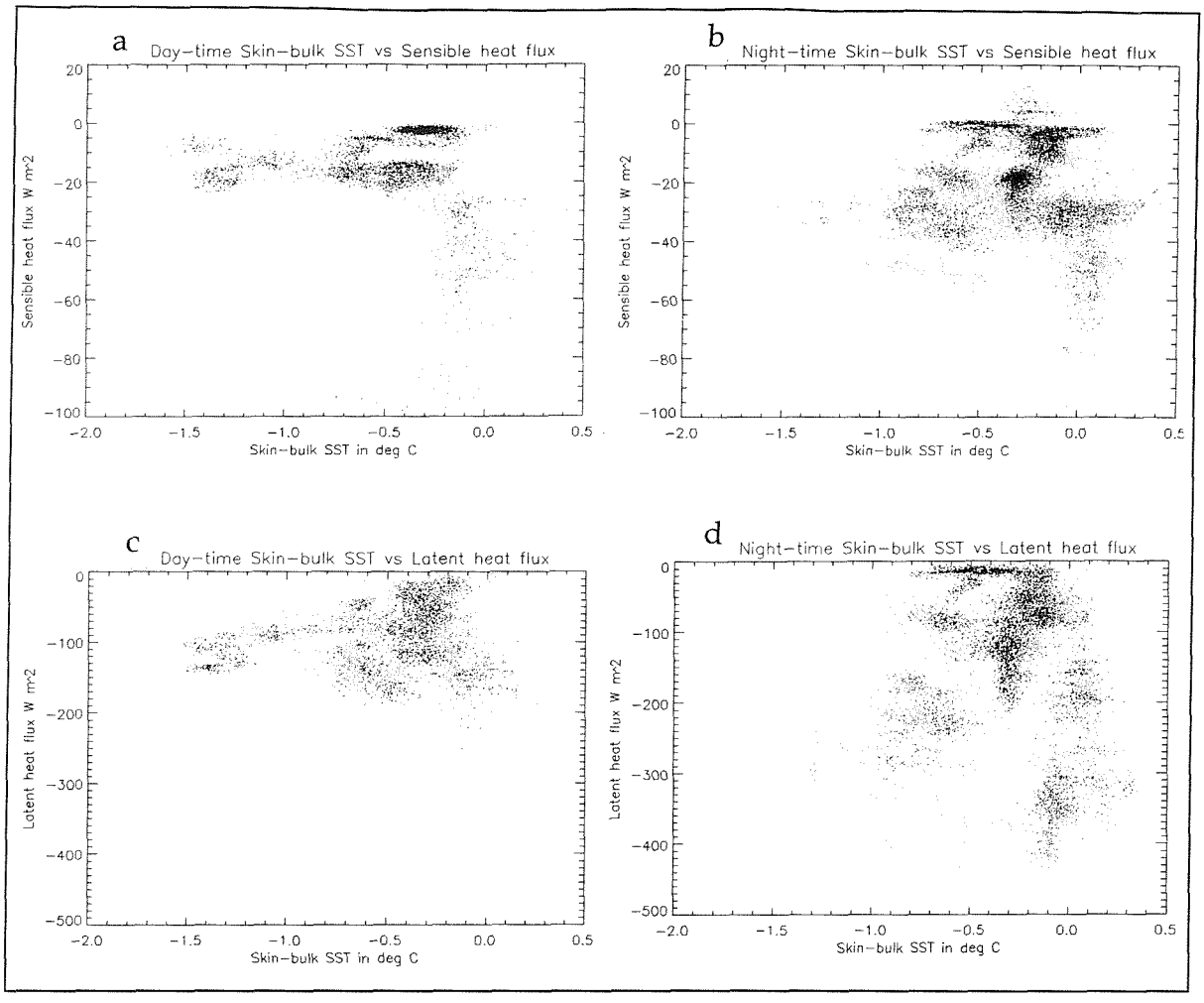

Figure 5.19 (a) daytime ΔT Vs Q_H (b) night time ΔT Vs Q_H (c) day time ΔT Vs Q_L and (d) night time ΔT Vs Q.

As for the general discussion in section 5.2, the same ΔT relationships will apply and the wind is the cause of the polarity change in ΔT at higher wind speeds. The maximum negative ΔT is seen when Q_L and Q_H are not at a minimum (values of -5 W/m^2 and -120 W/m^2 respectively) during the day time. Ignoring the Positive ΔT regime, there is a stronger ΔT relationship seen in the Q_L data at night as a consequence of the higher wind speed.

Figure 5.20 (a) and (b) show the terrestrial flux and from these and figure 5.19 the extreme values of negative ΔT found in the JCR SST experiment data can be explained during the day using the observations made so far.
During the day the turbulent fluxes are driven by a moderate wind under clear sky conditions resulting in a net radiative loss from the sea surface. Solar

radiation is insufficient to offset the cooling effect of the combined turbulent and radiative fluxes as described by Gemmrich and Hasse (1992) as discussed in section 5.3.1.

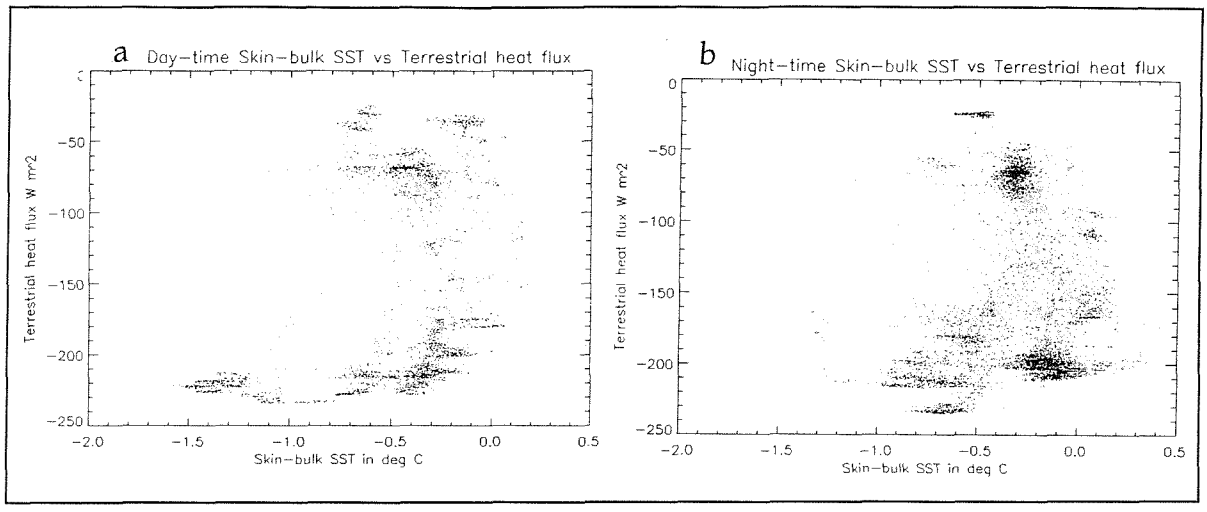

Figure 5.20 (a) Day time ΔT plotted against Q_T and (b) night time ΔT plotted against Q_T.

5.4. Individual time series analysis of JCR transects

To gain a thorough insight into the processes influencing the bulk-skin temperature distribution described in the above sections a series of case studies are presented for the data collected during transects I, C, E and F as defined in table 5.1 and figure 5.2. For each time series, 8 plots are presented which show key variables with which the local and regional conditions at the air-sea interface can be described.

The x axis represents time given in number of seconds since midnight GMT on the day of transect start.

5.4.1. Transect I

Data collected during transect 'I' are presented in figure 5.21. These plots demonstrates how variable ΔT can be in the presence of clouds. Figure 5.21 (a) shows the radiometric temperature (T_s solid line) plotted concurrently with the bulk SST at 5.5m depth (T_b dashed line). The data begin at 16:00 local solar time and run for 188 minutes which represents a distance of 67 km. The bulk SST

shows an initial fall in temperature of 0.4°C from 28.0°C before steadily rising to a maximum of 28.5°C at the end of the series and the radiometric temperature has significant departures from this. Although the general trend of the bulk SST is followed by the radiometric observations (a correlation of 0.8), figure 5.21 (b) shows that ΔT has a variation of between 0.5°C to -1.0°C. Figure 5.21 (c) plots the solar flux for the same period. High insolation is initially recorded during the early afternoon and a positive ΔT value is found. Under calm wind speeds this would be expected as a warm diurnal layer would be expected at the sea surface. In this case ΔT cannot be positive due to diurnal warming as figure 5.21 (e) indicates that a strong wind of >16 m/s is blowing. At this wind speed, mixing in the upper layers of the ocean is both vigorous and deep so that solar heating is efficiently redistributed throughout the water column. Positive ΔT in this case is probably due to the presence of foam as previously described. At ~5.45×10^6 seconds, a large bank of cloud passes overhead which significantly reduces insolation and a change of -900 Wm^2 is seen in figure 5.21 (c). As the base temperature of the cloud is warmer than the clear sky, there is a reduction in Q_T out of the ocean shown in figure 5.21 (f) as the dashed line. Also shown in this plot are the Q_L and Q_H which indicate a strong flux out of the ocean due to the high wind speeds. This combination of events has the effect of changing the sign and thus direction of Q shown in figure 5.20 (d); $Q_L + Q_H + Q_T$ (although reduced) is now able to dominate Q and in the absence of direct warming ΔT increases to a negative maximum. From 5.6×10^4 seconds, there is a steady reduction in the wind speed shown in figure 5.21(e) and a corresponding reduction in Q_L and Q_H. Negative ΔT is thus reduced. There is a mean negative skin temperature of 0.16°C having extreme values of -0.9 and +0.6°C during this period as shown in figure 5.21(g).

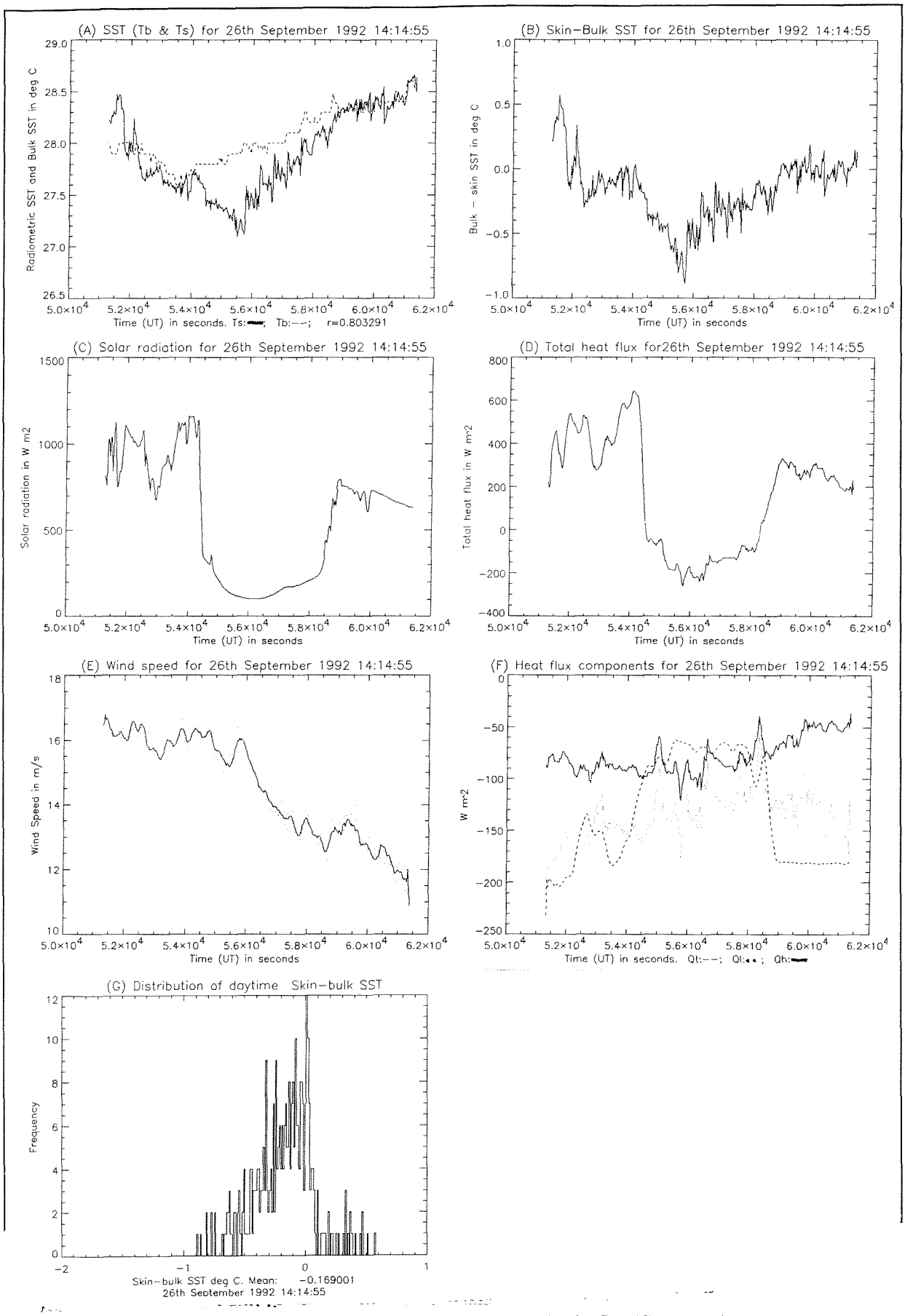

Figure 5.21 (a) Bulk (dashed line) and skin SST (solid line), (b) ΔT, (c) Solar flux, (d) net heat flux Q, (e) Wind speed (solid line is a 10 minute mean, (f) Latent heat flux (dotted line), sensible heat flux (solid line) and terrestrial heat flux (dashed line) and (g) the distribution of ΔT. All data from transect I given in table 5.1

5.4.2 Transect 'C'

Figure 5.22 presents the data from transect 'C'. This is the longest continuous record made during the whole experiment and extends over a distance of 548 km. The record begins at ~15:00 local time and continues for nearly 24 hours. Figure 5. 22(a) shows that during this time there was a steady warming of the bulk waters from 21.4°C to 25.0°C as the ship moved south. The correlation between the skin and bulk temperatures was r=0.899 indicating that the skin and bulk temperature fields are well correlated during this period. Figure 5. 22 (b) shows the calculated ΔT value for this transect, figure 5.22 (c) the solar flux, (d) the net heat flux, Q, (e) the wind speed, (f) the turbulent and radiative components of Q, (g) and (h) the distribution of ΔT for day and night respectively. The maximum negative ΔT is found during periods of high insolation and appear to be wind speed independent. The net heat flux is negative during the night and positive during the day with the latent heat flux, Q_L dominating this equation at night reaching a minimum value of -200 Wm^2. A near overcast sky prevailed during the entire data set shown by the low terrestrial flux, Q_T (figure 5.22 (f)) of ~-60 Wm^2 which is occasionally 'pierced' by a break in the clouds resulting in enhanced radiative cooling seen as sharp negative spikes in these data. Figures 5.22 (g) and (h) show that ΔT is significantly different during the day and night respectively. Not only is ΔT at a minimum during the day, but shows a greater variability and an opposite skewness to that observed during the night. Mean values of ΔT_{day}=-0.42°C and ΔT_{night}=-0.3°C are derived from this series.

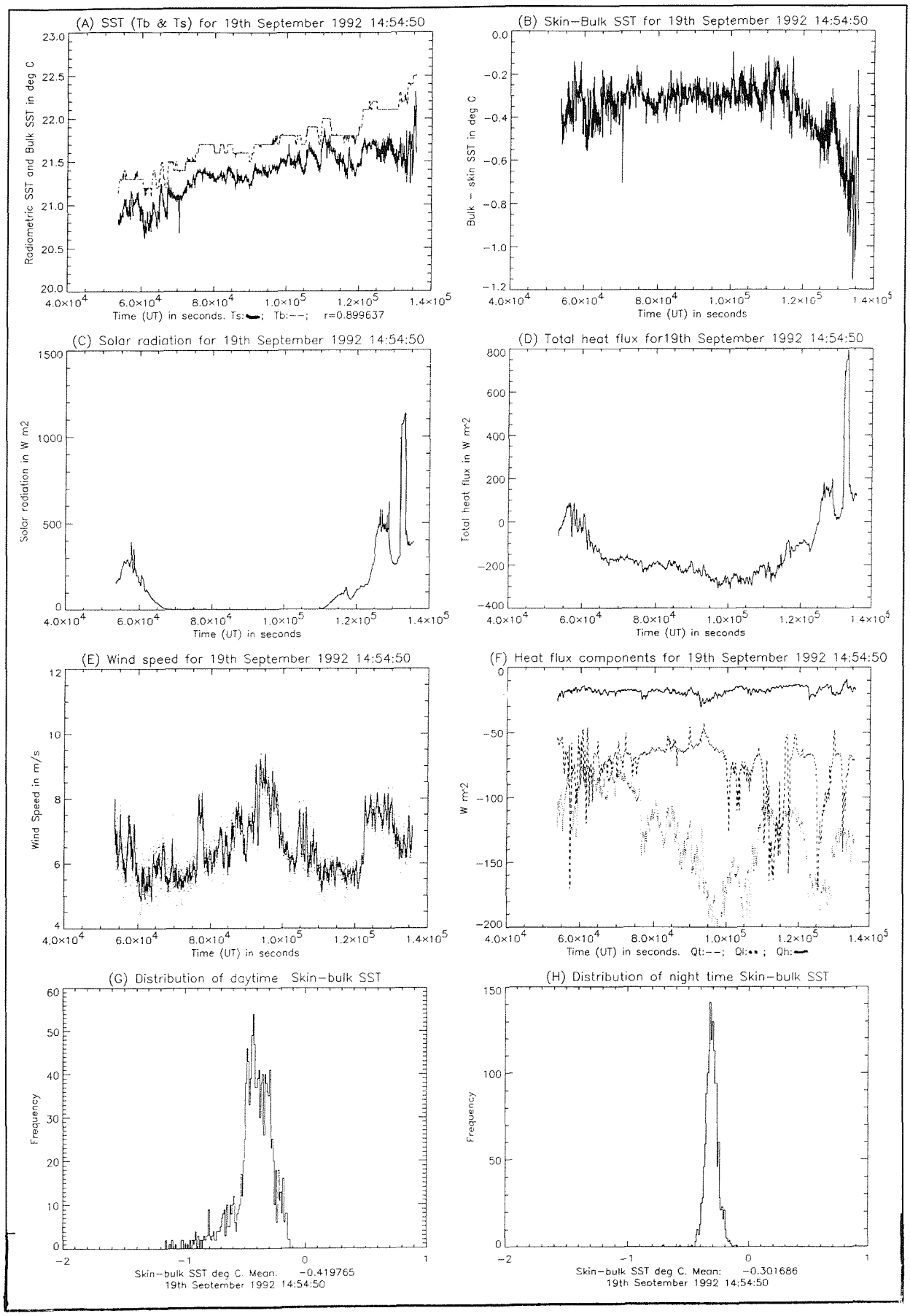

Figure 5.22 (a) Bulk (dashed line) and skin SST (solid line), (b) ΔT, (c) Solar flux, (d) net heat flux Q, (e) Wind speed (solid line is a 10 minute mean, (f) Latent heat flux (dotted line), sensible heat flux (solid line) and terrestrial heat flux (dashed line) and (g) the distribution of ΔT. All data from transect C given in table 5.1

5.4.3 Transect 'E'

Time series 'E' was made south of the Canary islands (see figure 5.2 and table 5.1) beginning at ~11:50 local time and run for a duration of 8 hours 17 minutes. Figure 5.23 describe the time series. 5.23 (a) clearly demonstrates the high correlation (r=0.98) between the skin and the bulk temperature fields for the duration of the series which has a length of 197 km. There is a large oceanic temperature front within these data which is manifested in both the SST measurements and the wind speed figure 5.23 (e), which is seen to fall from 5 m/s to below 2 m/s. The consequence of a reduction in wind speed is a corresponding reduction in the turbulent fluxes Q_H and Q_L is seen in figure 5.23 (f). The dominant process governing Q in this case is longwave radiative cooling which dominates until the sun begins to rise (figure 5.22 (d)). At this time Q begins to rise and the heat flow is directed into the ocean.

Figure 5.23 (f) shows the effect of broken cloud reducing the Q_T at the beginning of the series which clears to leave open skies and a lower value of Q_T. The effect of cloud here is to suppress the flow of longwave energy out of the ocean and is clearly seen in the ΔT plot 5.23(b). ΔT has an instantaneous response to these clouds and fluctuates by 0.4°C. An interesting feature of ΔT in this case is a reduction in the scatter as the frontal zone is approached followed by a cool spike and then a warm spike. Frontal regions are often characterised by surface slicks which are a consequence of vertical movements associated with these regions and the radiometric signature of these features remains an area of on going research. Although a slick was not observed the coincidence of a warm radiometric SST spike with the frontal region suggests that a slick may have been present.

In the conditions prevalent during this time series cooling of the sea surface is primarily via long wave radiative processes and ΔT has similar mean values for the day and night of -0.19 and -0.18°C respectfully. In contrast with section 'I', ΔT in the lower wind speed regime under clear skies is not as large as during moderate wind speed conditions. This is unexpected as radiative cooling under clear sky conditions and light winds should produce a large negative ΔT (Katsaros, 1977).

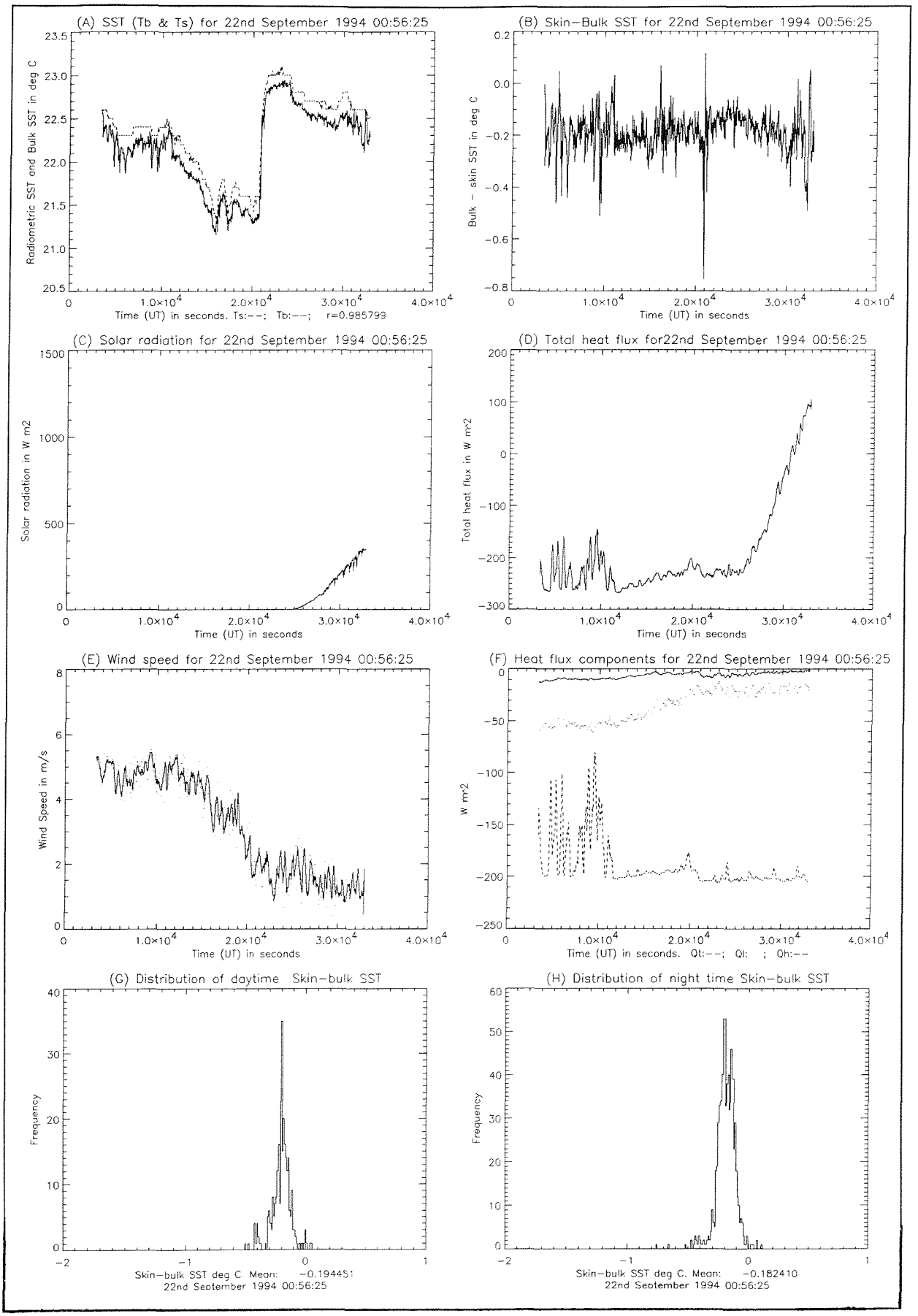

Figure 5.23 (a) Bulk (dashed line) and skin SST (solid line), (b) ΔT, (c) Solar flux, (d) net heat flux Q, (e) Wind speed (solid line is a 10 minute mean, (f) Latent heat flux (dotted line), sensible heat flux (solid line) and terrestrial heat flux (dashed line) and (g) the distribution of ΔT. All data from transect E given in table 5.1

5.4.4 Transect 'F'

Transect F was made in open ocean conditions between 20° 22 N and 17°02 N beginning at 08:50 hrs on the 23rd September having a duration of 16 hours 21 minutes and represents a total length of 438 km. Figure 5.23B describes the observations made. A steady increase in bulk SST is seen as the JCR moves south towards the equator. A temperature increase of 3.2°C is recorded during this transect. As seen in transect 'I', the lowest ΔT values are found during the daytime having a mean value of -0.31°C compared to -0.11°C for the night time 5.24 (g) and (h). A high correlation of r=0.98 is found between the bulk and skin observations shown in figure 5.23B (a). The solar flux Q_S, during this period was interrupted by the passage of cumulous cloud banks seen in figure 5.23 (c) reducing the solar input to the ocean which have a corresponding effect in the net heat flux, Q, shown in figure 5.23B (f). At $8x10^4$ seconds into the series there is a rise in the wind speed and a corresponding increase in the turbulent flux out of the ocean. However the effect is counterbalanced by a passing cloud leading to a reduction of Q out of the ocean allowing ΔT to become positive. Notice that there is a steady increase in the terrestrial flux as a consequence of the increased sky temperature relative to the sea surface temperature as the ship moves southward into the tropical regions which have an increasing atmospheric water vapour load. In this case it seems that wind induced mixing of the surface layer of the ocean is able to prevent the establishment of a cool skin overcoming radiative cooling and that a negative ΔT is seen during the day.

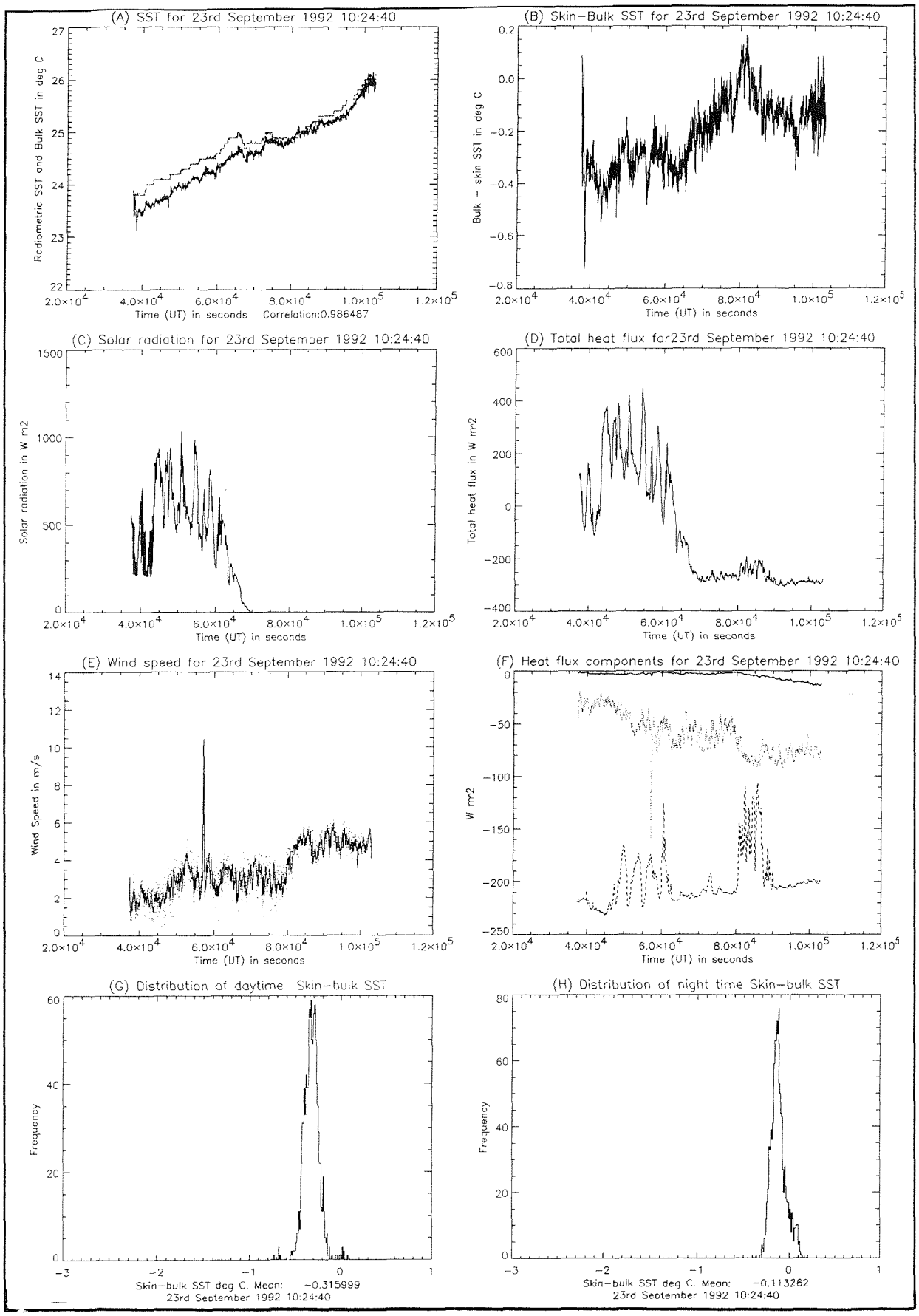

Figure 5.23B(a) Bulk (dashed line) and skin SST (solid line), (b) ΔT, (c) Solar flux, (d) net heat flux Q, (e) Wind speed (solid line is a 10 minute mean, (f) Latent heat flux (dotted line), sensible heat flux (solid line) and terrestrial heat flux (dashed line) and (g) the distribution of ΔT. All data from transect F given in table 5.1

These example observations indicate that ΔT has a rapid response time to the balance of the local Q, the surface wind field and the effect of clouds. Clouds have the effect of increasing negative ΔT. These data also show that the effect of solar radiation and Q have a significant effect on the magnitude of ΔT during daylight hours.

5.5 Cross correlation of skin and bulk temperatures.

One of the fundamental questions concerning the satellite skin temperature and the bulk SST temperature is: "to what degree does the skin temperature represent the temperature at depth i.e. how well coupled are the two temperature fields ?". In fact this was one of the main elements of the JCR SST experiment. The main concern is to determine whether the skin effect is biasing validation match ups between satellite data and *in-situ* data. As the skin temperature deviation is a variable quantity, individual pixel by pixel validation data pairs may be in error and in the case of the 'pseudo-bulk' SST validation required by the AVHRR radiometer, may not be representative of the bulk SST at all. Satellite integration times are of the order of microseconds for a single pixel field of view (which is much larger than an *in-situ* instrument field of view) and as such will be a near instantaneous measure of the ocean surface temperature field. The data presented above and by several other authors (ibid.) clearly demonstrate that radiometric validation measurements could vary in the order of 3 -10 seconds. Thus the skin temperature of the ocean has a characteristic time length scale which is different to that of the bulk temperature field and a satellite SST measuring the skin temperature may not be measuring a true representation of the bulk temperature. However, it is expected that at a sufficiently long length scale the bulk temperature field will have sufficient variability to dominate the skin temperature. Infra red satellite imagery is particularly good at resolving mesoscale features (see cover plate) and intuitively this length scale would suggest a dominance of the bulk temperature over the skin temperature. Schluessel *et al* (1990) show that in the NE Atlantic ocean the skin and bulk temperatures are well correlated only at

length scales greater than ~160 km. Data from the *James Clark Ross* experiment were used to verify these observations.

5.5.1 Correlation of Skin and bulk SST using the JCR SST data set.

Using the results from the *James Clark Ross* each data series given in table 4.1 was split into section lengths, Δ, of Δ= 20, 40, 80, 160, 320 and 500 km and the mean cross correlation of bulk and skin SST computed. The results of this analysis are given in table 5.3.

Δ in km	Correlation (r)	Standard deviation
20	0.598	± 0.372
40	0.725	± 0.278
80	0.795	± 0.238
160	0.804	± 0.369
320	0.931	± 0.14
500	0.957	± 0.01

Table 5.3 Mean correlation's between skin measured SST and bulk measured SST at 5.5 m at different length scales for the entire *James Clark Ross* data set.

The mean cross correlation rises from 0.5 at the lower scales to greater than 0.9 at a length scale greater than 230 km. Conversely the standard deviations decrease with increasing length scale. This suggests that at the longer length scales the skin and bulk temperature fields are indeed well coupled and at the smaller length scales there is a dominance of the skin variability over the bulk SST.

These data are in extremely good agreement with those reported by Schluessel *et al* (1990) who continue their analysis by taking coherence spectra of their longer data series. The coherence estimator is a highly biased operator (see for example Otnes and Enochnson, 1970) requiring long time series for a meaningful result. Spectral smoothing in the frequency domain can be used to generate enough statistical degrees of freedom to have confidence in the results (P Schluessel and W Emery, personal communication). As the data collected from the JCR SST experiment are discrete transects of relatively short length scales such a technique

is inappropriate. Given the similarity between the cross correlation analyses there is no reason to suggest that there should be a different result found in the JCR data set to that of Schluessel *et al* (1990).

5.5.2 Day and night time correlation of skin and bulk SST

To investigate the coupling of skin and bulk SST during day and night time situations the cruise data were split into day and night time sections and the cross correlation computed. Results from this analysis are presented in table 5.3.

Transect	Length km	r night	SD night	Length km	r day	SD Day
A	262	0.945	0.133	104	-0.213	0.319
B	273	0.951	0.188	103	0.886	0.215
C	287	0.940	0.05	260	0.919	0.158
D	89	0.941	0.087	145	0.797	0.126
E	145	0.987	0.078	53	0.659	0.0081
F	225	0.977	0.082	214	0.976	0.083
G	83	0.937	0.054	45	0.032	0.092
H	0	0.0	0	81	0.718	0.11
I	0	0.0	0	68	0.803	0.244
J	108	0.942	0.097	47	0.874	0.096
L	41	0.904	0.061	70	0.598	0.126
M	283	0.923	0.199	118	0.986	0.156

Table 5.4 Day and night time cross correlation's between skin and bulk SST for each of the *James Clark Ross* sections.

As day and night time transects are of different lengths and most of the data are below 160 km these results need to be treated with caution bearing in mind the previous discussion. However, there is a clear difference between the correlations for the night and day cases. Night time correlations are constantly high (>0.9) at all length scales compared to the day time data which have considerable variability at the shorter length scale. Longer length scale day time correlations are similar to those of the night time data.

The implication of these results is that most of the skin-bulk de-coupling takes place during the day time. In the context of satellite derived SST, this helps to explain the difference often found between day and night time SST such as those

presented by Mutlow *et al,* (in press) discussed in section 5.3. The night time satellite SST will be more representative of the bulk SST at the shorter length scales than for day time data. In this context the correct validation of satellite derived SST using bulk *in-situ* validation data should only be made during the night. Further as many authors use a 5x5 pixel mean as a satellite validation temperature in order to account for the inaccuracy of colocation in space between ship/buoy and satellite (Thomas *et al,* 1992) , this area could contain sufficient variability to invalidate the comparison during the day time. The problem here is that the single *in-situ* observation is not representative of the area sampled by the satellite.

5.6 Regionality of ΔT observations.

The relationships between ΔT and the parameters measured during the JCR SST experiment have been explored in the previous sections. In conclusion ΔT is shown to be dependent on the local conditions of the atmosphere and ocean. Such conditions have a mean value associated with the predominant pressure systems of the earth. In this context ΔT is expected to have a regional dependence. This Chapter explores this hypotheses using both *in-situ* data.

5.6.1 Observations of ΔT regionality.

Roberston and Watson (1992) calculate a global surface ΔT using the parametisation of Hasse (1971) given in equation 3.9. They use monthly mean wind speed, solar flux and heat flux to derive ΔT maps for December and June shown in figure 5.24 (a) and (b). Data are sparse in the southern ocean owing to the lack of observations. Clear differences exist between the seasons and the data in figure 5.24 suggest that ΔT will be larger for the winter hemisphere. In both cases ΔT is shown as a minimum for the higher latitudes. In the North Atlantic during winter the gulf stream and North Atlantic drift show a prominent anomaly due to the strong heat flux characteristics of the gulf stream. In both maps there is a larger effect in the northern hemisphere and Robertson and Watson argue that

this is due to the net interhemispheric transport of heat from the northern to the southern hemisphere.

Although the actual ΔT at any point in space or time will depend on the local conditions at the atmosphere - ocean interface, some similarity might be expected in the data collected during the JCR SST experiment to that shown in figure 5.24. Figure 5.25 shows a map of the JCR data sets and a mean ΔT figure is given adjacent to each transect. Day and night time mean and standard deviations for each transect are given in table 5.3. In this map, high negative ΔT values are found in the northern hemisphere at latitudes greater than 40° and in the southern hemisphere less than 10°S. The minimum ΔT are found in the tropical areas. (Maxima are separated by solid lines at -0.8°C) These data are in direct contradiction to the monthly mean data shown in figure 5.24. The data presented here are a clear indication of the global spatial variability of ΔT when compared to the mean monthly ΔT maps of figure 5.24. If the JCR SST observaations are representative of the mean conditions, the implication is that the uptake of CO_2 will be more significant at the higher latitudes rather than the sub-tropical and topical regions. However it should be remembered that the high wind speed conditions encountered in the tropical regions during the JCR experiment are anomalous.

Although there are insufficient data from which to draw any firm conclusions, the danger of using a mean climatology as an input to a ΔT parametisation is highlighted in this comparison. From the data presented it is clear that if the global climate prediction/monitoring community are to achieve their goal of satellite SST <0.1 K, then global corrections for the effect of ΔT will be necessary as ΔT differences are shown to be much greater than the desired accuracy.

Returning to the regionality of ΔT, it is difficult to detect any regional trends from the observations presented in figure 6.1 using the JCR SST experiment data set. As the previous sections have shown, ΔT is defined by the local conditions of the

atmosphere - ocean interface and also the measurement technique used. It is therefore important that the ΔT parameter is successfully parametised in order to ensure that the mean climatology is manipulated in the correct fashion. This is the subject matter of Chapter 6 which explores several of the more referenced ΔT parametisations with this question in mind.

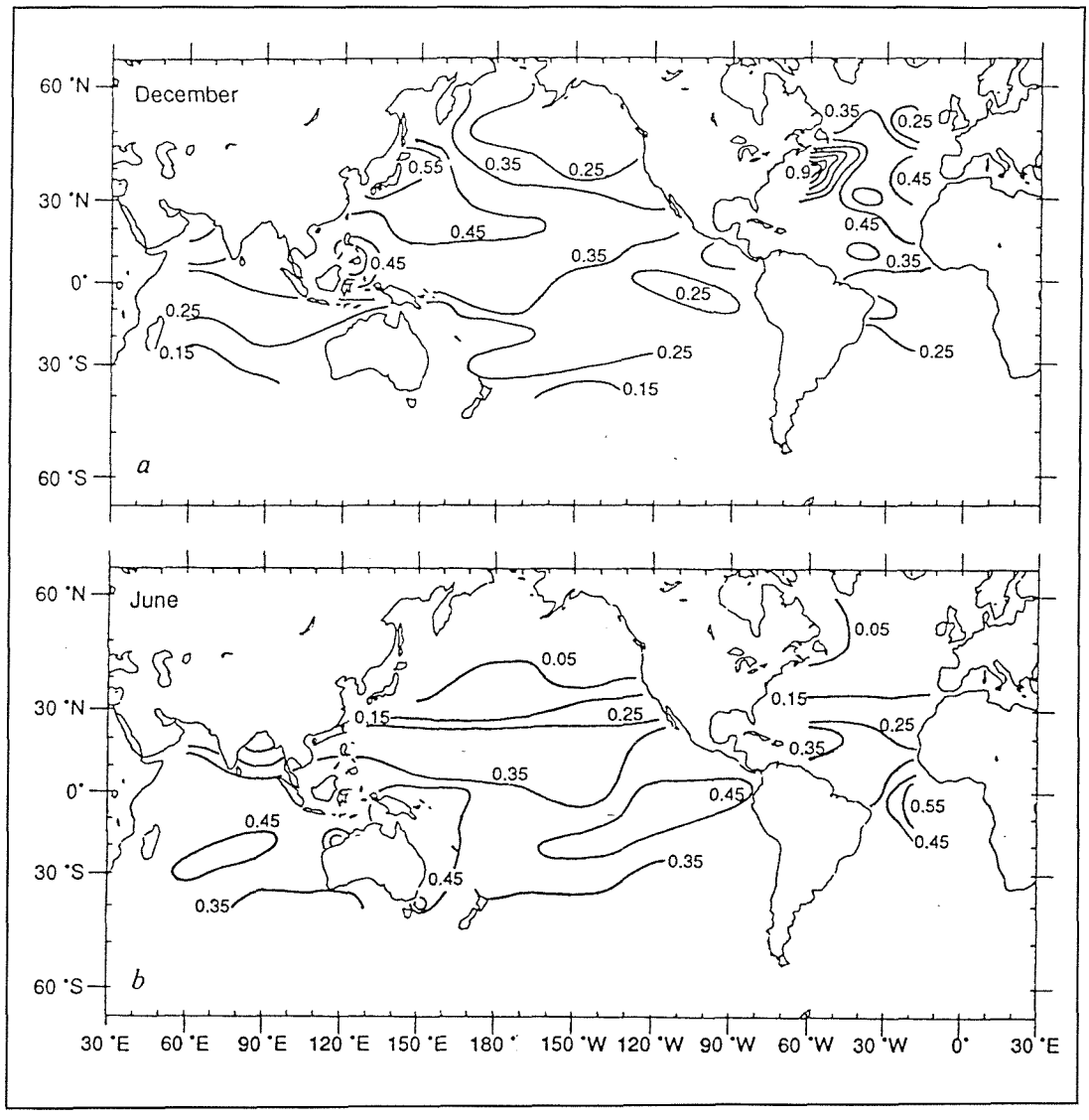

Figure 5.24 Maps of global ΔT for the months December and June calculated from monthly mean clmatological data using equation 2.9 (Hasse, 1971). From Robertson and Watson, 1992.

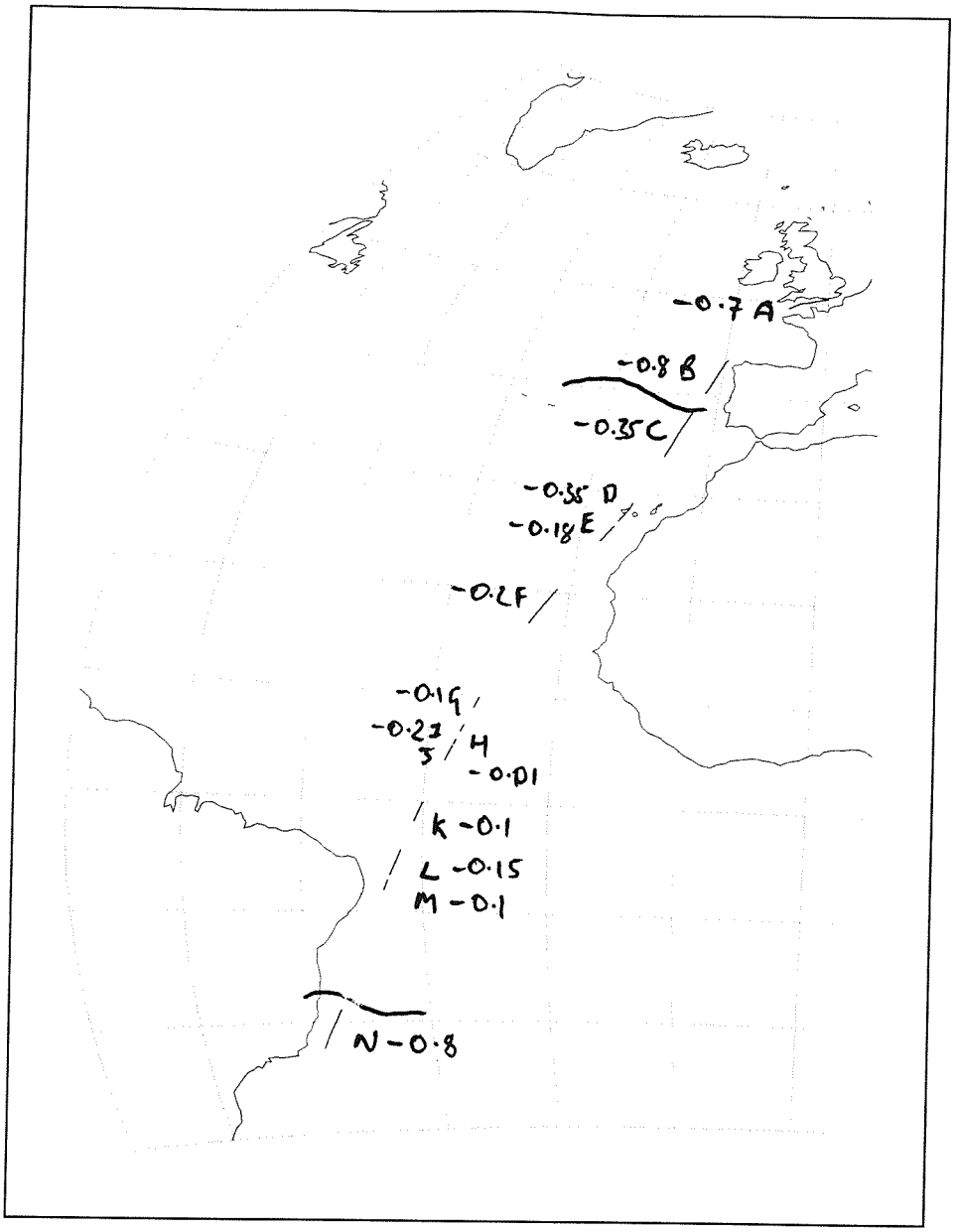

Figure 5.25 Mean ΔT for each leg of the *James Clark Ross* data set. The two heavy solid lines mark the boundary between 'high' and 'low' ΔT.

Chapter 6. An analysis of several ΔT parameterisation schemes.

The importance of correcting infra-red satellite SST observations for the ΔT effect has been demonstrated in Chapter 5 and the need to predict ΔT of the surface oceans has been highlighted. The maps presented in figure 5.24 of Robertson and Watson (1992) produce a global monthly mean ΔT using the ΔT parameterisation proposed by Hasse, (1971) These results are contradictory to the observations made during the *James Clark Ross* SST experiment. In this chapter several of the more referenced ΔT parameterisations are compared to the measured ΔT values derived from the JCR SST experiment in order to determine if a single model is able to represent global ΔT.

6.1 Background.

The accuracy requirements for the monitoring and detection of global climate change are extremely high; ≤0.1 K with ≤0.1 K long term stability, (Hadley Centre, 1994). Chapter 5 has shown that ΔT is a phenomenon which is a persistent and dynamic feature of the ocean surface and has deviations of up to 1.5 K. As new satellite radiometer systems such as the ATSR return a skin temperature rather than a 'pseudo-bulk' temperature (e.g. the AVHRR MCSST or CPSST SST algorithms discussed in Chapter 2), these data require a separate 'skin to bulk' algorithm for the derivation of a bulk SST (Hadley Centre, 1994).

Unlike the reports from volunteer ships or the deployment of moored and drifting buoys which can routinely report SST via global telemetry networks, the unattended deployment of *in-situ* radiometers is unpractical (Chapter 3). This is unfortunate as the development of such 'skin to bulk' SST transfer algorithms will be hindered if limited to regional short term data sets

Chapter 3 reviews all of the parameterisation schemes presented here. In summary, current parameterisation can be classed into free and forced convection

regimes and have built on engineering boundary theory. More recently, surface renewal mechanisms have received increased attention.

Table 6.1 shows the atmospheric and oceanic conditions constraining each of the parameterisations. The difficulty of accounting for solar radiation is exemplified by the observations presented in Chapter 5 and most authors choose to ignore these effects concentrating on the night-time only situation assuming that Q_N is more important than Q. This is sensible in terms of the modelling aspect as there is one less parameter to consider. However in practical terms, this situation is unsatisfactory as satellite SST data is also collected during the day time when a correction for ΔT may be more difficult to derive. Schluessel *et al* (1990) concentrate on deriving a suitable parameterisation for the correction of satellite SST data using on only the standard meteorological observations made by ships and drifting buoy systems. This approach has high merits as routine reports from ships of opportunity and the volunteer observation fleets (see Kent *et al*, 1991) can be used to derive a ΔT correction.

6.2 Methodology.

As the conditions encountered during the passage of the *James Clark Ross* were varied in terms of the wind speed and surface fluxes, these data can be used to examine the performance of the parameterisation schemes detailed in table 6.1 for a variety of conditions within these constraints.

Model	Wind speeds	Solar radiation	Convection
Hasse (1971)	> 2m/s	yes	Forced
Katsaros (1977)	<2 m/s	no	Free
Saunders (1969)	> 2 m/s	no	Forced
Eifler (1992)	>2 m/s	no	Forced
Soloviev and Schluessel (1994)	< 5m/s	no	Free
Soloviev and Schluessel (1994)	5 - 10 m/s	no	Forced
Soloviev and Schluessel (1994)	> 10 m/s	no	Forced
Schluessel *et al* night time (1990)	>2m/s	no	Forced
Schluessel *et al*, daytime (1990)	>2 m/s	yes	Forced

Table 6.1 General characteristics of ΔT parameterisation schemes compared in this work.

For each parameterisation the appropriate wind conditions were separated from the entire JCR data set and the parameterisation evaluated. Wind speeds were corrected to a standard height of 10 m following Smith, (1980;1988). A further reduction to a height of 4.0 m was required for use in the Hasse parameterisation and uncorrected winds at a height of 18.5 m were used for the Schluessel *et al* (1990) regression model. Wind speed was vertically corrected assuming a logarithmic profile as the air-sea interface is approached (Gill, 1982). Wind stress and friction velocity were calculated using stability dependent coefficients as given by Smith, (1988). Heat flux data were computed using the equations given in chapter 3 and a 10 minute mean smoothing filter passed over the data in order to account for bursting turbulence in the atmosphere above the sea surface (Gill, 1982). This was also required for evaluating the bulk formulae for heat and momentum. Each parameterisation was then computed using data from the whole data set and compared to the 10 minute mean of measured ΔT.

6.3 Results.

Table 6.2 shows the calculated bias (observed ΔT minus parameterisation) and rms. differences for all of the models implemented.

Parameterisation	Bias °C	RMS
Hasse night	-0.713	0.724
Katsaros	-0.569	0.592
Saunders	-0.15	0.197
Eifler	-0.16	0.257
Soloviev and Schluessel 0-5 m/s wind	0.11	0.17
Soloviev and Schluessel 5-10 m/s wind	0.06	0.14
Soloviev and Schluessel 0-5 m/s wind	-0.17	0.426
Schluessel and Emery night time	-0.1	0.2
Schluessel and Emery day time	-0.59	0.61
Hasse day	-0.54	0.73

Table 6.2 Mean bias (measured - parameterisation) between measured ΔT and ΔT parameterisation.

It is clear from this table that compared to the JCR SST experiment observations there are considerable differences between each model. The Soloviev and Schluessel 0 - 5 m/s wind speed model (equation 3.11) produces the best mean estimate of ΔT and the Hasse night model (equation 3.10) the worst case.

Parameterisations developed for use in conditions of solar heating do not perform well at all; the Schluessel and Emery day time (equation 3.20) and the Hasse day time (equation 3.10). In all but two cases the parameterisation predict a greater negative ΔT than was actually observed.

In order to investigate the differences shown in table 6.2, scatter plots of observed ΔT versus ΔT parameterisation are shown in the following figures. In each case the observed and parameterised ΔT distribution is also shown and extreme values of < -2°C are ignored. To aid interpretation a perfect correspondence line is drawn on to each scatter plot.

6.3.1 Hasse Parameterisation of ΔT

Figure 6.1 (a) show the results obtained when implementing the Hasse night time only parameterisation (equation 3.10).

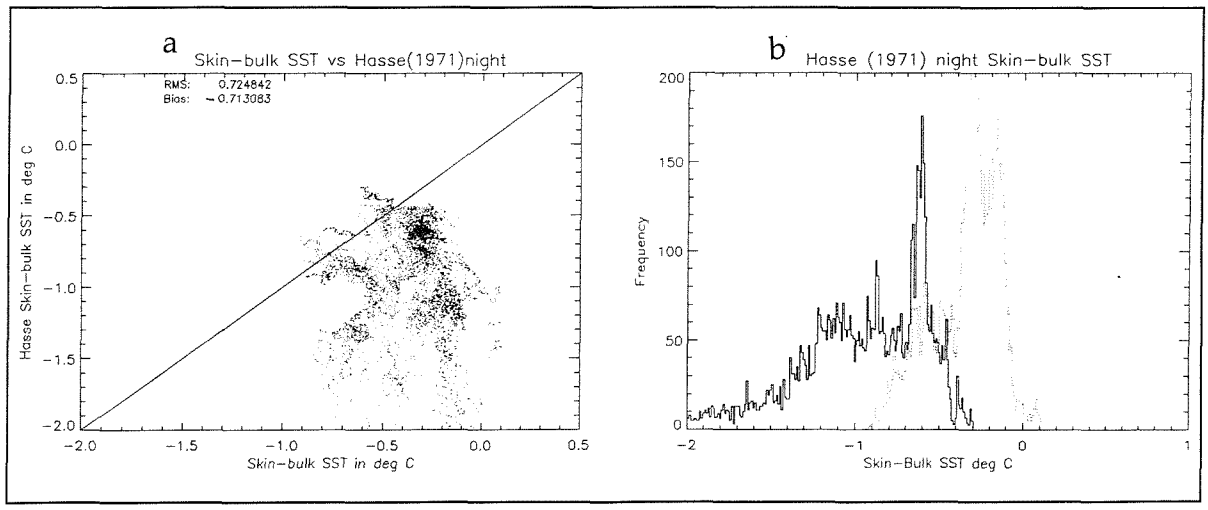

Figure 6.1 (a) Hasse (1971) night time only ΔT parameterisation and (b) the histogram of measured and parameter results. All data from the *James Clark Ross* are included according to table 6.1.

There is a large scatter in this plot which is due the changes in observed Q during cloudy conditions although the mean has a dense cluster. The model is essentially fine tuned by a set of coefficients which account for the depth at which the bulk temperature measure was made. Figure 6.1 (b) shows the distribution of the

Hasse ΔT calculation (shown as a solid line) and the observed ΔT (shown as a dotted line). There is a high degree of similarity in these distributions suggesting that the basic assumptions of the Hasse parameterisation are indeed correct but that the coefficients used to account for the depth of the bulk measurement are not. If the distribution were moved by ~0.6°C the model performs exceedingly well.

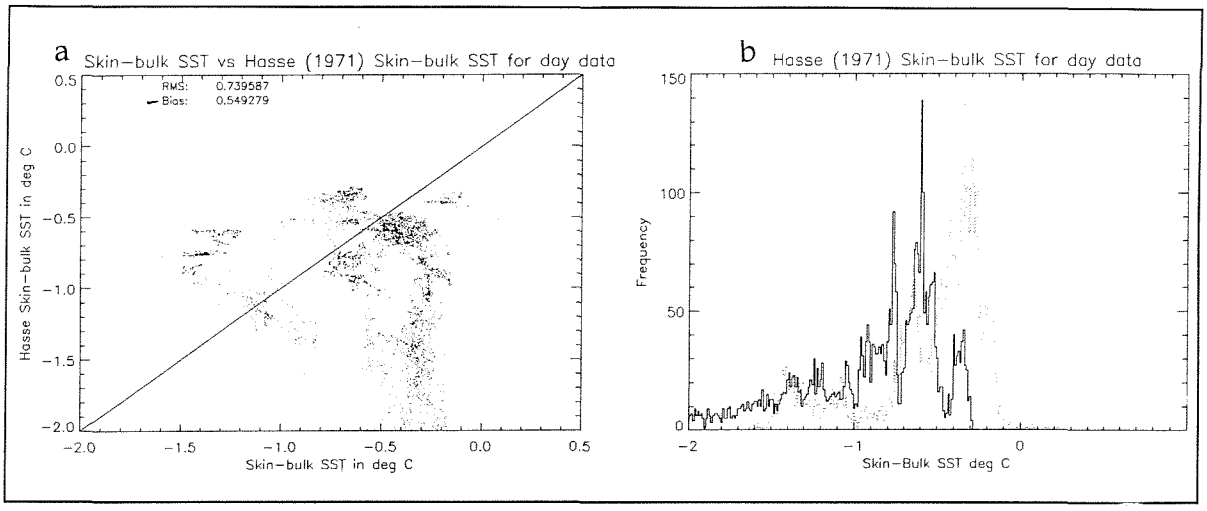

Figure 6.2 (a) Hasse (1971) day time only ΔT parameterisation and (b) the histogram of measured and parameter results. All data from the *James Clark Ross* are included according to table 6.1.

Figure 6.2 (a) shows the results from the Hasse day time parameterisation. There is a greater scatter in these data than for the night time case and again this will be due to rapidly changing values of Q. The parameterisation includes a term for the solar radiation and a steady state situation is assumed where all direct heating is transported by diffusive processes. Hence with scattered clouds producing large fluctuations in Q_S, it is not suprising that the observed data have such a high scatter. Figure 6.2 (b) shows the distribution of observed and parametised ΔT. As for figure 6.1 (b), the distribution of ΔT is very similar for both the observed and parametised case and if an offset of 0.6°C were added to the Hasse parameterisation there would be a substantial improvement in correspondence between these two data sets.

Using the JCR SST observations the Hasse parameterisation was re evaluated to determine the coefficients C_1 and C_2. Night time only data were used to evaluate C_1 which was then used to evaluate C_2 for the day time case. These coefficients were found to be C_1=4.75 and C_2=1.22 using the JCR data set and are plotted as figures 6.2B (a), (b) (c) and (d).

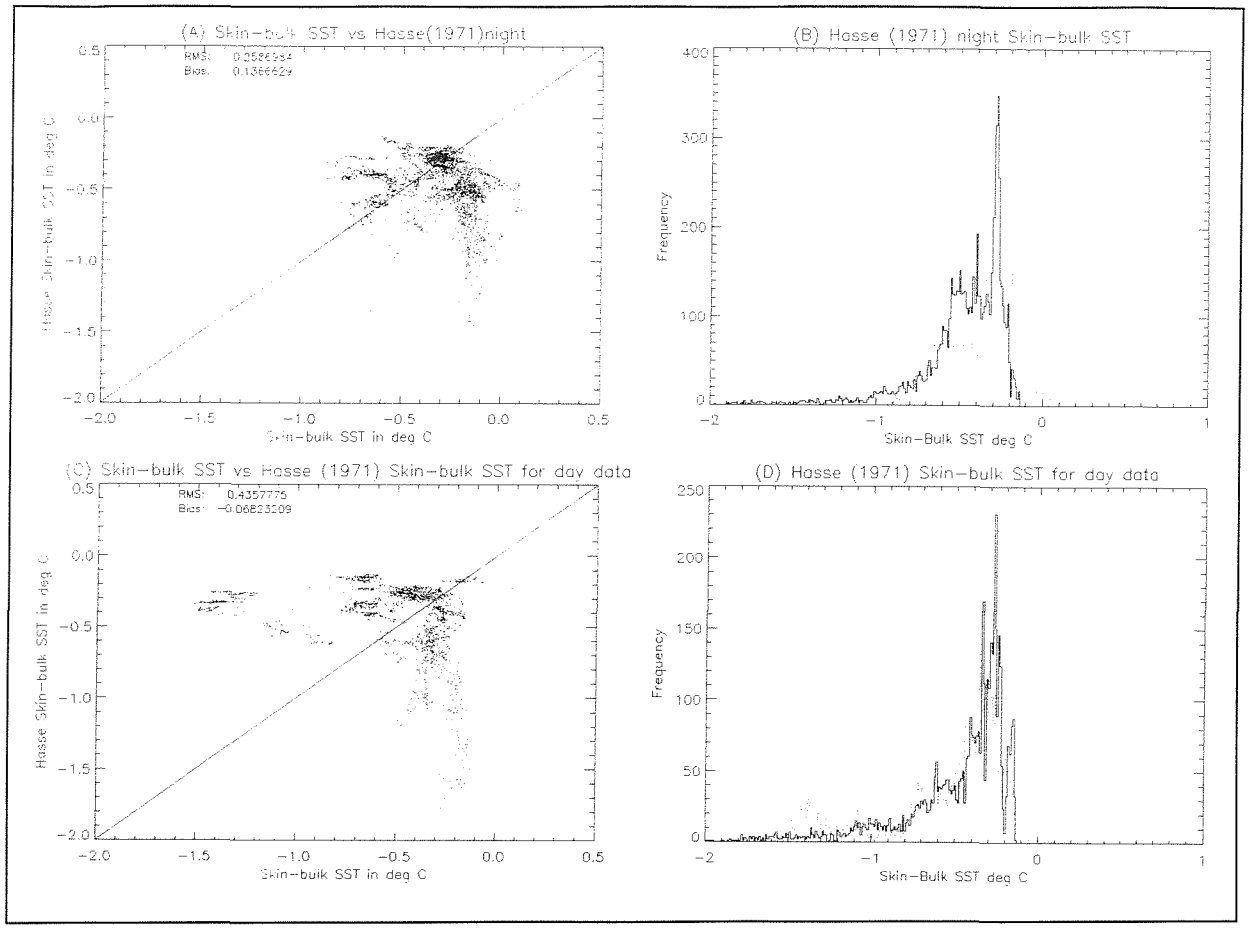

Figure 6.2B As for figures 6.1 and 6.2 using coefficients evaluated from the JCR data set.

6.3.2 Saunders parameterisation of ΔT

The Saunders parameterisation results are shown in figure 6.3 (a) and (b). For the mean case this model works well having a bias of 0.15°C. However the model fails to predict the lower ΔT values observed in the JCR data as all flux contributions are weighted by the same numerical constant λ (equation 3.7)

Values for λ have been computed by many authors (Paulson and Parker, 1972; Paulson and Simpson, 1981 and Coppin *et al* ,1991) and λ has been shown to have

a wind speed dependency. According to Grassl, (1976) λ takes values of 2.2 - 5.5 at wind speeds of 1.1 and 10 m/s using data from the tropical Atlantic. Schluessel *et al*, (1990) find a poor relation using these values and re-evaluate λ using data from the NE Atlantic finding a stronger wind speed dependence. λ in this case varied from 1.1 to 8.4 at wind speeds of 1 and 11 m/s respectively. The latter coefficients of Schluessel were used to compute the Saunders parameterisation shown here.

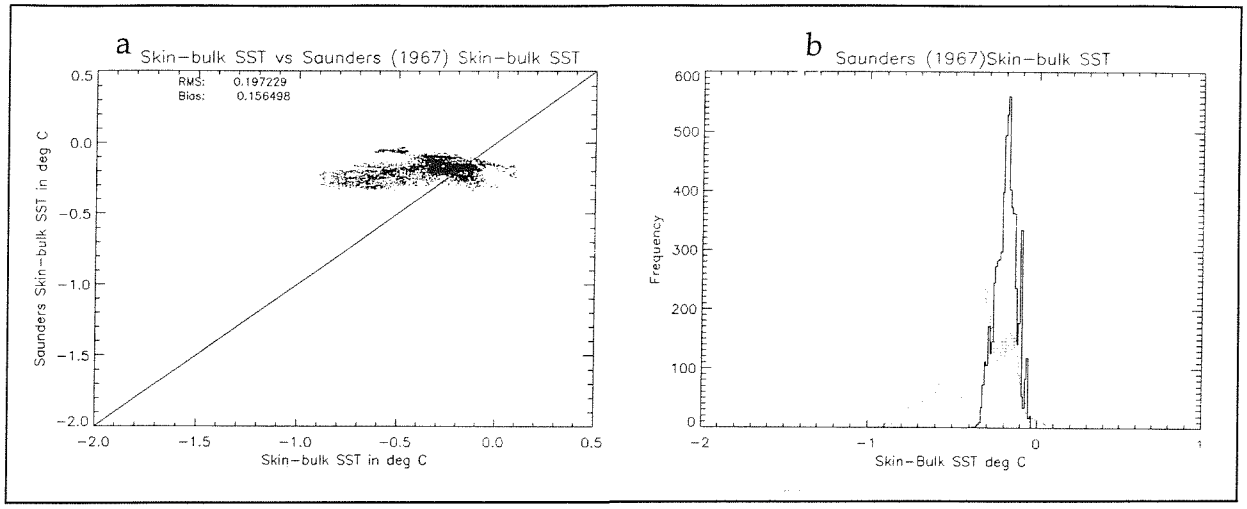

Figure 6.3 (a) Saunders (1969) day time only ΔT parameterisation and (b) the histogram of measured and parameter results. All data from the James Clark Ross are included according to table 6.1.

In order to investigate the wind speed dependency of the λ parameter, all data from the JCR experiment were used to re-evaluate λ using equation 3.8. The mean values of λ derived from the JCR SST experiment are given in table 6.3. The mean λ computed from the JCR SST experiment are in good agreement with those of Grassl (1976) showing that λ has a begins to reduce at the higher wind speeds. Grassl's λ begins to fall at wind speeds >9 m/s whereas the JCR λ begins to fall at wind speeds of > 8m/s.

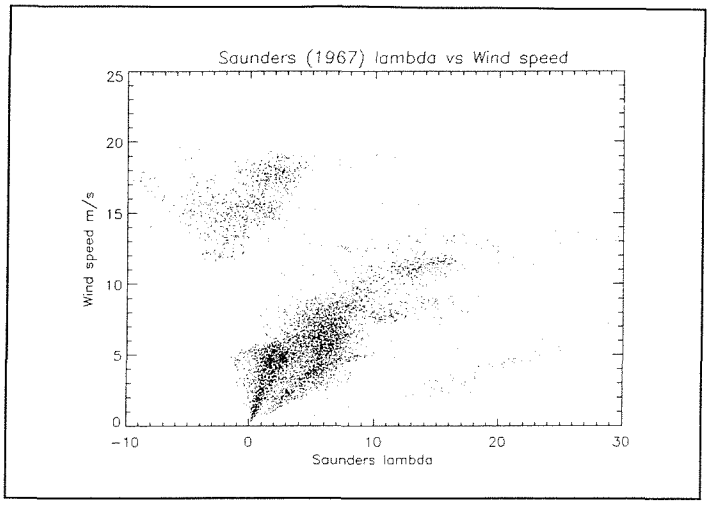

Figure 6.4 Saunders λ coefficient computed using all data from the *James Clark Ross* according to table 6.1.

Wind speed in m/	Saunders λ derived from Schluessel *et al* (1990)	Saunders λ derived form Grassl (1976)	Saunders λ derived from the JCR SST experiment	λ for u<12 m/s from the JCR SST experiment
1	1.1	2.1	0.83	0.87
2	2.2	2.9	1.8	1.7
3	2.2	3.3	2.56	3.4
4	2.0	3.9	2.73	4.3
5	2.9	4.5	4.78	4.4
6	4.0	4.8	5.42	4.7
7	4.5	5.3	6.31	6.2
8	4.7	5.5	6.91	7.1
9	5.9	5.8	5.86	8.3
10	8.0	5.5	5.85	9.8
11	8.4	5.3	5.79	10.9

Table 6.3 Saunders λ coefficient evaluated using the *James Clark Ross* data set.

However it is interesting to note that Grassl's data were computed using a Barnes PRT-5 radiometer and a similar stirred tank calibration to that of Schluessel *et al*, (1990) dismissing the possibility that differences in radiometer calibration are the cause of the different λ relationships shown here. The reduction of λ at high wind speeds is not seen in the data of Schluessel *et al* (1990). This may be due to a regional dependence of λ as the two data sets were collected from different regions; Schluessel's data in the mid latitudes where the turbulent fluxes of Q_L and Q_H will be more effective than in the tropics (Grassl's observations) where higher humidity values will limit their effectiveness in the determination of Q.

Changes in the emissivity characteristics of the sea surface at wind speeds > 10 - 12 m/s are clearly seen in figure 6.4 as a region of negative λ. However this figure is extremely helpful in explaining the differences found between Grassl's and Schluessel's data. If the negative λ data at wind speeds of 0 - 5 m/s are ignored in the determination of λ then the data from the JCR SST experiment agree well with those of Schluessel as shown in table 6.4. The λ values of Grassl may be in error due to the presence of negative λ at low wind speeds.

Figure 6.5 plots λ as a function of wind speed < 12 m/s for the entire *James Clark Ross* data set and figure 6.6 shows a three dimensional 'wire drape' visualisation of 6.5. In these plots it is clear that the relationships proposed by Grassl and Schluessel are both present. This suggests that the λ coefficient has a regional dependency and may offer a solution for a regional ΔT correction to satellite SST observations.

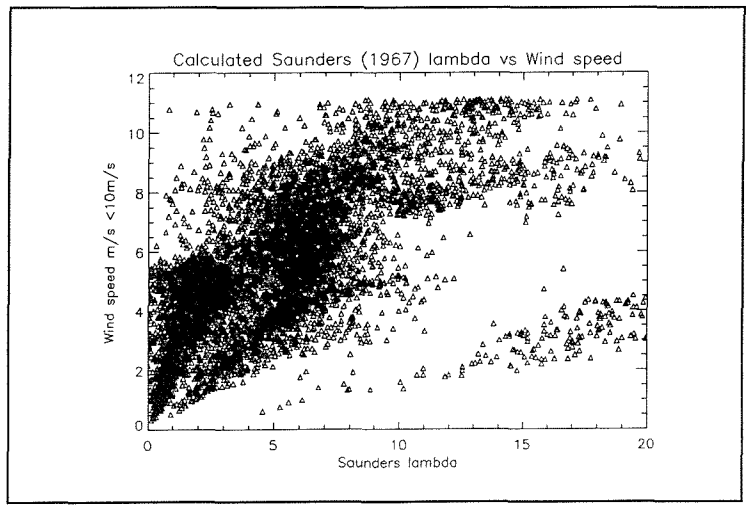

Figure 6.5. Recalculated Saunders λ coefficient for wind speeds < 12 m/s using the *James Clark Ross* data set.

The implications of these plots are that the Saunders model functions well and that the λ coefficient needs to be evaluated for a set of regions in order to describe a global distribution of ΔT.

However there are limitations to this parameterisation during light winds as discussed by Coppin *et al* (1991) and indeed Saunders himself claims that this model is flawed during such conditions (Saunders, 1973). This is due to the dominance of surface tension effects controlling the gravitational instabilities associated with the free convection regime which are not accounted for in this parameterisation.

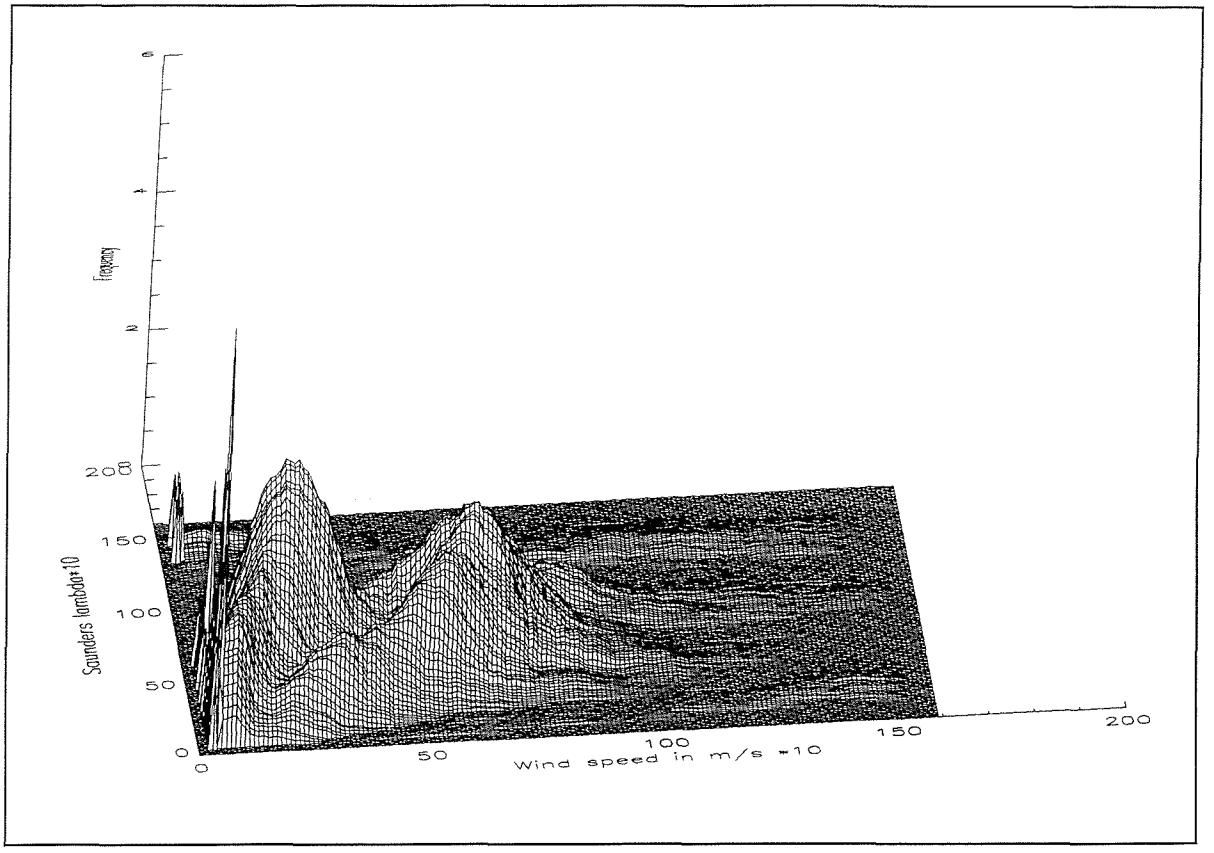

Figure 6.6 Three dimensional visualisation of figure 6.5. Note that both the wind speed and λ are multiplied by 10 in this plot and a smoothing filter of kernel size 3 x 3 has been applied to the data.

6.3.3 Linear regression parameterisation of ΔT

Schluessel *et al* (1990) use the technique of stepwise multiple regression working from equation 3.10. This type of approach has great potential as the data used in the regression were all of standard meteorological parameters measured routinely from ships. Table 6.2 shows that the night time parameterisation (equation 3.19) works well yielding a mean of 0.1°C. However this is not the case for the day time equation (equation 3.20). Figure 6.7 (a), (b), (c) and (d) show the scatter plots and

histograms derived from this parameterisation using the JCR SST data. In both the day and night case there is a large scatter as indicated in table 6.2 by the large rms. values.

Considering the night time case, figure 6.7 (a) shows two clusters of data. One cluster is in good agreement with the JCR SST data but the parameterisation tends to over estimate the ΔT shown as a second more negative cluster. The ΔT histogram shown in figure 6.7 (b) gives a clearer view of this feature.

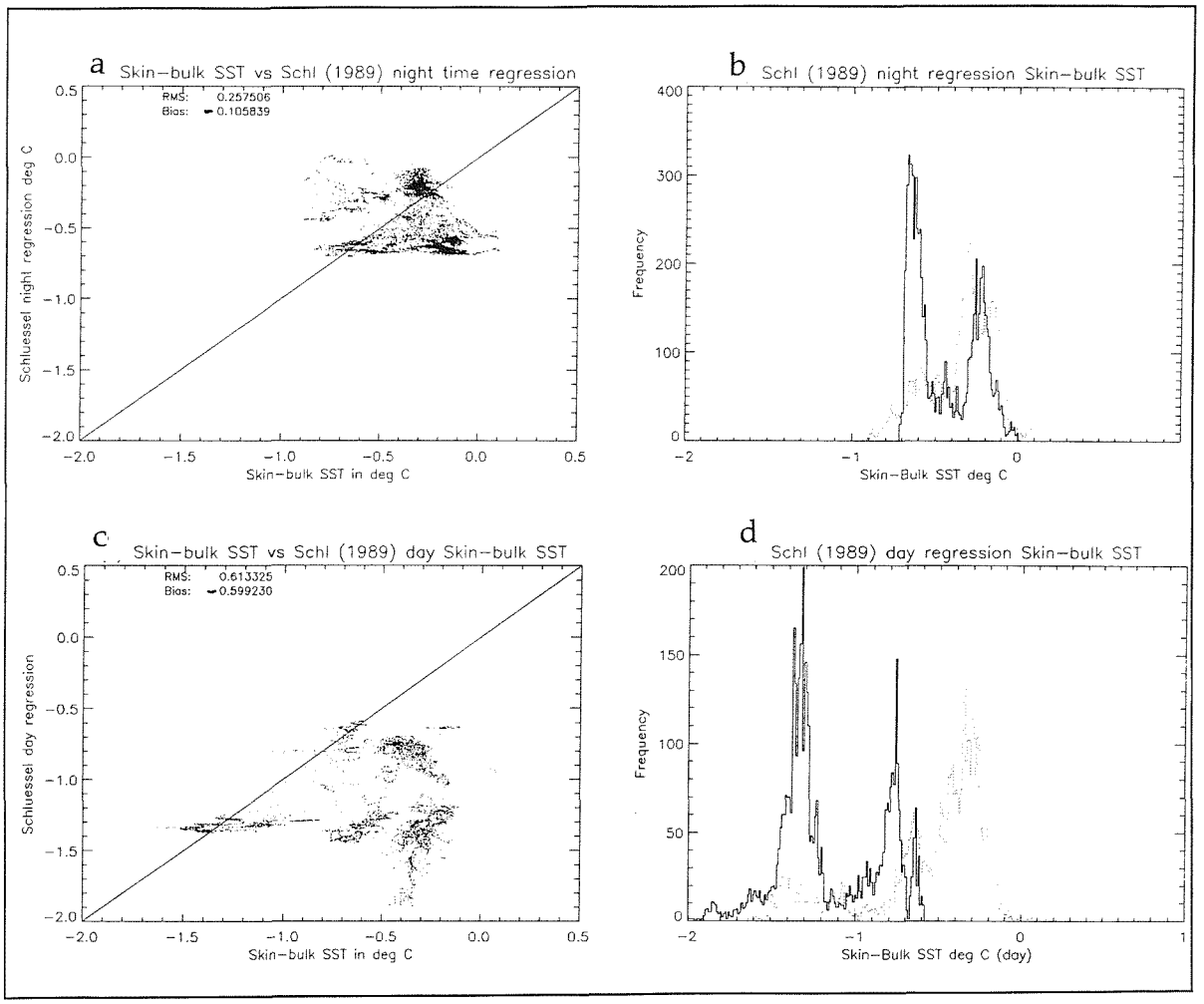

Figure 6.7 (a) Scatter plot of the Schluessel *et al* night time regression and (b) histogram of observed ΔT and parametised ΔT. (c) and (d) show the results of the Schluessel *et al* day time regression parameterisation.

Considering figures 6.7 (c) and (d), the distribution of ΔT predicted by this parameterisation is clearly over estimating ΔT. There is also a much greater scatter in these data than for the night time case. This will be due to the variability in the Q_S term in the Q equation as a consequence of clouds. However it is

important to note that this parameterisation is able to handle the extreme negative ΔT of -1.5°C. As in the night time case there are two clusters of data which indicate that the parameterisation works better for a particular set of atmosphere - ocean conditions.

6.3.4 Surface renewal parameterisations of ΔT.

As historical research into the turbulent conditions occurring at a rigid wall boundary developed it became clear that turbulence did not did not give way to laminar flow (as supposed by Prandl, 1948). In fact it has been shown that relatively large instantaneous velocities can be found as a rigid boundary is approached (Neddermann, 1960). The possibility of surface renewal processes defining the cool skin of the ocean was observed by Katsaros (1977) who used Schleiren photography to image descending sheets of water from the surface of a large laboratory tank. Surface renewal theory describes the movement of single elements of water which are exposed to the atmosphere at the surface of the ocean. Here each element is cooled and at a statistically determined time a sheet of cool water becomes gravitationally unstable and is subducted back into the water mass beneath. Surface renewal models are reviewed in chapter 3.

In this work two parameterisations were examined, that proposed by Soloviev and Schluessel (1994) and that of Eifler (1992). These models essentially differ only in the choice of surface renewal interval. In the case of the Soloviev and Schluessel model, three different wind speed regimes are considered;

1. Calm and low wind speeds of up to and including 5 m/s winds. In this regime cyclic injections of cooled surface water are considered convective in form(Foster, 1971)

2. Moderate wind speeds of 5 - 10 m/s. In this wind regime surface renewal is thought to be via viscous surface stress variations associated with rolling waves on breaking wavelets (Csanady, 1990).

3. High wind speeds of > 10 m/s where long surface waves break. In this regime the time scale of renewal is related to the friction velocity and gravitational instabilities.

As the radiometric SST data at wind speeds of > 10m/s are thought to be in error, the high wind speed model has not been shown and the convective regime will be considered in section 6.3.5 below

Figure 6.8 (a) and (b) show the results obtained from the Soloviev and Schluessel 5-10 m/s parameterisation. This parameterisation of ΔT seems to work well for the mean case but fails to account for the large negative ΔT present in the JCR SST data. Figure 6.8 (b) demonstrates this very clearly as the histograms are well registered for the mean case. The rms. and bias values for this model show it to be the best estimator of the JCR SST ΔT overall. However it should be remembered here that the agreement is for a limited wind regime only.

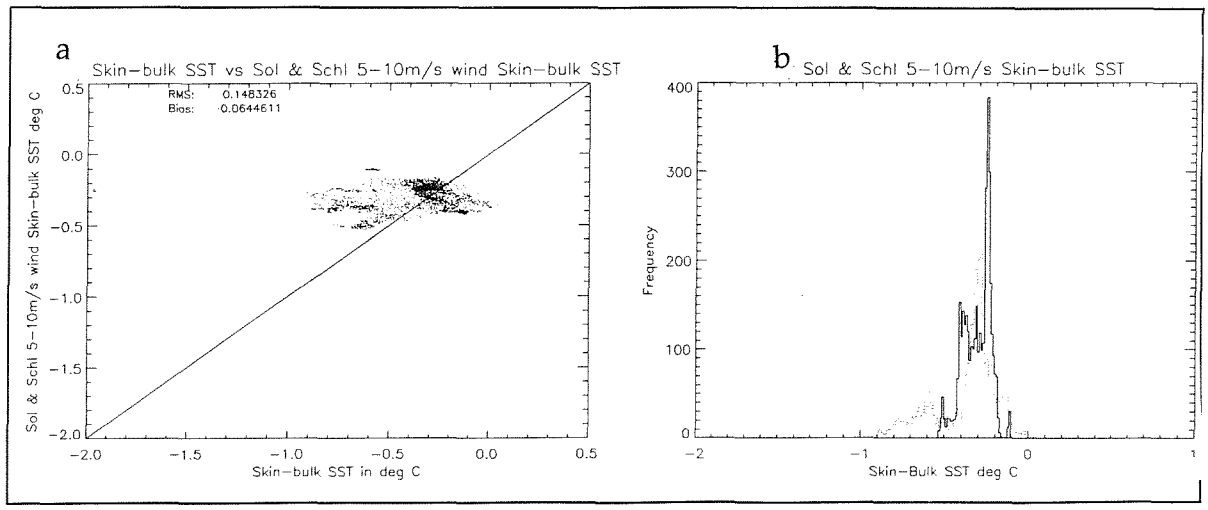

Figure 6.8 Results from the Soloviev and Schluessel 5 -10 m/s wind regime surface renewal model. (a) Observed ΔT plotted against the parameterisation and (b) distribution of observed and parametised. Observed data are shown with the dotted line.

Eifler (1992) builds on the work of Nijsing(1969) and modifies his boundary-layer growth-breakdown model to predict ΔT (equation 3.13). It is assumed that surface renewal is related to the burst and sweep phenomena occurring on the lee and

forward sides of wind waves and using the visual observations of Kawamura and Toba, (1988) the time of surface renewal is related to the dominant wind wave length. A wavelength of 0.03 m is assumed based on the measurements of Okunda *et al* (1971) and the assumption is made that young new waves should dominate the typical momentum, heat and mass transfer occuring at the air - sea interface. These waves are thought to be independent of the wind speed and therefore have a constant average wavelength (Eifler, 1992).

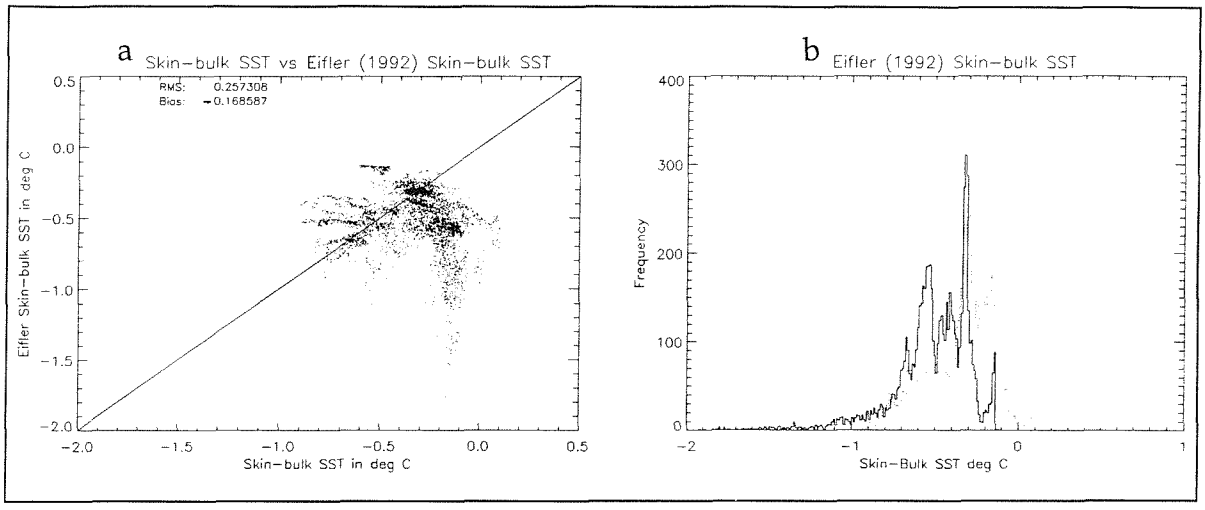

Figure 6.9 Results from the Eifler (1992) surface renewal model. (a) Observed ΔT plotted against the parameterisation and (b) distribution of observed and parametised. Observed data are shown with the dotted line.

Figure 6.9 (a) shows observed ΔT plotted against parameterised ΔT. This model is clearly able to handle a broad range of environmental conditions, making this the best 'general' purpose parameterisation (table 6.1). Considering the broad range of conditions encountered during the JCR SST experiment, this model functions extremely well.

6.3.5 Convective parameterisation of ΔT.

Figures 6.10 (a) and (b) show the results from the Soloviev and Schluessel convective surface renewal model (equation 3.11). From these figures it is clear that the model is unable to handle the range of ΔT found under light wind conditions. Changes in the net heat flux due to clouds at night will result in a

modified Q_T and under light wind conditions the response time of the ocean skin is rapid (Chapter 5). This parameterisation appears to fail under such conditions.

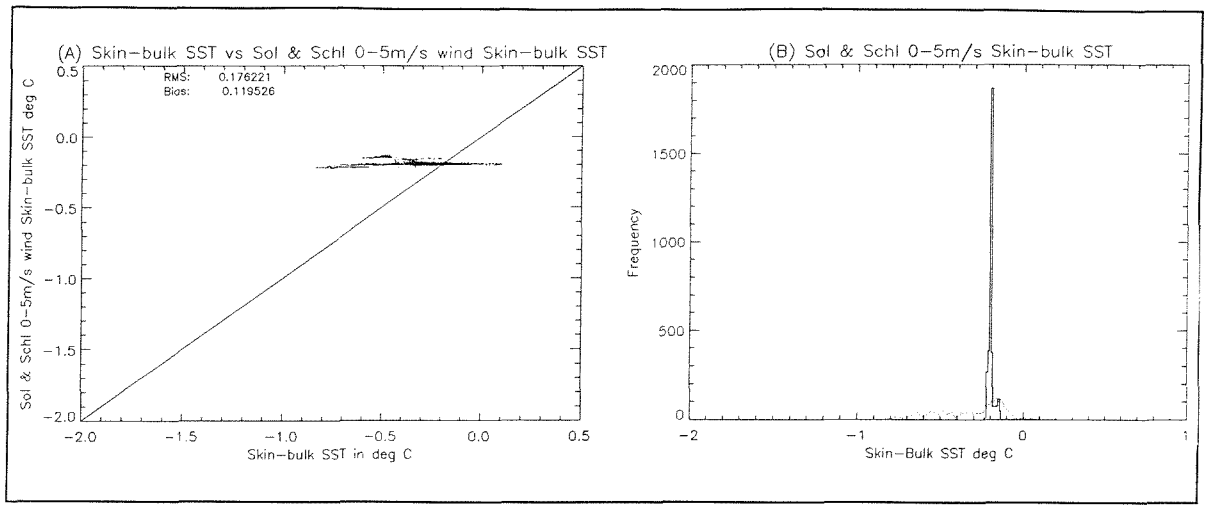

Figure 6.10 Results from the Soloviev and Schluessel convective regime surface renewal model. (a) Observed ΔT plotted against the parameterisation and (b) distribution of observed and parametised. Observed data are shown with the dotted line.

Conversely, the parameterisation of Katsaros *et al*, (1977) shown in figure 6.2 demonstrates that this parameterisation (equation 3.8) shows greater variation but has a large bias.. Katsaros *et al*, (1977) derive the non-dimenttional coefficient used in this model A=0.156, from laboratory measurements which in this case does not seem to be appropriate. As free convection is not a prevalent condition in the open ocean this model is of limited application.

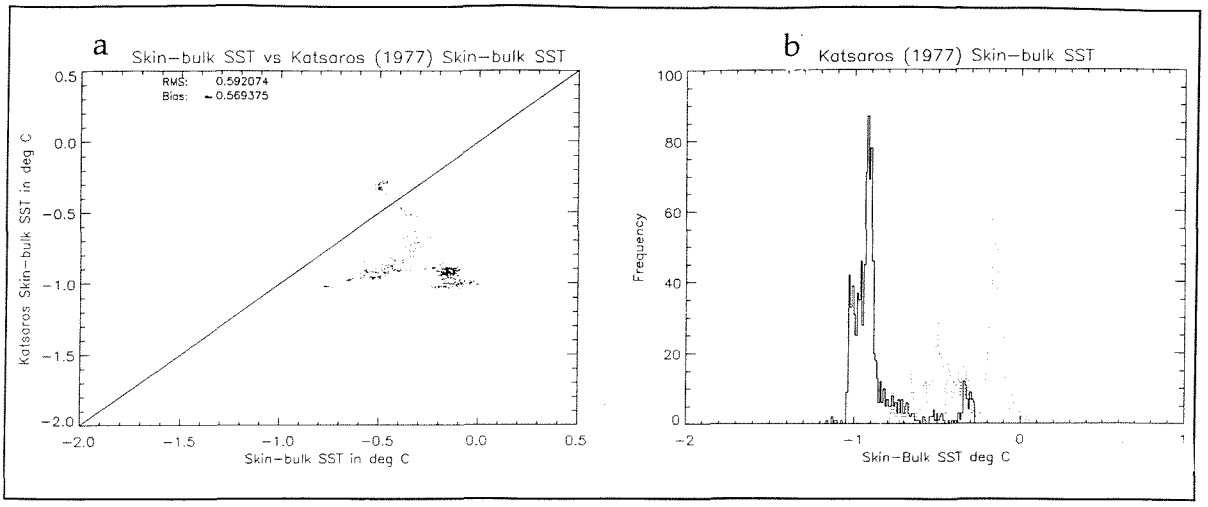

Figure 6.11 Results from the Katsaros *et al* (1977)convective regime surface tension model. (a) Observed ΔT plotted against the parameterisation and (b) distribution of observed and parametised. Observed data are shown with the dotted line.

6.4 Conclusions.

The results presented above indicate that there is considerable variation in performance between the current ΔT parameterisation schemes. By using the data collected from the JCR SST experiment, several important features have been identified:

1. That many of the parameterisations use an input of real data in their derivation. This has the effect of biasing the equations to a particular region or situation in which the data were collected. In the comparisons above, the Saunders model and regression models of Schluessel *et al* show good examples of this type of behaviour. This is an important feature of these parameterisations which can be used to regionalise a ΔT correction applied to satellite data.

The computed values of λ given by both Grassl (1971) and Schluessel *et al* (1990) are shown to be consistent with different parts of the JCR dataset and demonstrate a regional dependence of λ. A new set of λ coefficients have been computed using the JCR SST experiment data which should be representative of ΔT for the Atlantic ocean in general as tropical, sub-tropical and higher latitude regions are included in the derivation.

Although such parameterisations appear at first as a panacea, there are limitations. A case in question is the ability of the Saunders style models to properly account for ΔT during light winds. Here the convective regime is entered. The two convective models evaluated do not appear to predict ΔT well although small bias and rms. values are derived. In the case of the model proposed by Katsaros (1977) this may be due to an inappropriate value of the nondimensional coefficient A, as this was derived from laboratory measurements.

The best 'all round' parameterisation are those constrained to a set of definite wind speed conditions. A case in question is that of the Soloviev and Schluesel 5-10 m/s parameterisation. This model is statistically the most accurate predictor of ΔT. A more general application model is that proposed by Eifler (1992).

The parameterisations which include a term for solar radiation show that the high variability of the net heat flux is difficult to account for. The parameterisation of Hasse (1971) for instance is not able to handle such variations.

The coefficients of the Hasse (1971) formulae have been re-evaluated using the JCR SST data. Using a bulk SST measure at a depth of 5.5m the new coefficients are:

$$\mathbf{C_1=4.75} \qquad \textbf{and} \qquad \mathbf{C_2=1.22}$$

The discussion of surface renewal models highlights the need for firm evidence that such processes are controlling ΔT in the open ocean. One possible technique would be the use of thermal imagers to monitor the sea surface. Such a set of measurements made under different sea states may help to fine tune the current surface renewal models.

Chapter 7. A comparison between the ATSR Average Sea Surface Temperature (ASST) product and the JCR SST experiment SST data.

This Chapter compares the data collected from the RRS *James Clark Ross* to near simoultaneous ATSR ASST satellite observations.

7.1 The Along Track Scanning Radiometer

The ATSR radiometer was launched as part of the payload of the ERS-1 satellite in 1991 and is well described by Edwards *et al* (1990). In summary, ATSR is a 4 channel infra red radiometer (co-registered wavebands centered at 1.6, 3.7, 10.8 and 12.0 μm) and has been designed to retrieve global SST to an accuracy of better than 0.3 K. To achieve this goal the radiometer uses cooled HgCdTe and InSb detector elements (reducing instrumental noise) and continuous calibration against two stable high precision black body cavities. The unique feature of this instrument is its exploitation of a technique called 'along-track-scanning' to provide a further improvement in the accuracy of SST retrievals (Mutlow *et al*, in press). Figure 7.1 (a) shows a schematic of the along track scanning principle.

The ATSR uses an inclined rotating scan mirror to conically view the earth's surface in two curved swaths 500 km wide and separated by ~ 900 km shown in figure 1.7 (b). This gives a nadir view and a forward view in which a nominal instantaneous field of view (IFOV) is 1 km^2 at the central nadir IFOV and 1.5 x 2 km^2 for the central forward IFOV. SST retrieval is based on the algorithms proposed by McClain (1985) which are discussed in Chapter 2. However as the atmospheric path length is approximately doubled for the 55° zenith of the forward view, by comparing the forward and nadir views the atmospheric effect on the infra-red signal received by ATSR is directly measured. For each IFOV an improved atmospheric correction is thus possible (Saunders, 1969). Further improvements are possible if data from the Microwave sounder (MWS) are included in the ATSR SST retrieval scheme. The latter is an ongoing area of research (Mutlow *et al*, in press).

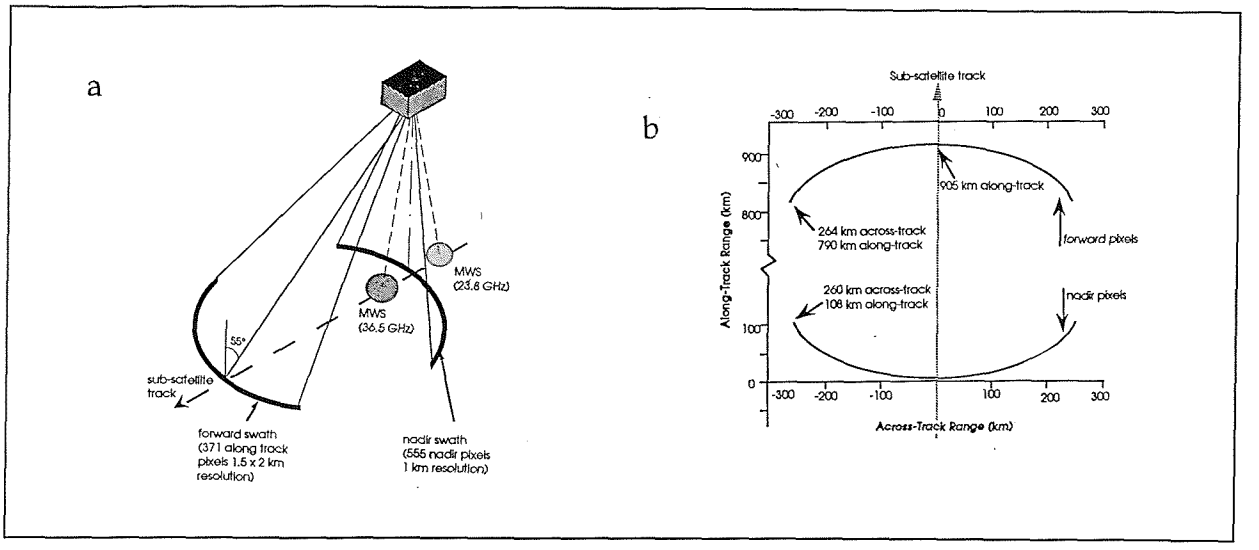

Figure 7.1 A schematic diagram describing (a) the geometry of the ATSR instrument and (b) ATSR scans projected onto the earth's surface. From Vass and Handoll, 1991.

7.2 Average SST (ASST) from the ATSR instrument

The primary product of the ATSR system (see Baily, 1994) is a high precision spatially averaged SST (ASST) measure with an accuracy of <0.3 K. This is designed for use in global climate research. Tha ASST is derived from a 50x50 km (½° latitude x longitude geocentric grid) mean SST of the high resolution data after stringent cloud clearing algorithms have been applied. The geocentric co-ordinate system used for these data is given in figure 7.2

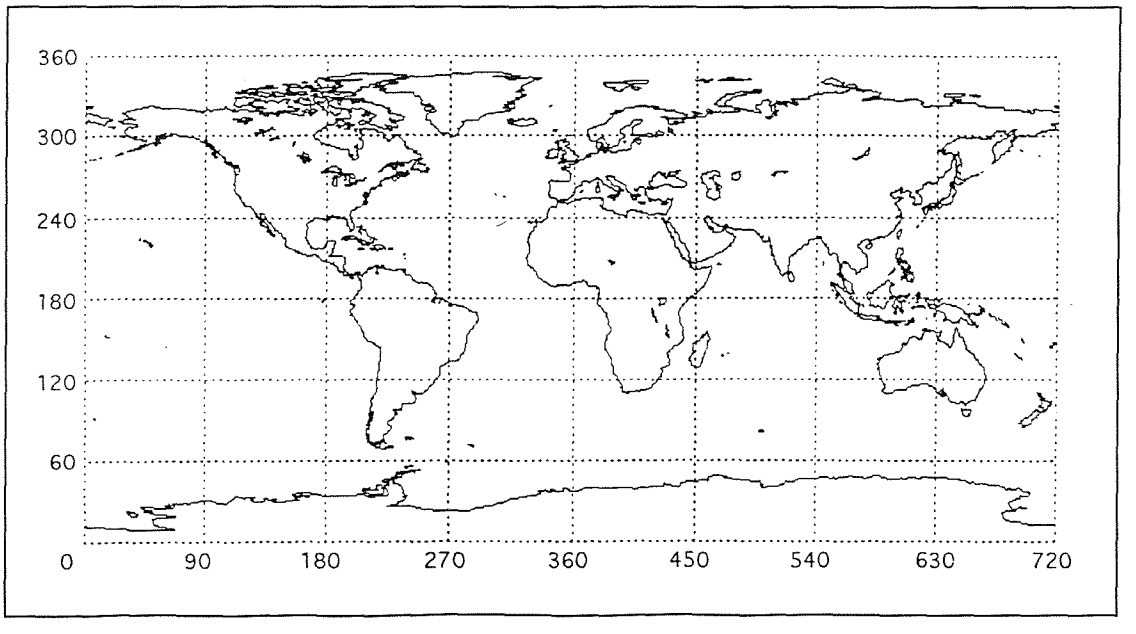

Figure 7.2 The geocentric co-ordinate system used for the ATSR ASST SST data. From Panter, 1994.

7.3 Comparison methodology

To assess the effect of ΔT variability within ASST data the entire *James Clark Ross* data set was re-sampled to a resolution identical to that of the ATSR ASST product described above. This resulted in a total of 99 ½° latitude/longitude geocentric cells.

SADIST v400 (Synthesis of ATSR Data Into Sea surface Temperature, Baily, 1994) ASST data for a period of ±48 hours either side of the ships position were supplied by the Rutherford Appleton Laboratories and the relevant data co-incident with the passage of the *James Clark Ross* were extracted. Comparisons with the *in-situ* data were made for the nadir only SST, dual look SST and mixed SST ASST products. It is recognised here that the co-incedence criteria required for validation (Minnet, 1990) of the ASST product have not been adhered to. However the purpose of this comparison is to investigate deviations from the monthly mean SST. It must be remembered that to validate the ASST product requires a certain amount of relaxation in the validation criteria to ensure that an *in-situ* SST representative of the spatial average is collected. Forrester *et al* (1993) used 10, 24 and 48 hours as a coincidence criteria in the Iceland Faeroes frontal region and found higher correlations at the longer temporal scale.

7.4 Results

Figure 7.3 (a) to (f) show the results obtained from this comparison. In this diagram skin - ATSR comparisons are shown to the left of the figure (5.28 (a), (c) and (e)) and comparisons with the bulk SST at 5.5 m are shown on the right (5.28 (b), (d) and (f)). In all mean cases the ASST product is cooler than the *in-situ* data and the majority of the scatter is at the warmer temperatures corresponding to the tropical regions. Considering that there is a large temporal difference between the *in-situ* and satellite observations the mean bias and rms. figures are extremely encouraging. Certainly when compared with the *James Clark Ross* radiometric *in-situ* observations the ATSR ASST product is clearly within its design accuracy of <0.3 K. As expected, the improved atmospheric correction made by the dual look

algorithm results in a smaller bias and rms. value compared to the nadir only algorithm.

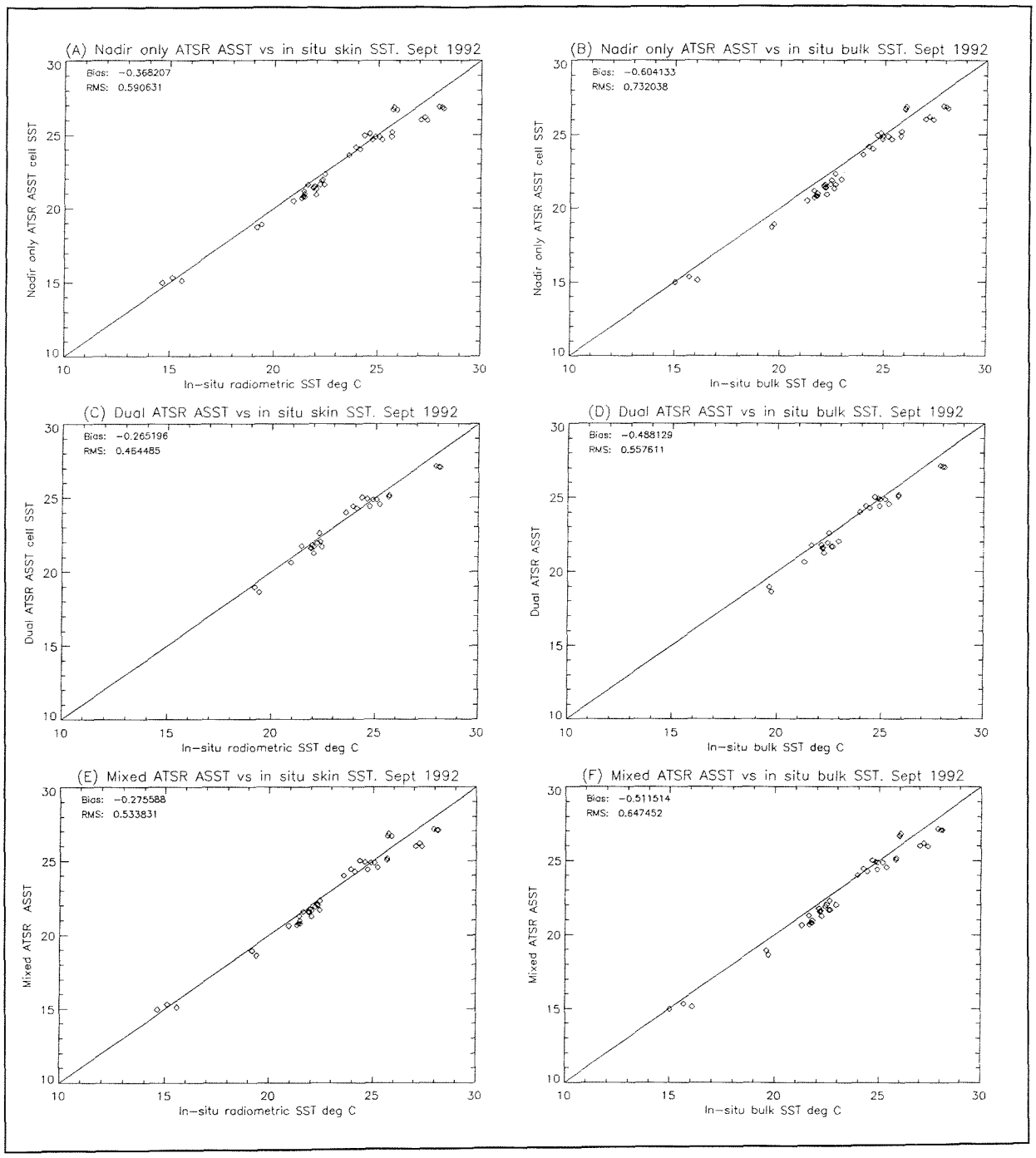

Figure 7.3 (a) ATSR nadir only ASST plotted against *in-situ* radiometric SST, (b) ATSR nadir only ASST plotted Vs *in-situ* bulk SST, (c) ATSR dual ASST plotted against *in-situ* skin SST, (d) ATSR dual ASST plotted against *in-situ* bulk SST, (e) ATSR mixed ASST plotted against *in-situ* skin SST and (f) ATSR mixed ASST plotted against *in-situ* bulk SST. Bulk SST is taken at 5.5 m and the temporal coincidence is ± 48 hrs.

In order to investigate the scatter of the collocated ASST and *in-situ* data measured during the *James Clark Ross* experiment these parameters were plotted as a function of ASST latitude cell number. Figure 7.4 shows the mean wind speed calculated for each ASST cell used here.

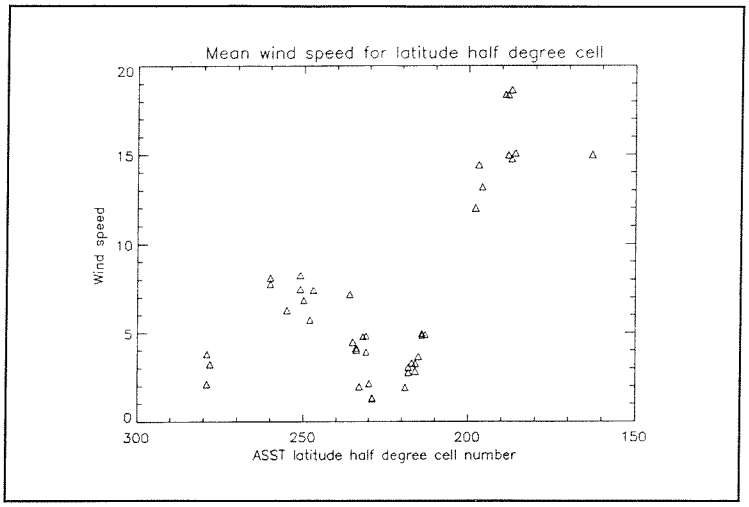

Figure 7.4 Mean *in-situ* wind speed plotted as a function of ATSR ASST latitude cell number.

Clearly there are extremely strong winds of up to 20 m/s in these data. At these wind speeds the radiometric SST becomes unreliable and any comparison with the ATSR unwise (Chapter 5). If the differences are attributed to emissivity changes which are assumed to be sufficient in magnitude to corrupt the ATSR measurement this can be examined by comparing ASST data to the *in-situ* bulk SST. Preferably the ASST dual look algorithm should be used as the high wind regime encountered in the JCR SST experiment was in the equatorial regions where humidity is high. However this was not possible as only the nadir SST has been returned from the ATSR in these cases which is probably due to the increased effect of a high sea state modifying the surface emissivity which is greater at large zenith angles (Masuda *et al,* 1988). At high wind speeds the latent and sensible heat flux components of the net heat flux will be high and under clear sky conditions the terrestrial flux out of the ocean will also be high. This should generate an extremely cool skin (although perhaps undetected *in-situ* due to the corruption of the radiometric SST). Figure 7.5 (a) shows the mean net heat flux Q plotted for each ASST latitude cell and figure 7.5 (b) shows the calculated ΔT

where ΔT is ATSR ASST - *in-situ* bulk SST. Comparing figure 7.4 with 7.5 (b) it is clear that all of the positive ΔT data are associated with high wind speeds.

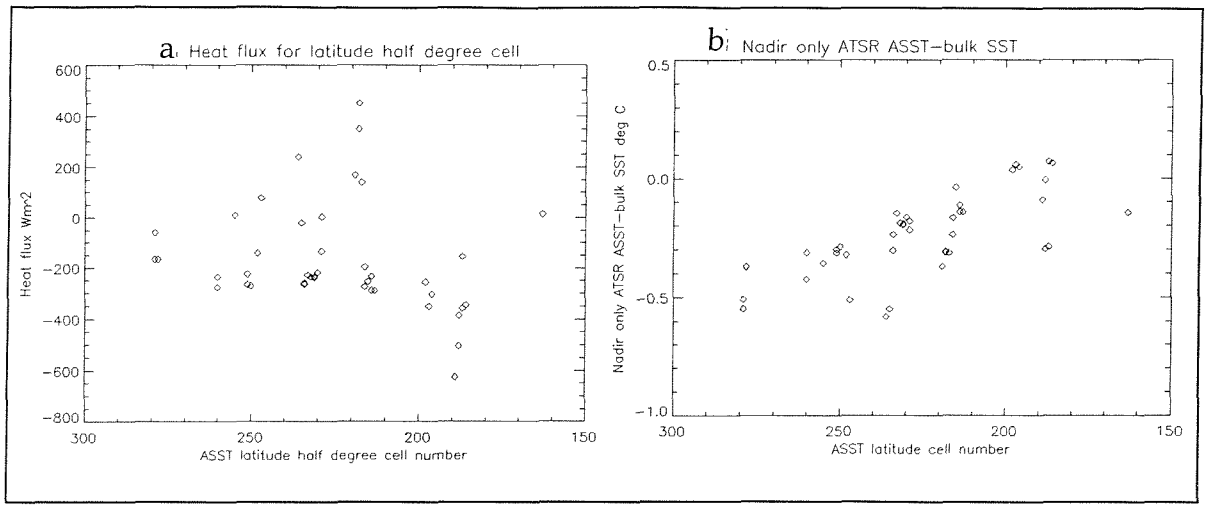

Figure 7.5 (a) Net heat flux Q plotted as a function of ATSR ASST latitude cell and (b) nadir only ASST -*in-situ* bulk SST (ΔT) plotted as a function of ATSR ASST latitude cell number.

Figure 7.5 (a) confirms that a large negative heat flux is present during the high wind events which should result in a negative ΔT which is not seen in ΔT (7.5 (b). The ΔT calculated from ATSR ASST for wind speeds > 13 m/s are positive and these results suggest that the ATSR data may also be corrupted by high sea state conditions modifying the emissivity characteristics of the ocean surface. It is difficult to be too confident in these latter statements as the simple analysis presented here is limited by the temporal differences between the *in-situ* and ATSR data.

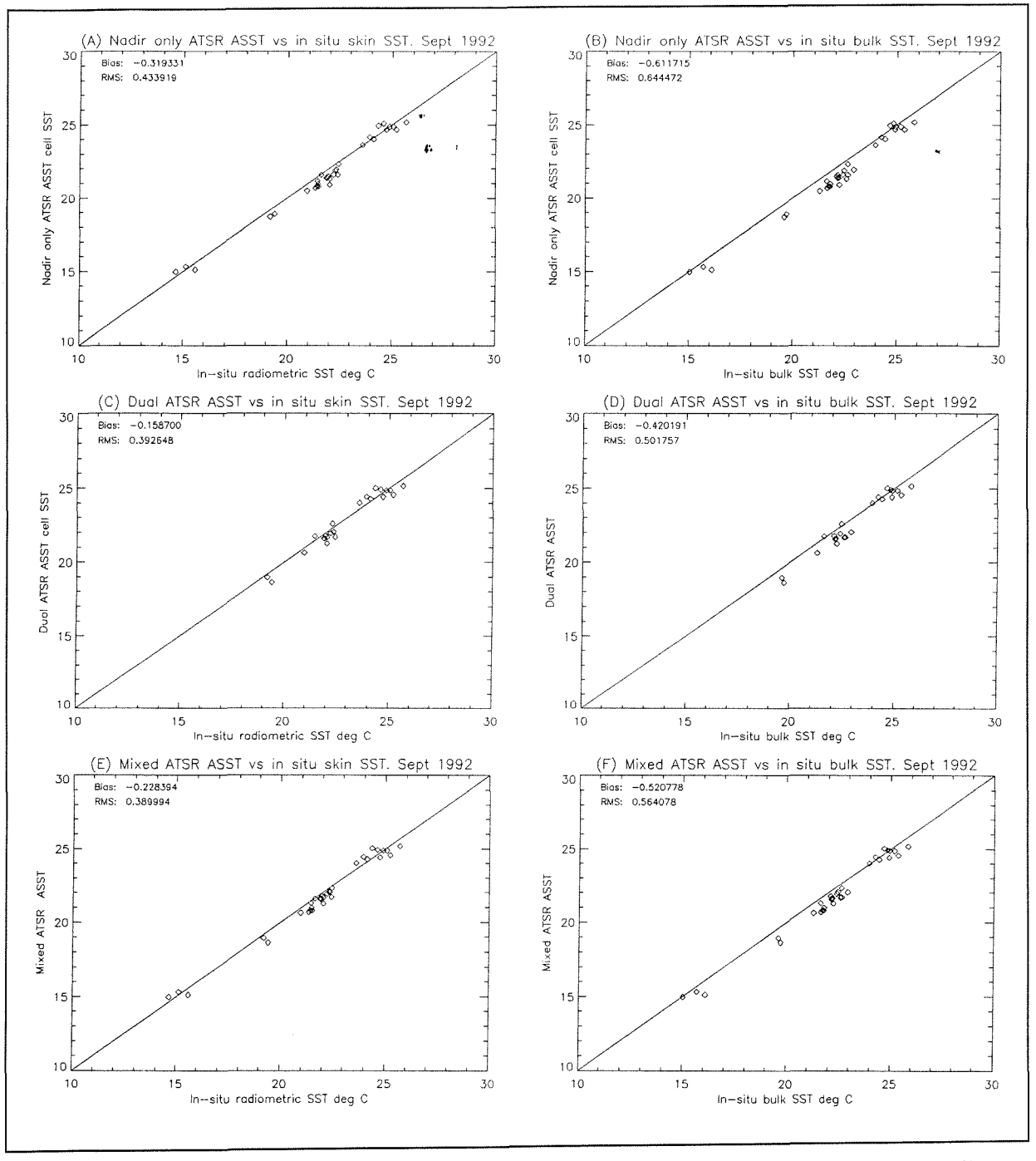

Figure 7.6 (a) ATSR nadir only ASST plotted against *in-situ* radiometric SST, (b) ATSR nadir only ASST plotted Vs *in-situ* bulk SST, (c) ATSR dual ASST plotted against *in-situ* skin SST, (d) ATSR dual ASST plotted against *in-situ* bulk SST, (e) ATSR mixed ASST plotted against *in-situ* skin SST and (f) ATSR mixed ASST plotted against *in-situ* bulk SST. Bulk SST is taken at 5.5 m and the temporal coincidence is ± 48 hrs and high wind conditions > 13m/s have been rejected.

However, if collocations at wind speeds of > 10 m/s (the wind speed defined by the Beaufort force for long wave breaking) are rejected both the bias and the rms.

differences between ATSR ASST and *in-situ* data is improved as shown in figure 7.6. The bias and rms. difference for the dual look algorithm now have values of -- 0.16 K and -0.39 respectively although only a slight decrease is found in the nadir only case. Note that little improvement in the bulk comparisons is seen.

Confining the discussion of collocated ATSR and *in-situ* data to the low wind regime, figure 7.7 plots the mean ΔT computed for the *in-situ* and ATSR ASST data and Table 7.1 gives the mean of ΔT for each case.

Computation	Mean K
In-situ skin - bulk	-0.29
Nadir ASST - bulk	-0.30
Dual ASST - bulk	-0.28
Mixed ASST- bulk	-0.29

Table 7.1 Mean ΔT calculated from all ASST cells with wind speeds < 10 m/s.

All of these data give a similar ΔT value in the mean but figure 7.7 indicates that ΔT decreases towards the tropical regions (the equator has an ASST cell number of 179.5). This is in contradiction to the mean ΔT maps produced by Robertson and Watson (1993) shown in figure 5.24. Under moderate wind conditions of 0 -10 m/s and clear sky conditions this phenomenon could be explained by the increase in humidity associated with the tropical regions. As discussed previously high humidity will reduce the effectiveness of the latent heat flux removing heat from the surface layers. The dominant cooling of the sea surface will be via the terrestrial heat flux which in the tropical regions will be reduced due to the higher atmospheric water vapour load.

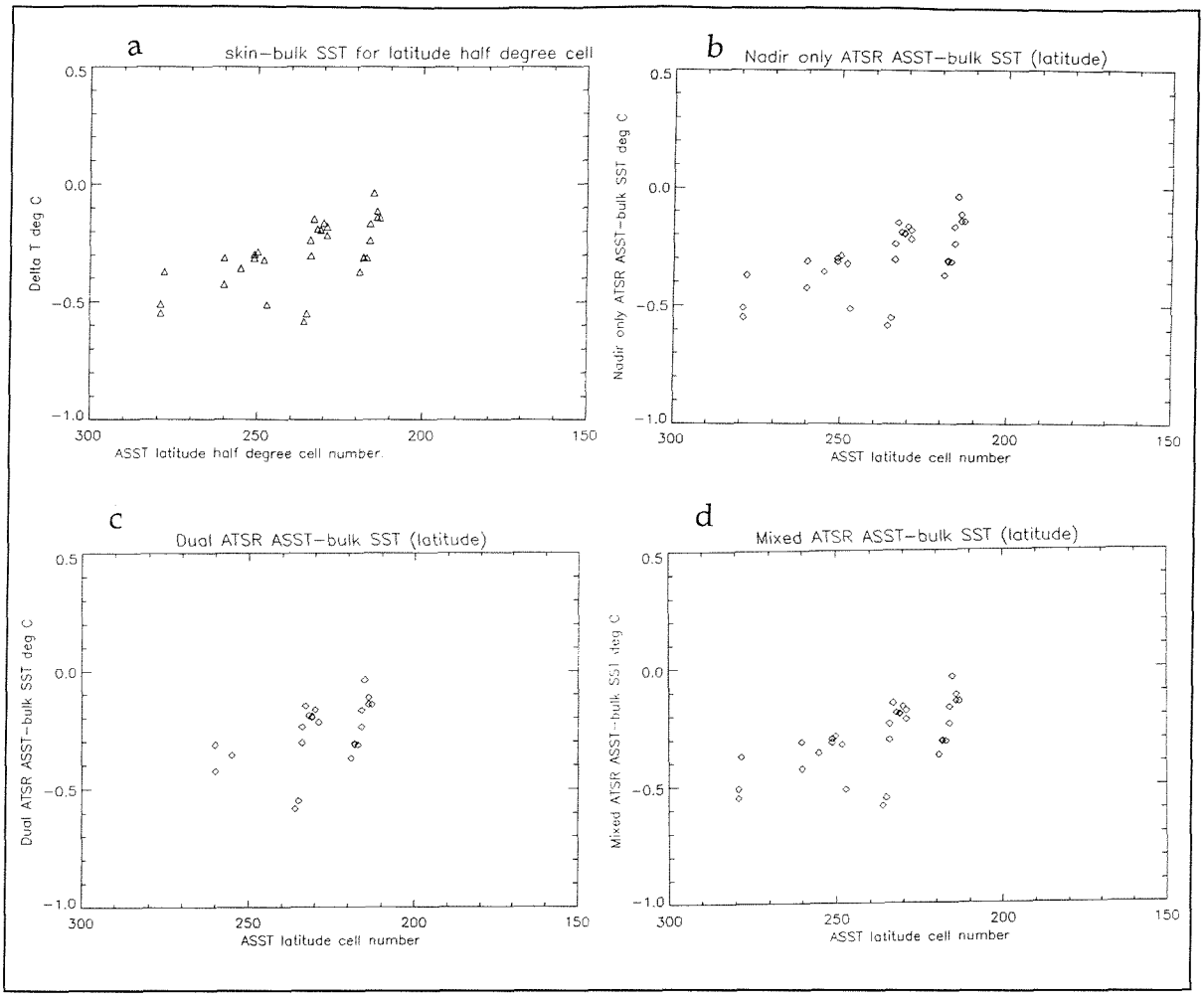

Figure 7.7 (a) ΔT calculated from *in-situ* observations, (b) ΔT calculated from ATSR nadir - *in-situ* bulk SST, (c) ΔT for ATSR dual - *in-situ* bulk SST and (d) ΔT calculated for ATSR mixed SST - *in-situ* bulk SST. All ATSR data are ASST and wind speeds > 10 m/s are not included.

Figure 7.8 plots the wind speed and net heat flux as a function of latitude cell number. These plots can be sub divided into three regions

1. A region in which ΔT is closely related to the net heat flux and where high positive Q is seen ΔT is reduced to a minimum. This occurs between latitude cells 220 - 210. In these cases there is a clear similarity in the distribution of wind speeds and ΔT decreases as the wind speed increases. This suggests that mixing of the upper layers of the ocean has a dominant role over the net heat loss due to radiative and turbulent processes.

2. Between latitude cells 240 - 260 the wind speed is at a maximum (excluding wind speeds greater than 10 m/s) and Q is generally negative indicating a net heat loss from the ocean. In these conditions assuming radiative losses due to clear sky conditions prevail as the ATSR returns an ASST measure, there is a negative ΔT. In this case the combined turbulent and radiative loss of heat from the ocean maintain a negative ΔT.

3. At latitude cells 270 - 280 there is a negative Q under low wind speed conditions and the largest negative ΔT is recorded at these latitudes. In this case a predominance of longwave terrestrial cooling results in a cool skin being maintained.

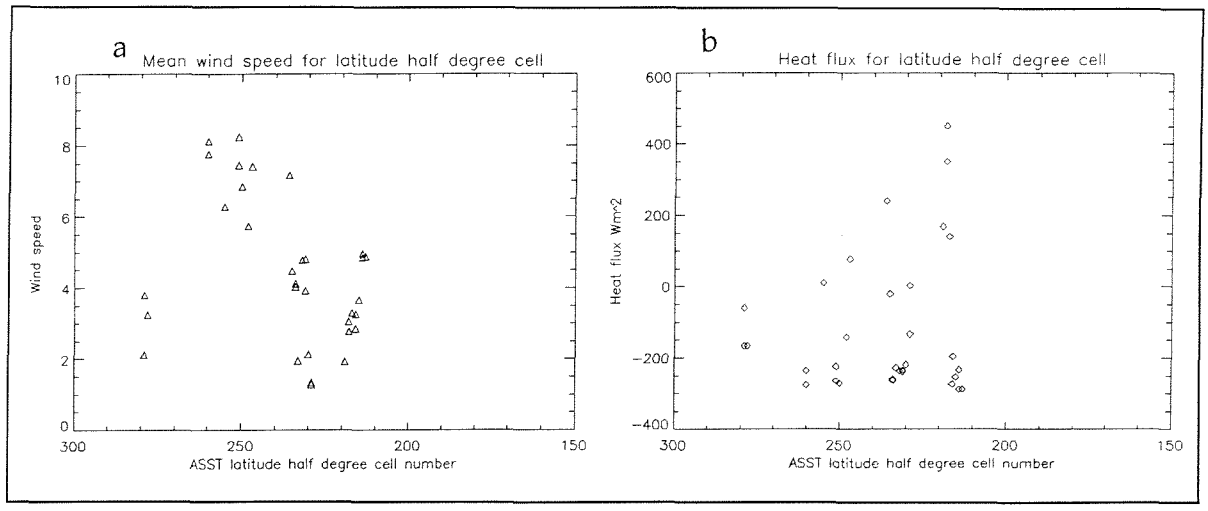

Figure 7.8 (a) Mean wind speed and (b) the net heat flux Q plotted as a function of ATSR ASST half degree latitude cell number. Wind speeds greater than 10 m/s have been rejected.

It is significant to note that the ATSR ASST product is capable of correctly returning a ΔT comparable to that recorded *in-situ* and suggests that satellite radiometers have the potential for determining very accurate SST from space. Further by investigating the detailed local situation at the sea surface the differences between the ATSR ASST product and *in-situ* observations can be explained.

Finally, these comparisons use SADIST 400 ASST data which has now been superceeded by new algorithms used in the SADIST 500 and 600 ATSR processing scheme. There is a need to repeat these comparisons with the new version of ATSR ASST data. This will be completed when these data are made available.

7.5 Conclusions

The ATSR ASST product has been compared to *in-situ* radiometric and bulk SST data and is shown to be producing extremely good SST when compared against *in-situ* radiometric SST. Differences between the ATSR SST and *in-situ* SST have been explained by the careful investigation of the local conditions prevalent at the air -sea interface during the *in-situ* observations. Comparing skin SST and bulk ATSR ASST collocations the bulk ASST comparisons have a higher bias and rms. figure than for the skin case. This is consistent with the cool skin of the ocean ΔT.

As the ATSR returns a skin temperature these results highlight the need for radiometric rather than bulk SST validation observations to be collected. Considering this effect on the pseudo bulk algorithms such as the CPSST and MCSST described in chapter 1, SST derived from these algorithms has only a limited future if the high accuracy SST requirements of the global climate monitoring and prediction community are to be met.

Problems in the measurement using both *in-situ* and remote infra red techniques under high wind and sea state conditions have been explored. Variations in the surface emissivity of the sea at high wind speeds is thought to be the cause of anomalously high SST data recorded both in situ and in ATSR ASST data. This prompts for the further investigation of such effects using new *in-situ* instruments having a spatial as well as temporal capability. Infra red thermal imagers will be most useful in this area of research.

Chapter 8. Conclusions and further work.

In the preceding Chapters the oceanic skin temperature deviation, ΔT, has been investigated using *in-situ* and satellite observations. The data collected during the RRS *James Clark Ross* experiment constitute a unique and comprehensive suite of measurements which have been used to explore the nature of ΔT and its implications when deriving satellite SST maps. The wide variety of environmental conditions (especially wind speed) and global regions (including tropical areas) encountered during the experiment has meant that a fuller description and greater understanding of the behaviour of ΔT has been gained.

During the course of this work operational and proposed *in-situ* SST infra-red radiometer systems have been reviewed and the discrepancies associated with the detailed calibrations of each radiometer system is highlighted as an area of concern. There appears to be a difference in the bias of ΔT associated with the use of a stirred tank calibration when compared to data collected using internally calibrated radiometers. This suggests the need for an international *in-situ* SST radiometer cross calibration exercise. Further, In the context of deriving an accurate skin-to-bulk SST transfer algorithm, a standard method for measuring ΔT should be chosen which will define a standard depth to which satellite calibration and validation bulk SST measurements should be referenced.

8.1 Conclusions from in-situ observations.

The analysis of *in-situ* radiometric and conventional SST data collected on a transect crossing the Atlantic ocean from 50°N 00 to 23°S 35°W has shown the skin-bulk temperature difference to be a persistent feature of the ocean surface. A mean skin-bulk temperature difference of ΔT= -0.4°C ±0.31°C has been calculated which is representative of the entire RRS *James Clark Ross* transect. The mean ΔT data are in good agreement with other authors' measurements (Schluessel *et al*, 1989). Extreme ΔT values of -1.8 and 0.5°C demonstrate that the ΔT of the ocean is

extremely variable. Most of the variability can be attributed to the delicate balance between the turbulent and radiative fluxes at the ocean surface. In particular, a strong relationship between ΔT and the surface wind field exists up to (and possibly beyond, but not confirmed by these data) a wind speed of ~ 10 m/s. The wind speed is shown initially to decrease the magnitude of ΔT as turbulent mixing in the upper layers of the ocean destroy the surface skin layer, while concurrently, the turbulent fluxes of latent and sensible heat act to increase the magnitude of ΔT. Longwave radiative cooling is independent of the wind speed and the largest magnitude ΔT are observed when the turbulent fluxes of heat outweigh the mixing effect of the surface wind field during clear sky conditions when the radiative flux is at its greatest.

Radiometric SST measurements made in conditions of moderate to high wind speed suggest that significant changes in the characteristics of the sea surface during these conditions make the retrieval of an accurate SST measure using *in-situ* radiometric techniques questionable. Positive ΔT values recorded during such wind conditions are observed in both *in-situ* and ATSR satellite radiometer skin SST data when compared to the *in-situ* bulk SST. This may be due to changes in the assumed surface emissivity characteristics of water as current models of surface emissivity are only valid for sea surface conditions in the absence of foam and white caps. This highlights the need for further infra-red measurements of such surface phenomenon. In the data presented here there is a clear change in the radiometric SST signature at high wind speeds (>12 m/s).

The data also show that the greatest ΔT values are found at the higher latitudes and that a minimum ΔT is found in the tropical regions. As the heat fluxes defining ΔT are primarily a product of the local wind speed, temperature and humidity conditions, which also have a strong regional mean, the ΔT values presented here indicate that ΔT has global differences. However in the case of the JCR experiment data, these differences are due to the anomalously high wind conditions encountered in the equatorial regions.

The radiometric skin temperature has more variability during the day time than during the night. Day time only cross correlations between skin and bulk SST are consistently lower than night time at all length scales. Day time ΔT distributions have a much larger spread than for the night time case and may be a consequence of increased environmental variability during the day as a consequence of solar warming.

Cross correlation of skin and bulk SST demonstrate that these SST fields become decoupled in regions of small bulk temperature variability, confirming the results of Schluessel *et al*, (1989). Poor correlations are found at a length scales of <150 km suggesting that at these length scales variability of the skin temperature field is able to mask the subsurface SST structure. However the length scale at which the skin temperature of the ocean is representative of the bulk beneath is the product of both the variability of the bulk SST field beneath and the meteorological conditions above which force ΔT. There is a poor cross correlation in regions of weak sub surface horizontal temperature gradients. In regions of strong bulk temperature variability the correlation increases and the skin temperature is a good representation of the sub surface SST structure even at length scales <150 km. In the open ocean where sub surface horizontal temperature gradients are at their weakest the influence of atmospheric variability will be at its greatest and radiometric skin temperatures are not well representative of the bulk SST field at length scales <150 km. In this latter case 'pseudo-bulk' SST algorithms will fail to accurately represent the bulk SST in such conditions and cannot be relied on at length scales <150 km.

8.2 Conclusions from ΔT parameterisations.

Current parameterisations of the thermal skin effect have been compared to the entire JCR experiment *in-situ* data set and are found to be inadequate in their ability to accurately determine ΔT. Several parameterisations appear to have a regional dependency inherent in the coefficients of proportionality used. The λ

coefficient , used in the ΔT parameterisation proposed by Saunders (1969), has a regional dependence. The JCR data indicate that the different λ results of Schluessel *et al* (1989) and Grassl (1977) can be explained either by the regional dependence of λ on other atmospheric/oceanic parameters apart from the wind speed (such as the degree of subsurface SST variability or the local atmospheric conditions of wind, temperature and humidity) or by the method of computation used. Schluessel *et al* (1989) may not have removed negative λ values in their derivation of a mean λ.

New values of λ have been computed from the JCR data which are representative of the Atlantic ocean incorporating tropical, sub-tropical and higher latitude conditions and these data agree well with those of Grassl (1977).
If a set of λ values can be derived for a variety of typical ocean/atmosphere conditions a parameterisation similar to that proposed by Saunders may be appropriate for a global prediction strategy for ΔT. Data derived from such an equation could then be used as a correction for air-sea gas exchange models and satellite SST measurements. For the derivation of a 'skin to bulk' SST transfer algorithm the author suggests that further investigation of the regional dependence of the Saunders λ coefficient is undertaken.

The danger of using regional parametisations to derive global estimates of ΔT is highlighted by comparing the results presented by Robertson and Watson (1992) and the *in-situ* measurements. The ΔT values reported here indicate that there is a significant difference between the two data sets which is due primarily to the anomalously high wind speeds found in the tropical regions during the JCR experiment. However, if the data of Robertson and Watson were to be used as input into a global ΔT correction scheme in which a correction were made to satellite observations, then the correction scheme would fail as these data predict a large ΔT in the tropical regions.

As the Hasse formulae is based on a set of regional coefficients the data collected form the JCR experiment was used to remove a bias in the parameterisation when compared to the *in-situ* observations. New coefficients for use in the Hasse formula were calculated as:

$$C_1=4.75 \qquad \text{and} \qquad C_2=1.22$$

where the bulk SST is measured at a depth of 5.5 m and the skin temperature is derived from radiometric measurements. These coefficients are derived using data for the entire JCR experiment and include regional variations. This suggests that part of the difference found between the ΔT maps derived by Robertson and Watson(1992) using the Hasse parameterisation and the *in*-situ observations shown here will be due to the different coefficients used. This parameterisation does not work well during the day time indicating an inability to handle solar radiation.

In all of the considered parameterisations, correlations between observed skin behaviour and parameterised skin behaviour are low ($r = <0.6$). There is considerable scatter in all calculated ΔT data and any agreement with the observed values is more related to the mean value returned by each parameterisation rather than an accurate prediction of ΔT.

Surface renewal parameterisations are no more accurate than diffusive or rigid boundary parameterisations. In the case of the Soloviev and Schluessel models (1994), agreement with the in-situ observations is due in part to the exclusion of extreme data values. In the mean wind speed conditions of 5 - 10 m/s the scheme has the least bias of all considered parameterisations primarily for this reason.

Convective parameterisation schemes are unable to reliably predict the magnitude of ΔT.

8.3 *Comparison with ATSR ASST data.*

A direct comparison between the Average Sea Surface Temperature (ASST) data derived from the ATSR instrument and the bulk SST of the JCR using a temporal coincidence of ±48 hours indicates that the satellite data are biased cool by --0.3°C. *In-situ* measurements of ΔT show that this difference has the same magnitude as the measured cool skin of the ocean and confirms the cool bias imposed on satellite SST retrievals by the oceanographic skin temperature deviation. These data are consistent with the cold bias seen in ATSR data when compared to *in-situ* buoy observations (Mutlow *et al*, in press) clearly demonstrating the need to use a skin validation measurement for satellite SST data returning a skin temperature (as in the case of the ATSR instrument).

In tropical conditions having anomalously high wind speeds the ATSR sometimes returns a warmer temperature than the *in-situ* bulk SST. This suggests that the effect of surface foam and white caps may be sufficient to influence SST retrievals from space. The author recommends that further research is required to investigate this phenomenon.

As ΔT is dependent on the local energy fluxes at the air-sea interface, for the correct interpretation of satellite and *in-situ* skin temperature satellite validation data, the local environmental conditions should also be including in the validation exercise. Important parameters to consider include the wind speed, sea state and local radiative and turbulent heat fluxes. However the complexity and sensitivity of the relationships between these variables suggest that it may be extremely difficult to derive a 'skin-to-bulk' SST algorithm for use in regions where the variability of the bulk SST is small and that satellite validation studies should only be conducted at night.

8.4 Further work

The results presented here are a selection of data from a larger data set collected from the JCR SST experiment. The entire data set will be analysed shortly. The comparison between ATSR ASST data and *in-situ* observations will be repeated using a new generation of ATSR SST algorithms which are now available (SADIST v600, Baily, 1994). Further insight into the relationship between satellite and *in-situ* infra red radiometer measurements will be made possible by using the high resolution ATSR data. AVHRR data offer a separate source of data with which to investigate ΔT. In this case the effect of ΔT on a 'pseudo bulk' SST algorithm (MCSST and CPSST) will be investigated.

There is a need to determine the exact nature of the infra-red emissions from the sea surface during conditions of high wind speed. This can be achieved by the use of new imaging thermal cameras. These devices will also allow the study of the spatial variability of the skin temperature fields especially if used from an aircraft platform. In this case the intra pixel variability of the thermal skin can be investigated with reference to a satellite radiometer IFOV.

As the current parameterisations for ΔT are poor there is a requirement to further investigate the detailed relationships between the fluxes of heat and momentum in the context of deriving a new skin to bulk algorithm. The RRS James Clark Ross data set can be used a foundation from which a skin to bulk SST algorithm can be built especially when compared to the high resolution ATSR SST data. It is proposed to use the Saunders parameterisation as the basis of a new transfer algorithm. However to confirm and fine tune these algorithm a larger set of in-situ measurements describing a longer temporal period will be required.

Appendix A. ROSSA Cruise report.

Radiometric Observations of the Sea Surface and Atmosphere - ROSSA

Operational report for the ROSSA experiment 15th September - 19th October 1992 aboard the RRS James Clark Ross.

C J Donlon January 1993

A.1 Introduction

The RRS "James Clark Ross" (JCR) departed from Grimsby bound for Montevideo (Uruguay), Bird Island (South Georgia) and Port Stanley (Falkland Islands) as part of the British Antarctic Survey (BAS) annual personnel and restocking effort in the Antarctic. During this passage I was responsible for the management and collection of a suite of oceanographic and meteorological measurements as part of the Radiometric Observation of the Atmospheric Boundary Layer Project (ROSSA). The objectives of ROSSA for this season can be summarized into three broad areas of interest:

a) To collect *in-situ* radiometric sea surface skin temperature (SSST - the difference between a radiometrically measured skin temperature and that measured several meter's below the sea surface using conventional methods) measurements co-incident with European Remote Sensing Satellite (ERS-1) Along Track Scanning Radiometer (ATSR) overpasses. The data collected will be used to calibrate and validate the ATSR instrument.

b) To collect atmospheric temperature and humidity data co-incident with ERS-1 overpasses using radiosonde ascents. These data will be used to verify the atmospheric transmission model currently used in the retrieval of sea surface temperature (SST) from the ATSR instrument.

c) To collect a suite of surface meteorological, SSST and *in-situ* SST data in order to characterize the sea surface skin temperature deviation in terms of a wide range of meteorological and oceanographic conditions.

This report is a discussion of the installation and operation of equipment used by the 1992 ROSSA experiment which ran from the 15th September 1992 - 19th October 1992 (leg 1).

2 Installation of ROSSA Equipment.

Final installation of all ROSSA equipment was carried out during the week prior to the departure date by BAS personnel and myself at Grimsby. On departure all systems were running satisfactorily and had been checked as far as was possible.

For the accurate measurement of SSST a ship mounted radiometer was required to the following specification:

Bandwidth	11mm and 12mm (centre)
Resolution	0.1°C
Accuracy	±0.15°C
Sample interval	1- 20 seconds

Table A.1 Specifications for infra-red measurement of SSST.

This specification was met by the Satellites International Ltd. (SIL) ship mounted infra-red radiometer which was installed on the forward mast of the JCR. In this position the instrument was able to view the undisturbed sea surface clear of the ships wake and bow wave. The radiometer had a custom cradle mount constructed which was securely attached to the mast island allowing the radiometer to be positioned quickly and accurately. Ideally, the radiometer should have been mounted looking vertically down onto the sea surface (nadir view) in order to minimize the effects of 'stray' radiation entering the instrument field of view by reflection at the sea surface. Unfortunately this was not possible from the JCR forward mast. The smallest deviation from the vertical was thus required and in order achieve this, the radiometer was turned on and initially positioned by eye to clear the ship's gunnel. By noting the temperature difference between the ships gunnel and the quayside (the quayside was cooler lying in the shade of a dock crane), the position was further refined. Finally, the radiometer look angle was reduced in small increments (less than a degree) after which I

walked across the instrument field of view with my neck at the height of the gunnel thus providing a strong thermal source. This operation was repeated until the radiometer was positioned in such a way that the field of view was just clear of the gunnel. The angle from the vertical was measured via a 360° protractor to be 37° as predicted from the ship's plans by J Thomas. Power supplies were mounted in the F'castle with a switch positioned in the starboard alley. Full cabling was installed from the radiometer to the UIC lab (to the stern of the ship) where full control of the radiometer was possible via a PC. Ben Althouse must be thanked for his excellent work installing this instrument. Further modifications included 'Denzo' tape being applied to the mounting frame joints in order to make these water tight and finally marking the position of the radiometer mounting arms (vertical) to the radiometer body - any movement as a consequence of inclement weather could then be noted during the voyage and the radiometer position accurately re-set.

As water is not a perfect black body, a certain amount of reflection takes place at the water surface regardless of the instrument look angle. Under clear sky conditions an apparent SSST deviation due to the reflected component entering the radiometer field of view (FoV) will occur reducing the true SSST. The opposite situation arises under cloudy conditions as back radiation from the cloud base will be reflected at the sea surface into the radiometer FoV causing an apparent *warming* of the SSST (Saunders, 1968). Clearly for the accurate determination of SSST measurements of the reflected component must be taken. For a similar model to the above instrument, an error of 15 K in the sky temperature measurement will give an apparent SSST error of 0.25 K (Knight, 1989). A Radiometer measuring the temperature of the sky was thus required to the following specifications:

Bandwidth	**10 - 12mm**
Resolution	better than 5°C
Accuracy	±10°C
Sample interval	1 - 20 seconds

Table A.2 Specifications required for accurate measurement of downwelling 'sky' radiation.

This was met in part by the Camlab THI-500S portable self calibrating radiometer. This instrument has a larger bandwidth than the SIL radiometer of 8 - 12mm and will thus measure ozone absorbtion at 9.0mm. However due to the low accuracy requirements placed on these data (see table 2 above) this effect will be marginal. The instrument was installed on the monkey island looking vertically up into the sky. The measurement probe was sealed with amalgamating tape against water ingress and a polystyrene housing was constructed in order to minimize environmental temperature effects while crossing tropical regions. Data was logged to a self contained data logger supplied by Southampton University department of Oceanography which was installed below the instrument on deck. Rechargeable batteries were used and were changed each day. The instrument operated in this mode until the 4th October at which point it was moved to the forward mast as a replacement to the SIL radiometer which had developed a fault. For this installation, the THI-500 was attached to the side of the SIL radiometer and the look angle set as for the SIL radiometer which proved to be more difficult while at sea. This configuration was to remain for the duration of the experiment as the SIL radiometer could not be repaired.

The following instrumentation was installed on the forward mast of the JCR by BAS personnel and made up the meteorological package for the ROSSA project:

1) A Kipp and Zonen Pyranometer 0.3 - 3.0mm measuring incoming solar radiation at a height of 16.0m above the water surface. This instrument was moved from the port side of the maintenance island to starboard before departure as the instrument was shadowed by the SIL radiometer storm cover.

2) A Vector instruments anemometer and wind vane located at a height of 18.5m above the water surface mounted on a custom arm protruding forwards from the mast.

3) A solid state humidity sensor mounted at a height of 16.0m above the water surface.

4) A digital barometer recording surface pressure within the UIC laboratory.

All of the meteorological instrumentation was cabled to the UIC laboratory via the ships scientific lines and data logged in real time by the ROSLOG data logging software.

A radiosonde receiving station was installed in the UIC laboratory comprising of a Beukers VHF receiver linked to an aerial located to the rear of the bridge deck. The position of this aerial was determined by many factors but principally the length of the connecting cable, the safety of the cable run for ship's personnel, the proximity to general working areas and the degree of 'radio shading' from the ships superstructure. A fault with a coaxial connector plug on the aerial cable was rectified by replacing the plug. A spare preamplifier unit for the system was obtained prior to departure as a spare unit.

The second unit within the receiving station system was a Viasäla PP11 data processor linked to an Amstrad PC. Data from the Beukers receiver was processed in real time by the PP11 and logged to the Amstrad PC via custom software. Both of these instruments were securely lashed to the UIC room desks using elastic bungee cords attached to the custom mounting hooks supplied with the desks. These were found to be most useful for their intended purpose.

In-situ "bulk" SST was measured by several instruments. A hull mounted Meteorological office thermistor at 6.0m depth was logged continuously to the ROSLOG computer as was a 'Sea Bird' temperature and salinity unit. The Sea Bird used the scientific pumped sea water supply taking sea water from 300 mm clear of the ships hull by extending a sample probe from within the ship. The accuracy of this instrument was quoted as better than 0.01°C. Both of these

instruments were cabled directly to the ROSLOG PC using the ship's scientific cable runs. Finally routine meteorological office 'bucket temperatures were taken throughout each day using the ship's meteorological thermometer and bucket. These instruments are permanently installed on the JCR and required checking prior to departure.

The ships position was taken using a Trimbell Global Positioning System (GPS) and logged in real time via a Sperry marine integrated navigation system. The time stamp obtained from these data will act as the absolute data co-registration parameter. A comprehensive demonstration of this system was given by the ships first officer before departure and data was logged to a local network node PC. This was an automated data logging system and required no maintenance during the passage.

A.3 Operations

The ROSSA experiment began once the RRS James Clark Ross had left the Humber estuary. Instrumentation was run continuously throughout the passage with breaks only due to port calls and a number of problems. These will be discussed in the following paragraphs.

SIL Radiometer

The SIL radiometer was run continuously even when capped (during bad weather) in order to maintain a constant temperature within the casing and to offer a warm drying atmosphere minimizing condensation within the instrument. All equipment installed on the forward mast was checked each day (weather conditions permitting) for salt contamination, water ingress and security of mounting. On a number of occasions bad weather required the SIL radiometer to be sealed off by capping the viewing aperture. The cap supplied was an extremely tight fit and on occasions was difficult to remove. I was satisfied that the instrument was 100% watertight which visually proved to be the case on detailed inspections after any severe weather.

THI-500 Radiometer

The THI-500 radiometer suffered as a consequence of the equatorial sun rendering the LCD display unusable. However, the data was quality checked and showed no discernible change and logging continued for the duration of the passage with no problems.

ROSLOG Software

It soon became apparent that the ROSLOG software was faulty as the system would inexplicably hang up completely requiring the computer to be re-started and the program reinitialized. A 24 hour watch rota was called using spare volunteer Fids which was disbanded after 3 days as the duty watchmen were able to check the system reporting directly to me if any problems were apparent. In all, a proportionally small amount of data was lost with respect to the passage as a whole and the problem was more infuriating than disastrous. These problems were a product of confusion as initially it was assumed that the ships central computer would be logging the ROSSA instrumentation throughout all JCR operations. Unfortunately computer support personnel were not available to maintain the ships mainframe system during this first leg of the JCR's itinerary, and an integrated PC based data logging routine was required. The software used by ROSSA was a modified version of a larger data logging package still undergoing tests and I am indebted to P Woodruff for the time and dedication spent on modifying this package for my use with extremely short notice. It was noted however that none of the temperature sensors recorded a negative temperature in situations where one may have expected small negative values. On reaching the Falkland Islands I was able to talk with Paul who confirmed that the software was not configured to record negative values and that only a zero would be recorded in the data file.

Radiosonde operations

Unfortunately a full operational test run of the radiosonde system was not possible before departure due to CAA regulations requiring notification of radiosonde launch and the lack of radiosonde units. Problems were encountered at sea stemming primarily from modifications to the PP11 output data format which were undertaken during the 1991-92 season. This resulted in a data format incompatibility between the logged data and the WMO meteorological message

generation software. After consultation with J Shanklin at BAS HQ the problem was identified and a computer program written to reformat the data solving the problem. Once radiosonde data had been reformatted the met message software ran without a problem. I decided to remove the tiresome operation of editing out transmission dropouts within the data by extending this program to remove any suspicious data. The program gives the option to remove all suspect data with or without user confirmation for each record removed. Unfortunately no WMO meteorological messages could be transmitted due to a fault in the communications system timing out the radio link before the whole meteorological message had been transmitted. The ships radio officer tried all communications routes to the WMO without success and as a consequence no messages reached the Bracknell met office for use in near real time.

Radiosonde performance was varied and was weather dependent. During inclement weather data reception was noisy and reception would fade as the ship rolled. 28 successful and 3 aborted ascents were made during leg 1 of the ROSSA experiment.

SIL Radiometer problems

The SIL radiometer functioned well to 35° south at which point a hot black body fault required the instrument to be shut down in fear of internal damage. An unstable hot black body temperature was reported from the radiometer with fluctuations of 50°C in » 15 seconds. This problem had been previously reported by T Forrester of the James Rennel Centre for Ocean Circulation using their SIL radiometer. At Montevideo a system overhaul was performed (given the limitations of working without circuit diagrams) with no obvious problems apparent. No water ingress could be found within the instrument case and all seals required breaking before beginning the investigation. I decided to leave the instrument unpowered but open for the duration of the Montevideo call in order

to dry out any moisture build up as suggested by T Forrester via communication with J Thomas. On re-powering the instrument, all was fine for about an hour at which point the problem began once again. In the interests of the instrument, it was decided to leave the radiometer unpowered for the remainder of the passage and replace it with the smaller solid state THI-500 radiometer supplied by Southampton University. This was duly installed on the forward mast and run until the Falkland's call. It was requested that circuit diagrams be brought to the Falkland's by BAS staff joining the JCR for the passage further south and that a full overhaul could be conducted. Confusion as to who had actually brought these documents to the Falklands resulted in no further investigations being carried out by myself at Port Stanley.

'Bulk' SST measurements

The scientific sea water supply functioned well with only one days break due to failure of a sea water pump bearing unit which was repaired by the ships engineers. No problems were encountered using the Sea Bird unit. I would suggest that one improvement could be made to this system by fitting an extension to the waste pipe of the unit which would minimise water splashes reaching the deck. A temporary pipe was fitted to this unit during this passage.

Inconsistencies between the Meteorological office temperature sensor and the Sea Bird T/S unit were noticed as the passage progressed. Standard Meteorological 'bucket' temperatures were taken each day in order to assess these inconsistencies. Figure 1 shows temperature residuals from both the scientific supply (Sea Bird T/S unit) and standard Met office 'bucket' temperatures. A mean residual of 1.3°C was calculated for both data series.

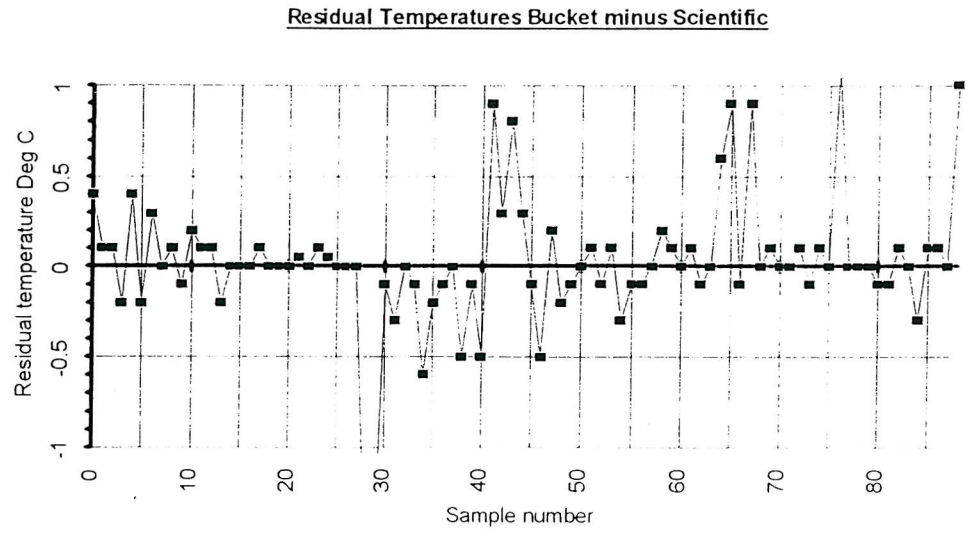

Figure A.1. Residuals of meteorological office sensor from scientific supply and standard meteorological buckets .

Figure 2 shows the temperature residual from the scientific supply and bucket temperatures. The mean residual from these data is calculated to be 0.2°C with the major part of the error introduced from reading the mercury-glass thermometer of the 'bucket' temperature.

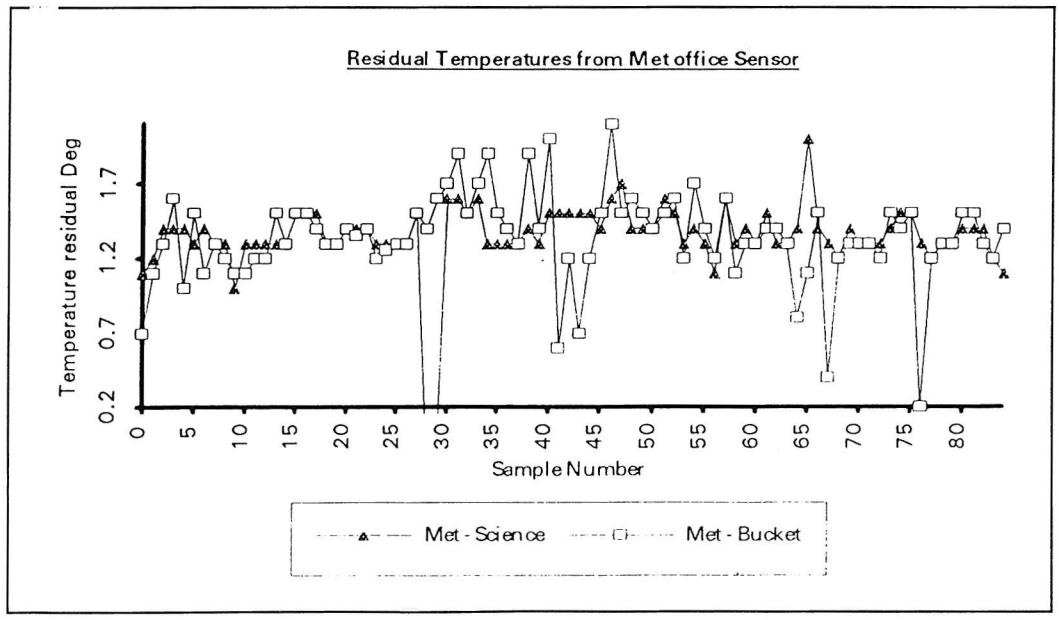

Figure A.2 Residual of scientific supply and 'bucket' temperatures.

In conclusion to this basic analysis I would suggest that the Meteorological temperature sensor carried aboard the JCR is in error either due to a poor calibration or the fact that the sensor lies close to a fuel tank which is heated. The latter was thought to be the cause after consultation with the ships chief engineer. This sensor requires a re calibration before any firm conclusions can be drawn although a correction coefficient of -1.2°C was given to the ships officers for use with the instrument while at sea.

MSGS Satellite receiving station

The MSGS satellite receiving station was used routinely throughout the passage and over 80 images have been archived from leg 1 of the ROSSA project. These are of varying quality as the ships position or predicted ship positions were not always entered into the system on a routine basis. The system struggled when applying a latitude/longitude grid or coastline overlay to data obtained below 40° south with MSGS manuals being of little help in tracing this problem. A suggested reason for these problems is that header information was only written to image data files scheduled for reception. The system will receive all NOAA APT data on registration of the NOAA APT carrier frequency which was often the case. A further comment on this system is that the image processing tools supplied by MSGS were found to be both time consuming and cumbersome to use and were of little help in analyzing APT data. I would suggest that the user manuals be re-written in a fuller manner with detailed explanations for each of the functions offered by the system. Recent contact with MSGS has resulted in the supply of series of C computer programs which allow these archived data sets to be read and used in a conventional image processing system during the following months. However no comment was made on the value of the MSGS system manuals carried aboard the JCR.

ERS-1 Orbital tracking - SATSCAN

To track the movements of the ERS-1 satellite the SATSCAN computer program used on the RRS Bransfield last season by J Thomas. New ephemiris data was received from BAS HQ each week and entered into the system. I found this program a worry as the program configuration would not always save correctly and the use of an LCD screen on a laptop computer was not the best of displays. Further no manuals were supplied which added to this confusion. However using this program at least six coincident overpasses of ERS-1 should have been made using a satellite elevation angle greater than 75° as successfully used by the ROSSA team last year.

ERS-1 ATSR Satellite data

ERS-1 ATSR satellite data are on order from the Rutherford Appleton Laboratories (RAL) as part of the ROSSA project. The cruise track has been bound by a 1024 Km 'corridor' which is split into 27 specific areas corresponding to the 27 days spent at sea. For each area (day) all satellite data for 2 days before the passage of the JCR, the day of passage and 2 days after the passage has been ordered. In this way the relevance of the point specific calibration validation data collected by the JCR can be related to a series of spatial and temporal SSST averages. Any co incedent satellite ship measurements will be apparent and will ensure that any mistakes made when using the SATSCAN satellite position program will not be a problem. As an extension to this a comparison between JCR *in-situ* data and global ATSR data will also be made. These data are currently being processed at RAL with the first delivery expected towards the end of January 1993.

4 Discussion and conclusion

It is well known that the collection of data such as these outlined above is notoriously difficult at sea. The RRS James Clark Ross was found to be an excellent oceanographic platform from which to base an experiment such as this.

The ship was found to be comfortable, quiet, very stable with a helpful ships company. This suite of measurements will allow the study of the SSST in relation to the thermodynamical processes occurring at the air - sea interface and will ultimately be used to clarify the SSST algorithm currently applied to ATSR data both in a conceptual understanding of the thermodynamic processes occurring at the sea surface, and in the absolute calibration of both the SST algorithm and radiative transfer model that it uses. It has been proposed that results obtained from the RRS Bransfield by J Thomas during the 1991-92 ROSSA experiment be combined with the 1992-93 JCR data and a joint paper be produced. Further work will involve a study of the SSST deviation in the Falklands - South Georgia area as a complimentary study to that already undertaken in the Weddel sea area.

I wish to take this opportunity to thank all those at the BAS for their time and effort in planning and supporting the ROSSA experiment especially Jeremy Thomas, Paul Woodruff, John Turner, John Shanklin and finally all of the JCR officers and crew.

Appendix B. Along Track Scanning Radiometer Data.

Table B.1 lists the coincident ATSR data supplied by the Rutherford Apelleton Laboratories.

½° x ½° average SST data (ASST) from the ATSR instrument were extracted from the above data by RAL and supplied at SADIST v400. In this case transects of satellite data coincident in space with the passage of the James Clark Ross were extracted. These were then compared to the *in-situ* data.

For a true calibration validation match up pair the criteria of Minnet (1990) were adhered to of 2 hours overpass and 10 km as representative of the SST at the time of satellite overpass. Clearly this criteria only applies to the bulk and bucket SST measurements as the radiometric measurements are heavily dependent on the local heat and momentum parameters.
Future work, already begun but incomplete, is based on the analysis of high resolution ATSR data and *in-situ* observations made during the JCR SST experiment. ATSR SADIST 500 SST and brightness temperature data will be used in these analyses.

SADIST v500 Filename	Date	Time (GMT)
soton_pk$209141111_14150_30201_500	14-09-92	11:47
soton_pk$209142114_05630_30116_500	14-09-92	21:30
soton_pk$209172120_06130_30115_500	17-09-92	21:37
soton_pk$209181045_14250_30201_500	18-09-92	11:22
soton_pk$209181045_14750_30201_500	18-09-92	11:23
soton_pk$209182229_03630_30128_500	18-09-92	22:39
soton_pk$209182229_04130_30128_500	18-09-92	22:41
soton_pk$209182229_04630_30128_500	18-09-92	22:42
soton_pk$209182229_05130_30128_500	18-09-92	22:43
soton_pk$209172301_04150_30301_500	17-09-92	23:12
soton_pk$209212235_03530_30301_500	21-09-92	22:45
soton_pk$209212235_04030_30301_500	21-09-92	22:46
soton_pk$209222344_01330_30301_500	22-09-92	23:48
soton_pk$209222344_01830_30301_500	22-09-92	23:50
soton_pk$209222344_02330_30301_500	22-09-92	23:51
soton_pk$209232312_02330_30302_500	23-09-92	23:19
soton_pk$209232312_02830_30302_500	23-09-92	23:20
soton_pk$209232312_03330_30302_500	23-09-92	23:22

soton_pk$209250021_00079_30302_500	25-09-92	00:23
soton_pk$209250021_00579_30302_500	25-09-92	00:24
soton_pk$209250021_01079_30302_500	25-09-92	00:25
soton_pk$209252350_01079_30302_500	25-09-92	23:53
soton_pk$209252350_01579_30302_500	25-09-92	23:55
soton_pk$209252350_02079_30302_500	25-09-92	23:56
soton_pk$209262318_01830_30302_500	26-09-92	23:24
soton_pk$209262318_39200_30303_500	26-09-92	00:57
soton_pk$209272246_39700_30303_500	28-09-92	00:26
soton_pk$209272246_40200_30303_500	28-09-92	00:28
soton_pk$209280027_00729_30303_500	28-09-92	00:30
soton_pk$209282355_00479_30303_500	28-09-92	23:58
soton_pk$209201122_16930_30426_500	20-09-92	12:05
soton_pk$209231128_17530_30428_500	23-09-92	12:13
soton_pk$209231128_18030_30428_500	23-09-92	12:14
soton_pk$209231128_18530_20425_500	23-09-92	12:15
soton_pk$209231128_19030_30428_500	23-09-93	12:16
soton_pk$209261134_17600_30428_500	26-09-92	12:19
soton_pk$209261134_18100_30428_500	26-09-92	12:20
soton_pk$209261134_18600_30428_500	26-09-92	12:21
soton_pk$209261134_19100_30428_500	26-09-92	12:22
soton_pk$209261134_19600_30428_500	26-09-92	12:24
soton_pk$209261134_20100_30428_500	26-09-92	12:25
soton_pk$209261134_20600_30428_500	26-09-92	12:26

Table B.1 High resolution ATSR data ordered for the JCR cruise.

Appendix C. SIL radiometer atmospheric correction errors.

C.1 Errors in the SIL radiometer SST due to atmospheric absorbtion.

Figure C.1 shows the combined response of the detector element and the 11 μm filter profile for the SIL radiometer. Although the filter has a large transmission peak centred around the desired waveband there is a smaller peak (a radiometric 'leak') centred at 20 μm.

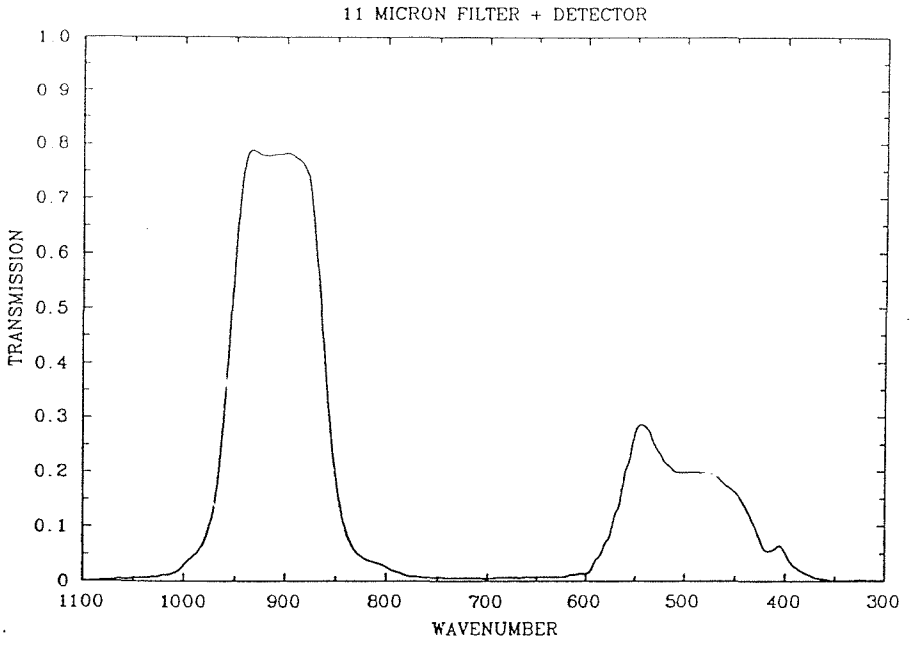

Figure C.1 The combined spectral response of the SIL radiometer pyroelectric detector window and the 11μm waveband filter (R Knight personal communication)

In order to asses the effect of such a leak, the SIL combined response function will be used in a line by line atmospheric transmission model of A Zavody (modified by the author to suit the SIL filter profile) to produce transmission profiles of H_2O and CO_2. Calculated transmission profiles for water vapour and carbon di-oxide are shown in figure C.2. Clearly strong absorption occurs in the region of the filter 'leak' and the magnitude of this effect needs to be estimated.

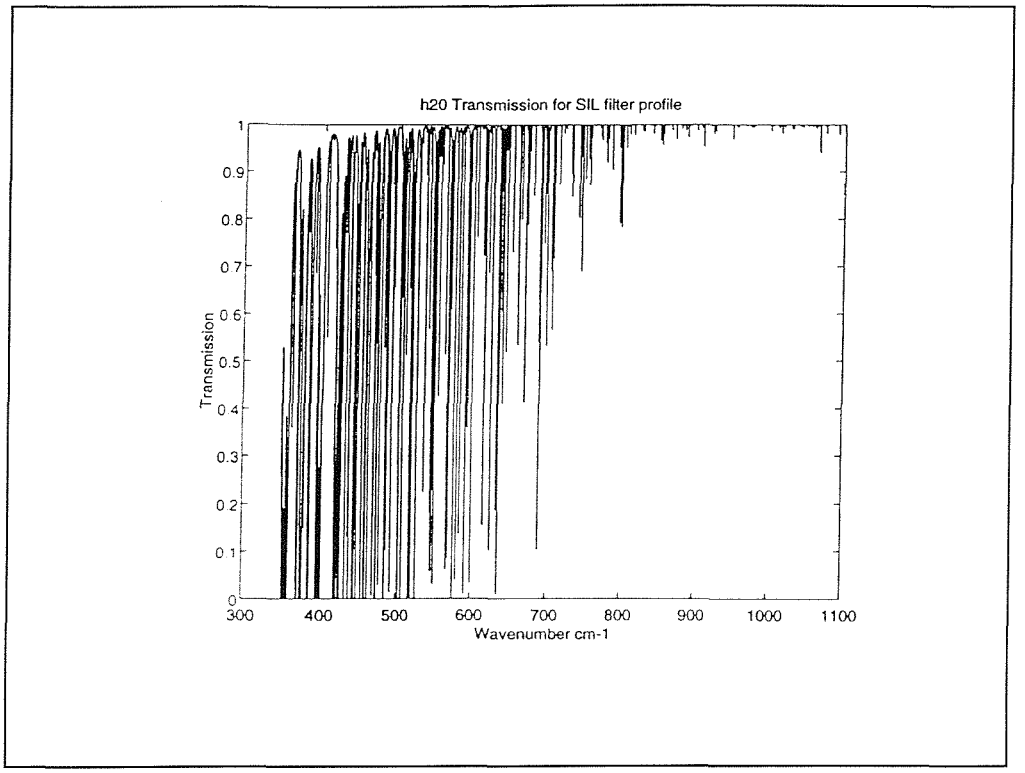

Figure C.2. Calculated transmission profiles for the SIL radiometer window and 11μm filter profile. (a) for H_20 at 273 K with 80% RH. and (b) for CO_2 at 273 K at a pp of 0.36 %. Profiles were calculated line by line using the RAL transmission model (A Zavody).

In order to do this the following model is assumed.

The contribution from each of these molecules to the signal measured by the SIL radiometer will vary as a function of the air sea temperature, the effect being to warm or cool the retrieved SST depending on sign of the air sea temperature difference. In the typical case the atmosphere is cooler than the sea so that the general effect is to bias the final SST cool. During the JCR experiment the atmospheric pathlength was 21 m. For this path length and maximum humidity value of >90% relative humidity assuming an air-sea temperature difference of -5 K, may produce an approximate error of 0.5 K in the calculated SST measurement (A Zavody personal communication).

The following scheme is currently being implemented to asses the effects of atmospheric absorbtion along the 21 m pathlength for the case of the JCR SST experiment.

1. The relevant water vapour and carbon dioxide absorbtion lines for the combined response of the SIL filter and detector window were calculated for the entire filter response 300-1000 cm^{-1} at 0.04 wavenumber intervals using data supplied by A Zavody of RAL.

2. These data were then used to calculate atmospheric transmittance for temperatures between 273 K and 308 K in 5 K intervals.

3 Air temperature and humidity data were extracted from the James Clark Ross meteorological measurements for each SIL measurement.

4 A log profile of humidity was assumed from the height of the radiometer to the sea surface and total saturation was assumed at the sea surface. A mean concentration of 0.036% was assumed for the CO_2 profile remaining constant across the entire path length.

5. Using the atmospheric transmittance curves, the air temperature and humidity data described in (4) the thermal emission/absorbtion of the intervening atmosphere is calculated for the range of conditions encountered during the JCR experiment.

6. The data generated in (6) will then be used to construct a look up table of radiometer SST to atmospherically corrected SST.

The many assumptions used in this scheme and the uncertainty in the water vapour continuum suggest that this scheme may not produce an accurate estimate of the effect of the atmospheric absorbtion for such a short path length.

This work has begun but has not been completed yet and is not used in the analyses presented here.

Bibliography.

Abbot M R and Chelton D B (1991), "Advances in Passive Remote Sensing of the Ocean" U S National Report to international Union of Geodesy and Geophysics 1987-1990 in *Rev Geophys Supp* 571-589

Allen M R , Panter M J, Blumberg G M C, Mutlow C T and Llewellyn-Jones D T (1993). " Prospects for Global Change Detection with Satellite SST Observations". *Proc.Sec.ERS-1 Symp.*, 1,103-1,108.

Bachmann M (1991), "Geocorrection of NOAA AVHRR Imagery. An algorithm based on orbital parameters and one ground control point" in *Proc 5th AVHRR Data Users Meeting Tromsø, Norway 25-28 June 1991*, 11-

Bailey P (1994). *SadistProducts, Version 600.* Space Science Department. Rutherford Appleton Laboratory. Didcot, Oxfordshire.

Barton I J (1992). "Satellite-Derived Sea Surface Temperatures - A Comparison Between Operational, Theoretical, and Experimental Algorithms". *J.App.Meteor.*, **31**, 433-442.

Barton I J and Knight R J (1988), "Design of a Precision Radiometer for the Geophysical Validation of Satellite Products" Internal report *Rutherford Appleton Laboratory*, Chilton

Bates J B and Diaz H F (1991), "Evaluation of Multichannel Sea Surface Temperature Products Quality for Climate Modelling: 1982-1988", in *J Geophys Res 96*, 20,613-20,622

Bernstein R L and Chelton D B (1988), "Large-Scale Sea Surface Temperature Variability from Satellite and Shipboard Measurements" in *J Geophys Res 90,* 11,619-11,630

Bitterman D S and Hansen D V (1993). "Evaluation of Sea Surface Temperature Measurements from Drifting Buoys". *J. Atmos.and Oceanic Tech.*, **10**, 88-96.

Blanc T V (1985), "Variation of Bulk-Derived Surface Flux, Stability, and Roughness of Results Due to the Use of Different Transfer Coefficient Schemes" in *J Phys Oceanography 15,* 650-669

Bottomly, M;Folland, C K; Hsiung, J; Newell, R E and Parker, D E, (1990) "Global Ocean Surface Temperature Atlas; GOSTA", *Joint project of the UK Meteorological Office and Massechusetts Institute of Technology. HMSO*

Bradley S G (1982), "Transient Radiant Influence of Cumulus Clouds on Surface Temperature and Fluxes" in *J Geophys Res 87,* 3,135-3,142

Caldwell D R (1987) " Small-Scale Physics of the Oceans". *US. Nat. report to Int. Union of Geodesy and Geophys. !983-1986,* 183-192.

Carson D J (1991). "The Role of Observations in Climate Prediction and Research". *Meteor.Mag.*, **120**, 107-113.

Coakley J A and Bretherton F P, (1982), "Cloud cover from high resolution scanner data: detecting and allowing for partially filled fields of view", *J Geophys res, 87, 4917-*

Constans J; Fraysse G; Leger G and Roux J (1984), "The Continuous Measurement of the Temperature of the Upper Layer of the Sea - A practical approach" in *Int J Remote Sensing 5,* 103-114

Coppin, P A; Bradley, E F; Barton, I J and Godfrey, J S (1991), "Simoultaneous observations of Sea Surface Temperature in the Western Equatorial Pacific Ocean by Bulk, Radiative and Satellite methods", *J Geophys Res, **96**, 3401 - 3409 (Supp)*

Csanady, G T; (1990), "The role of breaking wavelets in air-sea gas transfer", *J Geophys Res, **95**, 749-759*

Deschamps P Y and Phulpin T (1980), "Atmospheric Correction of Infrared Measurements of Sea Surface Temperature Using Channels at 3.7, 11 and 12 μm" in *Boundary Layer Meteorology 18*, 131-143

Edwards T, Browning R, Delderfield J, Lee D J, Lidiard K A, Milburrow R W, McPherson P H, Peskett S C , Toplis G M Taylor H S , Mason I, Mason G, Smith A and Stringer S (1990). "The Along Track Scanning Radiometer- Measurement of Sea-Surface Temperature from ERS-1". *J.of the Br.Interplan.Soc.*, **43**, 160-180.

Eifler, W (1992), "Modelling the skin-bulk temperature difference near the sea-atmosphere interface for remote sensing applications", *ESA SP-341, pp335-341*

Emery W J (1989). "Global Differences Between Skin and Bulk Sea Surface Temperatures". *EOS.* **70**, 211-212.

Emery W J (1994). "Global Calibration Measurements for Satellite Sea Surface Temperature". A White Paper by the SST Working Group.

Emery W J, Wick G A and Suarez M (1994) "OPHIR MISTRC Radiomater User's Guide"

Emery W J, Yu Y, Wick, G A, Schlussel P and Reynolds R W (1994). "Correcting Infrared Satellite Estimates of Sea Surface temperature for Atmospheric Water Vapour Attenuation". *J. Geophys. Res.***99**, 5,219-5,236.

Ewing G and McAlister E D (1960), "On the Thermal Boundary Layer of the Ocean" in *Science 131*, 1,374-1,376

Folland C K , Parker D E and Kates F E (1991). "Worldwide Marine Temperature Fluctuations 1856-1981". *Nature*, **310**, 670-673.

Folland C K, Reynolds R W, Gordon M and Parker D E (1993). "A Study of Six Operational Sea Surface Temperature Analyses". *J.Climate*, **6**, 96-113.

Forrester T N, Challenor P G, and Guymer T H (1993). "Validation of ATSR Sea Surface Temperatures near the Faeroes". *Proc.Sec. ERS-1 Symp.*

Foster, T D; (1971) "Intermittent Convection", *Geophys. Fluid dyn.*, **2**, *201-217*

Francois C and Ottle C (1993). "Estimation of the Angular Variation of Sea Surface Emissivity with the ATSR/ERS-1 Data" *Proc.Sec.ERS-1 Symp.*

Gardashov R G; Shifrin K S and Zolotova J K (1988), "Emissivity, Thermal Albedo and Effective Emissivity of the Sea at Different WInd Speeds" in *Oceanog Acta 11*, 121-137

Gemmrich, J and Hasse L, (1992) "Small-scale surface streaming under natural conditions as effective in air-sea gas exchange", *Tellus, 44B, 150-159*

Gill A E (1982) *Atmospher - Ocean Dynamics* Academic Press, London

Grassl H (1976), "On the Dependence of the Measured Cool Skin of the Ocean on Wind Stress and Total Hat Flux" in *Meteorology 10*, 465-474

Grassl H and Hinzpeter H, *"The cool skin of the Ocean"*, GATE rep. 14, 1 229-236, WMO/ICSU, Geneva, 1975

Hadley Centre for Climate Prediction and Research (1994). *Climate Data Requirements*. Meteorological Office. Braknell ,Berks.

Harris A R (1991), "An Extension to the Split-Window Technique"in *Proc 5th AVHRR Data Users Meeting Tromsø, Norway 25-28 June 1991*, 253-

Harris A R and Mason I M, (1992) "An extention to the "Split Window" Technique giving improved atmospheric correction and total water vapour", Int J Rem Sens, 13, 881-

Harrison D L (1993). "Validation of ATSR Near-Real-Time Products". United Kingdom Meteorlogical Office, Braknell.

Hasse L (1963), "Cooling of the Sea Surface by Evaporation and Heat Exchange" in *Tellus 15* No 4, 363-366

Hasse L (1970), "The Sea Surface Temperature Deviation and the Heat Flow at the Air-Sea Interface" in *Boundary-Layer Meteorology 1*, 368-379

Hasse L and Liss P (1980), "Gas Exchange Across the Air-Sea interface", *Tellus, 32*, 470-481

Hepplewhite C L (1989), "Remote Observation of the Sea Surface and Atmoshpere: The oceanic skin effect" in *Int J Remote Sensing 10*, 801-810

Hill R H (1971), "Laboratory Measurement of Heat Transfer and Thermal Structure Near an Air-Water Interface" *J Phys Oceanog 2, 190-198*

Ho D; Asem A and Deschamps P Y (1986), "Atmospheric Correction for the Sea Surface Temperature Using NOAA-7 AVHRR and METEOSAT-2 Infrared Data" in *Int J Remote Sensing 7* No 10, 1,323-1,333

Imbault D; Chedin A and Scott N A (1981) "Multichannel Sea Surface Temperature Retrievals" in *Oceanography from Space* Gower (ed), 115-122

Imberger J (1985), "The Diurnal Mixed Layer", in *Limnol and Oceanog 30(4), 737-770*

Jessup A T (1992). "Measurement of Small-Scale Variability of Infrared Sea Surface Temperature". Summary of Fall 1992 AGU Poster Session.

Katsaros K B (1976), "The Sea Surface Temperature Deviation at Very Low Wind Speeds; is there a limit?" *Tellus 29,* 229-239

Katsaros K B (1977), "The Sea Surface Temperature Deviation at very low wind speeds; is there a limit ?", Tellus, 29, 229

Katsaros K B (1979), "The Aquesous-Thermal Boundary Layer" in *Boundary Layer Meteorology 18* 107-127

Katsaros K B (1990). "Parameterization Schemes and Models for Estimating the Surface Radiation Budget". In Geernaert G L and Plant W J (eds) *Surface Waves and Fluxes, Volume II.* 339-368.

Katsaros K B, (1980), "The aqueous thermal boundary layer", B Lay Meteor, 18, 107-

Kawamura H and Toba Y (1988), "Ordered Motion in the Turbulent boundary layer over Wind Waves", J Flu. Mech, 197 pp 105-138

Kelly K A (1985), "Separating Clouds from Ocean in Infrared Images" in *Remote Sensing of Environment 17*, 67-83

Kent E C, Truscott B S, Taylor P K and Hopkin J S (1991) "The Accuracy of Ship's Meteorological Observations Results of the VSOP-NA". *Marine Meteorlogy and Related Oceanographic Activities* **Report No. 26**. WMO/TD-No 455.

Kim H I, Kliene, S J and Reynolds, W C (1971), "The Production of Turbulence near a Smooth Wall ina Turbulent Boundary Layer", *J Fl Mech*, 13, 457-

Knight R J (1988) "RAL Sea Surface Temperature Radiometer Operating Manual" Internal Report *Rutherford Appleton Laboratory*

Knight R J (1989) "Ral SST Radiometer Evaluation" *internal report Rutherford Appleton Laboratory*, Chilton

Lancaster, P F (1994) "The surface signature of mesoscale variability in the north east atlantic using satellite SST and *in-situ* data" , *PhD thesis, University of Southampton department of Oceanography*

Liu W T (1994). "Remote Sensing of Surface Turbulence Heat Flux". In Geernaert, G L and Plant, W J (eds) *Surface Waves and Fluxes, Volume II.* 293-309.

Liu, W T and Businger, J A; (1975), "Temperature profile in molecular sublayer near the interface of a fluid in turbulent motion", *Geopys. Res. Lett. 2, 403-404*

Llewellyn-Jones D T; Minnett P J; Saunders R W and Zavody A M (1984), "Satellite Multichannel Infrared Measurements of Sea Surface Temperature of the NE Atlantic Ocean Using AVHRR/2" in *Quart J R Met Soc 110*, 613-631

Mammen T C and Von Bosse, N (1989), "STEP - A Temperature Profiler for Measuring Oceanic Thermal Boundary Layer at the Ocean-Air Interface" in *J Atmos and Oceanic Tech 7*, 312-322

Mason G (1991), *ATSR Test and Calibration Report ER-RP-OXF-AT-0001*, internal report for Rutherford Appleton Laboratories

Mason I M; Sheather P H and Bowles J A (1987) "Design of a Black Body Sub-System for an Infra-red Radiometer" Internal report of *Mullard Space Science Laboratory*, University College London

Masuda K; Takashima T and Takayama Y (1988), "Emissivity of Pure and Sea Waters for the Model Sea Surface in the Infrared Window Regions" in *Remote Sensing of Environment 24*, 313-329

McAlister E D and McLeish W (1970), "A Radiometric System for Airborne Measurements of the Total Heat Flow from the Sea" in *App Optics 9*, 2,697-2,705

McClain E P (1981), "Multiple Atmospheric Window Techniques for Satellite-Derived Sea Surface Temperatures" in *Oceanography from Space*, Gower (ed)

McClain E P; Pichsel W G; Walton C C; Ahmad Z and Sutton J (1983), "Multi-Channel Improvements to Stalliet-Derived Global Sea Surface Temperatures" in *Adv Space Res 2* No 6, 43-47

McClain PE; Pichel W G and Walton C C (1985), "Comparative Performance of AVHRR-Based Multi-Channel Sea Surface Temperatures" in *J Geophys Res 90*, 11,587-11601

McMillin L M and Crosby D S (1984), "Theory and Validation of the Multiple Window Sea Surface Temperature Technique" in *J Geophys Res 89*, 3,655-3661

Minnett P (1990), "The Regional Optimisation of Infrared Measurements of Sea Surface Temperature from Space" in *J Geophys Res 95*, 13,497-13,510

Minnett P (1990), *Satellite Measurements of Sea-Surface Temperature: Some consequences of variability on validation and applications*, SACLANTEN Report SR-165

Minnett P J (1986), "A Numerical Study of the Effects of Anomalous North Atlantic Atmospheric Conditions on the Infrared Measurement of Sea Surface Temperature from Space" in *J Geophys Res 91*, 8,509-8,521

Minnett P J (1990). "Satellite Infrared Scanning Radiometer-AVHRR and ATSR/M" in Vaughan R A (ed), *Microwave Remote Sensing for Oceanographic and Marine Weather-ForecaseModels*, Kluwer Academic Publishers, Netherlands, 141-163.

Minnett P J (1993). " Preliminary Results of the Comparison of ATSR Measurements with *in situ* Sea Temperatures ". *ATSR Science Team Meeting, Validation Results.* Cosener's House Conference Centre. Abingdon, UK, March 30.

Minnett P J and Grassl H (1986), *Cooperative Studies of Climate Transients*, Rutherford Appleton Laboratory, Chilton, UK

Minnett P J and Stansfield K L (1993). "The Validation of ATSR Measurements with *in situ* Sea Temperatures". *Proc. Sec. ERS-1 Symp.* 1,233-1,237.

Minnett P J, Eyre J R and Pescod R W (1987), "The Variability of the North Atlantic Marine Atmosphere and its Relevance to Remote Sensing" in *Int J Remote Sensing 8* No 6, 871-880

Minnett P J; Eyre J R and Pescod R W (1985), *The Marine Atmosphere over the North-Eastern Atlantic Ocean: A monthly description of some variables relevant to satellite remote sensing of the ocean and atmosphere* internal report by NATO, SACLANT ASW Research Centre

Minnett P J; Zavody A M and Llewellyn-Jones D T (1984), "Satellite Measurements of Sea Surface Temerature for Cliimate Research" in *Large-Scale Oceanographic Experiments and Satellites,* Gautier C and Fieux M (eds), 57-85

Munk W H (1955). "Wind Stress on Water: An Hypothesis 320-332.

Mutlow C T, Llewellyn-Jones D T and Zavody A M (1993). "The Along Track Scanning Radiometer (ATSR) - Global Validation Results". *Proc. Sec. ERS-1 Symp.* 1245-1249

Mutlow C T, Zavody A M, Barton I J and Llewellyn-Jone D T (1994) "Sea Surface Temperature Measurements by the Along-Track Scanning Radiometer on ERS-1 Satellite: Early Results". *Int J Rem Sens, 15, 4, 827 - 843*

Neddermann R N, (1960), "Velocity Profiles Within Liquid Layers", PhD theses, St Johns College, Cambridge, England

Nichol J C J (ed) (1992). "Absracts: Sub-Mesoscale Air-Sea Interactions".*24th Interational Liege.Colloquium on Ocean.Hydrodynamics.*

Nightingale T (Draft Version 1)(1994*). "Ground Station Software Specification for the SISTeR Instruments"*. Rutherford Appelton Laboratory. Didcot, Oxfordshire.

Nijsing R (1969), "Predictions on Momentum, Heat and Mass Transfer in Turbulent Channel Flow with the Aid of a Boundary Layer Growth-Breakdown model", *Wärme-und Stoffübertragung* 2, 65-86

Njoku E G (1985). " Satellite-Derived Sea Surface Temperature: Workshop Comparisons". *Bulletin Am.Meter.Soc.*, **66**, 274-281.

Njoku E G (1994*). "Satellite Remote Sensing of Sea Surface Temperature" in Geernaert G L and Plant W J (eds) *Surface Waves and Fluxes, Volume II*, 311-347.

Ogura Y, Takeda A, Kimura R, Taira K and Nakai T (1969). "Survey of Sea Surface Temperature of the Tsushima Warm Current with Seabourne and Airbourne Radiation Thermometers, (GARP-Severe Rainstorm Research Project)". *J.Meteor.Soc.Japan*, **4**, 310-318.

Ogura Y, Tanaka H, Kimura R, Taira K, Misawa N, Ishikawa K, Yagihashi A, Hara Y, Kondo H and Otobe H (1969). "A comparison Between Sea Surface Temperature Measured by an Infrared Radiation Thermometer and that by the Bucket Method". *J.Oceanographical Soc.Japan*, **25**,5, 255-258.

Okuda K Kaiwai S and Toba Y (1977), "Measurement of Skin Froction distribution along the Surface of Wind Waves", *J Oceanogr. Soc Japan*, 33, 190-198

Panter M (1994). *ATSR Subset and Map (ASAM) Program Users Guide.* Rutherford Appleton Lab. Didcot, Oxfordshire.

Paulson C A and Parker T W (1972), "Cooling of a Water Surface by Evaporation, Radiation and Heat Transfer" in *J Geophys Res 77*, 491-495

Paulson C A and Simpson J J (1981), "The Temperature Difference Across the Cool Skin of the Ocean" in *J Geophys Res 86*, 11,044-11,054

Payne R E (1972), "Albedo of the Sea Surface", J Atmos. Sci, 29, 959-

Prandtl L (1948), "Strömungslehre, Braunschweig, Vieweg u. Sohn", 407p

Rao,K N, Narashimhia B, Narayanan, (1971), "The Bursting phenomenon in a turbulent boundary layer", J Flu Mech 48, 339-

Ray P S (1972), "Broad-Band Complex Reflective Indices of Ice and Water" in *App Optics 11* No 8, 1,836-1,844

Robertson J E and Watson A J (1992). " Thermal Skin Effect of the Surface Ocean and Its Implications for CO2 Uptake". *Nature*, **358**, 738-740.

Robinson I S (1985), *Satellite Oceanography: An Introduction for Oceanographers and Remote-Sensing Scientists*, Ellis Horwood Ltd Chichester

Robinson I S and Donlon C , Llewellyn-Jones D T and Mutlow C (1993). "Filaments and Fine Structure of Sea Surface Temperature in ATSR Image Data". *Proc. Sec. ERS-1 Symp.*

Robinson I S and Smith P S D (1991), *A Study of Procedures for the Estimation of Satellite-Based Sea Surface Temperature Data Sets*, Final report Dept. Oceanography University of Southampton

Robinson I S and Ward N (1989), "Comparison Between Satellite and Ship Measurements of Sea Surface Temperature in the North-East Atlantic Ocean" in *Int J Remote Sensing 10*, 787-799

Robinson I S; Wells N C and Charnock H (1984), "The Sea Surface Thermal Boundary Layer and its Relevance to the Measurement of Sea Surface Temperature by Airborne and Spaceborne Radiometers" Review article in *Int J Remote Sensing 5*, 19-45

Satellites International Limited (1991). Users Manual: Radiometer R102-0-02, Issue 2.

Saunders P M (1967a), "The Temperature at the Ocean-Air Interface" in *J Atmos Sci 24*, 269-273

Saunders P M (1967b), "Aerial Measurement of Sea Surface Temperatures in the Infrared" in *J Geophys Res 72* No 16, 4,109-4,117

Saunders R W (1986), "An Automated Scheme for the Removal of Cloud Contamination from AVHRR Radiances over Western Europe" in *Int J Remote Sensing 7* No 7, 867-886

Saunders R W and Kriebel K T (1988), "An Improved Method for Detecting Clear Sky and Cloud Radiances from AVHRR Data" in *Int J Remote Sensing 9* No 1, 123-150

Saur J F T (963). " A Study of the Quality of Sea Water Temperatures Reported in Logs of Ships' Weather Observations". *J.App..Meteor.* ,**2**, 417-425.

Schleussel P; Emery W J; Grassl H and Mammen T (1990), "On the Bulk Skin Temperature Difference and its Impact on Satellite Remote Sensing of Sea Surface Temperature" in *J Geophys Res 95*, 13,341-13,356

Schleussel P; Shin H Y; Emery W J and Grassl H (1987), "Comparison of Satellite-Derived Sea Surface Temperatures With in Situ Skin Measurements" in *J Geophys Res 92*, 2,859-2,874

Schluessel P (in press), *"Impact of the Skin Effect on the Remote Sensing of Sea Surface Temperature"*, manuscript submitted to D R Slogget (ed), "The Remote Sensing Reference Book"

Schluessel P, Wick G A and Emery W J (1992). "A Comprehensive Comparison between Skin and Multi-Channel Sea Surface Temperatures as Derived from AVHRR " *Proc. Cen.Symp. of the 'International Space Year'*. 341-345

Schlussel P and Meywek J (1993) "ATSR Correlative Skin Measurements of Sea Surface Temperature" *Proc. First ERS-1 Symp.* 779-784.

Schmidt, W (1908), "Absorption der Sonnenstrahlung im wasser", *S. B. Akad. Wiss. Wien, 117*

Schooley A H (1975). "Simple Method for Measuring Relative Humidity, Water and Air Temperatures within a few Millimeters of Wind-Generated Water Waves". *J.Phys.Oceanog.*, **5**, 519-522.

Schooley A H (1977). " Temperature of Ocean Skin Related to Cloud Shadows". *J.Phys.Oceanog.*, **7**, 486-488.

Selby J E; Shettle, E P and McClatchey, R A, (1978), "Atmospheric Transmittance from 0.25 to 28.5 μm", *AFGL Rep. AFGL-TR-76-0258*

Shonting D H, (1963), "Some observations of short term heat transfer through the surface layers of the ocean", *Report from US Naval Underwater Ordanance Station, Newport, Rhode Island*

Simpson J J and Paulson C A (1979), "Small-Scale Sea Surface Temperature Structure" in *J Phys Oceanog 10*, 399-410

Smith S (1980), "Wind Stress and Heat Flux Over the Ocean in Gale Force Winds" in *J Phys Oceanography 10*, 709-726

Smith S D (1988), "Coefficients for Sea Surface Wind Stress, Heat Flux, and Wind Profiles as a Function of Wind Speed and Temperature" in *J Geophys Res 93* 15,67-15,472

Soloviev A V and Vershinsky N V (1982), "The Vertical Stucture of the Thin Surface Layer of the Ocean Under Conditions of Low Wind Speed", in *Deep Sea Res 29*, 1,437-1,449

Steyn-Ross D A and Steyn-Ross M L (1992). " Radiance Calibrations for Advanced Very High Resolution Radiometer Infrared Channels". *J. Geophys.Res*, **97**, 5,551-5,568.

Stommel H; Saunders K; Simmons W and Cooper J (1969), "Observations of the Diurnal Thermocline", in *Deep Sea Res 16*, 269 - 284

Stramma L, Cornillion P , Weller R A , Price J F and Briscoe M G (1986). "Large Diurnal Sea Surface Temperature Variability: Satellite and *in situ* Measurements". *J.Phys.Oceanog*, **16**,827-837.

Takayama Y (1994). " Sea Surface Temperature Estimation by Application of Microwave Dual-Frequency Data to Infrared Data". *J.Geophys.Res.*, **99**, 14,311-14,319.

Thiermann V (1985), "Validation of the Meterological Data Measured During the METEOR Cruise No.69 and Some Results as Part of the METEOR 69 Satellite Data ~Verification Set" in *Cooperative Studies of Climate Transients* Rutherford Appleton Laboratory, Chilton

Thomas J P and Turner J (1993). " An Assessment of the Accuracy of ATSR Dual View Sea Surface Temperature Algorithms". *Proc. Sec.ERS-1Symp*, 1,093- 1097.

Thorpe S A (1985). "Small-Scale Processes in the Upper Ocean Boundary Layer". *Nature*. **318**, 519-522.

Vass P and Handoll M (1991), *UK ERS-1 Reference Manual*, Earth Observation Data Centre, RAE Farnborough

Walton C C (1988), "Nonlinear multichannel algorithm for estimating sea surface temperature with AVHRR satellite data", J Appl Meter, 27, 115-

Wick G A Emery W J and Schlussel P (1992). "A Comprehensive Comparison between Satellite-Measured Skin and Multichannel Sea Surface Temperature". *J. Geophys. Res.*.**97**, 5,569-5,595.

Wick G, Emery W J, Kantha H and Schluessel P, (1994), The Behavoiur of the Bulk-Skin Sea Surface Temperature Difference under Varying Wind Speed and Heat Flux", unpublished manuscript

Woodcock A H and Stommel, H (1947,, "Teperatures observed near the surface of a fresh water pond at night", *J Meteorol, 4, 102-103*

Woodcock a H, 1941, "Surface Cooling and Streaming in shallow fresh and salt waters", J Mar Res, 4, 153

Woolf D K and Thorpe S A (1991), "Bubbles and the air-sea exhange of gasses in near-saturation conditions", *J Mar. Res., 49, 435-466*

Wu J (1980), "Wind Stress Coefficients over Sea Surface Near Neutral Conditions - A Revisit" in *J Phys Oceanog 10*, 727-740

Wu J (1985), "On the cool skin of the ocean", B Lay Meteor, 31, 203-

Yokoyama R and Tanba S (1991). "Estimation of Sea Surface Temperature via AVHRR of NOAA-9 - Comparison with Fixed Buoy Data". *Int.J.Remote Sensing*. **12**, 2,513-2528.

Yokoyama R, Tanba S and Souma T (1993). " Air-Sea interacting Effects to the Sea Surface Temperature Observation by NOAA/AVHRR". *Int.J.Remote Sensing*, **14**, 2,631-2646.

Yu Y, Barton I J (1994). "A Non-Regression-Coefficients Method of Sea-Surface Temperature Retrieval from Space". *Int.J.Remote Sensing*, **6**, 1.189-1,206

Zavody A M , Mutlow C T, Llewellyn-Jones D T and Barton I J (1993) "Quantitative Remote Sensing in the 11μm Wavelength Region Using ATSR". *Proc.Sec.ERS-1 Symp.* 829-833.

Zavody A M, Gorman M R, Lee D J, Eccles D, Mutlow C t and Llewellyn-Jones D T (1994). "The ATSR Data Processing Scheme Developed for the EODC". *Int.J.Remote Sensing*, **15**, 827-843.